

METAL-ORGANIC FRAMEWORKS (MOFs) AND THEIR DERIVED MATERIALS AS ELECTROCATALYST FOR ENERGY CONVERSION AND STORAGE APPLICATION

By
RAJAT KUMAR TRIPATHY
CHEM11201604023

**National Institute of Science Education and Research (NISER)
Jatni, Odisha-752050**

*A thesis submitted to the
Board of Studies in Chemical Sciences*

*In partial fulfillment of requirements
for the Degree of*

DOCTOR OF PHILOSOPHY

of

HOMI BHABHA NATIONAL INSTITUTE

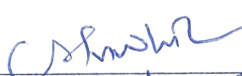
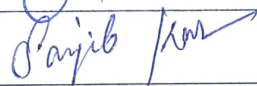


March-2022

Homi Bhabha National Institute¹

Recommendations of the Viva Voce Committee

As members of the Viva Voce Committee, we certify that we have read the dissertation prepared by **Rajat Kumar Tripathy** entitled “**Metal-Organic Frameworks (MOFs) and their derived materials as electrocatalyst for energy conversion and storage application**” and recommend that it may be accepted as fulfilling the thesis requirement for the award of Degree of Doctor of Philosophy.

Chairman – Prof. A. Srinivasan		Date: 13.07.22
Guide / Convener – Dr. J. N. Behera		Date: 13/07/22
Examiner – Prof. Paritosh Mohanty		Date: 13/07/22.
Member 1- Dr. C. S. Purohit		Date: 13/07/22
Member 2- Dr. Sanjib Kar		Date: 13/07/22
Member 3- Dr. Srikanta Patra	Sri Kanta Patra	Date: 13.07.22.

Final approval and acceptance of this thesis is contingent upon the candidate's submission of the final copies of the thesis to HBNI.

I/We hereby certify that I/we have read this thesis prepared under my/our direction and recommend that it may be accepted as fulfilling the thesis requirement.

Date: 13/07/22

Place: NISER, Bhubaneswar



(Dr. J. N. Behera)

Guide

¹ This page is to be included only for final submission after successful completion of viva voce.

STATEMENT BY AUTHOR

This dissertation has been submitted in partial fulfillment of requirements for an advanced degree at Homi Bhabha National Institute (HBNI) and is deposited in the library to be made available to borrowers under rules of the HBNI.

Brief quotations from this dissertation are allowable without special permission, provided that accurate acknowledgment of source is made. Requests for permission for extended quotation from or reproduction of this manuscript in whole or in part may be granted by the Competent Authority of HBNI when in his or her judgment the proposed use of the material is in the interests of scholarship. In all other instances, however, permission must be obtained from the author.



Rajat Kumar Tripathy

DECLARATION

I, hereby declare that the investigation presented in the thesis has been carried out by me. The work is original and has not been submitted earlier as a whole or in part for a degree / diploma at this or any other Institution / University.



Rajat Kumar Tripathy

List of Publications

Journal

(a) Published

1. “A Cobalt metal-organic framework (Co-MOF): a bi-functional electro active material for the oxygen evolution and reduction reaction”, **Rajat K. Tripathy**, A. K. Samantara and J. N. Behera, *Dalton Trans.*, **2019**, 48, 10557- 10564.
2. “Metal-organic framework (MOF)-derived amorphous Nickel Boride: an electroactive material for electrochemical energy conversion and storage application”, **Rajat K. Tripathy**, A. K. Samantara and J. N. Behera, *Sustainable Energy & Fuels*, **2021**, 5, 1184-1193.
3. “Cobalt metal-organic framework (Co-MOF) derived CoSe₂/C hybrid nanostructures for the electrochemical hydrogen evolution reaction supported by DFT studies”, **Rajat K. Tripathy**, A. K. Samantara, Pratap Mane, Brahmananda Chakraborty and J. N. Behera, *New Journal of Chemistry*, **2022**, 46, 2730-2738.
4. “Electrochemically activated Co-Prussian blue analogue derived amorphous CoB nanostructures: an efficient electrocatalyst for the oxygen evolution reaction”, **Rajat K. Tripathy**, A. K. Samantara and J. N. Behera, *Dalton Trans.*, **2022**, 51, 2782 – 2788.

5. “Monosaccharides linked Schiff base metal complexes of Cu (II), Zn (II) and Mn (II): Exploring the antiproliferative activity and cell death mechanism”, Shyam Sundar Mondal, Namita Jaiswal, **Rajat K. Tripathy**, Partha Sarathi Bera, Nripen Chanda, J. N. Behera, Subhas Ghosal, Tanmoy Kumar Saha, *Chemistry select*, **2022**, 7, e202200060.

6. “Prussian blue analogue (PBA) derived cobalt telluride nano-granules: an efficient catalyst for energy conversion and storage”, **Rajat K. Tripathy**, Abhisek Padhy, Nachiketa Sahu, J. N. Behera, *Sustainable Energy & Fuels*, **2022**, doi: 10.1039/d2se00665k.

b) Communicated

1. “Organically templated linear and layered Tin (II) sulphates”, Manisha Sadangi, Subba R. Marri, **Rajat K. Tripathy**, J. N. Behera.

c) Chapters in books and lectures notes

1. A. K. Samantara, **Rajat K. Tripathy** and J. N. Behera, Hybrid Nanocomposites Based on Graphene and Gold Nanoparticles: From Preparation to Applications, Springer, **2021**, Paperback ISBN: 978-981-334-987-2.

Conferences attended

1. Presented a poster in virtual conference on catalysis science and technology 10th anniversary symposium 2021 during 16-17 November 2021 by Royal Society of Chemistry.

2. Presented a poster in virtual international conference on Recent Advances on Catalysis Science and Engineering (RACSE-2021) held during 26-28th October 2021 by NIT Jamshedpur.

3. Participated in 1st International Conference on Emerging Porous Materials ePorMat-2021 held during 29th-30th July 2021 at NISER.

4. Presented a poster and secured **second** position in the Best poster presentation Award during 33rd Annual conference of Orissa Chemical Society (OCS-2019) and 5th National Conference on Recent Advancement in Material Sciences (RAIMS-2019).

5. Presented a poster in International Conference on Nanomaterials for Energy Environment and Sustainability (ICNEES-2019) and got **best poster award** during 20th-22nd December 2019 at CNSNT, ITER, BBSR.

6. Participated in national Conference on “National Bioorganic Chemistry Conference”, (NBCC)-2018, held during the 22nd-24th December at NISER.

7. Participated in national Conference on “INTER IISER and NISER CHEMISTRY MEET”, (IINCM)-2017, held during the 22nd-24th December at NISER.

Rajat Kumar Tripathy

Rajat Kumar Tripathy

**Dedicated to
Almighty**

ACKNOWLEDGEMENTS

*I would like to thank my supervisor **Dr. Jogendra Nath Behera**, for continuous support, encouragement, patience exhibited and believing in me.*

I am thankful to Prof. Sudhakar Panda, Director-NISER, for the laboratory facilities and financial support.

I thank my Doctoral committee members, Prof. A. Srinivasan and Dr. C. S. Purohit, Dr. S. Kar, Dr. Srikanta Patra, and all other faculties in SCS. I remember our collaborators, Dr. Brahmananda Chakraborty (BARC, Mumbai) (IIT-KGP). I appreciate the help provided by Prof. Paritosh Mohanty (IIT Roorkee), Dr. Sumanta Kumar Meher (NIT, Jaipur), Dr. A. Thurumurugan (IISER, Thiruvananthapuram), Dr. C. S. Rout (JAIN UNIVERSITY, BENGALURU), Satyajit Rath (IIT-BBSR) with immense pleasure for their valuable contributions.

I thank all my past lab members Dr. Subba Reddy Marri, Niharika, Saumya, Ipsha, Radhamadhab, Vamsi Krishna. I remain grateful for their help and support.

Thank my present lab members Dr. Aneeya Kumar Samantara, Dr. Jiban Krushna Das, Malay, Abhisek, Nachiketa, Manisha, Nisa, Nikhil, Rahul, Smruti, Deepak and Ayushi, for creating a healthy atmosphere in the lab and their valuable discussions.

*I remember all my friends in NISER with great gratitude and my juniors, especially Subhrakant and Debashis (IISC Bangalore). Above all, I would like to thank my parents allowing me to pursue this degree, my sisters for their unconditional love, care, affection, and support. Finally, this journey seems to be impossible without the blessings of “**Lord Jagannatha**” - the lord of the universe who made me realize “**I am always with you.**”*

Rajat Kumar Tripathy

Rajat Kumar Tripathy

CONTENTS

	Page No
Thesis title	I
Recommendations of Viva-Voce Board	II
Statement by the Author	III
Declaration	IV
Publication List	V
Dedications	VIII
Acknowledgments	IX
Contents	X
Synopsis	XI
List of Scheme	XXI
List of Figures	XXI
List of Tables	XXXI
List of Abbreviations	XXXII
Chapter-1	1
Chapter-2	57
Chapter-3	83
Chapter-4	109
Chapter-5	131
Summary	164

SYNOPSIS

Herein, my thesis has been divided into five parts. Chapter 1 is exclusively describing on MOFs and their derived materials exhibiting application towards energy conversion and storage. Chapter 2 gives idea on synthesis of Cobalt MOF and its application towards oxygen evolution reaction (OER) and oxygen reduction reaction (ORR). Chapter 3 deals with Co-MOF derived CoSe₂ for hydrogen evolution reaction (HER) supported by theoretical study. Chapter 4 describes on MOF (Co-PBA) derived Co-B; a pre-catalyst meant for oxygen evolution reaction (OER) and Chapter 5 narrates about MOF derived amorphous NiB for both oxygen evolution reaction (OER) and supercapacitor application.

Chapter-1: Emerging metal-organic frameworks (MOFs) and their derived materials for energy conversion and storage.

The clean energy production is now becoming a promising challenge due to limited abundance of fossil fuels and sustainability of human race. Among all the strategies conducted for clean energy production, electrochemical water splitting (EWS) plays a vital role producing H₂, O₂ which can be used as fuels.¹ In electrocatalysis process, initially noble metals were used as electrocatalysts for the generation of H₂ and O₂. However, the low abundance and high price of noble metals restrict their application, as a consequence, non-noble first row transition metals are used to replace such metals. As we know solar energy and wind energy are intermittent in nature; hence in this modern era, energy storage is much important than energy production especially for the natural calamity friendly territory. For the fulfillment of energy crisis in terms of production and storage metal-organic frameworks are considered as the most widely investigated materials due to availability of ultrahigh surface area, tunable structures and high porosity.^{2,3} Prussian blue analogue (PBA) also considered as a class of metal-organic framework due to presence of direct metal linker (N, O, S, C) bond.⁴ Therefore, in the last

decade PBA and their derived materials are considered as an emerging material for energy production and storage.

Chapter-2: ORR and OER study of Cobalt metal-organic framework (Co-MOF).

This chapter deals with the synthesis of Cobalt metal-organic framework via a conventional hydrothermal method and its electrocatalytic behavior towards oxygen reduction reaction (ORR) and oxygen evolution reaction (OER) in alkaline condition. In a typical three electrode measurement, first we studied the electrocatalytic behavior towards ORR (0.1 M KOH) in argon saturated as well as oxygen saturated electrolyte and found that unlike argon atmosphere, a distinct reduction peak was observed in oxygen saturated atmosphere confirms Co-MOF is a potential candidate towards ORR. Furthermore, the LSVs are taken in various rotation ranging from 100 to 1600 rpm and found that at higher rotation rate due to diffusion of more ions the reduction current density increases accordingly. To know the actual catalytic path, we draw the

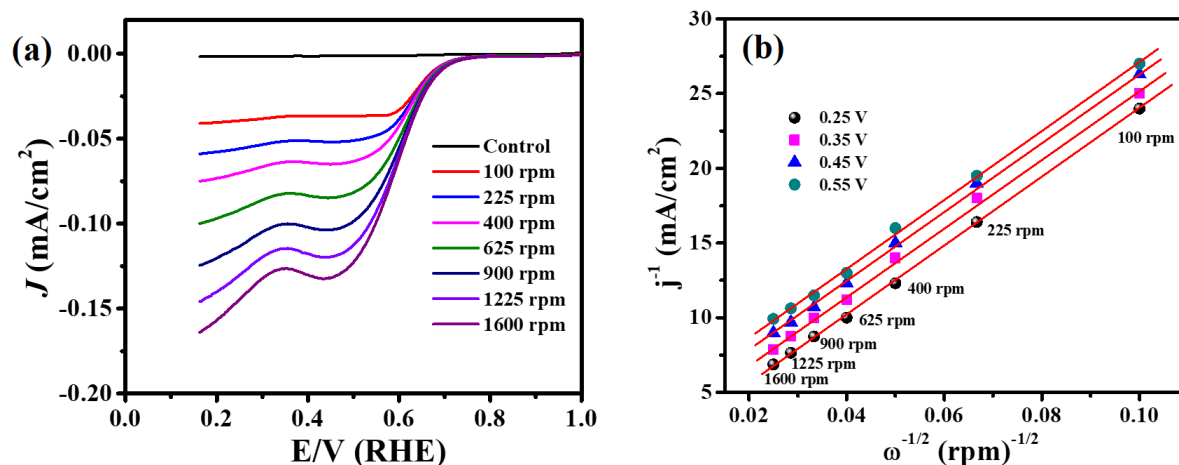


Figure 1. (a) Linear sweep voltammograms at different rotations of the electrode (b) the Koutecky–Levich plot.

K-L plot and found that the ORR undergoes 4e pathways.⁵

To know the durability of the material, chronoamperometric test was performed. The Co-MOF was stable in the 0.1 M KOH electrolyte up to 15 hours of constant electrocatalysis. We also explored its electrocatalytic behavior towards OER and observed that the Co-MOF required only 280 mV overpotential to reach benchmark current density $10 \text{ mA} \cdot \text{cm}^{-2}$. The reaction kinetics was obtained from Tafel plot and found that Co-MOF exhibits $51 \text{ mV} \cdot \text{decade}^{-1}$ Tafel slope better than the reference RuO_2 . To know the actual catalytic area responsible for electrocatalytic performance, electrochemical surface area (ECSA) was evaluated. To know the intrinsic catalytic behavior, turn over frequency (TOF) was calculated and found the Co-MOF has highest TOF compared to reported literature.⁶ To know the stability of MOF, we conducted chronopotentiometry test and observed that there was appreciable no change in morphology as well as pxd pattern after 13 hours of electrolysis revealing the durability and

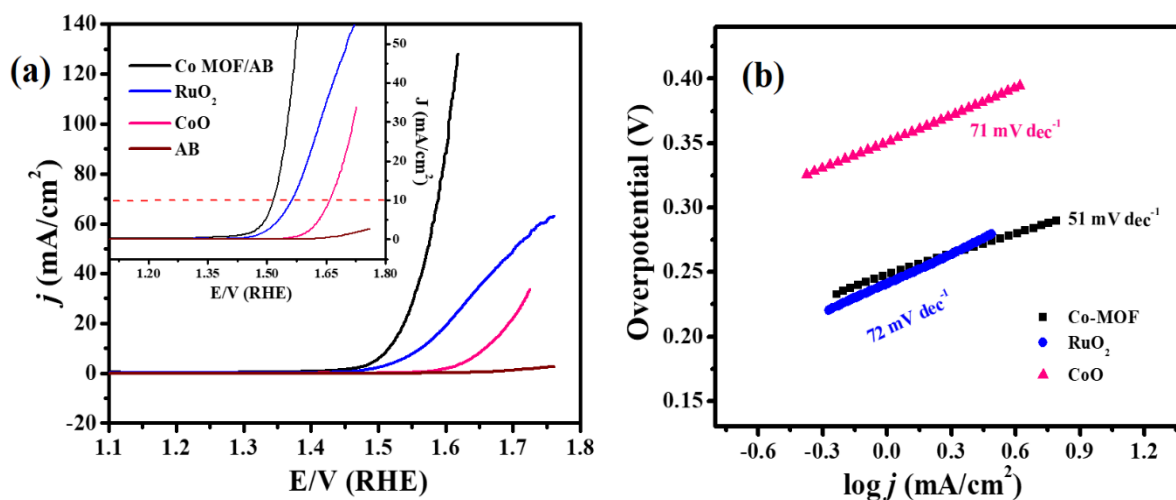


Figure 2. (a) LSVs for the OER by Co-MOF/AB, commercial RuO_2 , CoO (after TGA), and AB in a 1 M KOH electrolyte at the sweep rate of 5 mV s^{-1} and (b) the corresponding Tafel plot.

robustness of Co-MOF.

Chapter-3: DFT supported Cobalt metal-organic framework (Co-MOF) derived CoSe₂/C hybrid nanostructures for electrochemical hydrogen evolution reaction.

This chapter describes the typical synthesis of carbonaceous CoSe₂ via a hydrothermal method. In this method, Co-MOF taken as precursor and adding Se powder in DMF solvent at 200 °C for 12 hours. We observed selenization as well as graphitization, confirmed from PXRD, Raman and XPS study. To know the morphology, FESEM was conducted and found that CoSe₂/C exhibits rod shape like morphology with diminished dimension compared to Co-MOF precursor. Furthermore, the electrocatalytic behavior towards HER was explored in acidic

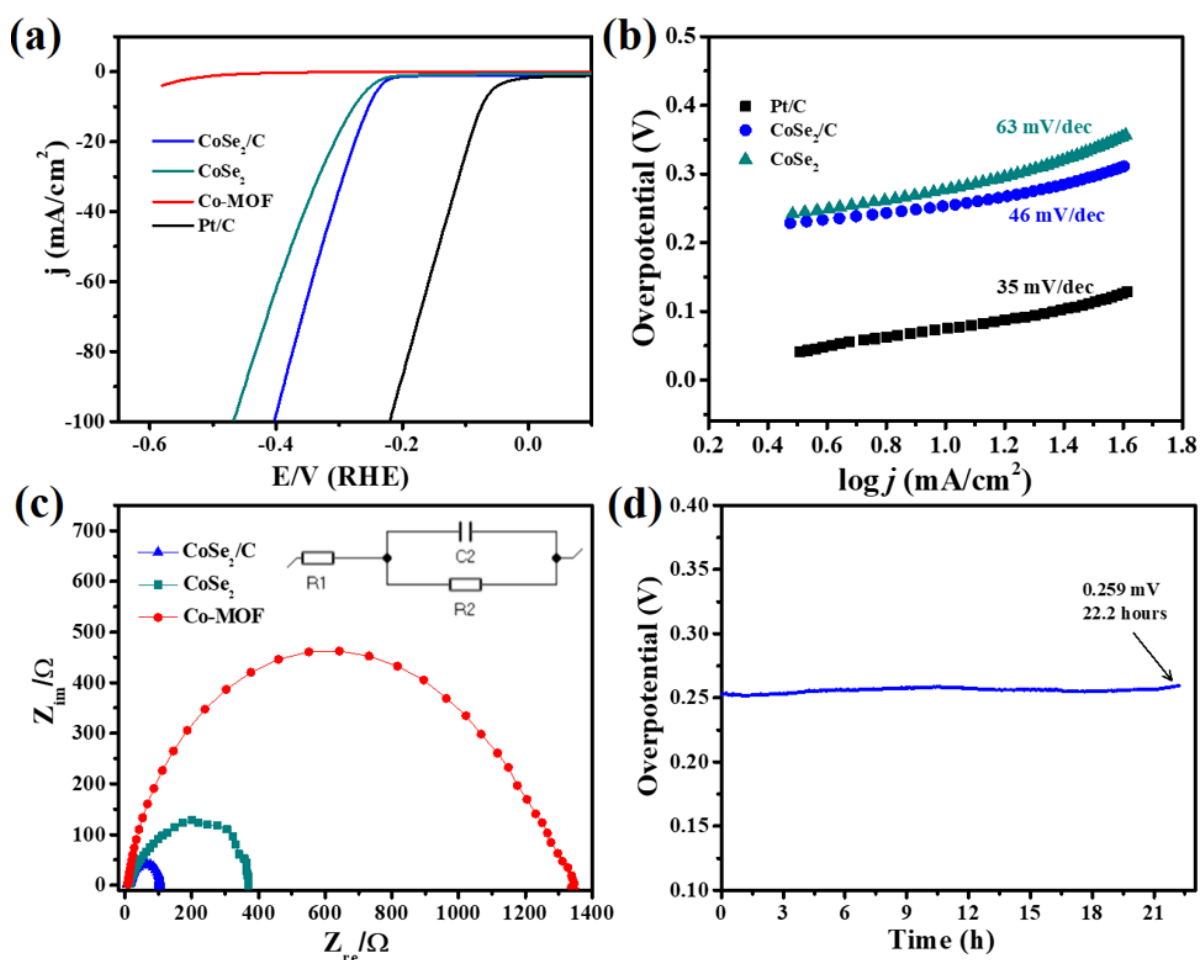


Figure 3. (a) Linear sweep voltammograms by CoSe₂/C, CoSe₂, Co-MOF and Pt/C showing HER in 0.5 M H₂SO₄, (b) corresponding Tafel slopes, (c) Nyquist impedance spectrum for CoSe₂/C, Co-MOF and CoSe₂ nanostructures and (d) stability of CoSe₂/C catalyst for HER at 10 mA/cm² current density.

medium.⁷ Unlike the precursor MOF, the derived CoSe₂/C required only 253 mV overpotential to exhibit 10 mA.cm⁻² current density, lower in compared to pristine MOF and bare CoSe₂. Also, small Tafel slope was observed for CoSe₂/C, confirms that it undergoes fast reaction kinetics. To know the conductivity, Nyquist impedance measurement was carried out and we concluded that the CoSe₂/C show small charge transfer resistance compared to bare cobalt selenide and pristine MOF. To know the actual electrochemical surface area ECSA was calculated. Chronopotentiometry test confirmed that carbonaceous cobalt selenide exhibits about 22 hours of electrocatalytic stability in 0.5 M H₂SO₄ better than the reported literature.⁸ To know the fate of our material after long term stability, FESEM and PXRD was taken and found appreciable no change after stability test. Furthermore, DFT analysis support the carbon doping of cobalt selenide.

Chapter-4: Electrochemically activated PBA derived amorphous CoB nanostructures: Efficient electrocatalyst for oxygen evolution reaction.

This chapter includes the synthesis of Cobalt Prussian blue analogue (Co PBA), a class of

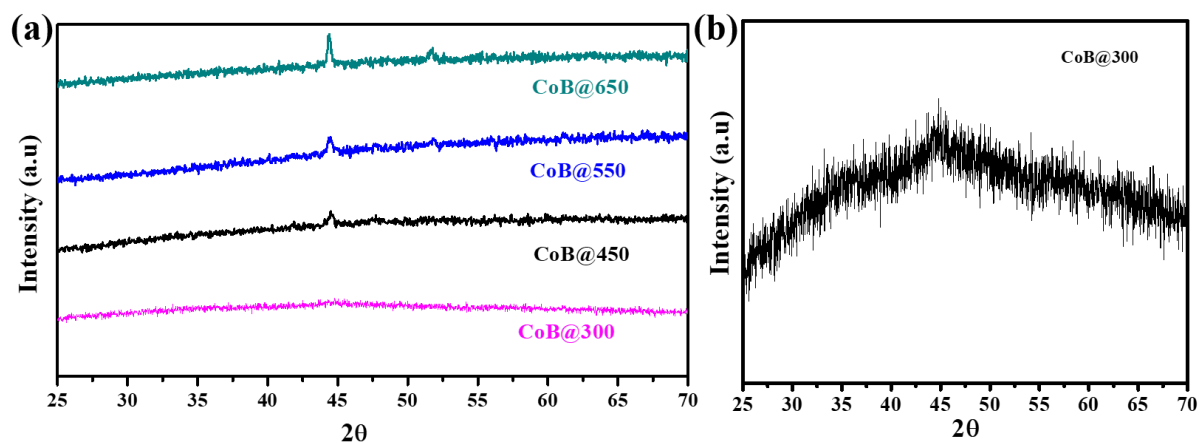


Figure 4. (a) PXRD pattern of CoB annealing at various temperature (b) Broad peak found at 45° for CoB@300.

metal-organic framework and its derived boride nanoparticles.^{4,9} We then studied its electrocatalytic behavior towards oxygen evolution reaction in alkaline condition.

We first synthesized series of CoB through simple chemical redox method by adding NaBH_4 dropwise manner followed by annealing at various temperature ranging from $300\text{ }^\circ\text{C}$ to $650\text{ }^\circ\text{C}$ and named as CoB@300, CoB@450, CoB@550 and CoB@650 respectively. We observed with increase in temperature the crystallinity of borides increases and CoB@300 is amorphous in nature due to presence of broad peak at 45° .

To know the morphology of all the fabricated borides, FESEM was taken and found that CoB@300 exhibits layer type morphology whereas spherical nanoparticles are formed and becomes agglomerated with increasing temperature. The composition of CoB was analyzed by

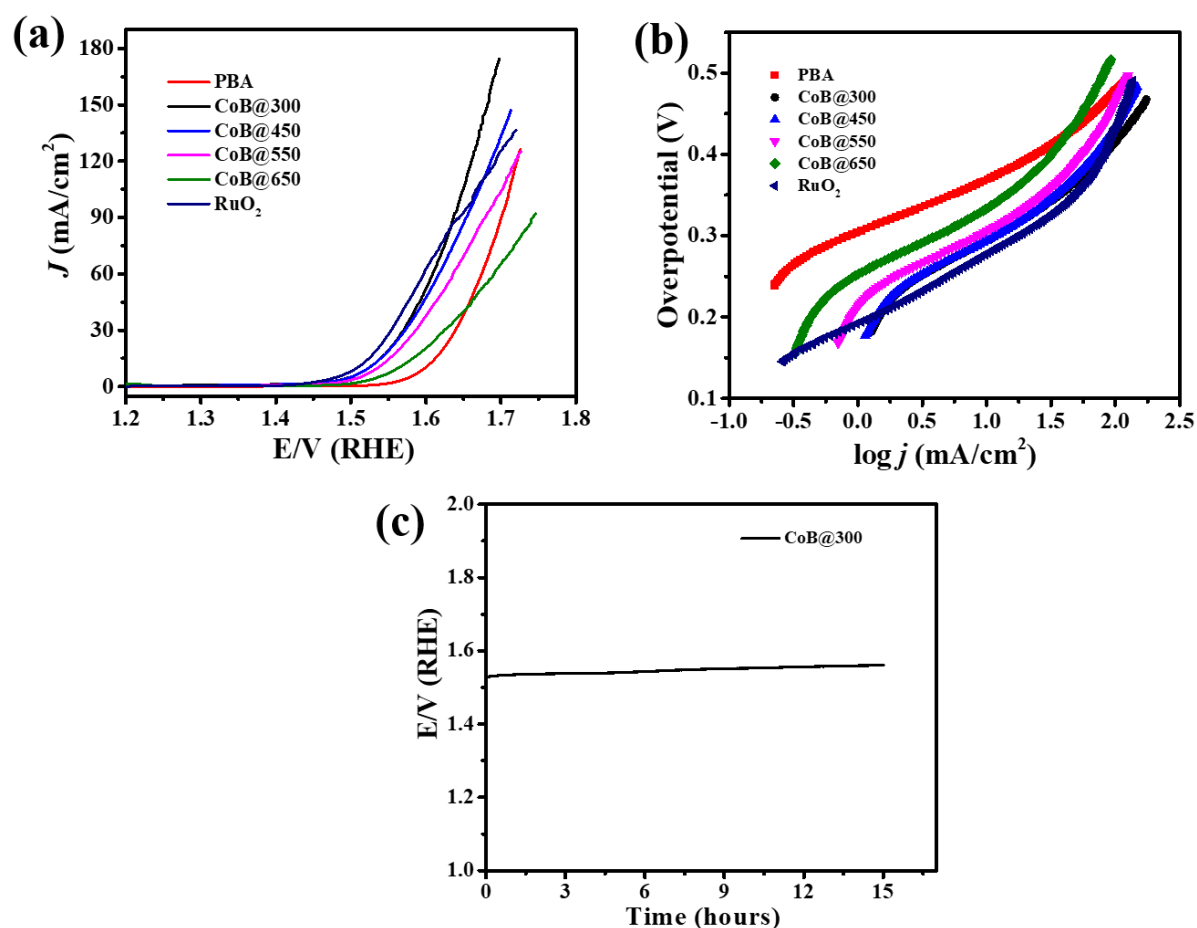


Figure 5. (a) LSV plot of CoB@300, CoB@450, CoB@550, CoB@650, PBA and RuO₂ in 1 M KOH (b) Corresponding Tafel plot (c) Chronopotentiometry test at $10\text{ mA}\cdot\text{cm}^{-2}$.

XPS and confirmed the presence of Co, B, N, C. We then explored its electrocatalytic behavior towards oxygen evolution reaction (OER) in 1 M KOH electrolyte. We observed around 290

mV overpotential is required to drive the water oxidation reaction. To know the actual catalyst involves in the catalytic cycle, we run a CV and performed PXRD after CV. We observed distinguished oxidation peak in CV for the transformation of Co^{+2} to Co^{+3} . The PXRD confirmed the formation of CoOOH and Cobalt metaborite presume to form core-shell structure with outer former and metaborite as inner core. Furthermore, the electrocatalytic properties like ECSA, roughness factor (R_f), TOF, mass activity was evaluated and found that the amorphous CoB@300 outperforms among all the boride materials. Also, the CoB@300 stable up to 15 hours of electrolysis and undergo appreciable changes confirmed from PXRD, FESEM and XPS.

Chapter-5: Amorphous nickel boride: A metal-organic framework derived electroactive material for energy conversion and storage.

This chapter describes the synthesis of metal-organic framework derived amorphous nickel boride and explore it's electrocatalytic behavior towards OER and supercapacitor application in alkaline condition. The phase purity of the precursor MOF and derived NiB was confirmed by PXRD pattern. The elemental composition and oxidation of element was verified by XPS analysis and found the presence of Ni, B, C, N. The morphology of sample was obtained by

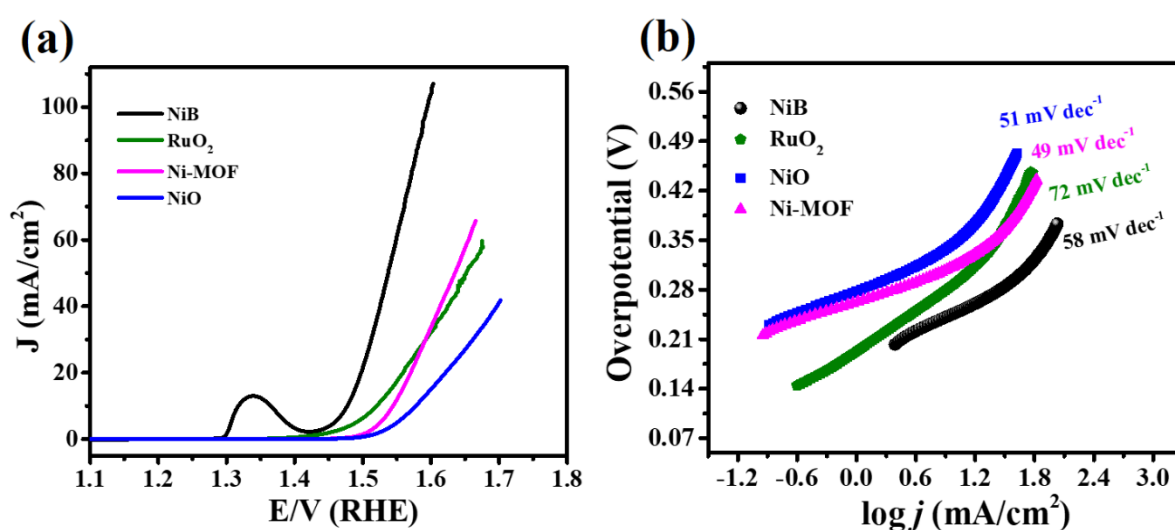


Figure 6. (a) LSV plots of NiB, Ni MOF, RuO₂ and NiO (b) Corresponding Tafel plot in 1 M KOH electrolyte.

FESEM. The Ni MOF exhibits block shaped whereas spherical nanoparticles were obtained for NiB. The absent of Debye ring obtained from SAED pattern and broad peak in PXRD pattern confirms the amorphous nature of NiB.

Moreover, the electrocatalytic behavior towards oxygen evolution reaction (OER) in 1 M KOH electrolyte was studied and found NiB required only 240 mV overpotential to exhibit 10 mA.cm⁻² current density. Due to metal metalloid interaction the NiB exhibits better stability test about among all the comparative materials. It stables up to 15 hours of electrocatalysis in 1 M KOH and found remarkable change. The post OER study was performed doing PXRD, FESEM and XPS. We presume there was formation of core-shell structure confirmed from XPS.^{10,11} Furthermore, to know the intrinsic catalytic activity, ECSA, TOF, R_f were calculated. Further the CVs and GCDs were recorded in 5 M KOH electrolyte and found the specific

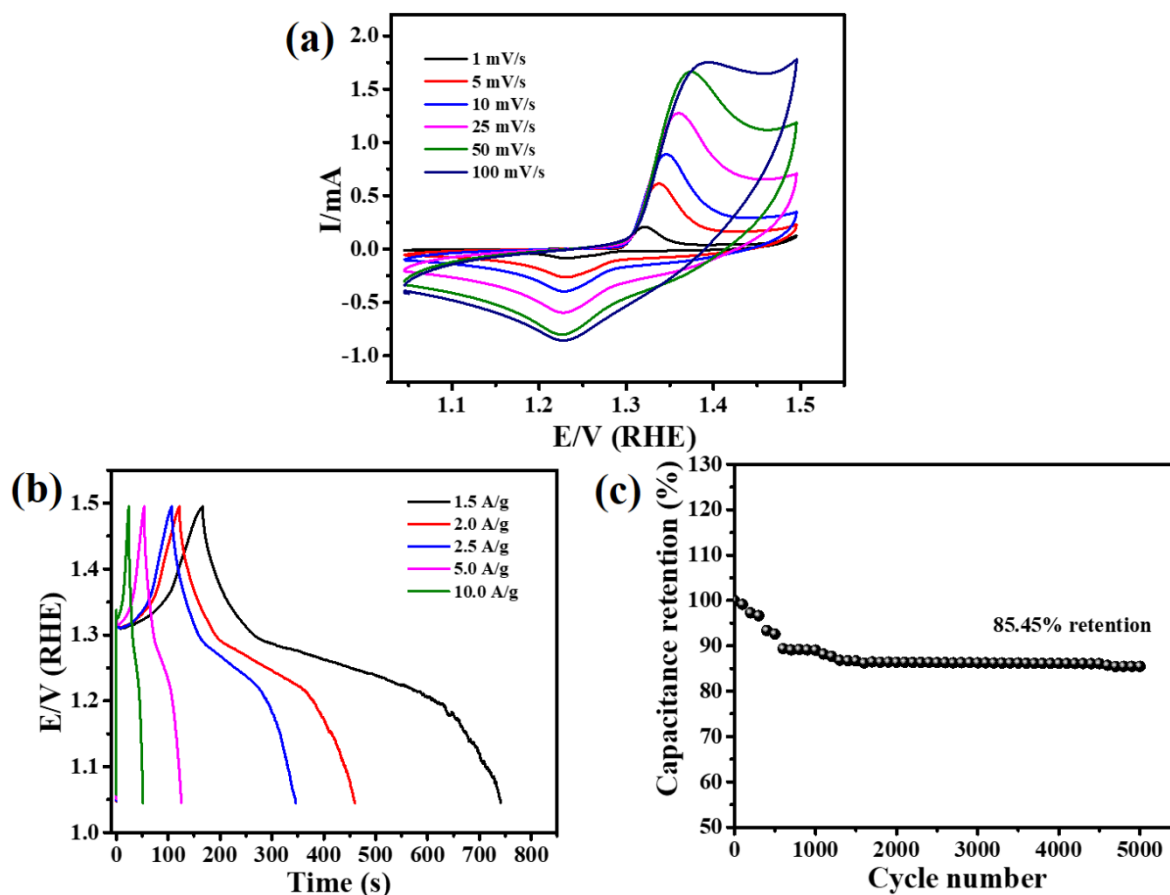


Figure 7. (a) CV at various scan rate (b) Corresponding GCD at different energy densities (c) Cyclic stability of NiB in 5 M KOH.

capacitance 2500 F/g. The capacitive retention was found around 85% after 5000 cycles. Then asymmetric supercapacitor was fabricated by taking rGO as cathode and NiB as anode. In a two-electrode measurement, by optimizing potential window we got specific capacitance 83.33 F/g. It shows the capacitive retention 96 % after 5000 cycles and coulombic efficiency around 90 %. The fate of sample was confirmed from PXRD, FESEM and Nyquist plot and found appreciable no change in alkaline condition.

References

- 1 H. Jin, C. Guo, X. Liu, J. Liu, A. Vasileff, Y. Jiao, Y. Zheng and S. Z. Qiao, *Chem. Rev.*, 2018, **118**, 6337–6408.
- 2 Y. Li, Z. Y. Fu and B. L. Su, *Adv. Funct. Mater.*, 2012, **22**, 4634–4667.
- 3 J. L. C. Rowsell, E. C. Spencer, J. Eckert, J. A. K. Howard and O. M. Yaghi, *Science.*, 2005, **309**, 1350–1354.
- 4 H. Yi, R. Qin, S. Ding, Y. Wang, S. Li, Q. Zhao and F. Pan, *Adv. Funct. Mater.*, 2021, **31**, 1–25.
- 5 H. Zhong, Y. Luo, S. He, P. Tang, D. Li, N. Alonso-Vante and Y. Feng, *ACS Appl. Mater. Interfaces*, 2017, **9**, 2541–2549.
- 6 L. Gan, J. Fang, M. Wang, L. Hu, K. Zhang, Y. Lai and J. Li, *J. Power Sources*, 2018, **391**, 59–66.
- 7 H. Lu, Y. Zhang, Y. Huang, C. Zhang and T. Liu, *ACS Appl. Mater. Interfaces*, 2019, **11**, 3372–3381.
- 8 J. Deng, P. Ren, D. Deng, L. Yu, F. Yang and X. Bao, *Energy Environ. Sci.*, 2014, **7**, 1919–1923.
- 9 W. J. Li, C. Han, G. Cheng, S. L. Chou, H. K. Liu and S. X. Dou, *Small*, 2019, **15**, 1–21.

- 10 K. Srinivas, Y. Chen, B. Wang, B. Yu, X. Wang, Y. Hu, Y. Lu, W. Li, W. Zhang and D. Yang, *ACS Appl. Mater. Interfaces*, 2020, **12**, 31552–31563.
- 11 X. Chen, Z. Yu, L. Wei, Z. Zhou, S. Zhai, J. Chen, Y. Wang, Q. Huang, H. E. Karahan, X. Liao and Y. Chen, *J. Mater. Chem. A*, 2019, **7**, 764–774.

List of Schemes

	Page No
1. Scheme 4.1 Synthesis of PBA and PBA derived CoBs.	116

List of Figures

1. Figure 1.1 Consumption of fuel cell per capita in various country is measured as the average consumption of energy from coal, natural gas and oil (Data based on BP statistical Review of World energy).	3
2. Figure 1.2 (a) Schematic representation of electrolytic cell and fuel cell (b) Polarization curve for the hydrogen involving (red curves) and oxygen involving (blue curves) reactions.	6
3. Figure 1.3 Mechanism of HER in different media.	9
4. Figure 1.4 Mechanism of OER reaction in different media. (red route for alkaline and green root for acidic condition, black line for MOOH path, light blue for direct combination of oxo species, M stands for electrocatalytic surface).	11
5. Figure 1.5 Free energy diagram for four (Blue) and two electron (Red) oxygen reduction reaction.	12
6. Figure 1.6 ORR mechanism in acidic medium to generate molecular oxygen.	13
7. Figure 1.7 (a) Involvement of OH^- in the electrolyte (b) OH_{ad} on the surface of electrocatalyst.	14
8. Figure 1.8 Volcano plot used for HER electrocatalyst.	22
9. Figure 1.9 Hopping of electron in MoS_2 layer.	22
10. Figure 1.10 HER activity of Co-B cluster.	24
11. Figure 1.11 OER performance and post OER study of Co-B nanoparticles.	24

12.	Figure 1.12	Co-operative effect of proton accepting group on the OER activity in MOFs.	25
13.	Figure 1.13	Volcano plot based on exchange current density Vs free energy of hydrogen adsorption at U=0.	26
14.	Figure 1.14	Cooperative effect of the proton relaying ligand on the ORR activity.	27
15.	Figure 1.15	Oxidative transformation of cubane shaped prusian blue analogue (PBA) into corresponding spinel oxide.	28
16.	Figure 1.16	MOFs derived material induces HER activity.	29
17.	Figure 1.17	Formation of NiS nanoframe using Ni-Co PBA MOF.	29
18.	Figure 1.18	Schematic representation and OER, ORR of active Co@Co ₃ O ₄ encapsulated in CNT grafted nitrogen doped carbon polyhedral.	29
19.	Figure 1.19	MOF derived CoSe ₂ microsphere for OER.	30
20.	Figure 1.20	Schematic procedure (top) and HER performance of of Fe-CoSe ₂ @NC (Bottom).	31
21.	Figure 1.21	OER performance of NiB and comparative materials in 1 M KOH.	32
22.	Figure 1.22	Set-up of a typical supercapacitor.	34
23.	Figure 1.23	Different electron movement in charge, fully charge and discharge level in supercapacitor.	34
24.	Figure 1.24	(a) EDLC behaviour by carbonaceous material (b) MnO ₂ pseudocapacitor following surface redox (c) Nb ₂ O ₃ pseudocapacitor following intercalation type reaction (d) NiO a battery type material follows faradic reaction.	38
25.	Figure 1.25	Cyclic voltammetry of nickel boride at various scan rate.	39
26.	Figure 1.26	(a) EDLC type (b) Pseudocapacitive via redox (c) Pseudocapacitive via intercalation (d) Battery type following faradic reaction.	40

27.	Figure 1.27	The charge-discharge (CD) shown by nickel boride.	41
28.	Figure 1.28	Nyquist plot of WO ₃ and WO _{3-x} nanowire electrode.	42
29.	Figure 1.29	Cyclic stability of Nickel boride with retention.	42
30.	Figure 1.30	Classification of Supercapacitor based on energy storage.	43
31.	Figure 1.31	Electrical double layer by Helmholtz.	44
32.	Figure 1.32	(a) Molecular structure of Ni ₃ (HITP) ₂ (b) Relative size of pores, green, lime, blue, grey, brown, and white spheres represent Ni, F, N, C, B, and H atoms, respectively.	46
33.	Figure 1.33	(a) Cyclic voltammetry at a scan rate of 10mV/s (b) Galvanostatic charge discharge curves at current densities of 0.5, 1.0, 2.0 A/g.	46
34.	Figure 1.34	Construction of graphene doped MOF as supercapacitor.	47
35.	Figure 1.35	Co ₉ S ₈ @C synthesis strategy from MOF.	48
36.	Figure 1.36	(a) CV curve of Co ₉ S ₈ -500, Co ₉ S ₈ @C-500, and Co ₉ S ₈ @C-600 at 5mVps (b) GCD of corresponding sample at 1A/g.	48
37.	Figure 2.1	(a) Asymmetric unit of the [Co ₄ (BTC) ₃ (BIM) ₆] [solvent] (b) Interconnection of paddle-wheel units forming an infinite chain along the c-axis (c) 3D view of [Co ₄ (BTC) ₃ (BIM) ₆] showing the channel along b-axis (d) 3D view of [Co ₄ (BTC) ₃ (BIM) ₆] along c-axis.	65
38.	Figure 2.2	(a) simulated and experimental X-ray diffraction patterns of Co-MOF (b) FTIR spectrum of Co-MOF.	66
39.	Figure 2.3	(a) Thermo gravimetric analysis of the Co-MOF (b) X-ray diffraction pattern of Co-MOF after the thermo gravimetric analysis.	66
40.	Figure 2.4	(a) FESEM image of the Co-MOF (b) EDS spectrum (c) elemental	67

		mapping of Co-MOF.	
41.	Figure 2.5	The cyclic voltammogram for the ORR by the Co-MOF-modified GCE in an oxygen saturated 0.1 M KOH electrolyte at the sweep rate of 10 mV s ⁻¹ . The control experiment was carried out in an argon-saturated electrolyte.	68
42.	Figure 2.6	(a) Linear sweep voltammograms at different rotations of the electrode (b) the Koutecky–Levich plot.	69
43.	Figure 2.7	(a) CV showing the methanol tolerance test in presence of 1 M Methanol (b) stability measurement of the Co-MOF-modified GCRDE in an oxygen saturated 0.1 M KOH electrolyte.	70
44.	Figure 2.8	(a) XRD pattern (b) FESEM, (c) EDS of Co-MOF after the ORR stability measurement.	71
45.	Figure 2.9	(a) LSVs for the OER by Co-MOF/AB, commercial RuO ₂ , CoO (after TGA), and AB in a 1 M KOH electrolyte at the sweep rate of 5 mV s ⁻¹ and (b) the corresponding Tafel plot.	72
46.	Figure 2.10	Nyquist impedance spectrum of Co-MOF.	72
47.	Figure 2.11	Linear sweep voltammograms for (a) Co-MOF (b) AB, (c) commercial RuO ₂ and (d) CoO after TGA for OER before and after the iR-compensation in 1 M KOH electrolyte at a sweep rate of 5 mV/s.	73
48.	Figure 2.12	(a) Cyclic voltammograms at different sweep rates in 1 M KOH electrolyte, (b) plot of current density at 0.23 V vs. Ag/AgCl to the sweep rate to determine the double layer capacitance of Co-MOF.	74
49.	Figure 2.13	Cyclic voltammogram at different sweep rates and plot of current density at 0.23 V vs. Ag/AgCl to the sweep rate to determine the	76

double layer capacitance by commercial RuO₂ (a, b), Co₃O₄ (c, d) and AB (e, f) modified GCE in 1 M KOH electrolyte.

- | | | | |
|-----|-------------|---|----|
| 50. | Figure 2.14 | (a) plot of turn over frequency against overpotential (b) stability test for OER at a current density of 10 mA cm ⁻² . | 77 |
| 51. | Figure 2.15 | (a) XRD pattern (b) FESEM, (c) EDS of Co-MOF after the OER stability measurement. | 78 |
| 52. | Figure 3.1 | (a) Powder X-ray diffraction and (b) Raman spectrum of CoSe ₂ /C hybrid nanostructure. | 91 |
| 53. | Figure 3.2 | High resolution X-ray photoelectron spectrum of (a) Co 2p, (b) Se 3d and (c) C 1s of CoSe ₂ /C hybrid nanostructure. | 92 |
| 54. | Figure 3.3 | (a) TGA of CoSe ₂ /C hybrid (b) Powder X-ray diffraction pattern of post TGA CoSe ₂ /C hybrid sample. | 93 |
| 55. | Figure 3.4 | (a, c) FESEM images (b) EDS Spectrum of CoSe ₂ /C hybrid nanostructure (d, e) FESEM images of pristine Co-MOF. | 93 |
| 56. | Figure 3.5 | (a) TEM images and (b) corresponding SAED pattern for CoSe ₂ /C hybrid nanostructure. | 94 |
| 57. | Figure 3.6 | (a) Linear sweep voltammograms by CoSe ₂ /C, CoSe ₂ , Co-MOF and Pt/C showing HER in 0.5 M H ₂ SO ₄ , (b) corresponding Tafel slopes, (c) Nyquist impedance spectrum for CoSe ₂ /C, Co-MOF and CoSe ₂ nanostructures and (d) stability of CoSe ₂ /C catalyst for HER at 10 mA/cm ² current density. | 95 |
| 58. | Figure 3.7 | (a) FESEM and (b,c) PXRD of CoSe ₂ /C after HER stability test. | 97 |
| 59. | Figure 3.8 | (a-c) Cyclic voltammograms showing the charging currents measured in a non-Faradaic region at a scan rate of 25, 50, 100, 150, 200 mV/s respectively and (d-f) the plot of cathodic and | 98 |

		anodic charging currents measured at -0.13 V (vs. Ag/AgCl) against scan rates for CoSe ₂ /C, CoSe ₂ and Co-MOF respectively.	
60.	Figure 3.9	DFT optimized structure of (a) bulk CoSe ₂ (b) CoSe ₂ (101) layer (c) bulk CoSe ₂ after C doping (d) CoSe ₂ (101) layer after C doping; blue, green and brown represent Cobalt, Selenium and Carbon respectively.	99
61.	Figure 3.10	TDOS plot for CoSe ₂ (101) layer.	100
62.	Figure 3.11	TDOS plot for Bulk CoSe ₂ (Upper) and CoSe ₂ /C (Lower).	101
63.	Figure 3.12	PDOS plot before and after C adsorption on CoSe ₂ for (a) Co 3d orbital (b) Se 4p orbital and (c) C 2p orbital; dotted line shows Fermi level at zero eV.	102
64.	Figure 3.13	Charge density difference plot between CoSe ₂ /C and CoSe ₂ for an iso value of $0.117e$; the charge gain region is shown in red and the charge loss region is shown in yellow.	102
65.	Figure 3.14	DFT optimized structure after H adsorption for (101) layer of (a) CoSe ₂ (b) CoSe ₂ /C; blue, green, brown and cyan represent Cobalt, Selenium, Carbon and Hydrogen.	104
66.	Figure 3.15	Reaction coordinates for HER of (101) layer of CoSe ₂ and CoSe ₂ /C.	104
67.	Figure 4.1	(a) X-ray diffraction pattern and (b) FESEM for the Co-PBA.	116
68.	Figure 4.2	(a) Powder X-ray diffraction pattern of CoB@300, CoB@450, CoB@550 and CoB@650 and (b) the PXRD pattern for CoB@300 showing a broad peak at 2θ of 45° .	117
69.	Figure 4.3	(a–d) FESEM and (a’–d’) TEM for CoB@300, CoB@450, CoB@550 and CoB@650. The inset in (a’–d’) shows the	118

		corresponding SAED patterns.	
70.	Figure 4.4	Elemental mapping for CoB@300. The EDS showing the presence of different elements in CoB and the inset shows the corresponding weight and atomic percentage of elements.	119
71.	Figure 4.5	High-resolution X-ray photoelectron spectrum of (a) Co 2p, (b) B 1s, (c) C 1s and (d) N 1s of CoB@300.	120
72.	Figure 4.6	(a) Linear sweep voltammogram, (b) Tafel plot (c) chronopotentiometric curve collected at an applied current density of 10 mA cm^{-2} .	121
73.	Figure 4.7	(a) cyclic voltammogram, (b) X-ray diffraction spectrum after the first CV cycle.	123
74.	Figure 4.8	(a-d) Cyclic voltammograms and (e-h) plot of current at different sweep rate for CoB@300, CoB@450, CoB@550 and CoB@650.	124
75.	Figure 4.9	Plot showing the turnover frequency for CoB@300, CoB@450, CoB@550 and CoB@650.	125
76.	Figure 4.10	(a) X-ray diffraction pattern, (b) FESEM, high-resolution X-ray photoelectron spectrum for (c) Co 2p and (d) B 1s of CoB@300 after 15 hours of electrolysis.	126
77.	Figure 5.1	(a) 3D view of $[\text{Ni}(\text{HBTC})(4, 4'\text{-bipy})\cdot 3\text{DMF}]$ showing the (b) honeycomb channels along <i>c</i> -axis and (c) rectangular channels parallel to the layers extending through out <i>ab</i> -plane.	140
78.	Figure 5.2	(a) simulated and experimental X-ray diffraction pattern of	141

		Ni-MOF, (b) powder Xray diffraction pattern of NiB.	
79.	Figure 5.3	High-resolution X-ray photoelectron survey spectrum of (a) NiB (b) Ni 2p (c) B 1s and (d) C 1s of NiB.	142
80.	Figure 5.4	(a) Thermogravimetric analysis and (b) powder X-ray diffraction pattern of post TGA NiB after 800 °C.	143
81.	Figure 5.5	(a) FESEM image of Ni-MOF, (b) FESEM, (c) TEM and (d) SAED pattern of NiB.	144
82.	Figure 5.6	Adsorption and desorption isotherms for nitrogen (at 77 K) of NiB.	145
83.	Figure 5.7	OER activity of NiB. (a) linear sweep voltammograms of NiB, RuO ₂ , Ni-MOF and NiO electrocatalysts in 1 M KOH solution on GCRDE at a scan rate of 5 mV s ⁻¹ and rotation of 1600 rpm, (b) corresponding Tafel plots, (c) comparison on the overpotential at 10 mA cm ⁻² and Tafel slopes of recently reported boride based OER catalysts, (d) chrono potentiometric curve of NiB, Ni-MOF, NiO and RuO ₂ dripped glassy carbon electrode at constant current density of 10 mA cm ⁻² .	146
84.	Figure 5.8	Cyclic voltammograms of NiB, NiO and Ni-MOF at 5 mV/s scan rate in 1 M KOH electrolyte.	147
85.	Figure 5.9	Nyquist impedance spectrum of (a) NiB and (b) RuO ₂ , Ni-MOF and NiO in 1 M KOH electrolyte.	148
86.	Figure 5.10	OER polarization curve obtained with the NiB, RuO ₂ , Ni-MOF and NiO modified electrodes in 1 M KOH electrolyte at scan rate of 5 mV/s with and without iR-	148

		compensation.	
87.	Figure 5.11	(a) CV for NiB and RuO ₂ showing the charging currents measured in a non-Faradaic region at a scan rate of 5, 10, 20, 40, 80, 100, 200 mV/s respectively and (b) the plot of cathodic and anodic charging currents measured at 0.13 V (vs. Hg/HgO) against scan rates.	149
88.	Figure 5.12	(a) CV for Ni-MOF and NiO showing the charging currents measured in a non-Faradaic region at a scan rate of 5, 10, 20, 40, 80, 100, 200 mV/s respectively and (b) the plot of cathodic and anodic charging currents measured at 0.13 V (vs. Hg/HgO) against scan rates.	150
89.	Figure 5.13	(a) powder X-ray diffraction and (b) FESEM of post OER stability (c) XPS of NiB.	151
90.	Figure 5.14	(a) CV curves of NiB modified electrode at different scan rates, (b) Cyclic voltammogram of Ni-MOF modified electrode at Different sweep rate in 5 M KOH electrolyte (c) the CV curve at 5 mV/s scan rate showing the capacitive and diffusion contribution towards the net charge storage by NiB.	153
91.	Figure 5.15	(a) CV curves at various scan rates of NiB and (b) plot of logarithm of anodic peak current and logarithm of scan rate.	155
92.	Figure 5.16	(a) GCD profiles at different applied current densities and (b) cycle life of NiB modified electrode.	155
93.	Figure 5.17	(a) CV curves showing the optimized potential window for rGO and NiB, (b) CV, (c) GCD of rGO//NiB ASC device.	157
94.	Figure 5.18	Cyclic voltammograms showing the potential window	158

Optimization for the (a) NiB and (b) rGO in 5 M KOH electrolyte at a scan rate of 25 mV/s.

- | | | | |
|-----|-------------|---|-----|
| 95. | Figure 5.19 | (a) Plot showing capacitance retention and coulombic efficiency of the ASC. (b) Nyquist impedance spectrum of the rGO//NiB ASC before and after 5000 GCD cycles. The inset in (a) is the Swagelok electrode of rGO//NiB ASC device. | 159 |
| 96. | Figure 5.20 | (a) powder X-ray diffraction and (b) FESEM of post supercapacitor stability NiB. | 160 |

List of Tables

- | | | | |
|----|-----------|--|-----|
| 1. | Table 1.1 | Comparison of some basic parameters among capacitor, supercapacitor and battery. | 33 |
| 2. | Table 2.1 | Comparison of activity of the Co-MOF with the reported metal organic frameworks for oxygen evolution reaction. | 75 |
| 3. | Table 2.2 | Comparison of various parameters of Co-MOF, commercial RuO ₂ , and CoO under similar electrochemical condition with similar loading of electrocatalyst. | 77 |
| 4. | Table 3.1 | The electrocatalytic activity of CoSe ₂ /C hybrid with other reported nanostructures. | 96 |
| 5. | Table 3.2 | Comparison of overpotential between experimental and computational study. | 105 |
| 6. | Table 4.1 | Table showing the comparison of the electrocatalytic activity of CoB with the reported literatures. | 122 |
| 7. | Table 4.2 | Table showing the OER activity of different catalysts. | 125 |
| 8. | Table 5.1 | Electrocatalytic OER activity of different electrocatalyst. | 152 |

9.	Table 5.2	Comparison of electrochemical charge storage performances of NiB with reported materials.	156
----	-----------	---	-----

Chapter-1.

Chapter 1. Emerging metal-organic frameworks (MOFs) and their derived material for energy conversion and storage.

1.1	Introduction	3
1.2	Electrolysis and electrochemical setup	5
1.3	Mechanism of electrolysis process	8
1.4	Common parameters for catalytic evolution process	14
1.5	Types of Electrode material used	21
1.6	Supercapacitors (SCs) or Ultra capacitor	32
1.7	MOFs as supercapacitor materials	45
1.8	MOFs derived material as supercapacitor	47
1.9	References	48

Chapter-2

Chapter 2. ORR and OER Study of Cobalt Metal-Organic Framework (Co-MOF).

2.1	Abstract	58
2.2	Introduction	59
2.3	Motivation of the work	61
2.4	Experimental section	61
2.5	Characterization	62
2.6	Electrochemical measurements	62
2.7	Calculations of ECSA and R_f	64
2.8	Results and discussions	64
2.9	Conclusions	79

2.10 References	80
-----------------	----

Chapter-3

Chapter 3. DFT supported cobalt metal-organic framework (Co-MOF) derived CoSe₂/C hybrid nanostructures for electrochemical hydrogen evolution reaction.

3.1 Abstract	84
3.2 Introduction	85
3.3 Motivation of the work	87
3.4 Experimental section	87
3.5 Characterization	88
3.6 Electrochemical measurements	88
3.7 Calculations of ECSA and R_f	90
3.8 Results and discussions	90
3.9 Conclusions	105
3.10 References	106

Chapter-4

Chapter 4. Electrochemically activated prussian blue analogue (PBA) derived amorphous CoB nanostructures: Efficient electrocatalyst for oxygen evolution reaction.

4.1 Abstract	110
4.2 Introduction	111
4.3 Motivation of the work	113
4.4 Experimental section	113
4.5 Characterization	114
4.6 Electrochemical measurements	114
4.7 Calculations of ECSA and R_f	115

4.8 Results and discussions	116
4.9 Conclusions	127
4.10 References	127

Chapter-5

Chapter 5. Amorphous nickel boride: A metal-organic framework-derived electroactive material for energy conversion and storage.

5.1 Abstract	132
5.2 Introduction	133
5.3 Motivation of the work	136
5.4 Experimental section	136
5.5 Characterization	138
5.6 Electrochemical measurements	138
5.7 Calculations of ECSA and R_f	139
5.8 Results and discussions	140
5.9 Conclusions	160
5.10 References	161

List of Abbreviations

FCNTs	Functionalized carbon nanotubes
RGO	Reduced graphene oxide
1D	One dimensional
HER	Hydrogen evolution reaction
OER	Oxygen evolution reaction
LSVs	Linear sweep voltammetry
R_f	Roughness factor
R_s	Solution resistance

R _{ct}	Charge transfer resistance
C _{dl}	Double-layer capacitance
CPE	Constant phase elements
ECSA	Electrochemical active surface area
CP	Chronopotentiometry
TOF	Turn over frequency
FE	Faradaic efficiency
Td	Tetrahedral
GO	Graphene oxide
RGO	Reduced graphene oxide
WE	Working electrode
GCE	Glassy carbon electrode
SCE	Saturated calomel electrode
NMP	N-Methyl-2-pyrrolidone
CE	Counter electrode
RE	Reference electrode
RHE	Reversible hydrogen electrode
NHE	Normal hydrogen electrode
TGA	Thermogravimetric analysis
PXRD	Powder X-ray diffraction
FTIR	Fourier transform infrared
FESEM	Field emission scanning electron microscope
TEM	Transmission electron microscope
HRTEM	High resolution transmission electron microscopy
EDAX	Energy dispersive analysis of X-rays

3D	Three-dimensional
2D	Two-dimensional
SC	Supercapacitor
C_{sp}	Specific capacitance
PD	Power density
ED	Energy density
PPC	Propylene carbonate
ILs	Ionic liquids
CNTs	Carbon nanotubes
CV	Cyclic voltammetry
CCCD	Constant current charge/discharge
EIS	Electro chemical impedance spectroscopy
EDLC	Electrical double-layer capacitance
PC	Pseudocapacitance
PCS	Pseudocapacitance supercapacitor
HS	Hybrid supercapacitors
CVD	Chemical vapor deposition
DI	De-ionized
GCRDE	Glassy carbon rotating disk electrode
XPS	X-ray photoelectron spectroscopy

CHAPTER – 1

Emerging metal-organic frameworks (MOFs) and their derived materials for energy conversion and storage

- 1.1 Introduction
- 1.2 Electrolysis and electrochemical setup
- 1.3 Mechanism of electrolysis process
 - 1.3.1 Reaction mechanism involved in hydrogen evolution reaction (HER)
 - 1.3.2 Reaction mechanism involved in oxygen evolution reaction (OER)
 - 1.3.3 Reaction mechanism involved in oxygen reduction reaction (ORR)
 - 1.3.4 Mechanism involved in hydrogen oxidation reaction (HOR)
- 1.4 Common parameters for catalytic evolution process
 - 1.4.1 Overpotential
 - 1.4.2 Tafel slope
 - 1.4.3 Electrochemical active surface area
 - 1.4.4 Turn over frequency
 - 1.4.5 Nyquist plot
 - 1.4.6 Mass activity
 - 1.4.7 Faradic efficiency
 - 1.4.8 Cyclic stability
 - 1.4.9 K-L plot
- 1.5 Types of Electrode material used
 - 1.5.1 Precious metal-based catalyst
 - 1.5.2 Transition metal selenide
 - 1.5.3 Transition metal boride
 - 1.5.4 MOFs as an electrocatalyst

- 1.5.5** MOFs derived material as an electrocatalyst
 - 1.5.5.1** MOFs derived transition metal selenides
 - 1.5.5.2** MOFs derived transition metal borides
- 1.6** Supercapacitors (SCs) or Ultra capacitor
 - 1.6.1** Basic components of SCs
 - 1.6.2** Key parameters used in supercapacitor
 - 1.6.2.1** Specific capacitance
 - 1.6.2.2** Specific energy and specific power
 - 1.6.2.3** Cyclic stability
 - 1.6.2.4** Coulombic efficiency
 - 1.6.3** Electrolytes used
 - 1.6.3.1** Aqueous electrolytes
 - 1.6.3.2** Non-aqueous electrolytes
 - 1.6.4** Calculation of supercapacitance from various technique
 - 1.6.4.1** Cyclic voltammetry technique
 - 1.6.4.2** Constant current charge/discharge
 - 1.6.4.3** Electro chemical impedance spectroscopy
 - 1.6.4.4** Cyclic stability
 - 1.6.5** Mechanism involved in SCs
 - 1.6.5.1** Electric double layer capacitor (EDLC) mechanism
 - 1.6.5.2** Pseudocapacitive mechanism (PC)
 - 1.6.5.3** Hybrid supercapacitor (HS)
- 1.7** MOFs as supercapacitor materials
- 1.8** MOFs derived material as supercapacitor
- 1.9** References

1.1 Introduction

The urging for clean energy increases globally day by day due to rapid industrial globalization and non-stop deterioration of environmental conditions. The significant increase in energy consumption demands for alternative sustainable energy sources necessary for a developed modern society. For fulfillment of energy demand, fossil fuel contributes nearly 81% of total energy expenditure globally. According to a survey, around 6,303 MWh energy is used from fossil fuel per capita in our country, securing 9th position in the table of world most user of fossil fuel shown in Fig1.1. However, the limited abundance of fossil fuels and CO₂ emission creates an alarming stage causing serious environmental issues like air pollution, and global warming motivates researchers to find an alternative energy source.¹ Even if spectacular measures have been taken to convert solar energy and wind energy to electrical energy in last few decades; however, climate and calamity are becoming a big barrier for them. Nuclear reactors have a history of catastrophic disasters. Therefore, searching for green energy sources would be essential to solve the current dilemma. The Earth provides plenty of H₂O, N₂, CO₂ and can act as fuels for the electrochemical process.

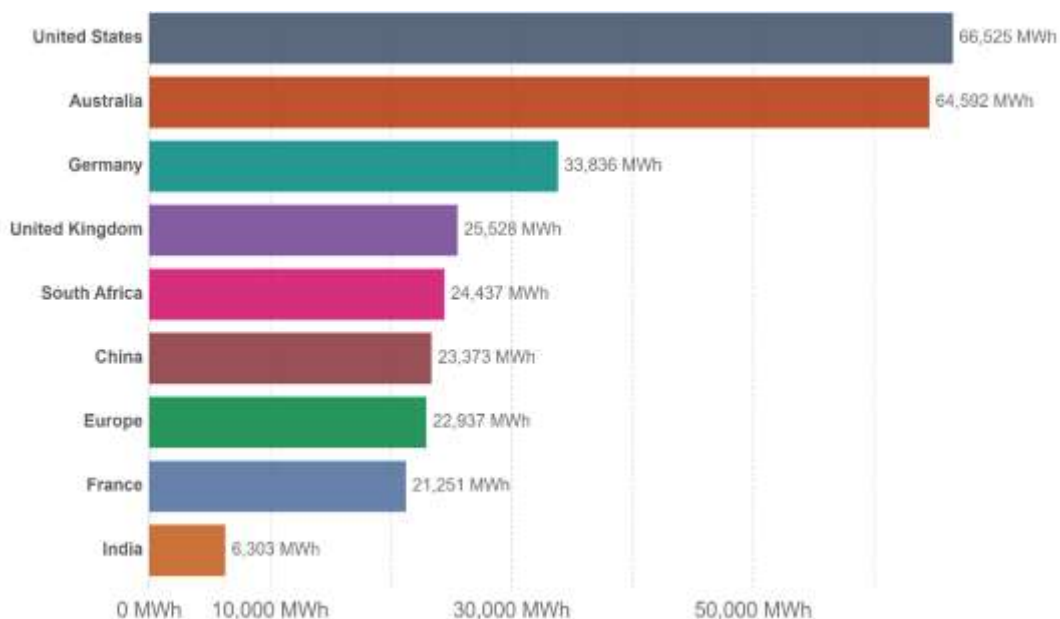


Figure 1.1 Consumption of fuel cell per capita in various country is measured as the average consumption of energy from coal, natural gas and oil.

Water electrolysis is a decisive strategy to produce hydrogen and oxygen in a green and clean manner and a promising alternative to conventional fossil fuels. Hence, in the modern era, reducing our reliance on conventional energy sources like fossil fuels and mitigating the impact of climate change, and affording energy in a green and clean way electrochemical water splitting (EWS), mainly hydrogen evolution reaction (HER) and oxygen evolution reaction (OER) becoming a good alternative. The wide use of precious metals (Pt, Pd, Ru, etc) and metal oxide-based nanostructures is restricted due to high cost, low durability, and detrimental environmental effect pushing researchers to develop new electroactive material.

From another point of view, the intermittent nature of wind and solar energy depending on environmental conditions demand large-scale energy storage and conversion system made researchers think for a promising alternative. To overcome this issue, researchers have innovated electrochemical and photoelectric energy storage devices such as fuel cells, supercapacitor (SC), Li-ion batteries (LIBs), Solar cells for the storage and use of intermittent clean energy. Despite the better performance of cyclic stability, power density, energy density, safety, these devices need further improvement. Of the various materials studied, porous materials are a promising candidate for energy conversion and storage devices due to the large surface area meant for chemical reaction and interfacial transport pathways for shortened diffusion paths.²

Among all classes of porous materials, metal-organic frameworks (MOFs), first reported by Yaghi et al.³ in 1995, got wide attention in the past two decades. MOFs are considered a class of crystalline materials composed of either metal or clusters coordinated with organic ligands with different dimensionality. The structure of MOFs containing metal center and organic linker. By tuning the design of linkers, MOFs with different dimensionality can be tailored. The large structural diversity and permanent porosity of these materials encourage to exhibit an array of applications, including gas capture and storage,^{4,5} separations,⁶⁻⁸ magnetism,⁹

sensing¹⁰ , catalysis¹¹⁻¹³ and luminescence.^{14,15} However, what is less explored is the application of MOF towards energy conversion and storage. Though MOFs are promising candidates nowadays, much more needs to be investigated and analyzed. The diverse structure of secondary building units or linkers produces different MOFs. Despite several favorable properties exhibited by MOFs, this field contains various restraints restricting its wide usability.

In most cases, their electrochemical application is restricted due to the poor intrinsic conductivity and surface area, and adsorption capacity dramatically decreases when exposed to moisture. However, by tuning the chemical composition and optimizing the reaction conditions, MOF-derived materials such as sulfide, selenide, carbide, boride, phosphide¹⁶⁻¹⁸ etc can be easily tailored to possess more exposed active sites, produces well-dispersed metal species in a carbon-based material, enhances the intrinsic activity and facilitates mass transport in electrocatalytic reaction. Prussian blue analog is a sort of metal-organic framework that has been used as a precursor for metal sulfide, selenide, nitride, carbide, telluride, boride. Therefore, we believe that MOFs and MOF-derived materials could be a new hope in sustainable energy production and uses in the early future.

It was found the anisotropic nature of crystalline material inhibits their electrocatalytic behavior.¹⁹ Amorphous materials have received increased attention due to their unique isotropic structures, and the high concentration of coordinatively unsaturated sites made them desirable catalysts. Therefore, tuning crystalline material into amorphous via a simple redox method is significant.²⁰

1.2 Electrolysis and electrochemical setup

Electrolysis involves cleaving a stable water molecule into molecular oxygen and hydrogen by passing current across electrodes in an aqueous electrolyte. By applying appropriate potential,

the splitting of water molecules occurs. The molecular hydrogen (H₂) and oxygen (O₂) evolve via water splitting at cathode and anode, respectively. The overall reaction is given below:²¹

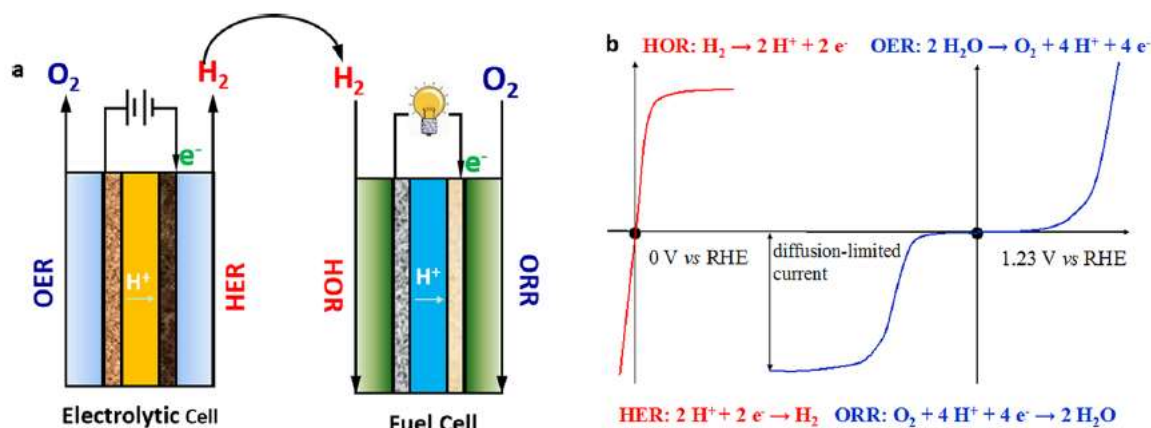
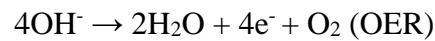
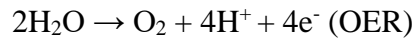


Figure 1.2 (a) Schematic representation of electrolytic cell and fuel cell (b) Polarisation curve for the hydrogen involving (red curves) and oxygen involving (blue curves) reactions.

In heterogeneous electrocatalysis, generally, the electrochemical reaction occurs at the surface of electrode material. In electrocatalysis, energy-related applications are associated with the water cycle. The water cycle consists of a series of oxygen and hydrogen electrocatalytic processes shown in Fig 1.2.²² The oxygen reduction reaction (ORR) and the hydrogen oxidation reaction (HOR) occur at the cathode and anode of a typical hydrogen-oxygen Fuel cell respectively. Similarly, in the electrolytic cell, the whole process consists of two half-cell reactions (a) hydrogen evolution reaction (HER) and (b) oxygen evolution reaction (OER), i.e., hydrogen and oxygen gas liberated at cathode and anode due to reduction and oxidation of water respectively. There is a loop generated; at first, hydrogen and oxygen are generated through water splitting, followed by power generation by ORR and HOR in the fuel cell. Generally, HER and ORR involve two-electron transfer processes, whereas HOR and OER involve multi- electron pathways leading to sluggish kinetics shown in Fig.1(b). In an

electrolytic cell, the HER and OER reactions occur depending upon the pH of the electrolyte. The active ions are the proton and hydroxide ions in acidic and alkaline electrolytes, respectively. The equations are given below-



The above said reactions have occurred at a particular potential for HER and OER called thermodynamic potential and calculated from the following equation-

$$\Delta G = -nFE^\circ \dots\dots\dots(1.2)$$

Thermodynamically the potential required for the overall water splitting for HER and OER calculated from the above reaction is 1.23 V.

The whole electrolysis process is carried out in an electrochemical cell consisting of either two or three electrodes depending upon the setup requirement. The three electrodes system contains a working electrode (WE) on which material is deposited, counter electrode (CE), reference electrode (RE). In contrast, in a two-electrode system, either two electrodes are separated by porous frit, or sometimes two half-cells are connected via a salt bridge. The working electrode is prepared according to the nature of the catalyst. For example, suppose the catalyst is in powder form. In that case, it is dispersed in a suitable solvent like ethanol and binder like nafion sonicated for several minutes to complete dispersion to make homogenous slurry or ink. Sometimes to adhere electrocatalyst, nickel foam, titanium plate, and nickel foil are used for measurement, but glassy carbon electrode (GCE) is mainly used as a working electrode. This ink is drop-casted on the working electrode and dried either by vacuum oven or kept at room temperature for a few minutes. Sometimes electrodeposition method can be applied to fabricate a self-supported working electrode. Platinum wire (Pt) is chosen to work as a counter electrode.

For reference electrodes, silver or mercury (also known as calomel electrode) in saturated KCl are commonly used for electrochemical measurement. The redox reaction is-----



However, the leaching of chlorine from silver and calomel electrodes raises the question on the performance of electrocatalysts. To avoid interference of chlorine ion, either oxide (mercury oxide) based or sulfate (mercury sulfate, silver sulfate) based reference electrode can be used. The different reference electrodes used for water splitting are calibrated into reversible hydrogen electrodes (RHE) by using well known Nernst equation-

In the case of aqueous Ag/AgCl reference electrode,

$$E_{RHE} = E_{Ag/AgCl} + E^0_{Ag/AgCl} + 0.059 p^H; E^0_{Ag/AgCl} = 0.21 V \dots\dots\dots (1.5)$$

For saturated calomel electrode (SCE),

$$E_{RHE} = E_{SCE} + E^0_{SCE} + 0.059 p^H; E^0_{SCE} = 0.24 V \dots\dots\dots (1.6)$$

For Hg/HgO electrode,

$$E_{RHE} = E_{Hg/HgO} + E^0_{SCE} + 0.059 p^H; E^0_{Hg/HgO} = 0.897 V \dots\dots\dots (1.7)$$

1.3 Mechanism involved in various processes in the water cycle

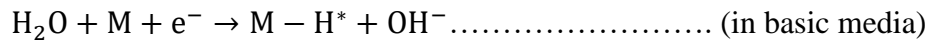
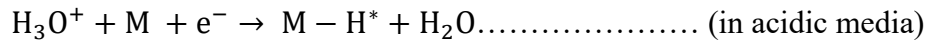
The water cycle consists of two steps (1) fuel generation (2) power generation. Hydrogen and oxygen are generated in water splitting utilized by fuel cells for power generation through ORR and HOR processes. However, the reaction path of these processes depends on the pH of the electrolyte.

1.3.1 Reaction mechanism involved in Hydrogen Evolution Reaction (HER)

In the HER process, the reduction of proton or water molecules occurs to generate molecular hydrogen in acidic and alkaline media, respectively, by applying minimum external potential. Three main steps are involved in HER mechanistic path; (a) electrochemical hydrogen

adsorption (Volmer reaction), (b) electrochemical desorption (Heyrovsky reaction), (c) chemical desorption (Tafel reaction).

Volmer reaction:



In the first step, protons combine with electrons to generate adsorbed hydrogen atoms (H*) on the electrode material surface (M). The proton sources for HER process are the hydronium cation (H₃O⁺) and the water molecule in acidic and alkaline electrolytes, respectively. Then molecular hydrogen is produced either by Heyrovsky or Tafel reaction or both. In the Heyrovsky step, another proton combines with the adsorbed species (H*) and then reacts with a second electron to produce H₂.

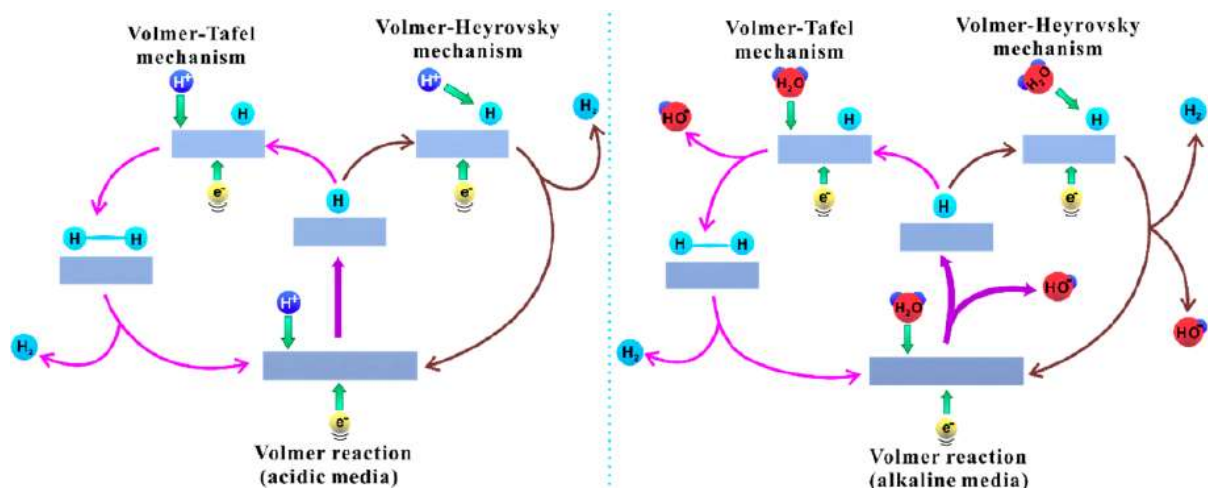
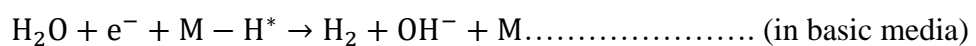


Figure 1.3 Mechanism of HER in different media.

Heyrovsky reaction:



In the Tafel step, two adsorbed species come closer to combine on the surface of the electrode to evolve H₂.²³

Tafel reaction:



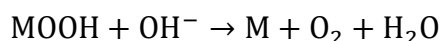
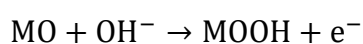
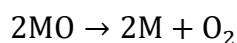
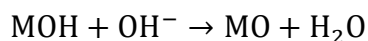
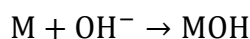
The overall mechanical path in acidic and alkaline media in different pH is given in Fig 1.3. ²⁴

The slopes representing the intrinsic nature of the catalyst are derived from the polarization curves by plotting the log of reduction current density against the overpotential (called the Tafel plot). It has been considered that for Tafel, Heyrovsky, Volmer rate-determining step, the slopes are ~29 mV/dec, ~39, and ~118 mV/dec respectively. The Heyrovsky and Volmer step is considered the rate determining step in the case of acid medium and the alkaline medium, respectively. ²⁵

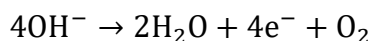
1.3.2 Reaction mechanism involved in oxygen evolution reaction

Oxidation occurs during water splitting to generate molecular oxygen (O₂) at the anode. The oxidation process follows a four-electron reaction path in acidic and alkaline media.

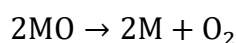
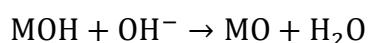
In alkaline medium;



The overall reaction is



In acidic medium;



The overall reaction is $2\text{H}_2\text{O} \rightarrow 4\text{H}^+ + 4\text{e}^- + \text{O}_2$

It has been observed that the intermediate MO follows two different reaction paths in water oxidation to form molecular oxygen. In both alkaline and acidic conditions, MO can generate oxygen molecules. In an alkaline medium, the decomposition of oxide (MO) intermediates simultaneously the combination of peroxide (MOOH) with the hydroxide to form O_2 . In contrast, in an acidic medium, molecular oxygen is formed only when the direct decomposition of MO intermediates and the coupled of peroxide (MOOH) with water occurs. Here MO, MOH, MOOH intermediates are produced and participate in the O_2 generation process. The whole mechanism in alkaline and acidic media is given in Fig 1.4.²⁶

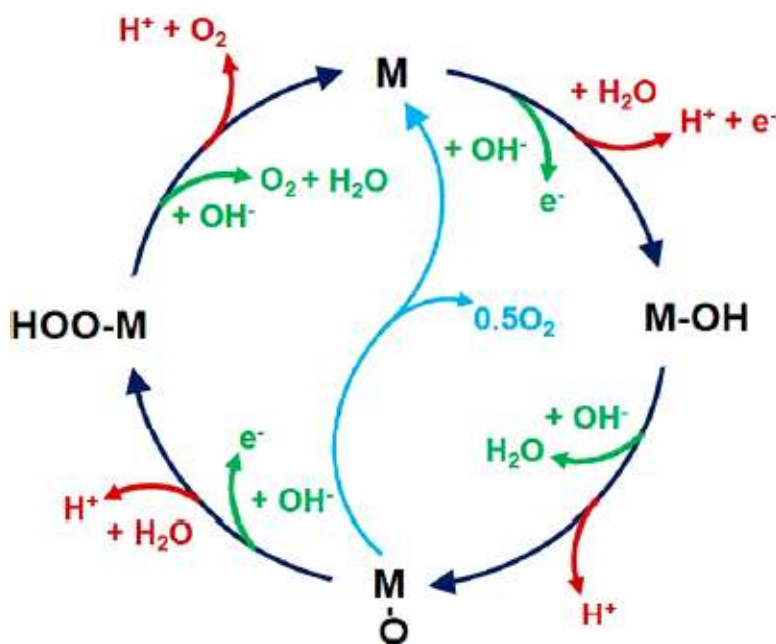


Figure 1.4 Mechanism of OER reaction in different media. (red route for alkaline and green route for acidic condition, black line for MOOH path, light blue for direct combination of oxo species, M stands for electrocatalytic surface.)

1.3.3 Reaction mechanism involved in oxygen reduction reaction (ORR)

The ORR process can proceed via two (2e^-) or four electrons (4e^-) processes. The selectivity towards 2e^- or 4e^- depends upon the adsorption energy of the intermediates and the reaction

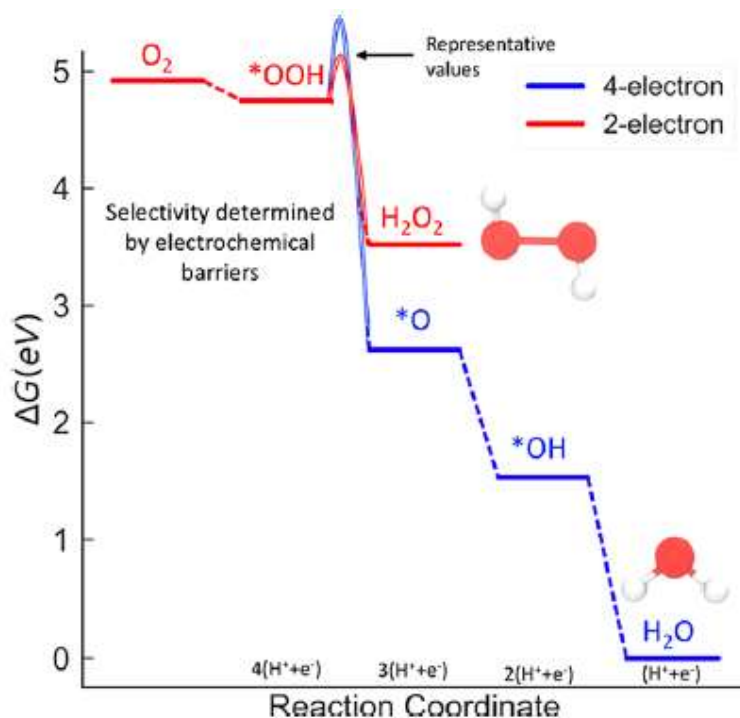


Figure 1.5 Free energy diagram for four (Blue) and two electron (Red) oxygen reduction reaction.

barrier on its surface. At the molecular level, associative and dissociative mechanisms are possible depending on the initial O_2 dissociation energy barrier. The electron transfer number for carbon materials is always less than four, i.e., two, whereas the electron transfer number is four for the metal surface like Pt. The DFT data also support these experimental findings.²⁷⁻²⁹ Sometimes the path is also dependent on the relative adsorption energy of the intermediate. The intermediate OOH^* if adsorb strongly follow $4e^-$ path while $2e^-$ path followed by weakly adsorbed intermediate as shown in Fig 1.5.³⁰

In the acidic medium, the two-step $2e^-$ path intermediate H_2O_2 and $4e^-$ path H_2O is formed, as shown in Fig 1.6.³¹

In alkaline medium, the intermediates are HO_2^- and OH^- in $2e^-$ and $4e^-$ path respectively. However, depending upon the demand suitable path is followed. For instance, in the fuel cell process, $4e^-$ path is preferred as it provides high current efficiency, while in industry $2e^-$ path is favorable as it produces H_2O_2 . All the possible mechanistic paths in alkaline media are given in detail as follows:

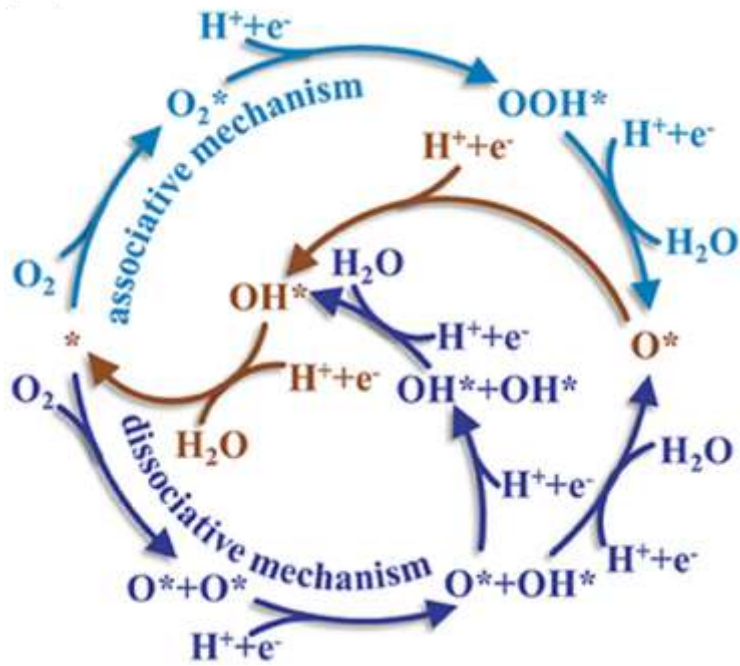
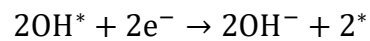
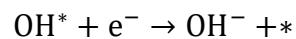
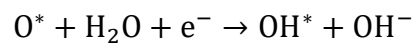
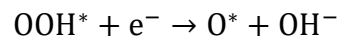
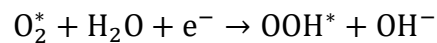
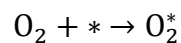


Figure 1.6 ORR mechanism in acidic medium.

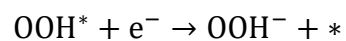
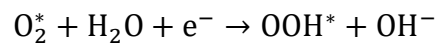
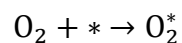
Dissociative ($4e^-$) mechanism:



Associative ($4e^-$) mechanism:

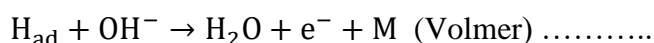
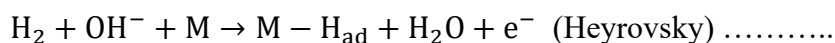
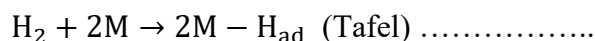


Associative ($2e^-$) mechanism:



1.3.4 Mechanism involved in hydrogen oxidation reaction (HOR)

The HOR takes place at the anode of a typical hydrogen-oxygen fuel cell. In alkaline media, HOR proceeds through the Tafel-Volmer or Heyrovsky-Volmer mechanism. The detailed mechanism is given as follows: ³²⁻³⁴



Herein M stands for the surface site for hydrogen adsorption and H_{ad} for adsorbed hydrogen. The mechanism is debatable due to the involvement of OH⁻ in the Heyrovsky and Volmer step. So the mechanism is divided into two parts (i) OH⁻ in the solution (ii) OH_{ad} on the electrocatalyst surface as shown in Fig. 1.7. ³⁵

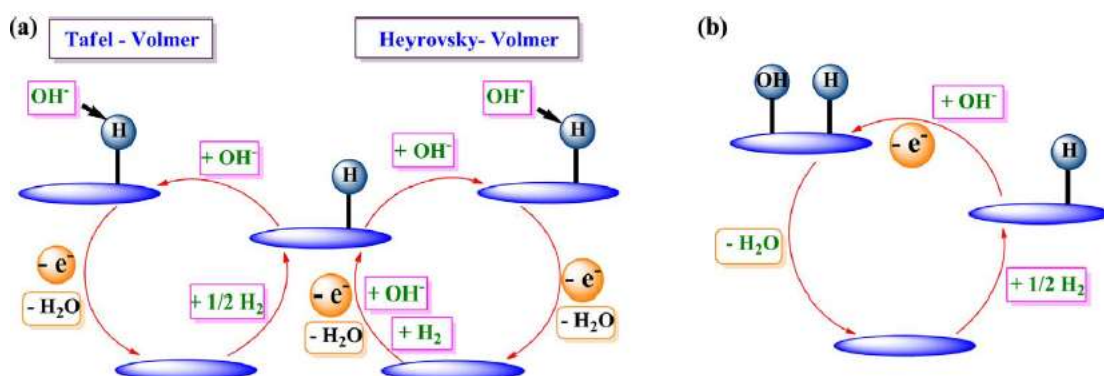


Figure 1.7 (a) Involvement of OH⁻ in the electrolyte (b) OH_{ad} on the surface of electrocatalyst.

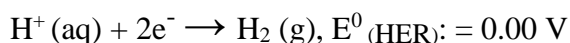
1.4 Key parameters for electrocatalysis

To evaluate the nature of electrocatalyst and to know the surface reaction mechanism, it is necessary to gain an idea about the basic parameters such as overpotential, Tafel plot, impedance spectroscopy (Nyquist plot), turn over frequency (TOF), electrochemical active surface area (ECSA), mass activity, cyclic stability, faradic efficiency. The brief idea is given as follows.

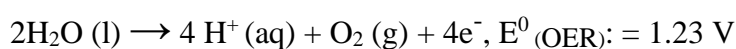
1.4.1 Overpotential (η)

In electrochemical water splitting, either hydrogen evolution or oxygen evolution is thermodynamically not feasible in the standard condition of temperature and pressure. So, this process needs some extra energy. According to the Nernst equation, 1.23 V (vs. NHE) water oxidation and 0 V (vs. NHE) require for water reduction, respectively.

In HER process



In OER process



However, this does not happen as these calculations are theory-based. The sluggish reaction kinetics of these reactions need some extra energy to overcome the activation barrier. Therefore, overpotential is the difference of potential between experimentally observed and thermodynamic one of a particular electrochemical reaction. Strictly speaking, materials with higher the value of overpotential lower will be its activity and vice-versa. This overpotential depends on some parameters like reaction activation, series resistance, and diffusion of charge carriers. A suitable catalyst with proper loading can activate the reaction properly by reducing overpotential. Using a rotating disc electrode (RDE) will enhance the diffusion of charge minimize the overpotential. Due to uncompensated resistance of ionic conduction between reference and working electrode in the electrolyte, ohmic resistance appears. Hence, verifying the intrinsic catalytic activity of a given catalyst ohmic drop (iR) is subtracted from the observed potential. Generally, various electroactive materials are compared based upon their overpotential evaluated at $10 \text{ mA}\cdot\text{cm}^{-2}$. It is due to potential getting at that current density is assumed the standard metric in solar water splitting system under the illumination of one sun. It is believed that current density is assumed as a 12.3 % efficient solar hydrogen device.^{36,37} Some catalysts are presumed to be evaluated for their overpotential at 50 mA cm^{-2} and 100 mA cm^{-2} .³⁸⁻⁴⁰

1.4.2 Tafel slope

To evaluate the intrinsic activity of the electrocatalyst, the Tafel slope is an essential parameter. It entails the reaction kinetics of the catalytic process. It shows the relation between overpotential and current density (both are iR corrected) as follows-

$$d \log(j) / d\eta = 2.303RT / \alpha nF \quad \dots\dots\dots (1.8)$$

The equation shows that the Tafel slope is inversely proportional to the diffusion coefficient. It becomes a common parameter to evaluate electrocatalyst. Simply plotting the log of current density and overpotential Tafel plot can be obtained. After that, fitting the linear portion, Tafel slope can be obtained by using the following equation ⁴¹

$$\eta = a + b \log j \dots\dots\dots (1.9)$$

Where η is overpotential, a and b are Tafel constant, Tafel slope, and j is the obtained current density.

Here in the figure, the exchange current density shown is the equilibrium position where both cathodic and anodic currents are equal. This can be obtained from the intersection of extrapolated fitted Tafel plot to the X-axis. For a particular catalyst, the higher the exchange current density better is the catalytic behavior. ⁴²

1.4.3 Electrochemical active surface area (ECSA)

The actual surface area of the catalyst can be evaluated either by the in-situ or ex-situ method. In the in-situ method, the surface area can be obtained by BET gas adsorption or particle size by scanning electron microscope. However, the percentage of accuracy is found to be less than the average surface area obtained from these methods. Secondly, all the surfaces need not be electrochemically active, so a better method should be chosen. ECSA value can be obtained by evaluating double-layer capacitance (C_{dl}) from a non-faradic region of a static cyclic voltammetry (CV) curve. Non-faradic region means a portion where neither oxidation nor

reduction occurs. The current getting from the CV curve is directly proportional to scan rate and double-layer capacitance (C_{dl}) from the equation as follows-

$$i = vC_{dl} \dots \dots \dots (1.10)$$

Moreover, ECSA can be calculated by dividing double-layer capacitance and specific capacitance given in equation as follows-

$$ECSA = \frac{C_{dl}}{C_s} \dots \dots \dots (1.11)$$

C_s , the specific capacitance depends upon the nature of the electrolyte and varies from 20-60 μF .⁴³⁻⁴⁵

If ECSA is divided further with the geometrical surface area of electrode roughness factor (R_f) can be obtained. The equation is given as follows-

$$R_f = \frac{ECSA}{S_{geo}} \dots \dots \dots (1.12)$$

ECSA also has been predicted from the non-faradic potential region of electrochemical impedance spectroscopy.

1.4.4 Turnover frequency (TOF)

To evaluate the intrinsic catalytic activity of an electrocatalyst, turnover frequency plays a vital role. It is defined as the number of molecules of hydrogen or oxygen evolved per second per active site of an electrocatalyst.^{46,47}

$$TOF = \frac{\text{Number of } H_2 \text{ or } O_2 \text{ molecule evolved per second}}{\text{Number of active sites}} \dots \dots \dots (1.13)$$

So, it is necessary to calculate the number of active sites of the electrocatalyst. It can be obtained from CV by assuming one-electron oxidation process.⁴⁸ For HER process, the calculations are given as follows-

$$H_2 \text{ evolved per second} = x = \frac{i}{96485 \text{ C.mol}^{-1}} \times \frac{6.022 \times 10^{23} e^{-} \text{mol}^{-1}}{2e^{-} \text{ per } H_2} \dots \dots \dots (1.14)$$

$$\text{Number of active sites} = y = \frac{Q_{CV}}{96485 \text{ C.mol}^{-1}} \times \frac{6.022 \times 10^{23} e^{-} \text{mol}^{-1}}{1e^{-} \text{ per active site oxidised}} \dots \dots \dots (1.15)$$

Hence TOF can be obtained by dividing equations 1.14 and 1.15 as follows

$$TOF = \frac{x}{y} = z s^{-1} \dots\dots\dots (1.16)$$

Generally, 2 and 4 is divided in the denominator for the HER and OER process as the evolution of hydrogen and oxygen requires two and four electrons, respectively. The equation is given as follows

$$(TOF)_{HER} = \frac{i}{2F_n} \dots\dots\dots (1.17)$$

$$(TOF)_{OER} = \frac{i}{4F_n} \dots\dots\dots(1.18)$$

1.4.5 Nyquist plot

During water splitting, solution resistance (R_s), charge transfer resistance (R_{CT}), and mass transfer activity are observed. To investigate these terms, electrochemical impedance spectroscopy or Nyquist plot is necessary. In the desired electrolyte, the imaginary axis (Z'') Vs real axis (Z') is known as the Nyquist plot. Applying a particular potential due to charge transfer between the electrode surface and electrolyte generates response conduct from lower to higher. A lower charge transfer resistance refers to higher conductivity of electrode material and vice-versa. Therefore, the electrocatalyst showing better water splitting has low charge transfer resistance. Randles circuit observed from Nyquist plot from which R_s , R_{CT} is clearly calculated.

Also, specific capacitance can be evaluated from EIS measurement by using the following equation: ^{49,50}

$$C_m = \frac{1}{m \times j \times 2\pi f \times Z''} \dots\dots\dots(1.19)$$

Here C_m , m , f , and Z'' represent specific capacitance, the mass of sample, frequency, and imaginary part.

1.4.6 Mass activity

The noble metal electrocatalysts deliver almost the same overpotential to achieve the benchmark current density. Gravimetric normalization is assumed to be more suitable as these

noble metal electrocatalysts are porous. Therefore, mass activity can be obtained by dividing the observed current and mass of the catalyst for a particular study. The equation is given as follows:

$$\text{Mass activity} = \frac{I(A)}{m(g)} \dots\dots\dots (1.20)$$

1.4.7 Faradic efficiency (FE)

FE is one of the most important parameters to evaluate the character of the electrocatalyst. Generally, it is the ratio of electrons that participated in the particular electrochemical reaction to electron supply. However, in the HER or OER process, FE is the number of hydrogen or oxygen that evolves experimentally to the theoretical one.^{51,52} Rotating ring disc electrode (RRDE) is used for the calculation of FE. The disc is made up of glassy carbon and surrounded by a platinum ring. The electrocatalyst is drop cast on disk swept over the particular potential window and keeping the ring at a constant potential. The role of the disc is to catalyze the OER and evolved oxygen reduction to H₂O₂ by the ring. The FE of an electrochemical reaction is calculated as follows:

$$FE = \frac{I_R n_D}{I_D n_R N_{CL}} \dots\dots\dots (1.21)$$

Where I_R, I_D, n_R, n_D are the ring current, disc current, number of electrons transferred at the ring and disc, respectively.

1.4.8 Cyclic stability

An electrocatalyst's practical application and commercialization always depend upon its stability or durability. Frankly, the catalytic performance is measured by long cyclic stability. The long cycle stability is measured by mostly chronopotentiometry (CP) and chronoamperometry (CA). Chronopotentiometry is the measurement of the variation of current density over a period of time at a particular overpotential, whereas chronoamperometry is the measurement of the change of overpotential over a time period at constant current density. It can also be evaluated by performing continuous CV in a potential window. The recorded LSV

polarisation curve after and before stability also tells the change in overpotential. Moreover, a further shift in diffraction angle, change in surface morphology, and change in oxidation state also reveal the post stability results.

1.4.9 Koutecký-Levich plot

The ORR kinetics and reaction mechanism are evaluated by using Koutecký-Levich Plot or K-L plot. This plot also correlates the number of electrons (n), the concentration of dissolved oxygen (C_{O₂}), diffusion coefficient, the viscosity of the electrolyte, and rotation speed of the electrode, etc. The K-L equation is given by ⁵³

$$\frac{1}{J} = \frac{1}{J_k} + \frac{1}{J_{dl}} \dots\dots\dots (1.22)$$

Where J, J_k and J_{dl} stand for the disk, kinetic and diffusion-limited current densities, respectively. Furthermore, J_k and J_{dl} are defined by the following equations

$$J_k = nFK_{O_2}C_{O_2} \dots\dots\dots (1.23)$$

$$J_{dl} = B \omega^{1/2} \dots\dots\dots (1.24)$$

Herein, n, F, K_{O₂}, C_{O₂}, B and ω stands for the total number of electrons transferred in the ORR, Faraday constant (96485 C mol⁻¹), oxygen solubility constant, the concentration of oxygen in the electrolyte (1.2 × 10⁻⁶ mol cm⁻³), slope derived from the K–L plot and the rotation speed of the rotating disk electrode, respectively.

The K-L slope obtained by the following equation ⁵⁴

$$B = 0.62nFC_{O_2}D_{O_2}^{2/3}\nu^{-1/6} \dots\dots\dots (1.25)$$

Here D_{O₂} is the diffusion coefficient of oxygen (1.9 × 10⁻⁵ cm² s⁻¹) and ν is the kinematic viscosity of the electrolyte (1.1 × 10⁻² cm² s⁻¹). The K–L plot is presented between J_k⁻¹ (kinetic current density) and ω^{-1/2} (electrode rotation rate). By putting all the values, the number of electrons is calculated. Getting the number of electrons (n) two or four related to the reaction

proceeds through hydrogen peroxide (H_2O_2) intermediate or direct conversion of dissolved oxygen to water without intermediate, respectively.

1.5 Types of electrode material used

In the electrocatalytic process, various electrode materials are used to evolve oxygen or hydrogen. Generally, noble metal-based and noble metal-free electrocatalysts are used to evolve gases in this process. Precious metals (like platinum (Pt), palladium (Pd), and noble metal-based oxides like RuO_2 and IrO_2) show benchmark current density for HER and OER, respectively. However, the high cost, limited availability, and detrimental environmental effect restricts the wide application of noble metal-based catalyst. Hence, later on, the researcher focused on the noble metal-free electrocatalyst as an emerging material for electrocatalysis.

1.5.1 Precious metal-based catalyst

The electrocatalytic process needs a higher overpotential than expected. To minimize overpotential, a suitable electrocatalyst is used, such as noble metals such as Pt, Pd, RuO_2 , IrO_2 . Initially, precious metals are only considered electrocatalysts for water splitting. For the HER process, Platinum (Pt), Palladium (Pd) are considered benchmark catalysts. The HER activity of various metals against free energy is given in Fig 1.8.⁵⁵ Similarly, the oxide of ruthenium and iridium are exhibiting benchmark performance for the OER process. However, the high cost and scarce availability of these materials always restrict their wide application.

Therefore, the researcher gives more attention to the non-noble metal catalyst as a promising alternative in the modern era. So, these non-noble electrocatalysts (metal oxides, metal sulfides, metal selenides, metal nitrides, metal borides, metal carbides, metal phosphides) and, nowadays, metal-organic framework (MOFs) and their derived materials are considered as an emerging material for electrocatalysis.

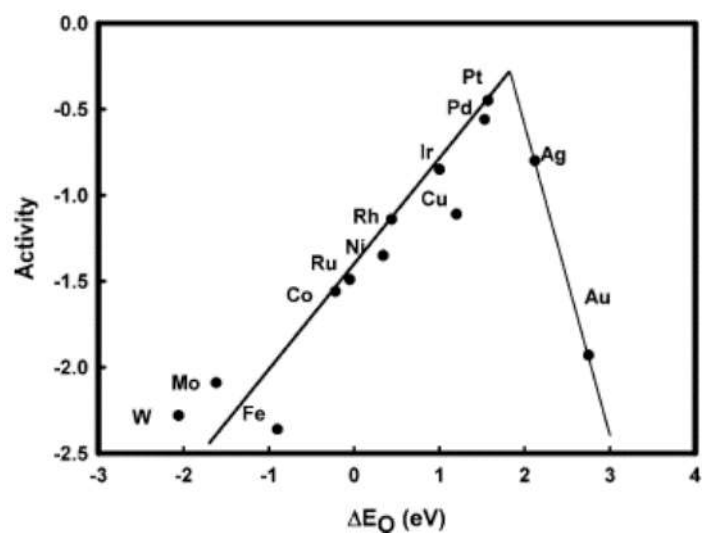


Figure 1.8 Volcano plot used for HER electrocatalyst.

1.5.2 Transition metal selenide

Among all the materials used for electrocatalytic study, transition metal chalcogenides (TMC) are given more attention due to their unique layer structure. A transition metal bonded to two chalcogens through a covalent bond like a sandwich forming layer structure.

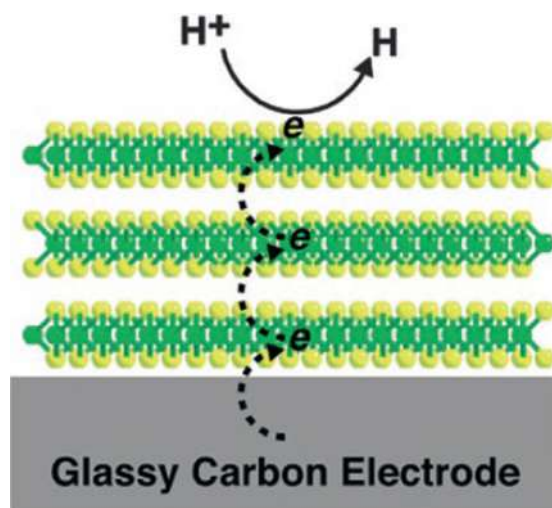


Figure 1.9 Hopping of electron in MoS₂ layer.

Each layer is connected by van der Waal's force of attraction can be easily exfoliated. Transition metal selenides are given more attention among all having formula MX or MX₂, where M stands for transition metal such as Fe, Co, Ni, V, W, Mo, etc, and X represents Se. The layer structure and easy exfoliation of each layer made transition metal selenide a suitable

electrocatalyst towards the evolution of H₂ and O₂. The greater the diffusion of ions between the MX₂ layer and electrolyte faster will be the transfer of electrons. Furthermore, the diffusion of ions depends upon the thickness of electrocatalyst loading. A larger thickness of electrocatalyst loading leads to an increase in the interlayer potential barrier, decreasing the catalytic behavior as shown in Fig 1.9.⁵⁶ Since HER is a surface phenomenon, catalysis is deeply affected by overloading. Various selenides such as CoSe, CoSe₂, NiSe₂, MoSe₂, WSe₂ are exhibiting better catalytic performance towards HER, OER, and ORR in the different electrolytic medium. For instance, CoSe and CoSe₂ are active for HER, OER and ORR.⁵⁷⁻⁵⁹ The outstanding achievements to explore this research area are deploying non-noble metal electrocatalyst found to be inexpensive, abundant, easy scalable synthetic procedure, unique structure, and significantly less detrimental effect compared to noble metals. NiSe₂ exhibiting HER performance with a very lower Tafel slope 29.4 mV/s even less than reference noble metal platinum (Pt, 30.8 mV/s) very rare report published by Yu et al.⁶⁰

1.5.3 Transition metal boride

For the replacement of noble metal electrocatalyst, researchers focus on transition metal sulfides, selenides, phosphides, and nitrides and put interest in alloys type material by incorporating metalloid (C, B, As, Te) with the transition metal. Transition metal boride is one of the most emerging fields used for hydrogen evolution and oxygen evolution reaction. It was believed the boron species dissolve in aqueous media from catalyst-producing voids. Hence porosity increases filled by the interfacial metal atom creating more contact with electrolyte enhancing the performance. In another way, the host metal gets oxidized to permit the diffusion of OH⁻ ion into MB/MO interface to form a metal oxyhydroxide (MOOH) shell.⁶¹ Patel et al. first time reported a non-noble, robust Co-B electrocatalyst delivering HER in a wide range pH (4-9) value. The material shows 250 mV overpotential at 10 mA/cm² current density with 75

mV/dec Tafel slope.⁶² The XPS survey exhibits the electron transfer occurs from boron to metal center responsible for significant HER activity as shown in Fig 1.10.

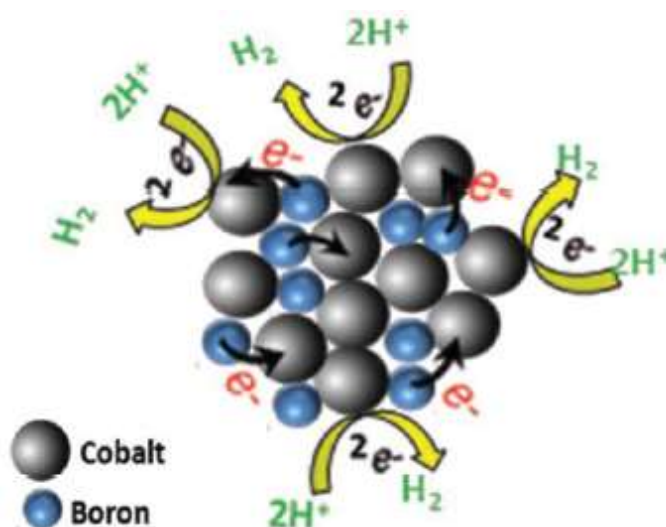


Figure 1.10 HER activity of Co-B cluster.

Similarly, Gupta et al. prepared a nanocrystalline Co-B sample and explored its OER activity. The surface of this thin film is believed to be composed of $CoOOH$, enhancing the OER performance. Co-B delivered 280 mV overpotential at 10 mA/cm^2 current density with potential stability around 45 h.⁶³

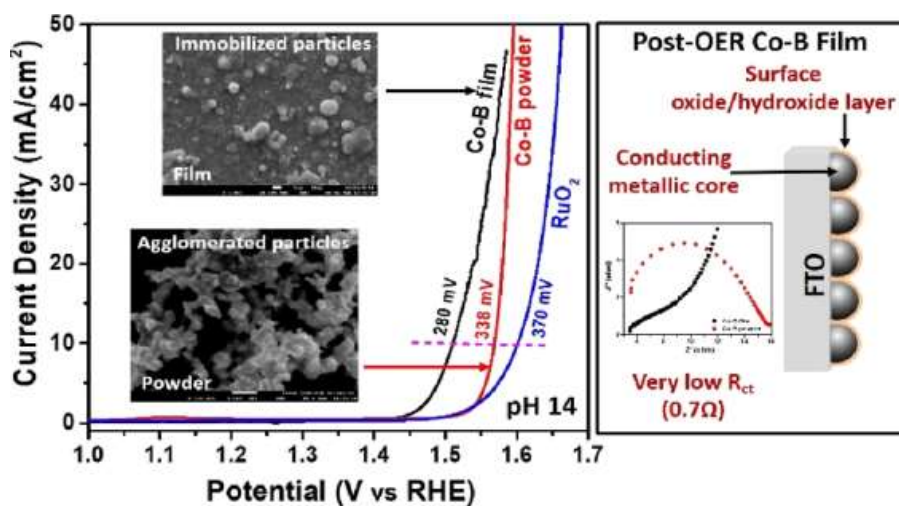


Figure 1.11 OER performance and post OER study of Co-B nanoparticles.

1.5.4 Metal-organic frameworks (MOFs) as an electrocatalyst

As relatively young and rapidly growing materials, metal-organic frameworks (MOFs) have generated tremendous interest in the modern era. The diversity of composition and structure of MOFs leads to exhibit different functionalities. The storage and interaction with guest molecules observed by MOFs due to the availability of excellent porosity and high surface area trigger broad research interest to explore its electrochemical energy conversion processes. The redox-active center deliberately produced by the metal center in MOFs (especially first-row transition metal Fe, Co, Ni) plays a key role in the electrochemical energy conversion process. In comparison to inorganic and polymeric functional material, MOFs provide electrochemically active centers and functional groups. Apart from this, accessible organic molecule coordinated metal sites, easily tuneable pore structures make MOFs suitable candidates for electrocatalysis. During electrocatalysis, ligand, as well as metal, plays a vital role in MOFs. During oxygen evolution reaction (OER), ligands are believed to act like protophilic and help in the deprotonation of the water molecule, thereby facilitating the formation of "O-O" bond formation as shown in the figure:⁶⁴

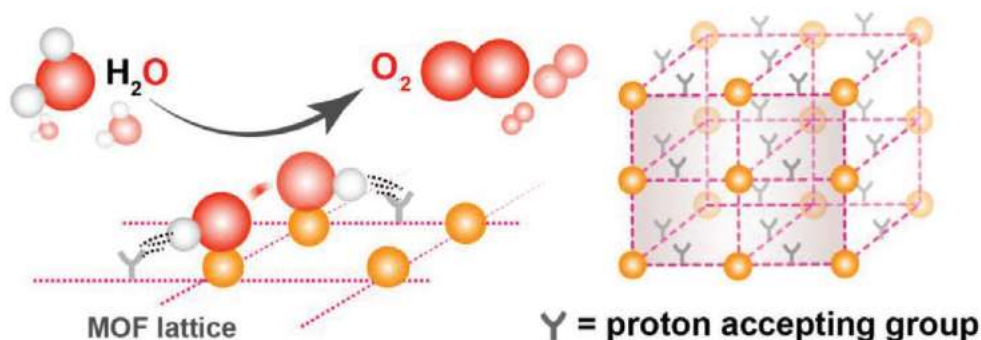


Figure 1.12 Co-operative effect of proton accepting group on the OER activity in MOFs.

For example, in Co-ZIF-9, the benzimidazolate motif in the vicinity of Co (II) centers accept a proton for the dehydrogenation of water molecule.^{65,66} In a nutshell, MOFs with electron-withdrawing ligands and high oxidation state metal center preferably exhibit OER. Hydrogenases and nitrogenases catalyzing hydrogen evolution reaction (HER) contain Ni-Fe,

Fe-Mo active sites, respectively. Largely accepted water dissociation center of Ni and superior hydrogen adsorption properties of Mo motivate for better HER catalysis. Furthermore, MOFs with strong π -acceptor ligand like CO, CN^- ligand leads to form low spin complexes supposed to exhibit excellent HER catalysis.⁶⁷ Briefly, the surface that promotes dissociation of water molecules and helps in the hydrogen recombination step performs better catalyzing towards HER. The volcano plot of current density Vs. free energy is shown in Fig. 1.13.⁶⁴

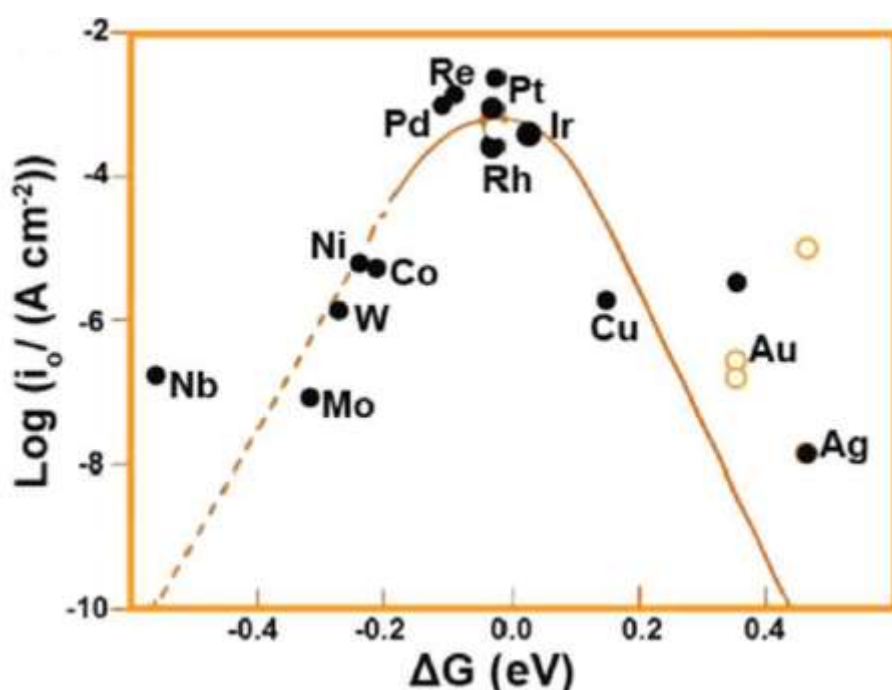


Fig.1.13 Volcano plot based on exchange current density Vs free energy of hydrogen adsorption at $U=0$.

Moreover, the multidimensional architecture of MOFs allows them to exhibit greater catalytic sites, enhanced stability, improved adhesion to the surface, making them an emerging material for HER electrocatalysis. The nature of the metal center and ligand also modulates the kinetics and selectivity of oxygen reduction reaction (ORR). It proceeds typically through a concerted proton-electron transfer pathway either by complete reduction or partial reduction. In complete reduction, molecular oxygen (O_2) is converted to water (H_2O) through a $4e^-$ transfer ($4e^- + 4H^+$) whereas partial reduction involves the formation of hydrogen peroxide (H_2O_2) from

oxygen via a $2e^-$ process ($2e^- + 2H^+$). The four-electron process is considered the most desirable and energy-rewarding conversion out of two.⁶⁸ MOFs build up with transition metal center (typically Fe, Co) efficiently catalyzes the ORR. The employment of proton relaying ligand plays a major role in transferring proton across the ORR active centers shown in Fig 1.14.⁶⁴

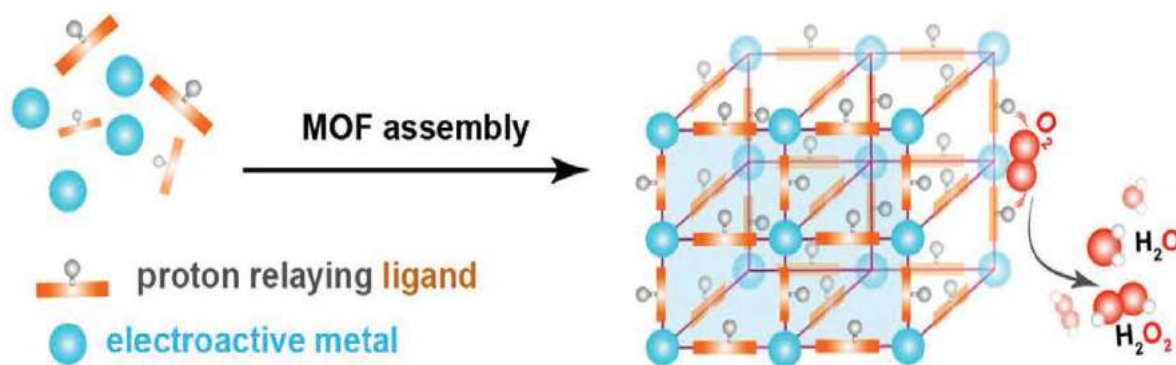


Figure 1.14 Cooperative effect of the proton relaying ligand on the ORR activity.

The redox activity and pK_a of organic struts also control the intrinsic catalytic activity of MOFs. One such explicit display of such behavior is found in electrically conductive HITP (2,3,6,7,10,11-hexaiminotriphenylene)-based Ni-MOF, $Ni_3(HITP)_2$. The charge delocalization across the framework is possible due to HITP ligand. Also seen in a typical 3D porphyrinic MOF, Co (II) center is stabilized by the electron-withdrawing effect of tetrapyrrole moiety.⁶⁹ It is perceived that in an extended system, ORR catalytic activity increases as the separation of the unsaturated metal centers by the ligands increase.

1.5.5 MOFs derived material as an electrocatalyst

A large proportion of MOFs suffer from acute stability issues both in acidic and basic electrolytes. Also, the metal-ligand bond succumbs to hydrolysis in the presence of water, restricting the direct use of virgin MOFs as electrocatalysts. The hard M^+ - redox ligand center in MOFs furnishes poor electronic conduction for long-range architecture. Thus, proper measures have been made to transform MOFs into carbon or hetero atom doped moiety so-called MOFs derived material able to overcome the conductivity and stability issue faced by

the predecessors. Generally, two basic strategies are followed to produce MOFs-derived material (i) By tuning the composition of MOFs precursor and/or (ii) manipulating the conversion process. In either of the process, MOFs acted like a self-sacrificial template and lost their molecular structure. However, the active metal coordination centers are largely available and made possible to resolve the above-said issues. Annealing is an ideal approach to convert MOFs to carbon-based or hetero atom-doped material by utilizing and integrating significantly large number of metal-ligand atoms not only chemically stable but also free from poor conductivity. Also, fabricating such electrocatalyst agglomeration of particles should be avoided by choosing appropriate annealing temperature. Morphology of derived sample also plays a vital role in optimizing the catalytic activity of electrocatalyst. For instance, "cubane" structures are considered the excellent electrocatalyst for water oxidation shown in Fig 1.15.⁶⁴

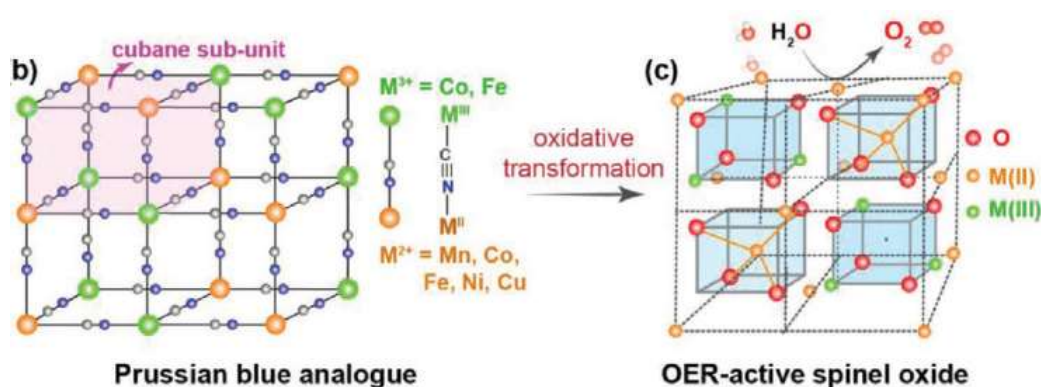


Figure 1.15 Oxidative transformation of cubane shaped prussian blue analogue (PBA) into corresponding spinel oxide.

MOFs-derived materials also exhibit HER activity in acidic as well as alkaline media.^{70,71} In addition to metal oxide, metal sulfide, selenide, phosphide, boride are also promote HER in both acidic and alkaline media. Porosity becomes a key attraction for the MOFs-derived material to be HER active, as shown in Fig 1.16.⁶⁴ Furthermore, annealed MOFs in some cases undergo sulfurization, selenization, phosphorization to produce M-S, M-Se, M-P coordination

centers. For instance, nanocube Ni-Co PBA under annealing condition treated with Na₂S to form hollow NiS shown in Fig 1.17.⁷²

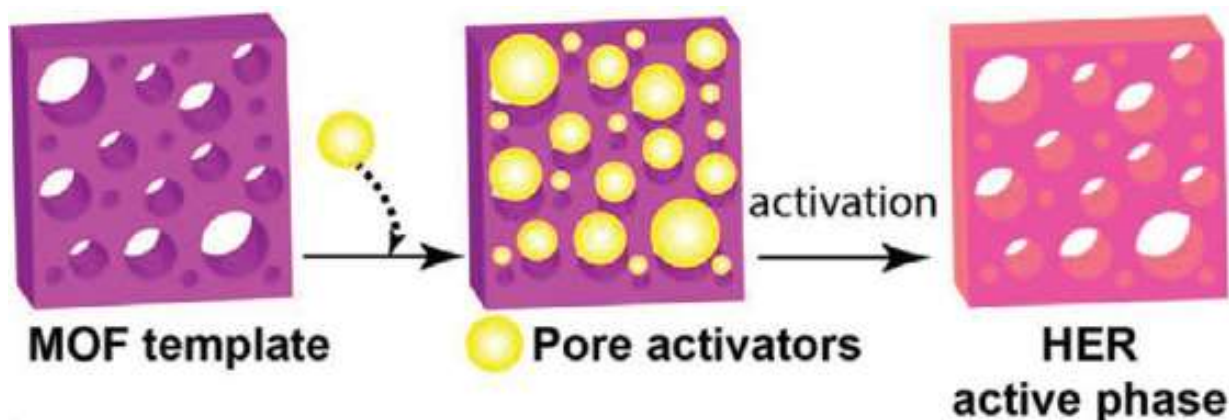


Figure 1.16 MOFs derived material induces HER activity.

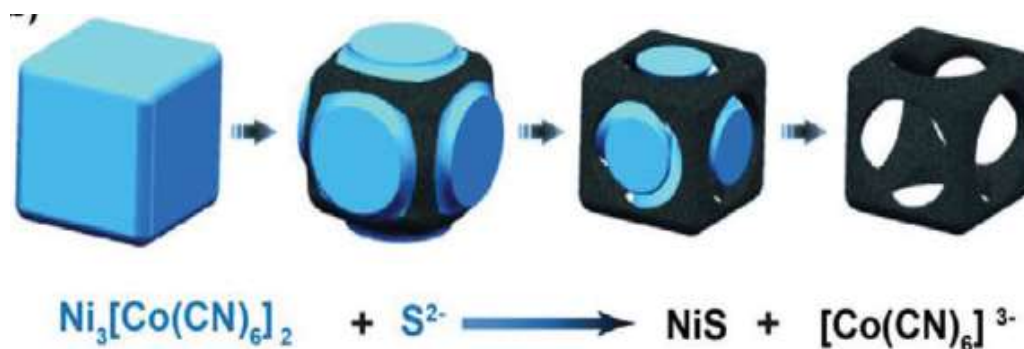


Figure 1.17 Formation of NiS nanoframe using Ni-Co PBA MOF.

Roland A. Fischer et al. reported the formation of OER and ORR active Co@Co₃O₄ encapsulated in CNT grafted nitrogen-doped carbon polyhedral derived from ZIF-67 under He

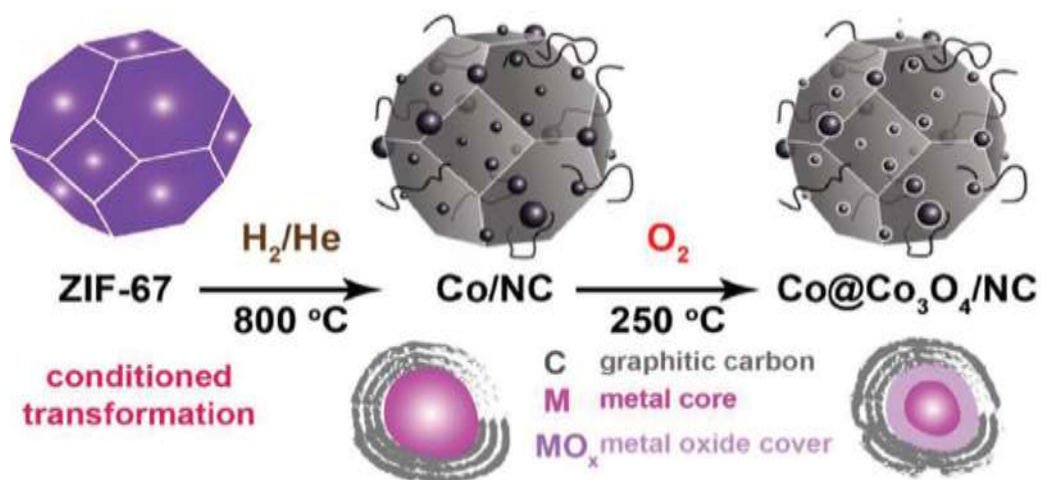


Figure 1.18 Schematic representation and OER, ORR of active Co@Co₃O₄ encapsulated in CNT grafted nitrogen doped carbon polyhedral.

containing H₂ atmosphere shown in Fig 1.18.⁷³

1.5.5.1 MOFs derived transition metal selenide

The conductivity and stability issue of the MOFs encourage the synthesis of MOF-derived material such as oxide, sulfide, selenide, phosphide, carbide etc. as electrocatalysts. The synthetic procedure either follows hydrothermal or annealing. There has been a lot of work done on MOF-derived selenide containing transition metal such as Fe, Co, Ni, Mo, W etc. MOFs used as sacrificial template react with selenium (Se) powder producing bare MOF-derived metal selenides or heteroatom (N, S) doped metal selenide or carbon-based MOF-derived selenide.⁷⁴ Sometimes to get the spectacular result, researchers doped MOF with other metals like Zn, Fe, Ag, etc.^{75–78} Morphology also plays a vital role in the enhancement of electrocatalytic properties. Among all hollow structures, MOFs-derived selenides are more attracted in the field of electrocatalysis.⁷⁹ The easy synthetic procedure and large-scale synthesis made MOF-derived metal selenide an emerging catalyst for hydrogen and oxygen evolution.

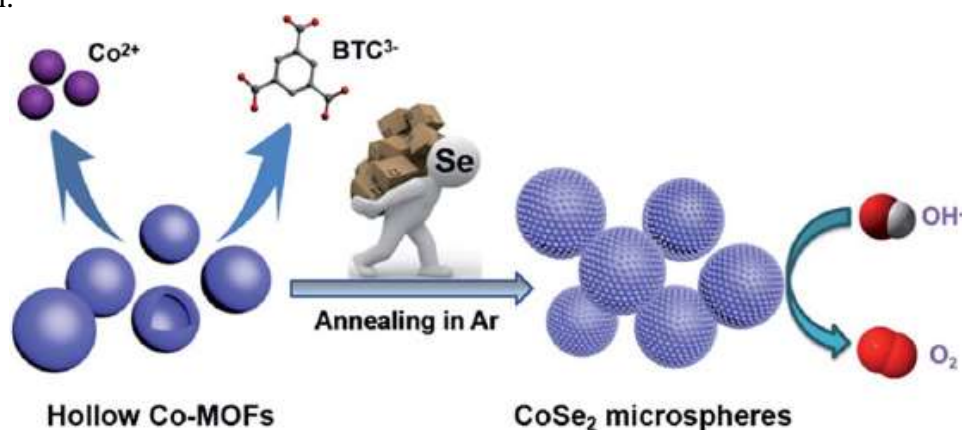


Figure 1.19 MOF derived CoSe₂ microsphere for OER.

Zhang et al. reported the MOF-derived Fe doped CoSe₂ for efficient Hydrogen Evolution Reaction.⁷⁵ They synthesized Fe doped MOF (ZIF-67) initially and then selenized by annealing with Se vapor to produce Fe-CoSe₂@NC. It exhibits excellent HER performance with a low

overpotential of 143mV at 10 mA/cm². The Tafel slope was found to be 40 mV/decade as shown in Fig. 1.20.

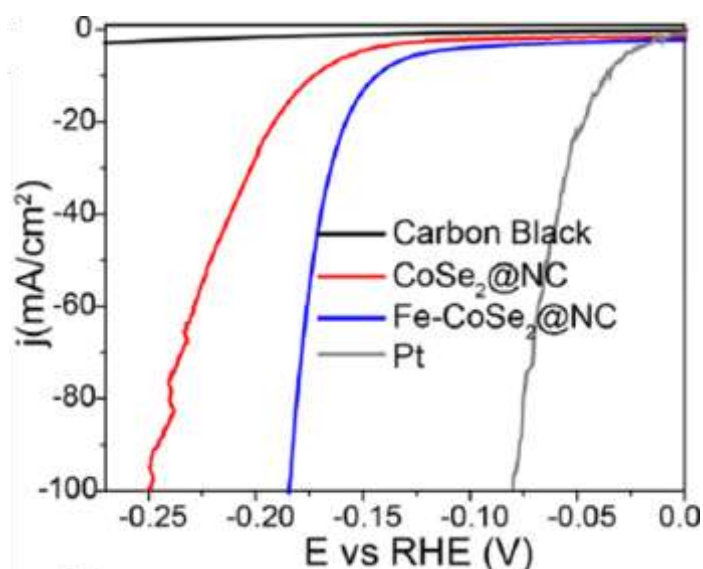
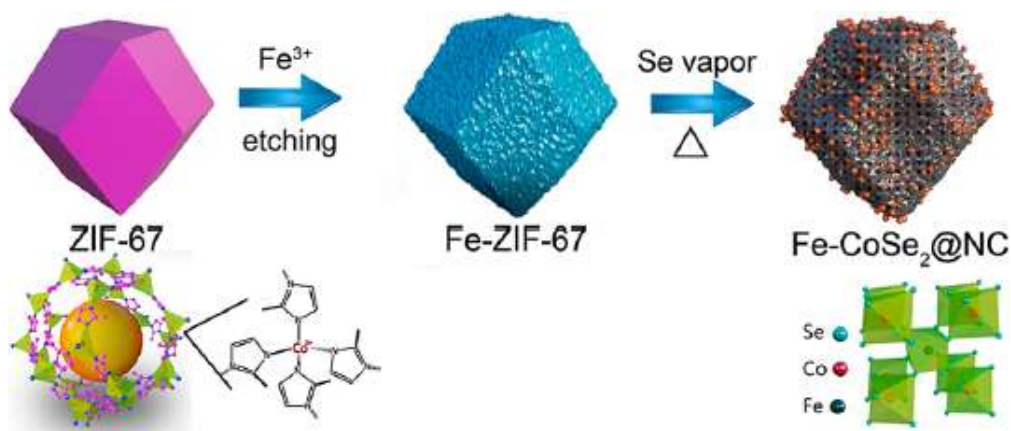


Figure 1.20 Schematic procedure (top) and HER performance of of Fe-CoSe₂@NC (Bottom).

1.5.5.2 MOFs derived transition metal boride

The electron deficiency of elemental boron and high conductivity of metal boride urges to study in the electrochemical application. Though MOF-derived oxide, sulfide, selenide, phosphide show spectacular activity in hydrogen and oxygen evolution as well as oxygen reduction, the incorporation of metalloids (B, As, Te, etc.) brings noticeable results in these fields. Particularly, MOF-derived boride materials being amorphous, having high surface area, and

developed porosity and unique morphology have been considered an emerging material in energy conversion issues. The transformation of crystalline MOF structure to amorphous MOF-derived boride material via a simple redox technique is significant. Keeping all the above-said criteria, Behera et al. synthesized MOF-derived amorphous Nickel boride (NiB) and explored its OER properties in 1 M KOH electrolyte.⁸⁰ Our material needs only 240 mV Overpotential at benchmark 10 mA/cm² current density to deliver Oxygen evolution with a Tafel slope of 58 mV/decade shown in Fig 1.21.

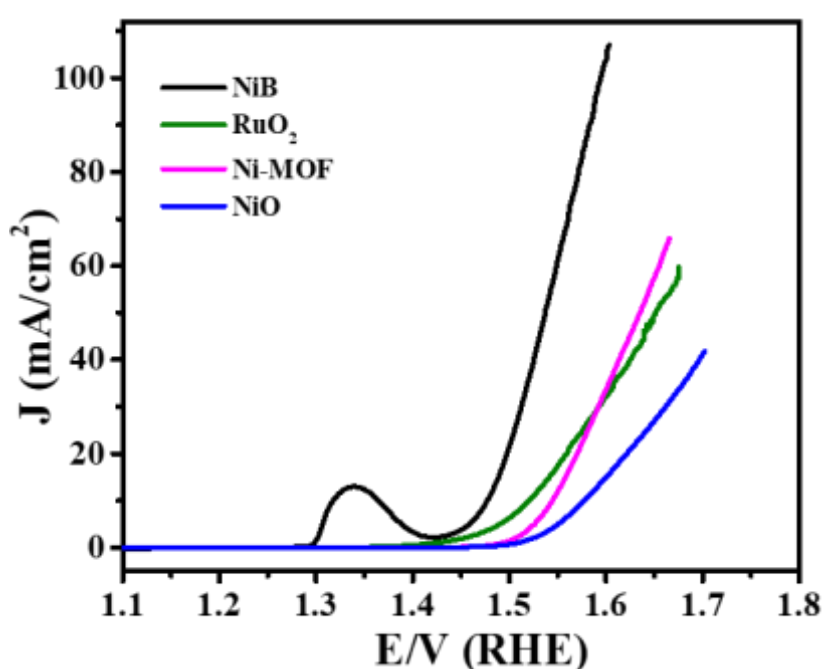


Figure 1.21 OER performance of NiB and comparative materials in 1 M KOH.

1.6 Supercapacitor or Ultracapacitor

The depletion in fossil fuel and the environmental condition dependable intermittent renewable solar and wind energy demand for the large-scale energy storage system.⁸¹ Therefore, alternative measures should be given for future generations to produce clean energy, and sufficient emphasis should be given to its storage. The high power supply, long cycle life, easy operation of supercapacitor attracts researchers to focus more on it. Supercapacitors have a higher power density than batteries and higher energy density than a capacitor. The comparison of various parameters among capacitor, supercapacitor, and batteries are listed below.

Table 1.1 comparison of some basic parameters among capacitor, supercapacitor and battery.⁸²

Parameter	Capacitor	Supercapacitor	Battery
Charge Time	10^{-6} - 10^{-3} sec	1-30 sec	0.3-3hrs
Discharge Time	10^{-6} - 10^{-3} sec	1-30 sec	1-5hrs
Cycle Life	>500,000	>100,000	500-2000
Power density (kW/kg)	>10,000	1000-2000	50-200
Energy density (Wh/kg)	<0.1	1-10	20-100

From the parameters shown in the above table, the cycle life and power density of the supercapacitor are superior to the battery. Further charging time, discharging time, and energy density of supercapacitor are superior to a capacitor. In short, a supercapacitor acts like a bridge between capacitor and battery.

1.6.1 Basic component of supercapacitor

The electrochemical energy storage device with high energy density (ease to store electrical energy) power density (ease the rate of flow of energy or discharge process) than capacitor and battery respectively. In very short, it compensates for the deficiency of battery and capacitor acting as a bridge between them. Supercapacitor consists of two porous electrodes, two current collectors, a separator, and an electrolyte. The two electrodes are immersed in an appropriate electrolyte separated by a separator, as shown in Fig 1.22.⁸³

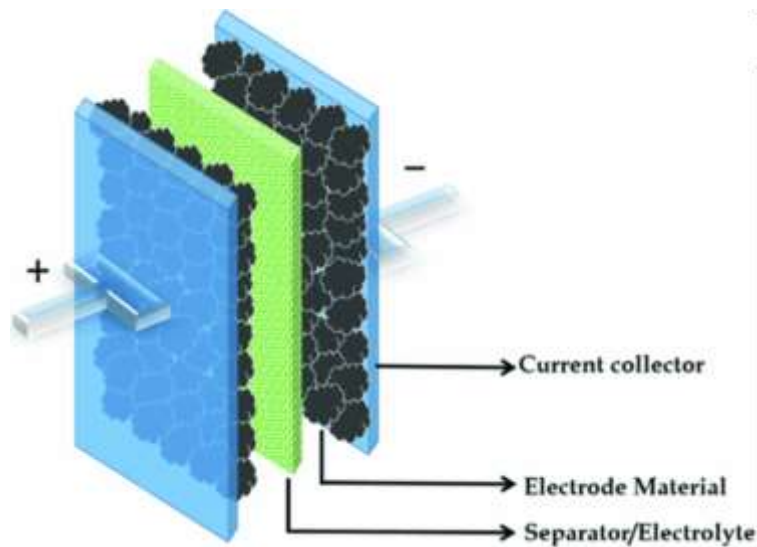


Figure 1.22 Set-up of a typical supercapacitor.

When voltage is applied to the current collector, positive ions move towards the negative electrode and vice-versa, known as charging. The charges will accumulate on both the electrodes creating layers of opposite charge when it completely charges and starts to generate energy when it undergoes discharging, as shown in Fig 1.23.⁸⁴ The performance of a supercapacitor depends upon the nature of the electrolyte, type of electrode used, electrode material, the porosity of the separator, and the nature of the current collector.

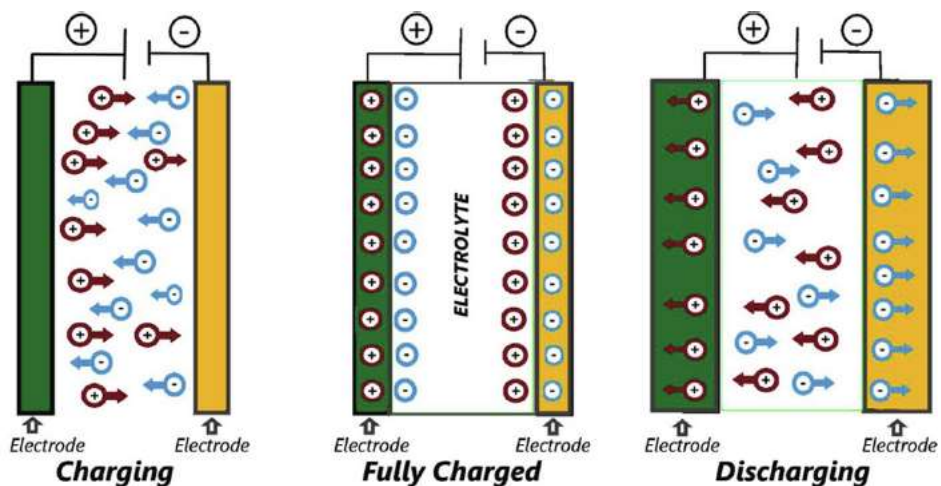


Figure 1.23 Different electron movement in charge, fully charge and discharge level in supercapacitor.

1.6.2 Key parameters used in supercapacitor

Various parameters describe the performance of a supercapacitor. Among them, specific capacitance (C_s), power density or specific power (P_d), energy density or specific energy (E_d), cyclic stability, and coulombic efficiency are always in focus.

1.6.2.1 Specific capacitance (C_s)

The performance of a supercapacitor is described by specific capacitance, which is the amount of charge stored over a potential change. It is the intrinsic capacitance when normalized with mass called gravimetric capacitance ($F g^{-1}$), with the area called areal capacitance ($F cm^{-2}$), with length called linear capacitance ($F cm^{-1}$), with volume known as volumetric capacitance ($F cm^{-3}$). This intrinsic capacitance depends on mass loading, the thickness of active material, dimension, electrode density, types of electrolytes, and experimental setup. The specific capacitance of a particular active material can be obtained either from cyclic voltammetry (CV) or from the galvanostatic charge-discharge (GCD) technique.^{85,86}

1.6.2.2 Specific energy and specific power

The most important parameters of supercapacitor, widely used in practical purposes are energy density and power density. Energy density or specific energy can be defined as the amount of energy stored per unit (mass in kg or area in cm^{-2} or volume in L.). Similarly, power density is the amount of energy flow per unit (mass, area, volume) time per unit time (s). To evaluate specific energy and specific power, either cyclic voltammetry (CV) or galvanostatic charge-discharge (GCD) are the technique commonly used. Following the CV curve, the energy density (E_d) of active material can be obtained by using the following equation^{80,87}

$$E_d = \frac{1}{2} C_s (\Delta V)^2 \dots\dots\dots(1.26)$$

Similarly, power density can be obtained by using the following equation^{-80,88}

$$P_d = \frac{1}{2} C_s (\Delta V) r \dots\dots\dots(1.27)$$

Herein, E_d and P_d represent the energy density in Wh kg⁻¹ and power density of kW kg⁻¹, respectively. C_s is the specific capacitance, ΔV stands for the specified potential window, and r is the scan rate at which all CV cycles were performed.

1.6.2.3 Cyclic stability

This is the most desirable criterion that defines the practical applicability of the active material. The durability and robustness of the material are evaluated from the cyclic stability of the desired material. It has been found that supercapacitors are very robust in nature and run more than one lakh cycles. So, it is very difficult to calculate such a higher value. So suitable measures are taken, and the capacitance retention rate is included. The retention rate can be obtained by comparing the specific capacitance of the initial cycle to the final cycle and plotted by taking time versus percentage of capacitance retention.

1.6.2.4 Coulombic efficiency

From galvanostatic charge-discharge (GCD), charging time and discharging time are obtained. Coulombic efficiency can be calculated by using the following equation⁸⁰

$$\eta = \frac{t_D}{t_C} \times 100\% \dots\dots\dots(1.28)$$

1.6.3 Electrolytes used

Considering various factors like the high electrical stability, low solvated ionic radius, low resistivity, high ionic concentration and low toxicity, wide operational potential window, low volatility, light expensive with pure form availability in supercapacitor study, it is believed the role of electrolyte seems to be significant. Therefore, electrolytes are generally divided into two categories aqueous and non-aqueous electrolytes.⁸²

1.6.3.1 Aqueous electrolyte

The liquid electrolyte containing various inorganic salt materials forms the aqueous electrolyte. Depending on pH of the solution, the electrolytes are categorized as acidic (H_2SO_4), basic (KOH , NaOH), and neutral electrolytes (NaCl , KCl , K_2SO_4 , Na_2SO_4). High conductivity of the aqueous electrolyte preferred over non-aqueous being able to store charge due to availability of many solvated ions. Furthermore, the low resistance and high ionic concentration made the aqueous electrolyte superior to the non-aqueous one. Also, the mode of synthesis is very easy and needs no particular reaction condition. However, the narrow operational voltage window needs further improvement, and as a result, non-aqueous electrolyte comes into the picture.

1.6.3.2 Non-aqueous electrolyte

Ionic liquids and organic electrolytes are categorized as non-aqueous electrolytes. The high thermal and electrical stability, low vapor pressure, high electrochemical stability, and the high range of voltage windows make this electrolyte suitable for SCs devices.^{89,90} The wide range of the voltage window, generally 2.5-3.5 V, made non-aqueous electrolyte more preferable than the former. Commonly used non-aqueous electrolytes are propylene carbonate (PPC), acetonitrile etc. Considering the toxic effect and eco-friendly nature of the electrolyte, propylene carbonate is better than acetonitrile. Ionic liquids used as a non-aqueous electrolyte consist of cations and anions. The cations include organic or inorganic, whereas inorganic refers to anions. The most used cationic/anionic ionic liquids such as sulfonium, imidazolium, phosphonium, pyrrolidinium, ammonium salts, and the anions such as hexafluorophosphate, tetrafluoroborate, and bis (trifluoromethanesulfonyl) imide, etc.

1.6.4 Calculation of super capacitance from various techniques

Capacitance, power density, energy density, cyclic stability are measured from CV, GCD, Nyquist plot, or Impedance spectroscopy for supercapacitor measurement.

1.6.4.1 Cyclic voltammetry technique

By linearly varying the potential across the electrode in a two-electrode system or between working and reference electrodes in a three-electrode system, cyclic voltammetry technique of the desired material can be obtained. To collect information regarding charge storage for supercapacitor measurement, CV in three-electrode measurement is considered to be the best practice. A rectangular type CV is generally found for electrical double-layer capacitor (EDLC) material. Similarly, quasi rectangular is observed for pseudocapacitive material whether the charge storage mechanism follows either intercalation reaction or redox reaction at or near the surface (shown in Fig. 1.24).⁹¹ RuO₂ and MnO₂ are the typical pseudocapacitors following the redox mechanism, and layered oxide like Nb₂O₅ and MoO₃ undergo intercalation-type reactions. Another class of material found is called battery-type material following faradic reactions during the electrochemical process. Oxide and hydroxide of a transition metal like Co, Ni, Cu show such behavior.

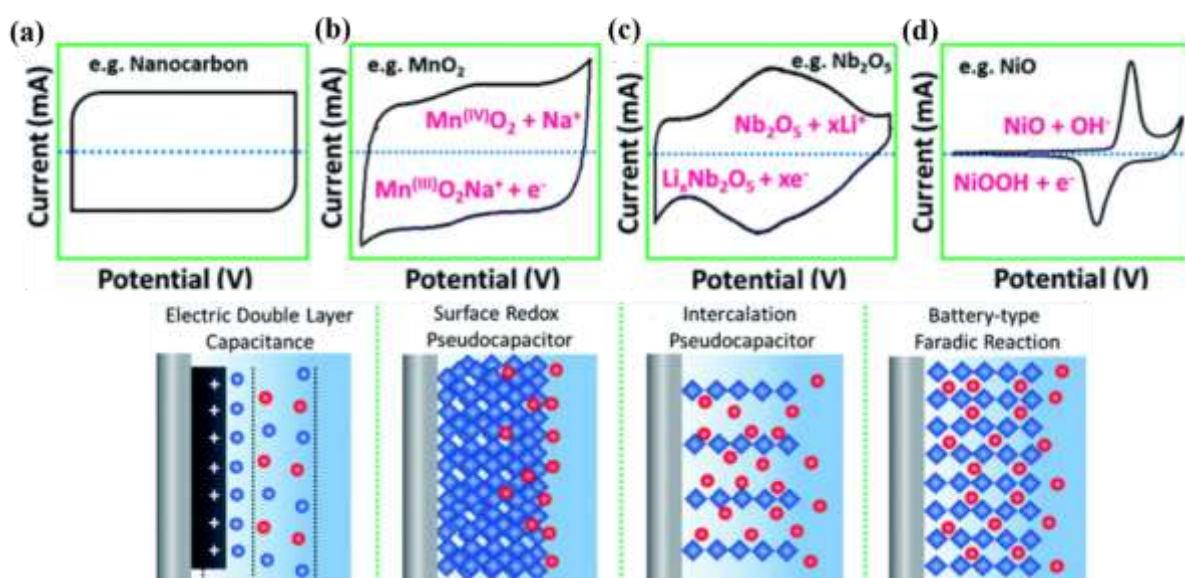


Figure 1.24 (a) EDLC behaviour by carbonaceous material (b) MnO₂ pseudocapacitor following surface redox (c) Nb₂O₃ pseudocapacitor following intercalation type reaction (d) NiO a battery type material follow faradic reaction.

The specific capacitance is obtained from the following equation-

$$C_s = \frac{\int_{V_a}^{V_b} I(V) dV}{mr(V_a - V_b)} \dots\dots\dots(1.29)$$

Here $\int_{V_a}^{V_b} I(V) dV$ is the area under the curve, m denotes the mass of the sample, r is the sweep rate, and $(V_a - V_b)$ represents the operating potential window, respectively.

Behera et al. synthesized MOF-derived nickel boride and explored its charge storage property. The amorphous Nickel boride exhibits specific capacitance 2580 F/g in 5 M KOH electrolyte.⁸⁰ The CV recorded at different scan rates is shown in Fig 1.25.

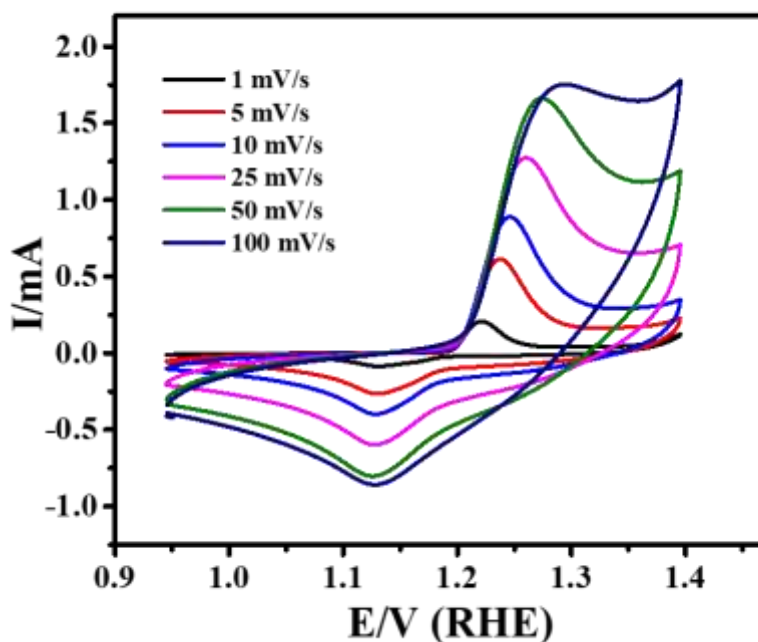


Figure 1.25 Cyclic voltammetry of nickel boride at various scan rate.

1.6.4.2 Constant current charge-discharge

In this technique, potential varies with time at a constant current for the continuous charging-discharging process. As constant current is maintained throughout the experiment, no potential step variation observed preferring charge-discharge than CV technique. Symmetrical triangle for EDLC type and quasi triangle for pseudocapacitive material observed shown in Fig 1.26.⁹¹

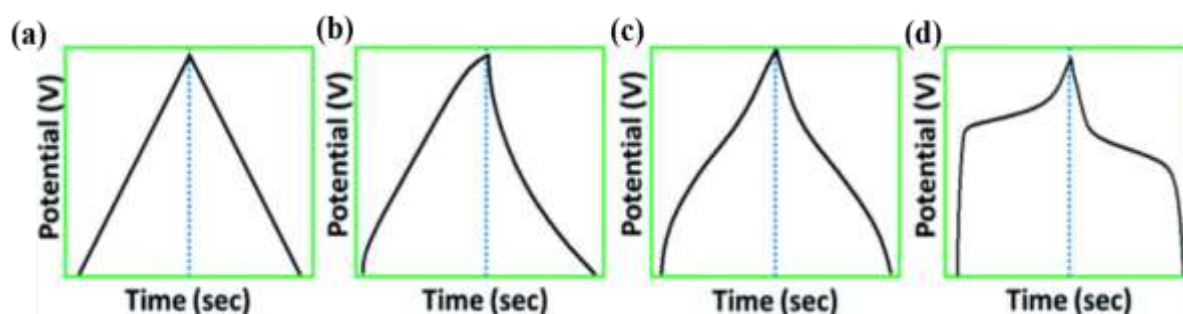


Figure 1.26 (a) EDLC type (b) Pseudocapacitive via redox (c) Pseudocapacitive via intercalation (d) Battery type following faradic reaction.

The specific capacitance can be calculated from CD by the following formula

$$C_s = \frac{I \times \Delta t}{\Delta V \times m} \dots\dots\dots(1.30)$$

Where I, Δt, ΔV, m stands for discharge current in ampere (A), discharging time, discharging voltage, and mass of electrode material, respectively. MOF-derived nickel boride is synthesized and supercapacitor property studied by our group. The charge-discharge is recorded at a constant current of this material is shown in Fig. 1.27.

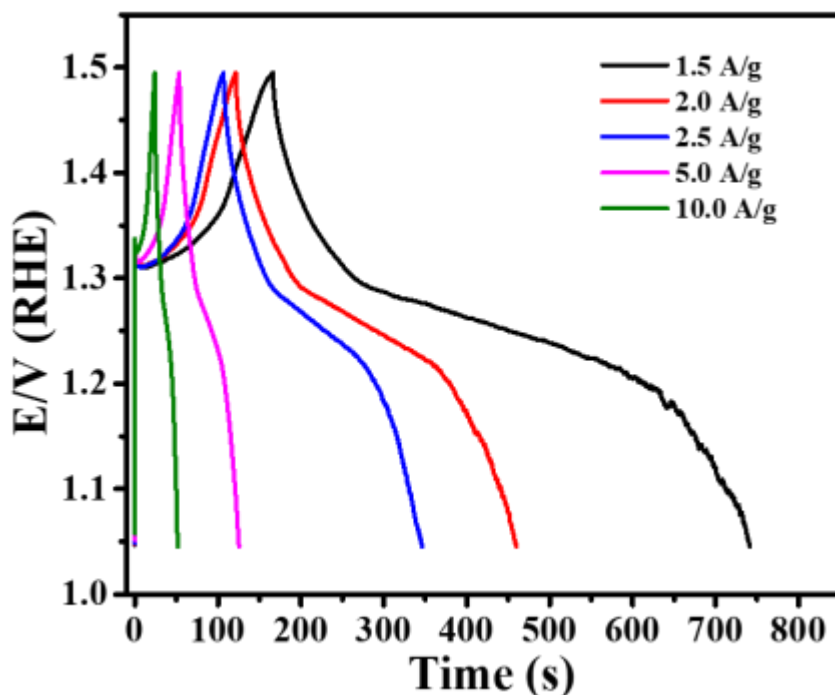


Figure 1.27 The charge-discharge (CD) shown by nickel boride.

From the galvanostatic charge-discharge experiment, we also able to get the specific capacitance value 2580 F/g well matched with the cyclic voltametric technique.

1.6.4.3 Electrochemical Impedance Spectroscopy (EIS)

The intrinsic parameter of the electrode active material is evaluated with the help of Nyquist plot or electrochemical impedance spectroscopy (EIS). This technique not only help to calculate charge transfer resistance, solution resistance, mass transfer etc but also gives an idea about specific capacitance, power density, energy density etc. For example, power density is inversely proportional to charge transfer resistance. Tianyi Ma et al. compared the WO_3 and oxygen-deficient WO_{3-x} material and found latter exhibits better capacitive behavior in terms of capacitance. The EIS study further confirms the better capacitive behavior of the latter one as the slope is closer to 90. The inset figure tells much smaller equivalent series resistance (R_s ,

0.86 ohm) and charge transfer of oxygen-deficient WO_{3-x} as compared to WO_3 as shown in Fig 1.28.⁹²

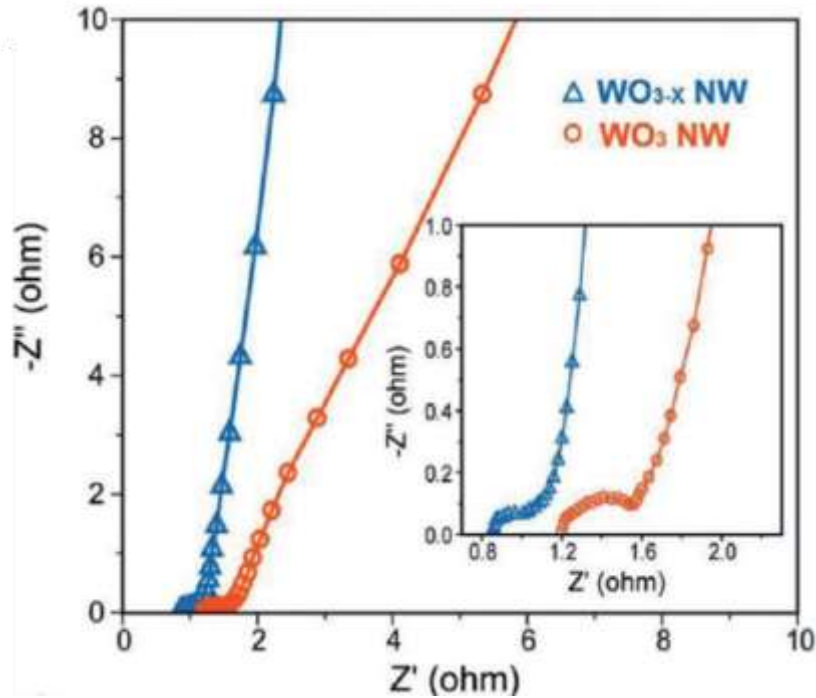


Figure 1.28 Nyquist plot of WO_3 and WO_{3-x} nanowire electrode.

1.6.4.4 Cyclic stability

It measures the capacitive retention and stability of the material after running a definite cycle as shown in Fig. 1.29.⁸⁰

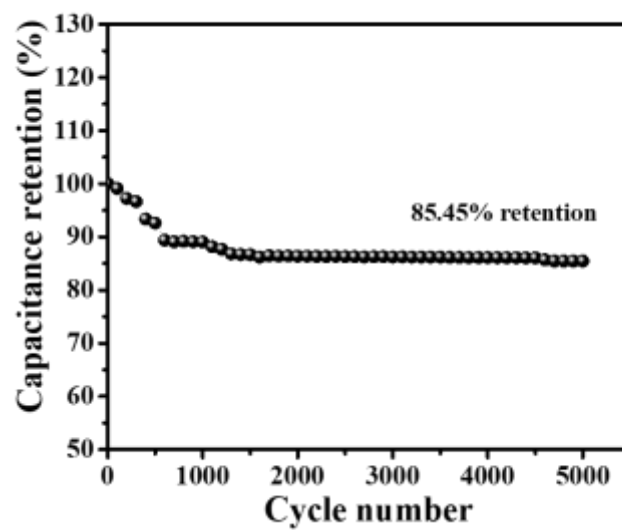


Figure 1.29 Cyclic stability of Nickel boride with retention.

1.6.5 Mechanism involved in supercapacitor

Based on the energy storage mechanism, the supercapacitor is divided into the following types.

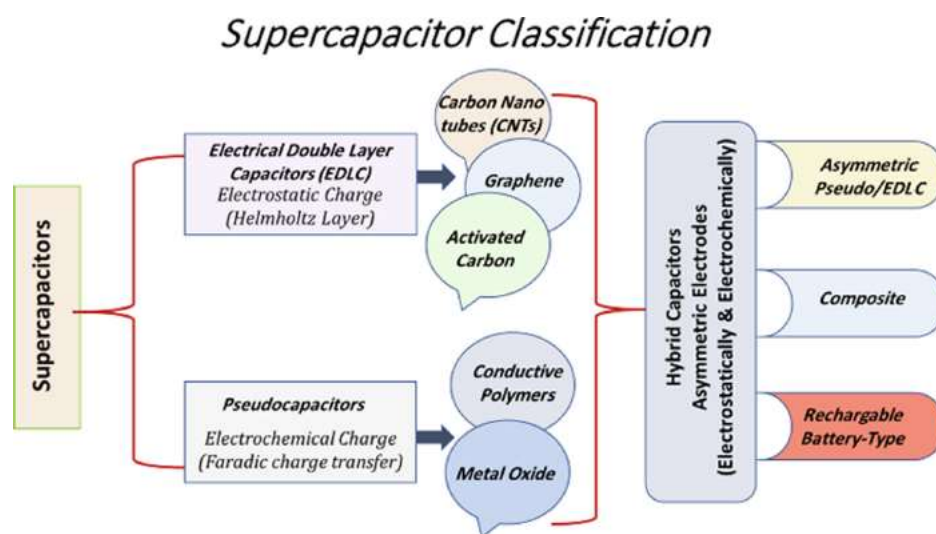


Figure 1.30 Classification of Supercapacitor based on energy storage.

In EDLC, capacitive procedure based on electrostatic interaction between electrodes and electrolytic ions whereas in pseudocapacitor the overall capacitance originated from Faradic reaction containing redox reaction, electro-sorption, intercalation due to electronic charge transfer between electrode and electrolyte.⁸⁴

1.6.5.1 Electrical double layer mechanism⁹³

Non-faradic reactions occurred in the EDL mechanism, i.e., charge storage takes place in this type of capacitor via electrostatic process, unlike reduction-oxidation. In this concept, the formation of two layers with opposite charges on the interface occurs, which consists of a minimal distance separating a molecular dielectric. Accumulation of charges will take place on the respective electrode of opposite charges when voltage is applied. Different models are proposed to understand this type of behavior. In the 19th century, the first theoretical model for electrochemical double layer was developed by Helmholtz.⁹⁴ According to him, out of two layers of charge at the electrode surface, the first in the solid material in one sign and the second layer in electrolyte with opposite sign to first one as shown in Fig 1.31.⁹⁵

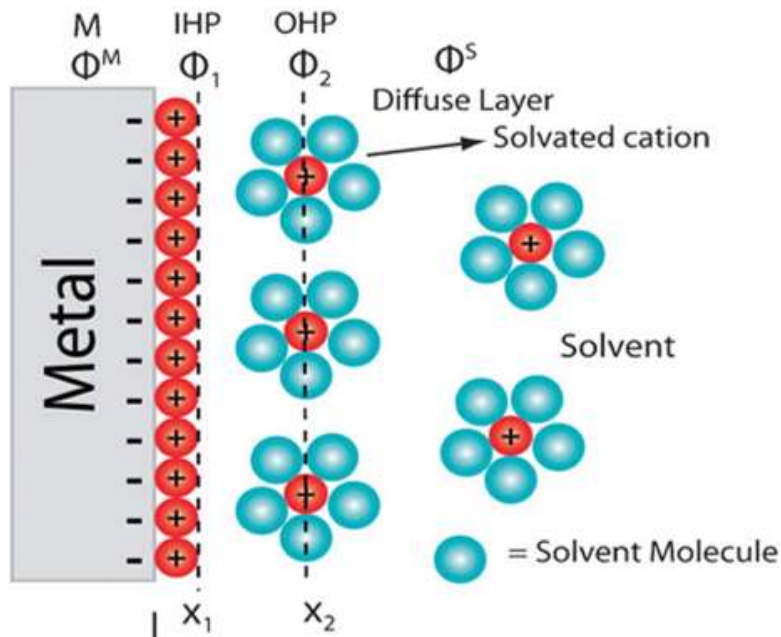


Figure 1.31 Electrical double layer by Helmholtz.

The potential in the electrochemical double layer decreases linearly with distance from the electrode surface. Then Gouy introduced point charges to the electrochemical double-layer concept. The overestimation of capacitance by him needs correction and developed by Chapman on the distribution of ions in electrolyte known as Gouy-Chapman model.⁹⁶ Adsorption of ions at electrode surface proposed by Stern for further correction.⁹⁷ He also told the total capacitance of double layer (C_{dl}) is the combination of the capacitance of layer closet to the electrode (C_H) and diffuse layer capacitance (C_{diff}) according to the equation-

$$\frac{1}{C_{dl}} = \frac{1}{C_H} + \frac{1}{C_{diff}} \dots\dots\dots(1.31)$$

Later Helmholtz layer is divided by outer Helmholtz plane (OHP) and inner Helmholtz plane (IHP) by Grahame.⁹⁸ He also proposed when charges are supplied to the polarizable electrode, the only double layer is charged. That's why no faradic reaction takes place across a double layer.

1.6.5.2 Pseudocapacitance (PC) Mechanism

Unlike EDLC, in pseudocapacitive mechanism, fast and reversible reaction takes place on electrode material when potential is applied. The redox reaction occurs in PC-type material made relatively less stable during the cyclic process. Because the faradic processes are slower than the non-faradic process, PCs have a relatively lower power density than EDLC. However, PCs exhibit large values of capacitance and energy density than EDLC because, in pseudocapacitor, the electrochemical process occurs both on the surface and in bulk near the surface of the solid electrode. Conducting polymers and metal oxides like RuO₂, MnO₂, Co₃O₄, etc., exhibit redox reactions at electrodes. Three types of faradic processes take place at PC electrodes. (a) Reversible adsorption (adsorption of hydrogen on platinum or gold) (b) Redox reactions of transition metal oxides (RuO₂) (c) Reversible electrochemical doping-dedoping (in conducting polymer-based electrode).⁹⁹⁻¹⁰¹

1.6.5.3 Hybrid supercapacitor (HS)

HS is an asymmetric electrode configuration i.e. one electrode made of carbonaceous material and another capacitive material. Both EDLC and faradic mechanisms occur simultaneously, but one dominant over the other. High cell voltage, high power density and high energy density can be achieved by this type of supercapacitor. Wang et al. fabricated a hybrid capacitor, taking highly porous graphitic carbon fibers (HPGCFs) as a positive electrode and anthraquinone functionalized HPGCFs as negative electrodes. While this hybrid capacitor exhibits excellent SCs performance in terms of higher energy density (19.3 Wh kg⁻¹) with a better power supply.¹⁰²

1.7 MOFs as supercapacitor material

As we know, the poor intrinsic conductivity and instability towards moisture become a big barrier to use MOFs widely in the electrochemical application. However, its diverse structure,

high specific surface area and large internal pore volume made a promising electrode for energy conversion and storage application. Taking all the possible benefits, M.Dinca et al. synthesized a $\text{Ni}_3(2,3,6,7,10,11\text{-hexaiminotriphenylene})_2$ or $\text{Ni}_3(\text{HITP})_2$ MOF and explored its areal capacitance.¹⁰³ This MOF is made of a stacked conjugated two-dimensional layer penetrated by a one-dimensional channel of 1.5 nm diameter, as shown in Fig 1.32.

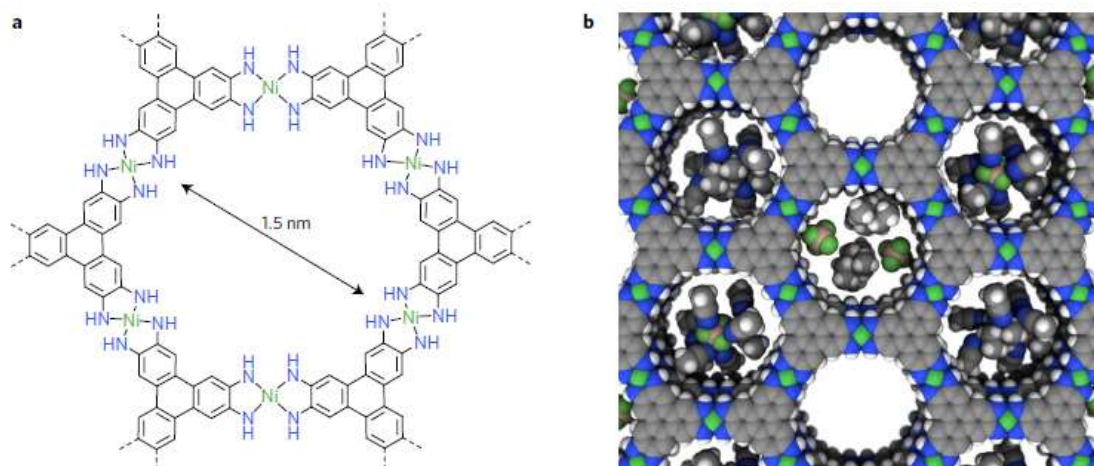


Figure 1.32 (a) Molecular structure of $\text{Ni}_3(\text{HITP})_2$ (b) Relative size of pores, green, lime, blue, grey, brown, and white spheres represent Ni, F, N, C, B, and H atoms, respectively.

The high porosity nature of MOF made attractive precursors for charge storage application. $\text{Ni}_3(\text{HITP})_2$ exhibits a specific capacitance 111 F/g at 0.05 A/g .

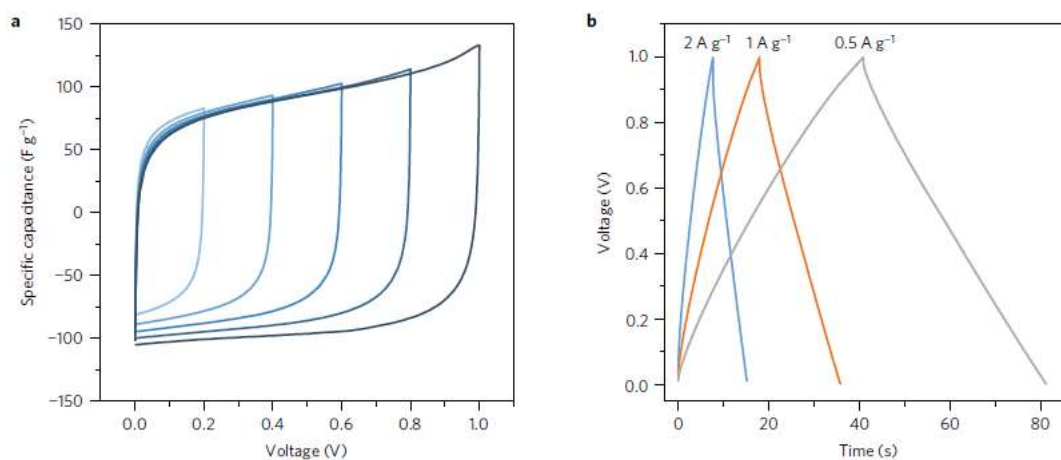


Figure 1.33 (a) Cyclic voltammetry at a scan rate of 10mV/s (b) Galvanostatic charge/discharge curves at current densities of 0.5, 1.0, 2.0 A/g.

Without the addition of any conductive additive or binder, this capacitance value is several times higher than most carbon-based materials. The CV and GCD of the sample found nearly rectangular and triangular shapes, respectively, further revealing the EDLC type material shown in Fig 1.33. The conductive MOF not only stops here but also shows capacity retention of more than 90% after running 10000 cycles.

1.8 MOFs-derived material as supercapacitor

The poor stability in different electrolyte media and conductivity of MOFs motivate to fabricate MOF-derived material for energy storage purposes. The most used technique is annealing. In this process, MOFs are annealed at a different temperature to produce either carbon-based composite or heteroatom emblazoned MOF depending upon the structure of the precursor. The self-sacrificial template after annealing consists of huge metal-ligand coordination able to overcome this issue in terms of chemical stability and conductivity. Yaghi et al. investigated graphene doped 23 number MOFs and incorporated these separately in supercapacitor devices.¹⁰⁴ Exceptionally zirconium-based MOF exhibits an areal capacitance of 5.09 mF/cm^2 which is 6 times higher than commercial activated carbon materials.

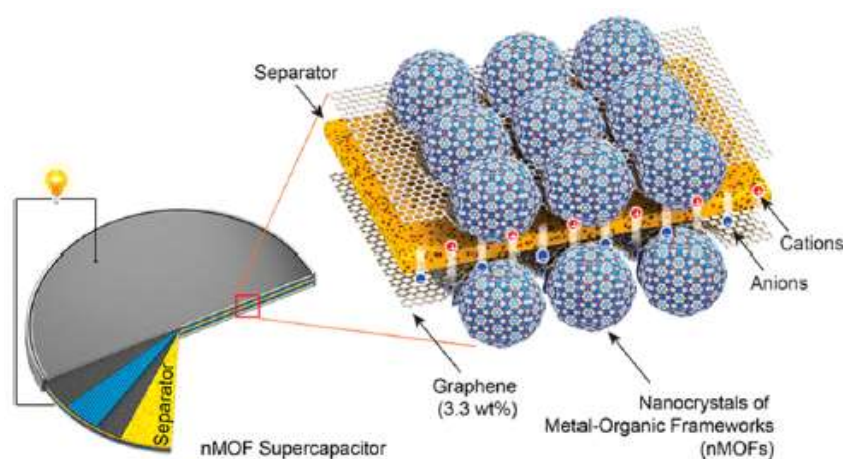


Figure 1.34 Construction of graphene doped MOF as supercapacitor.

J.Han et al. constructed a MOF-derived honeycomb-like $\text{Co}_9\text{S}_8@\text{C}$ porous structure exhibiting a high-performance supercapacitor with 1887 F/g capacitance. By annealing the MOF, it sacrifices itself, converting to 3D cobalt sulfide in a carbon matrix porous structure.¹⁰⁵

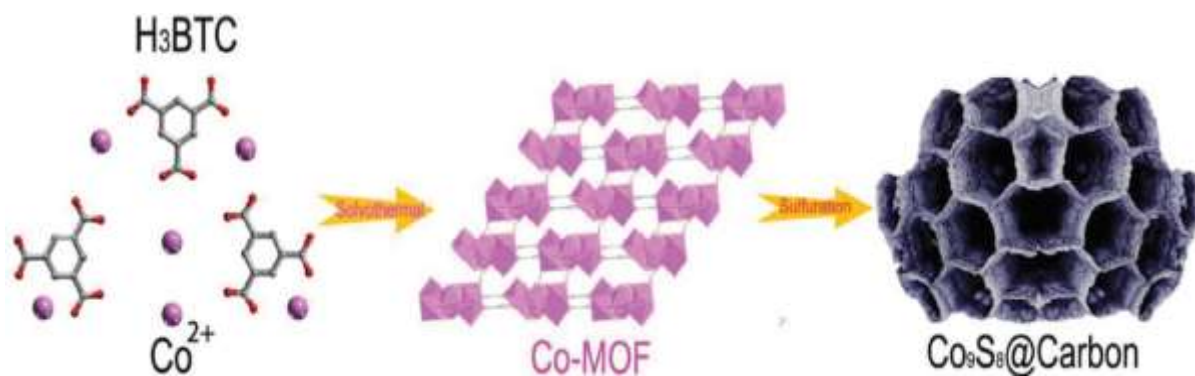


Figure 1.35 $\text{Co}_9\text{S}_8@\text{C}$ synthesis strategy from MOF.

They also annealed the MOF at different temperatures and compared the CV and GCD data, where they found a high energy density of 58 Wh/kg and power density of 1000 W/kg. The capacitive retention is 90% by running more than 10000 continuous cycles.

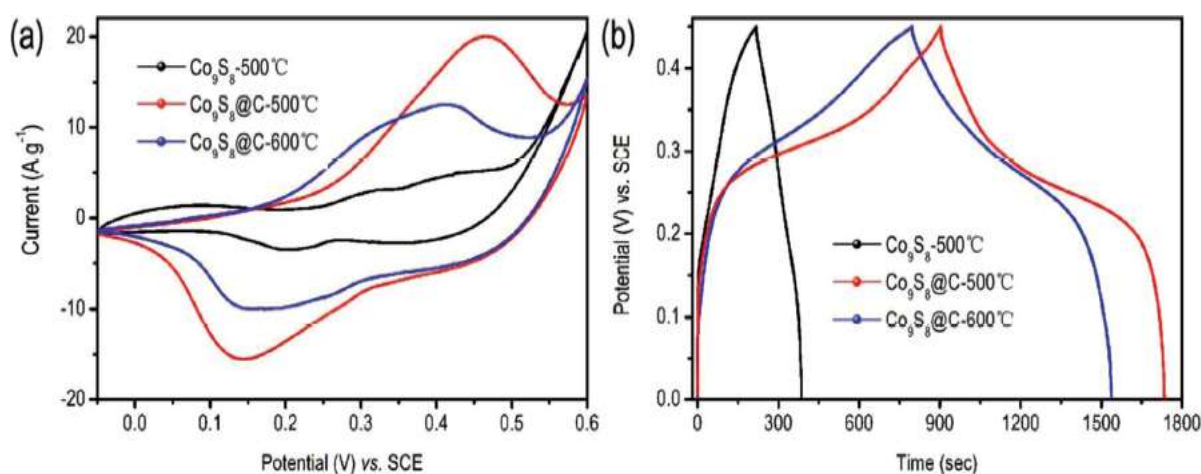


Figure 1.36 (a) CV curve of Co_9S_8 -500, $\text{Co}_9\text{S}_8@\text{C}$ -500, and $\text{Co}_9\text{S}_8@\text{C}$ -600 at 5mVps (b) GCD of corresponding sample at 1A/g.

1.9 References

- 1 F. Perera, *Int. J. Environ. Res. Public Health*, 2017, **15**, 16.
- 2 Y. Li, Z. Y. Fu and B. L. Su, *Adv. Funct. Mater.*, 2012, **22**, 4634–4667.
- 3 Yaghi, O. and Li, H., *J. Am. Chem.Soc.*, 1995, **117**, 10401–10402.
- 4 J. L. C. Rowsell, E. C. Spencer, J. Eckert, J. A. K. Howard and O. M. Yaghi, *Science*, 2005, **309**, 1350–1354.

- 5 G. Férey, M. Latroche, C. Serre, F. Millange, T. Loiseau and A. Percheron-Guégan, *Chem. Commun.*, 2003, **3**, 2976–2977.
- 6 E. Haque, J. E. Lee, I. T. Jang, Y. K. Hwang, J. S. Chang, J. Jegal and S. H. Jung, *J. Hazard. Mater.*, 2010, **181**, 535–542.
- 7 E. Haque, J. W. Jun and S. H. Jung, *J. Hazard. Mater.*, 2011, **185**, 507–511.
- 8 S. H. Jung, J. H. Lee, J. W. Yoon, C. Serre, G. Férey and J. S. Chang, *Adv. Mater.*, 2007, **19**, 121–124.
- 9 S. M. Humphrey and P. T. Wood, *J. Am. Chem. Soc.*, 2004, **126**, 13236–13237.
- 10 S. Achmann, G. Hagen, J. Kita, I. M. Malkowsky, C. Kiener and R. Moos, *Sensors*, 2009, **9**, 1574–1589.
- 11 S. Bhattacharjee, D. A. Yang and W. S. Ahn, *Chem. Commun.*, 2011, **47**, 3637–3639.
- 12 J. Kim, S. N. Kim, H. G. Jang, G. Seo and W. S. Ahn, *Appl. Catal. A Gen.*, 2013, **453**, 175–180.
- 13 J. Lee, O. K. Farha, J. Roberts, K. A. Scheidt, S. T. Nguyen and J. T. Hupp, *Chem. Soc. Rev.*, 2009, **38**, 1450–1459.
- 14 N. A. Khan, M. M. Haque and S. H. Jung, *Eur. J. Inorg. Chem.*, 2010, **2**, 4975–4981.
- 15 J. Rocha, L. D. Carlos, F. A. A. Paz and D. Ananias, *Chem. Soc. Rev.*, 2011, **40**, 926–940.
- 16 J. Wang, B. Wang, X. Liu, J. Bai, H. Wang and G. Wang, *Chem. Eng. J.*, 2020, **382**, 123050.
- 17 W. Zhang, H. Zhang, R. Luo, M. Zhang, X. Yan, X. Sun, J. Shen, W. Han, L. Wang and J. Li, *J. Colloid Interface Sci.*, 2019, **548**, 48–55.
- 18 T. He, J. M. V. Nsanzimana, R. Qi, J. Y. Zhang, M. Miao, Y. Yan, K. Qi, H. Liu and B. Y. Xia, *J. Mater. Chem. A*, 2018, **6**, 23289–23294.
- 19 M. Zeng, H. Wang, C. Zhao, J. Wei, K. Qi, W. Wang and X. Bai, *ChemCatChem*,

- 2016, **8**, 708–712.
- 20 Q. Wang, Y. Luo, R. Hou, S. Zaman, K. Qi, H. Liu, H. S. Park and B. Y. Xia, *Adv. Mater.*, 2019, **31**, 1–8.
- 21 Q. Wang, C.-S. Cha, J. Lu and L. Zhuang, *Phys. Chem. Chem. Phys.*, 2009, **11**, 679–687.
- 22 Y. Jiao, Y. Zheng, M. Jaroniec and S. Z. Qiao, *Chem. Soc. Rev.*, 2015, **44**, 2060–2086.
- 23 J. Janata, *Angew. Chemie Int. Ed.*, 2011, **50**, 9538–9538.
- 24 J. Zhu, L. Hu, P. Zhao, L. Y. S. Lee and K. Y. Wong, *Chem. Rev.*, 2020, **120**, 851–918.
- 25 S. Anantharaj, S. R. Ede, K. Sakthikumar, K. Karthick, S. Mishra and S. Kundu, *ACS Catal.*, 2016, **6**, 8069–8097.
- 26 H. Jin, C. Guo, X. Liu, J. Liu, A. Vasileff, Y. Jiao, Y. Zheng and S. Z. Qiao, *Chem. Rev.*, 2018, **118**, 6337–6408.
- 27 H. J. Yan, B. Xu, S. Q. Shi and C. Y. Ouyang, *J. Appl. Phys.*, 2012, **112**, 1–5.
- 28 G. L. Chai, Z. Hou, T. Ikeda and K. Terakura, *J. Phys. Chem. C*, 2017, **121**, 14524–14533.
- 29 J. Park, Y. Nabaee, T. Hayakawa and M. A. Kakimoto, *ACS Catal.*, 2014, **4**, 3749–3754.
- 30 A. Kulkarni, S. Siahrostami, A. Patel and J. K. Nørskov, *Chem. Rev.*, 2018, **118**, 2302–2312.
- 31 J. Ma, L. Gong, Y. Shen, D. Sun, B. Liu, J. Zhang, D. Liu, L. Zhang and Z. Xia, *Front. Mater.*, 2019, **6**, 1–9.
- 32 J. S. Spendelov and A. Wieckowski, *Phys. Chem. Chem. Phys.*, 2007, **9**, 2654–2675.
- 33 S. Uhm, H. J. Lee and J. Lee, *Phys. Chem. Chem. Phys.*, 2009, **11**, 9326–9336.
- 34 A. B. Anderson, *Phys. Chem. Chem. Phys.*, 2012, **14**, 1330–1338.

- 35 Y. Cong, B. Yi and Y. Song, *Nano Energy*, 2018, **44**, 288–303.
- 36 Q. Gao, W. Zhang, Z. Shi, L. Yang and Y. Tang, *Adv. Mater.*, 2019, **31**, 1802880.
- 37 J. D. Benck, T. R. Hellstern, J. Kibsgaard, P. Chakthranont and T. F. Jaramillo, *ACS Catal.*, 2014, **4**, 3957.
- 38 S. Chen, J. Duan, M. Jaroniec and S. Z. Qiao, *Angew. Chemie Int. Ed.*, 2013, **52**, 13567–13570.
- 39 M. Gong, Y. Li, H. Wang, Y. Liang, J. Z. Wu, J. Zhou, J. Wang, T. Regier, F. Wei and H. Dai, *J. Am. Chem. Soc.*, 2013, **135**, 8452.
- 40 Z. Lu, W. Xu, W. Zhu, Q. Yang, X. Lei, J. Liu, Y. Li, X. Sun and X. Duan, *Chem. Commun.*, 2014, **50**, 6479–6482.
- 41 R. D. L. Smith, M. S. Prévot, R. D. Fagan, S. Trudel and C. P. Berlinguette, *J. Am. Chem. Soc.*, 2013, **135**, 11580–11586.
- 42 S. Anantharaj, S. R. Ede, K. Karthick, S. Sam Sankar, K. Sangeetha, P. E. Karthik and S. Kundu, *Energy Environ. Sci.*, 2018, **11**, 744–771.
- 43 T. Y. Ma, S. Dai, M. Jaroniec and S. Z. Qiao, *J. Am. Chem. Soc.*, 2014, **136**, 13925–13931.
- 44 C. Tang, W. Wang, A. Sun, C. Qi, D. Zhang, Z. Wu and D. Wang, *ACS Catal.*, 2015, **5**, 6956–6963.
- 45 C. Zhang, Y. Huang, Y. Yu, J. Zhang, S. Zhuo and B. Zhang, *Chem. Sci.*, 2017, **8**, 2769–2775.
- 46 C. Costentin, S. Drouet, M. Robert and J.-M. Savéant, *J. Am. Chem. Soc.*, 2012, **134**, 11235–11242.
- 47 G. Zhao, K. Rui, S. X. Dou and W. Sun, *Adv. Funct. Mater.*, 2018, **28**, 1803291.
- 48 D. Merki, S. Fierro, H. Vrubel and X. Hu, *Chem. Sci.*, 2011, **2**, 1262–1267.
- 49 J. Zang, S.-J. Bao, C. M. Li, H. Bian, X. Cui, Q. Bao, C. Q. Sun, J. Guo and K. Lian, *J.*

- Phys. Chem. C*, 2008, **112**, 14843–14847.
- 50 Y. Y. Liang, H. L. Li and X. G. Zhang, *J. Power Sources*, 2007, **173**, 599–605.
- 51 Y. Shi and B. Zhang, *Chem. Soc. Rev.*, 2016, **45**, 1529–1541.
- 52 X. Zou and Y. Zhang, *Chem. Soc. Rev.*, 2015, **44**, 5148–5180.
- 53 J. Masa, C. Batchelor-McAuley, W. Schuhmann and R. G. Compton, *Nano Res.*, 2014, **7**, 71–78.
- 54 A. K. Samantara, S. Chandra Sahu, A. Ghosh and B. K. Jena, *J. Mater. Chem. A*, 2015, **3**, 16961–16970.
- 55 J. J. Lingane, *J. Electroanal. Chem.*, 1961, **2**, 296–309.
- 56 Yu, Y., Huang, S.-Y., Li, Y., Steinmann, S. N., Yang, W., and Cao, L. 2014, *Nano Letters*, **14**, 553–558.
- 57 Y. Feng, T. He and N. Alonso-vante, *Chemistry of Materials*, 2008, **20**, 26–28.
- 58 Y. Liu, H. Cheng, M. Lyu, S. Fan, Q. Liu, W. Zhang, Y. Zhi, C. Wang, C. Xiao, S. Wei, B. Ye and Y. Xie, *J. Am. Chem. Soc.*, 2014, **136**, 15670–15675.
- 59 D. Kong, H. Wang, Z. Lu and Y. Cui, *J. Am. Chem. Soc.*, 2014, **136**, 4897–4900.
- 60 B. Yu, X. Wang, F. Qi, B. Zheng, J. He, J. Lin, W. Zhang, Y. Li and Y. Chen, *ACS Appl. Mater. Interfaces*, 2017, **9**, 7154–7159.
- 61 J. Masa and W. Schuhmann, *ChemCatChem*, 2019, **11**, 5842–5854.
- 62 S. Gupta, N. Patel, A. Miotello and D. C. Kothari, *J. Power Sources*, 2015, **279**, 620–625.
- 63 S. Gupta, H. Jadhav, S. Sinha, A. Miotello, M. K. Patel, A. Sarkar and N. Patel, *ACS Sustain. Chem. Eng.*, 2019, **7**, 16651–16658.
- 64 H. B. Aiyappa, J. Masa, C. Andronesco, M. Muhler, R. A. Fischer and W. Schuhmann, *Small Methods*, 2019, **3**, 1–13.
- 65 K. Jayaramulu, J. Masa, D. M. Morales, O. Tomanec, V. Ranc, M. Petr, P. Wilde, Y.

- T. Chen, R. Zboril, W. Schuhmann and R. A. Fischer, *Adv. Sci.*, 2018, **103**, 1801029.
- 66 S. Wang, Y. Hou, S. Lin and X. Wang, *Nanoscale*, 2014, **6**, 9930–9934.
- 67 H. Ogata, W. Lubitz and Y. Higuchi, *J. Biochem.*, 2016, **160**, 251–258.
- 68 M. L. Pegis, C. F. Wise, D. J. Martin and J. M. Mayer, *Chem. Rev.*, 2018, **118**, 2340–2391.
- 69 M. Lions, J. B. Tommasino, R. Chattot, B. Abeykoon, N. Guillou, T. Devic, A. Demessence, L. Cardenas, F. Maillard and A. Fateeva, *Chem. Commun.*, 2017, **53**, 6496–6499.
- 70 R. Miao, B. Dutta, S. Sahoo, J. He, W. Zhong, S. A. Cetegen, T. Jiang, S. P. Alpay and S. L. Suib, *J. Am. Chem. Soc.*, 2017, **139**, 13604–13607.
- 71 Q. T. Nguyen, P. D. Nguyen, D. Nguyen, Q. D. Truong, T. T. Kim Chi, T. T. D. Ung, I. Honma, N. Q. Liem and P. D. Tran, *ACS Appl. Mater. Interfaces*, 2018, **10**, 8659–8665.
- 72 X. Y. Yu, L. Yu, H. Bin Wu and X. W. Lou, *Angew. Chemie Int. Ed.*, 2015, **54**, 5331–5335.
- 73 A. Aijaz, J. Masa, C. Rösler, W. Xia, P. Weide, A. J. R. Botz, R. A. Fischer, W. Schuhmann and M. Muhler, *Angew. Chemie Int. Ed.*, 2016, **55**, 4087–4091.
- 74 F. Yang, P. Zhao, X. Hua, W. Luo, G. Cheng, W. Xing and S. Chen, *J. Mater. Chem. A*, 2016, **4**, 16057–16063.
- 75 X. Wu, S. Han, D. He, C. Yu, C. Lei, W. Liu, G. Zheng, X. Zhang and L. Lei, *ACS Sustain. Chem. Eng.*, 2018, **6**, 8672–8678.
- 76 X. Wang, F. Li, W. Li, W. Gao, Y. Tang and R. Li, *J. Mater. Chem. A*, 2017, **5**, 17982–17989.
- 77 X. Zhao, H. Zhang, Y. Yan, J. Cao, X. Li, S. Zhou, Z. Peng and J. Zeng, *Angew. Chemie Int. Ed.*, 2017, **56**, 328–332.

- 78 Q. Dong, Q. Wang, Z. Dai, H. Qiu and X. Dong, *ACS Appl. Mater. Interfaces*, 2016, **8**, 26902–26907.
- 79 X. Liu, Y. Liu and L. Z. Fan, *J. Mater. Chem. A*, 2017, **5**, 15310–15314.
- 80 R. K. Tripathy, A. K. Samantara and J. N. Behera, *Sustain. Energy Fuels*, 2021, **5**, 1184–1193.
- 81 B. Dunn, H. Kamath and J. M. Tarascon, *Science*, 2011, **334**, 928–935.
- 82 G. Wang, L. Zhang and J. Zhang, *Chem. Soc. Rev.*, 2012, **41**, 797–828.
- 83 A. K. Samantara and S. Ratha, Materials Development for Active/Passive Components of a Supercapacitor, *SpringerBriefs Mater.*, ISBN 978-981-10-7263-5.
- 84 F. Boorboor Ajdari, E. Kowsari, M. Niknam Shahrak, A. Ehsani, Z. Kiaei, H. Torkzaban, M. Ershadi, S. Kholghi Eshkalak, V. Haddadi-Asl, A. Chinnappan and S. Ramakrishna, *Coord. Chem. Rev.*, 2020, **422**, 213441.
- 85 S. Ratha and C. S. Rout, *ACS Appl. Mater. Interfaces*, 2013, **5**, 11427–11433.
- 86 M. Winter and R. J. Brodd, *Chem. Rev.*, 2004, **104**, 4245–4269.
- 87 J. K. Das, A. K. Samantara, S. R. K. A., C. S. Rout and J. N. Behera, *Dalt. Trans.*, 2019, **48**, 15955–15961.
- 88 S. Ratha, S. R. Marri, J. N. Behera and C. S. Rout, *Eur. J. Inorg. Chem.*, 2016, 259–265.
- 89 M. Galiński, A. Lewandowski and I. Stepniak, *Electrochim. Acta*, 2006, **51**, 5567–5580.
- 90 G. A. Snook, P. Kao and A. S. Best, *J. Power Sources*, 2011, **196**, 1–12.
- 91 N. R. Chodankar, H. D. Pham, A. K. Nanjundan, J. F. S. Fernando, K. Jayaramulu, D. Golberg, Y. K. Han and D. P. Dubal, *Small*, 2020, **16**, 1–35.
- 92 Z. H. Huang, H. Li, W. H. Li, G. Henkelman, B. Jia and T. Ma, *Small*, 2020, **16**, 1–10.
- 93 A. J. Bard and L. Faulkner, *Electrochemical Methods, Fundamental and Applications*,

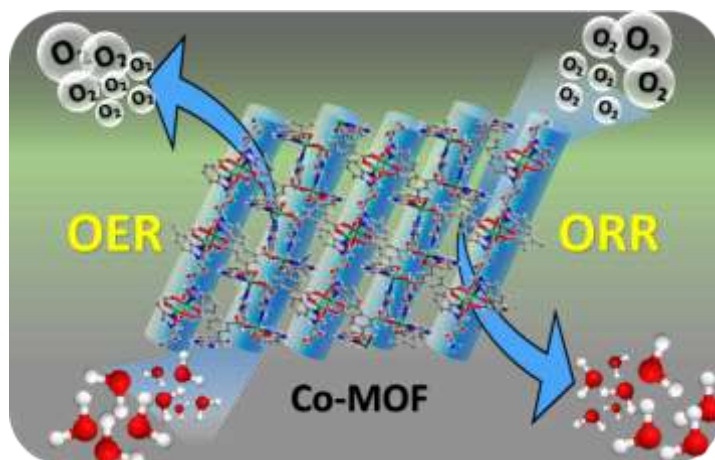
- Willey; Newyork, 2nd Edition., 2001.
- 94 V. Helmholtz, *Ann. Phys. Chem*, 1853, **89**, 211.
- 95 H. Du, X. Lin, Z. Xu and D. Chu, *J. Mater. Sci.*, 2015, **50**, 5641–5673.
- 96 D. . Chapman, *London, Edinburgh Dublin Philos. Mag. J. Sci.*, 1913, **25**, 475.
- 97 Stern. O, *Zeit. Elektrochem*, 1924, **30**, 508.
- 98 D. Grahame, *Chem. Rev.*, 1947, **41**, 441.
- 99 W. Sugimoto, H. Iwata, Y. Murakami and Y. Takasu, *J. Electrochem. Soc.*, 2004, **151**, A1181.
- 100 X. Dong, W. Shen, J. Gu, L. Xiong, Y. Zhu, H. Li and J. Shi, *J. Phys. Chem. B*, 2006, **110**, 6015–6019.
- 101 B. E. Conway, V. Birss and J. Wojtowicz, *J. Power Sources*, 1997, **66**, 1–14.
- 102 H. Wang, H. Yi, C. Zhu, X. Wang and H. Jin Fan, *Nano Energy*, 2015, **13**, 658–669.
- 103 D. Sheberla, J. C. Bachman, J. S. Elias, C. J. Sun, Y. Shao-Horn and M. Dincă, *Nat. Mater.*, 2017, **16**, 220–224.
- 104 K. M. Choi, H. M. Jeong, J. H. Park, Y.-B. Zhang, J. K. Kang and O. M. Yaghi, *ACS Nano*, 2014, **8**, 7451–7457.
- 105 S. Sun, J. Luo, Y. Qian, Y. Jin, Y. Liu, Y. Qiu, X. Li, C. Fang, J. Han and Y. Huang, *Adv. Energy Mater.*, 2018, **8**, 1801080.

CHAPTER-2

ORR and OER Study of Cobalt Metal-Organic Framework (Co-MOF)

- 2.1** Abstract
- 2.2** Introduction
- 2.3** Motivation of the work
- 2.4** Experimental section
 - 2.4.1** Synthesis of Co-MOF
 - 2.4.2** Synthesis of Co-MOF/AB composites
- 2.5** Characterization
- 2.6** Electrochemical measurements
- 2.7** Calculations of ECSA and R_f
- 2.8** Results and discussions
- 2.9** Conclusions
- 2.10** References

2.1 Abstract



This chapter describes the synthesis of cobalt containing metal-organic framework (Co-MOF) and explores its electrocatalytic application towards oxygen evolution reaction (OER) and oxygen reduction reaction (ORR). The Co-MOF efficiently catalyses the ORR with a lower onset (0.85 V vs. RHE)/reduction potential and higher reduction current density by a four-electron reduction path. Moreover, the MOF shows higher durability with >70% performance retention after 25 hours of reaction and tolerance towards methanol; this demonstrates its potential for application in direct methanol fuel cells (DMFCs). Furthermore, due to the availability of more active sites and accessible surface area, the Co-MOF performs well towards the OER with lower onset potential and small Tafel slope as compared to the commercial RuO₂ nanoparticles. Moreover, it needs only 280 mV overpotential to deliver the state-of-the-art current density of 10 mA cm⁻² and robust stability. It shows the high TOF value of 93.21 s⁻¹ at the overpotential of 350 mV as compared to the reported MOF/nanoparticle-based electrocatalysts and the state-of-the-art RuO₂.

2.2 Introduction

The scarce availability of traditional energy sources (fossil fuels) motivates the energy researchers throughout the globe to develop alternative sources of energy.¹ Therefore, several energy conversion and storage systems (such as fuel cell, batteries, etc.) have been developed, which use fuels such as oxygen, hydrogen and small organic molecules such as methanol and formic acid. Among these, hydrogen is considered to be a clean and green energy source for these purposes; one of the efficient ways to generate hydrogen is the catalytic splitting of water, in which both hydrogen (via the HER) and oxygen (via the OER) are liberated.^{2,3} It has been observed that the effective generation of hydrogen depends on the conversion of water to oxygen. Since the OER occurs via a multistep reaction mechanism, it faces sluggish reaction kinetics, and more overpotential is needed to execute the reaction. Therefore, stable and efficient electrocatalysts are highly imperative for the generation of these gaseous fuels and their efficient conversion to energy for the smooth operation of these conversion/storage systems to achieve future sustainability. Traditionally, noble metals (Pt, Ru, Ir, etc.) and oxides of some noble metals (RuO₂, IrO₂, etc.) are used as catalysts for these purposes.⁴ However, they are associated with disadvantages such as high cost, limited availability in the earth crust, lower durability, poor selectivity and detrimental environmental effects. This strongly impedes the commercialization of these materials; thus, the development of new substitutes is urgent; in this regard, significant efforts have been dedicated, leading to the development of various non-noble metal nanostructures. However, still, there is a demand of electrocatalysts having more active centres along with better durability for these oxygen electrocatalysis reactions. The hierarchy surface morphology, tunable chemical structure, higher specific surface area and presence of more number of active centres make metal–organic frameworks (MOFs) a suitable alternative to noble metal-based electrocatalysts.^{5–8} These are a class of materials with different dimensionalities built from metal cations and organic ligands under optimized reaction

conditions. In most of the cases, the MOFs have been found to act as electrical insulators; this restricts their electrochemical application.⁹⁻¹¹ However, by tuning the chemical composition and optimizing the reaction conditions, conductive MOFs have been successfully synthesized, and their electrocatalytic performances have been explored.¹²⁻¹⁴ In a particular reaction, Dinca's group has prepared a conductive MOF, i.e. $\text{Ni}_3(\text{hexaiminotriphenylene})_2$, and used it as a cathode electrocatalyst for the ORR. They have observed that the designed MOF catalyses the ORR via a two-electron mediated path, in which the dissolved oxygen is predominantly converted into hydrogen peroxide.¹⁴ Zhao et al. have reported in situ hybridized 2D cobalt 1,4-benzenedicarboxylate with $\text{Ti}_3\text{C}_2\text{Tx}$ using an inter-diffusion assisted process. The composite shows good electrocatalytic performance for the OER and needs the overpotential of 410 mV to achieve 10 mA cm^{-2} .¹⁵ Similarly, a few studies have been carried out on the design of a conductive MOF and its composite for either the ORR or the OER process.^{13,16} However, the development of highly efficient MOF-based electrocatalysts having activity towards both the ORR and the OER process is still indispensable. In this study, we presented the synthesis of a three-dimensional rod-like Co-MOF using cobalt (II) acetate tetrahydrate, dimethylformamide (DMF), benzene tricarboxylic acid (BTC), and benzimidazole (BIm) as the starting materials via a single step hydrothermal method. Interestingly, we observed better electrocatalytic performance of the Co-MOF towards both the oxygen reduction (ORR) and evolution reaction (OER). It catalyses the ORR with a lower onset potential (0.85 V vs. RHE)/ reduction potential and higher reduction current density via a four-electron reduction path. Moreover, it shows higher durability with >70% performance retention after 25 hours of reaction and is tolerant towards methanol; this demonstrates its potential for application in direct methanol fuel cells (DMFCs); furthermore, due to the availability of more active sites and accessible surface area, the Co-MOF performs well towards the OER with lower onset potential and small Tafel slope as compared to the commercial RuO_2 nanoparticles. It needs only 280 mV overpotential to

deliver the state-of-the-art current density of 10 mA cm^{-2} and robust stability. It shows the high TOF value of 93.21 s^{-1} at the overpotential of 350 mV as compared to the reported MOF/nanoparticle-based electrocatalysts and the state-of-the-art RuO_2 .

2.3 Motivation of the work

Though metal-organic framework built from metal cations and organic ligands under optimized reaction conditions have various advantages over noble metal-based electrocatalysts on several aspect like hierarchy surface morphology, tunable chemical structure, specific surface area and number of active centres, however in most of the cases these are electrical insulator which restrict their electrochemical application. Tuning chemical composition and optimizing reaction condition conductive MOFs can be synthesized and will be a new hope but is a heavy task for electrochemical application. In this study we presented the synthesis of a three-dimensional rod like metal-organic frameworks called Co-MOF by using cobalt (II) acetate tetrahydrate, dimethyl formamide (DMF), benzene tricarboxylic acid (BTC), and benzimidazole (BIm) as the precursor via a single step hydrothermal method and explored it's electrocatalytic property. To encounter the above said issue we prepared composite with carbonaceous material like acetylene black (AB). Interestingly, we observed better electrocatalytic performance towards both the oxygen reduction (ORR) and evolution reaction (OER) in 0.1 M KOH and 1 M KOH electrolyte respectively. Furthermore; the electrocatalyst is tolerant towards methanol and demonstrates its potential for application in direct methanol fuel cells (DMFCs). The OER performance was excellent in terms of onset potential and Tafel slope as compared to the commercial RuO_2 nanoparticles. It needs only 280 mV overpotential to deliver the state-of-the-art current density of 10 mA cm^{-2} make more attractive towards future energy conversion system.

2.4 Experimental section

2.4.1 Synthesis of Co-MOF

In a typical synthetic procedure, the Co-MOF [Co₄(BTC)₃ (BIM)₆] [solvent] was synthesized by following the synthetic procedure of our previous study.¹⁷ Typically, 0.25 mmol of cobalt acetate tetrahydrate was dissolved in 1 ml of dimethylformamide (DMF); then, 0.25 mM benzene tricarboxylic acid (BTC) and 0.25 mM benzimidazole (BIm) were added in a molar proportion (Co : BTC : BIm = 1 : 1 : 1) under constant stirring for 60 minutes to make a homogeneous solution, which was transferred to a 7 ml autoclave and heated at 120 °C for 2 days. The as-synthesized Co–BTC–BIm MOF was named as Co-MOF.

2.4.2 Synthesis of Co-MOF/AB

The Co-MOF and acetylene black (AB) were measured in 2:1 molar ratio by weight and grinded properly in a mortar pestle before using as catalyst ink.

2.5 Characterization

The phase and crystallinity of the sample were analysed via the X-ray diffraction patterns. The surface morphology of the Co- MOF was verified by a field emission scanning electron microscope (FESEM, Merlin Compact with a GEMINI-I electron column, Zeiss Pvt. Ltd, Germany). Moreover, Fourier transform infrared (FTIR) spectroscopy was employed to verify the functional groups present in the as-prepared MOF. Furthermore, the thermal stability of the sample was verified by thermogravimetric analysis (by TA Instruments-Waters Lab) at the ramp rate of 10 °C min⁻¹ under a constant flow of nitrogen gas. Furthermore, the powder X-ray diffraction pattern was obtained using the Bruker D8 Advance diffractometer equipped with a Cu-K α radiation source ($\lambda = 1.5418 \text{ \AA}$).

2.6 Electrochemical measurement

All the electrochemical measurements were performed by a standard two-compartment three electrode electrochemical cell using a computer-controlled Biologic Electrochemical workstation (SP-200). Using the sample modified glassy carbon electrode, bare platinum wire and aqueous Ag/AgCl as the working, auxiliary and reference electrode, respectively, all the

cyclic voltammogram (CV) and linear sweep voltammograms (LSVs) were obtained. Prior to each measurement, the rotating disk glassy carbon electrode (GCRDE, geometrical surface area: 0.19 cm²) and glassy carbon electrode (GCE, geometrical surface area: 0.07 cm²) were mirror polished with alumina slurry (0.1, 0.3 and 0.05 μm) followed by bath sonication in deionized water. The sample ink was prepared by mixing the as synthesized samples and acetylene black (in 2: 1 ratio) in absolute ethanol and Nafion through ultra-sonication. The freshly prepared catalyst ink was drop-casted onto the mirror finished electrodes (GCRDE and GCE) and properly dried using vacuum desiccators prior to each measurement. The catalyst loading was 0.25 mg cm⁻² throughout the measurements. For the oxygen reduction reaction, all the CVs and LSVs were obtained using an oxygen-saturated electrolyte, and the controlled experiments were carried out in an argon-saturated 0.1 M KOH electrolyte. The kinetic study of the reaction was performed by analysing the linear sweep voltammograms obtained at different rotations applied to the GCRDE (from 100 to 1600 rpm). All the experiments were carried out with an Ag/AgCl reference electrode, and data are presented in the reversible hydrogen electrode as per the following equation:

$$E_{RHE} = E_{Ag/AgCl} + 0.059 (P_H) + E^{\circ}_{Ag/AgCl} \dots\dots\dots (2.1)$$

Herein, the pH value of the electrolyte is 14, and E^o Ag/AgCl is the standard electrode potential (0.216 V) for Ag/AgCl. The oxygen evolution reaction was furnished using the GCRDE in a 1 M KOH electrolyte. The overpotential was calculated by subtracting the standard potential for water oxidation from the experimental (E_{exp}) value as per the following reaction:

$$\eta = E (vs. RHE) - 1.23 \dots\dots\dots (2.2)$$

The Nyquist impedance measurement was carried out in the frequency range from 1 MHz to 0.1 Hz, with the amplitude of 5 mV, and the potentials presented were iR compensated. Further, the Tafel slopes were derived from the polarization curves as per the following equation:

$$\eta = a + b \log j \dots\dots\dots (2.3)$$

Herein, η , a , b and j are the overpotential, Tafel constant, Tafel slope, and current density, respectively.

2.7 Calculation of ECSA and R_f

The electrochemical accessible surface area was calculated from the double layer capacitance measured from the cyclic voltammograms as per the following equation:

$$ECSA = \frac{C_{dl}}{C_s} \dots\dots\dots (2.4)$$

For this measurement, the CVs were obtained in a non-faradaic region (0.2 to 0.26 V vs. Ag/AgCl) of the potential window in a 1 M KOH electrolyte at different sweep rates (10, 20, 25, 50, and 100 mV s⁻¹). The C_s is the specific capacitance of an atomically smooth surface of the material and is taken as 0.04 mF cm⁻². From the ECSA, the roughness factor (R_f) was calculated by dividing the geometrical surface area of the working electrode.

2.8 Result and discussions

The Co-MOF was synthesized by a single-step solvothermal method using cobalt acetate tetrahydrate as the metal source and a mixture of benzene tricarboxylic acid and benzimidazole as a ligand. Via the structure analysis, it has been observed that the asymmetric unit contains 53 non-hydrogen atoms, two crystallographically distinct Co²⁺ ions (Co1 is square pyramidal, and Co2 is tetrahedral), three BIm and one and a half molecules of BTC anions (Fig. 2.1a). Moreover, four bidentate carboxylate groups offered by four different BTC anions around the metal–metal axis form a one-dimensional interconnected paddle-wheel-like arrangement (Fig. 2.1b). The alternate right and left-handed helical structure found in the crystal lattice further

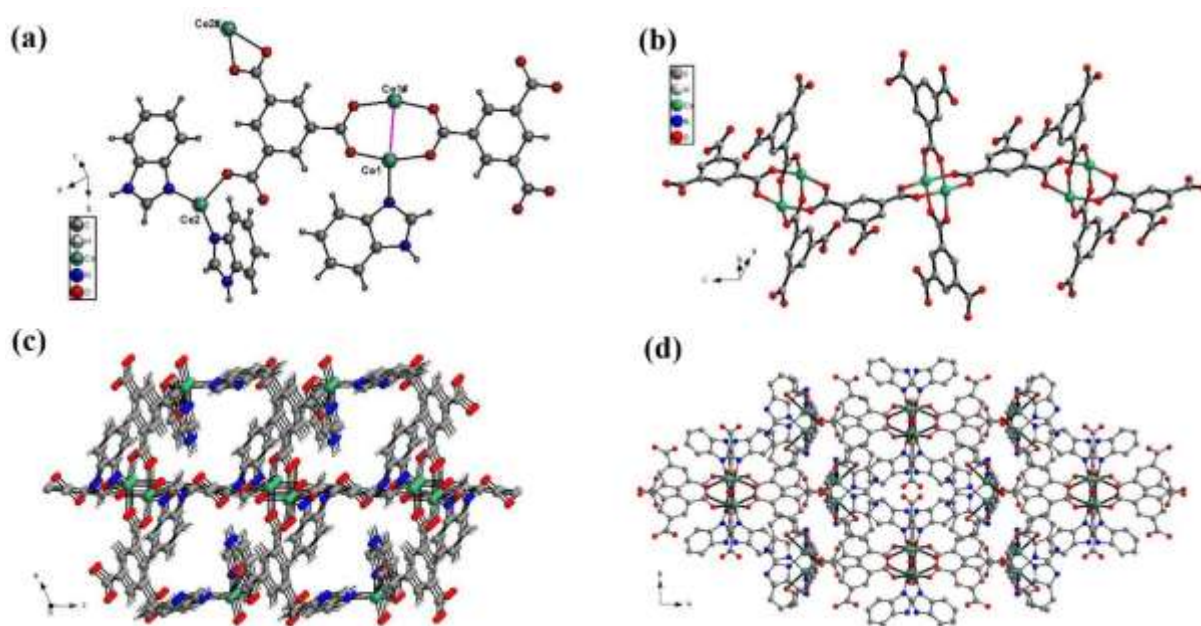


Figure 2.1 (a) Asymmetric unit of the $[\text{Co}_4(\text{BTC})_3(\text{BIM})_6]$ [solvent] (b) Interconnection of paddle-wheel units forming an infinite chain along the c -axis (c) 3D view of $[\text{Co}_4(\text{BTC})_3(\text{BIM})_6]$ showing the channel along b -axis (d) 3D view of $[\text{Co}_4(\text{BTC})_3(\text{BIM})_6]$ along c -axis.

connected via the paddle-wheel secondary unit; this led to the formation of a layered structure, producing overall a three-dimensional (3D) network structure, where the axial position was occupied by BIM. The $\text{Co}\cdots\text{Co}$ distance in the paddlewheel was calculated to be $2.8714(3)$ Å. Moreover, the $\text{Co}_{\text{Sq.py}}\text{-O}$ bond length range was $2.0249(3)\text{--}2.0575(4)$ Å, which was higher than the $\text{Co}_{\text{Td}}\text{-O}$ bond length range ($1.9721(2)\text{--}2.0194(3)$ Å). The $\text{Co}_{\text{Sq.py}}\text{-N}$ bond length was $2.0244(2)$ Å, whereas the $\text{Co}_{\text{Td}}\text{-N}$ bond length was $2.0152(4)\text{--}2.0379(2)$ Å. The hydrogen bonding interactions between BIM-NH groups with acceptor carboxylate oxygen atoms of the BTC anion further stabilize the crystal lattice. After synthesis, the phase and crystal structure were analysed via the X-ray diffraction patterns. The sharp peaks clearly indicate high crystallinity of the sample. Moreover, the good agreement between the powder XRD pattern and the simulated pattern suggests the purity of the synthesized Co-MOF (Fig. 2.2a).

Furthermore, FTIR spectroscopy was employed to analyse the molecular structure of the synthesized Co-MOF, and the spectra are shown in Fig. 2.2b.

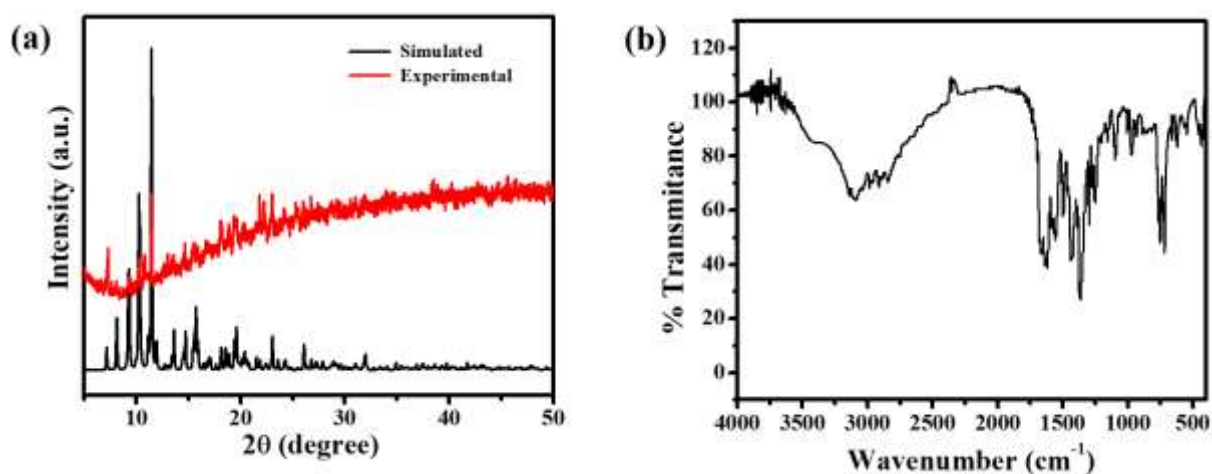


Figure 2.2 (a) simulated and experimental X-ray diffraction patterns of Co-MOF (b) FTIR spectrum of Co-MOF.

The spectrum showed the characteristic peaks of N–H, O–H, and C–H around 3000–3500 cm^{-1} , the C–O and C–N peak in the range 1000–1350 cm^{-1} , the aromatic C=C peak at 1300–1500 cm^{-1} and the C=O peak around 1680 cm^{-1} .

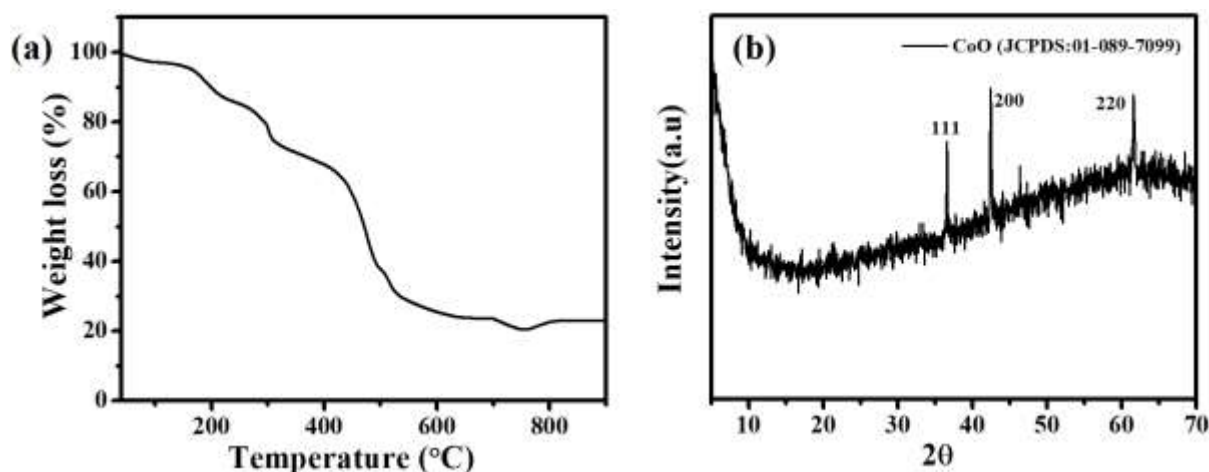


Figure 2.3 (a) Thermo gravimetric analysis of the Co-MOF (b) X-ray diffraction pattern of Co-MOF after the thermo gravimetric analysis.

The thermal stability of the compound was accessed via the thermogravimetric analysis (Fig. 2.3a), and the compound showed a continuous weight loss up to 200 $^{\circ}\text{C}$, corresponding to the loss of nearly four DMF and two water molecules (observed

15.87%; calculated 16.95%); the network was stable up to 250 °C; however, it started decomposing in the temperature range of 260–490 °C with the loss of nearly two dimethyl amine cations and six BIm molecules, which accounted for 44.29% (calculated 39.08%) of weight loss. In the temperature range of 500–700 °C, continuous disintegration takes place, corresponding to the decomposition of the BTC unit. After 900 °C the final calcined product CoO was identified from the post-calcined PXRD data presented in Fig. 2.3b.

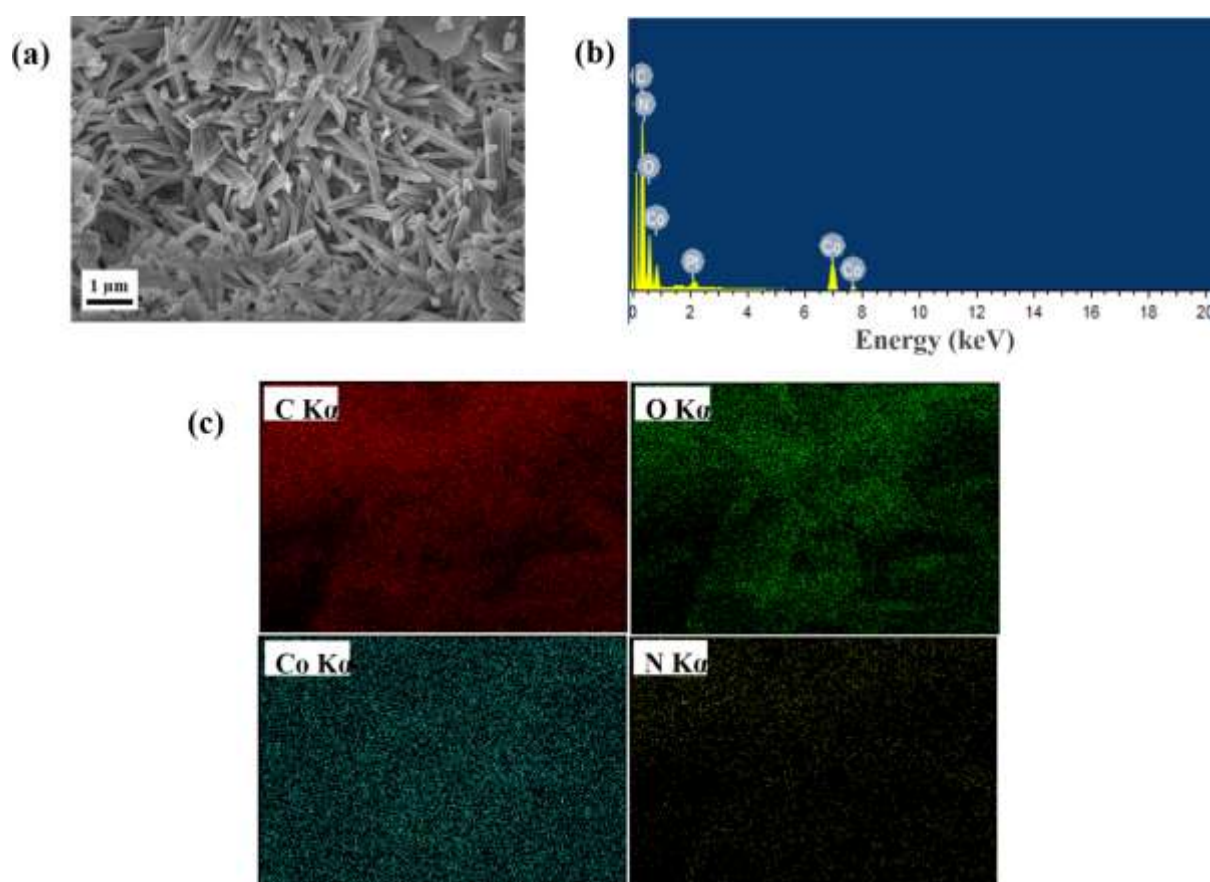


Figure 2.4 (a) FESEM image of the Co-MOF (b) EDS spectrum (c) elemental mapping of Co-MOF.

The as prepared Co-MOFs were observed to exhibit a rod-like structure by a scanning electron microscope (Fig. 2.4a). The elemental analysis was carried out by EDS, and the results are presented in (Fig. 2.4b). It clearly shows the presence of Co, N, O and C elements; this is in agreement with the presented chemical structure (Fig. 2.4c). The interesting 3D structure, crystallinity and thermal stability of the proposed MOF provoked us to explore its electrochemical performances. In this study, both the cathodic and the anodic performances

of the as-synthesized Co- MOF were explored towards the oxygen reduction and oxygen evolution reaction in an alkaline medium. As can be seen in Fig. 2.5, a featureless current was observed from the Co-MOF modified GCRDE in an argon-saturated 0.1 M KOH electrolyte. However, in the presence of oxygen, a sharp increase in the reduction current has been found with the onset potential of 0.85 V vs. RHE, demonstrating that the proposed MOF is a potential cathode electrocatalyst for the oxygen reduction reaction.

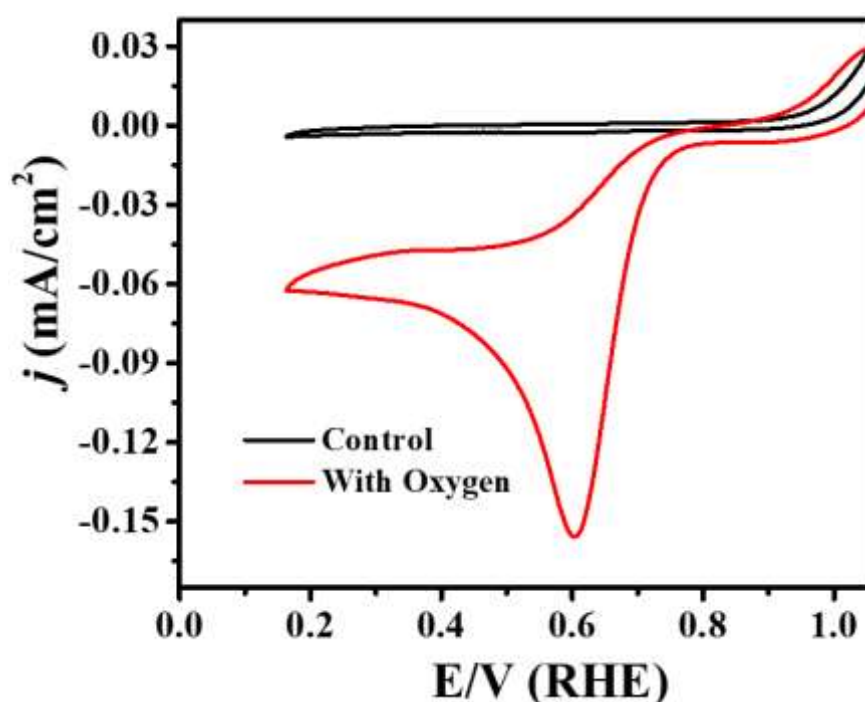


Figure 2.5 The cyclic voltammogram for the ORR by the Co-MOF-modified GCE in an oxygen saturated 0.1 M KOH electrolyte at the sweep rate of 10 mV s^{-1} . The control experiment was carried out in an argon-saturated electrolyte.

Furthermore, the ORR pathways were evaluated by calculating the number of electrons via the linear sweep voltammograms obtained at different rotation rates of the electrode. For this, the LSVs were obtained with the rotation of the Co-MOF modified RDE from 100 to 1600 rpm in an oxygen-saturated 0.1 M KOH electrolyte at the sweep rate of 10 mV s^{-1} and are presented in Fig. 2.6a.

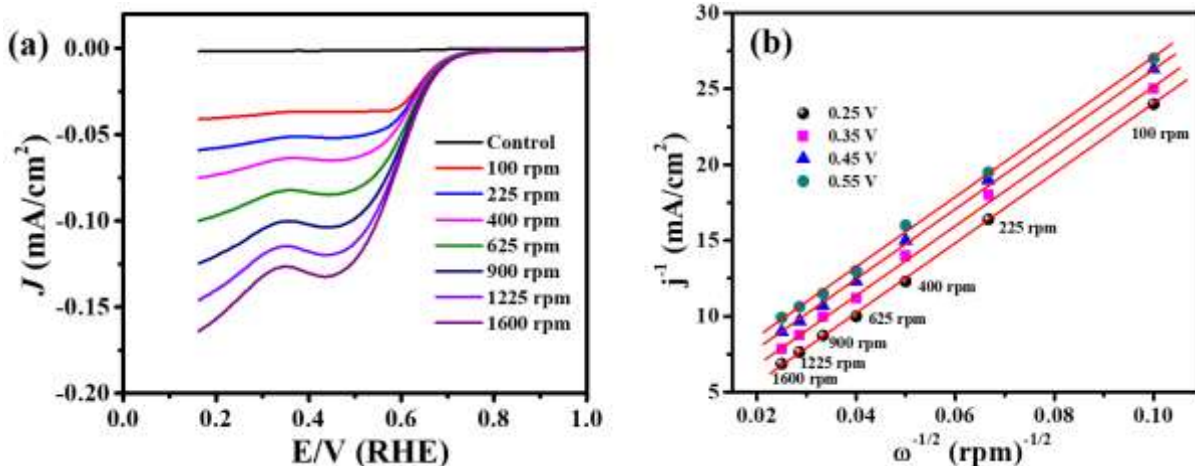


Figure 2.6 (a) Linear sweep voltammograms at different rotations of the electrode (b) the Koutecky–Levich plot

The ORR kinetics and reaction mechanism were studied by correlating some important parameters, such as number of electrons (n), concentration of dissolved oxygen (C_{O_2}), diffusion coefficient, viscosity of the electrolyte and rotation speed of the electrode, via the Koutecky–Levich (K–L) equation as follows:¹⁸

$$\frac{1}{J} = \frac{1}{J_k} + \frac{1}{J_{dl}} \quad \dots\dots\dots (2.5)$$

where J , J_k and J_{dl} are the disk, kinetic and diffusion-limited current densities, respectively.

Furthermore, J_k and J_{dl} are defined by the following equations:

$$J_k = nFK_{O_2}C_{O_2} \quad \dots\dots\dots (2.6)$$

$$J_{dl} = B \omega^{1/2} \quad \dots\dots\dots (2.7)$$

Herein, n , F , K_{O_2} , C_{O_2} , B and ω are the total number of electrons transferred in the ORR, Faraday constant ($96\,485\text{ C mol}^{-1}$), oxygen solubility constant, concentration of oxygen in the electrolyte ($1.2 \times 10^{-6}\text{ mol cm}^{-3}$), slope derived from the K–L plot and the rotation speed of the rotating disk electrode, respectively. Furthermore, the value of the K–L slope is directly related to the value of “ n ” as per the following equation:

$$B = 0.62nFC_{O_2}D_{O_2}^{2/3}\nu^{-1/6} \quad \dots\dots\dots (2.8)$$

where DO_2 is the diffusion coefficient of oxygen ($1.9 \times 10^{-5} \text{ cm}^2 \text{ s}^{-1}$) and ν is the kinematic viscosity of the electrolyte ($1.1 \times 10^{-2} \text{ cm}^2 \text{ s}^{-1}$). The K–L plot is presented in Fig. 2.6b, and it clearly shows a linear relationship between J_k^{-1} (kinetic current density) and $\omega^{-1/2}$ (electrode rotation rate). From this, the average value of “n” was determined to be ~ 3.7 , suggesting that the electro-reduction of oxygen by the Co-MOF followed a four-electron pathway i.e., the

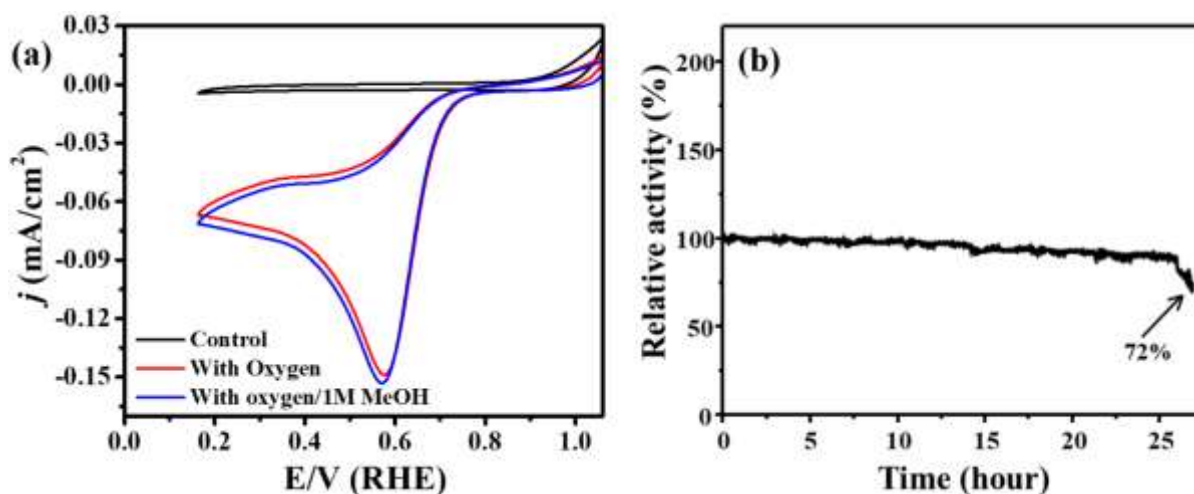


Figure 2.7 (a) CV showing the methanol tolerance test in presence of 1 M methanol (b) stability measurement of the Co-MOF-modified GCRDE in an oxygen saturated 0.1 M KOH electrolyte.

dissolved oxygen was directly converted to water without the formation of intermediate peroxides (H_2O_2). The suitability of the Co-MOF as a cathode electrocatalyst for the ORR was verified by performing the methanol tolerance test (MTT). Using similar experimental conditions, the CV and LSVs were obtained by adding 1 M methanol to the oxygen saturated 0.1 M KOH electrolyte (Fig. 2.7a). It can be seen that the presence of methanol has not made any prominent alteration in the shape of the cyclic voltammogram pattern, reduction current density as well as the reduction potential. This observation establishes the methanol tolerance of the catalyst, proving its suitability to be used as a cathode in the direct methanol fuel cell (DMFC). Furthermore, we performed steady-state chronoamperometry at 0.65 V (vs. RHE) in an oxygen-saturated 0.1 M KOH electrolyte. Around 72% of the initial reduction current

density was observed to be retained even after 25 hours, suggesting the better durability of the Co-MOF as an ORR catalyst (Fig. 2.7b). This observation was also supported by the unaltered surface morphology and X-ray diffraction pattern obtained via the FESEM and XRD analysis of the post-catalysis sample (Fig. 2.8a-c), respectively.

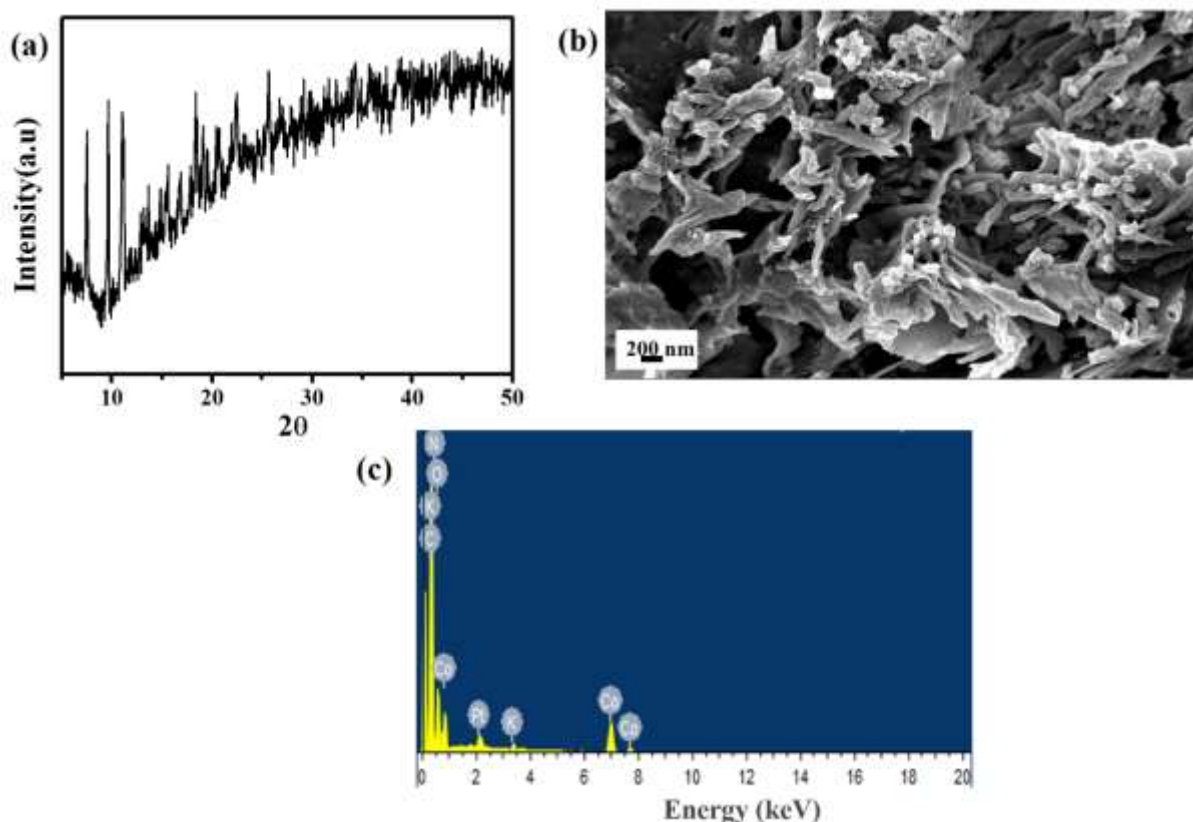


Figure 2.8 (a) XRD pattern (b) FESEM, (c) EDS of Co-MOF after the ORR stability measurement.

This robust stability of the material was observed to be higher than that of some of the recently reported MOFs, noble metal nanostructures and composite electrocatalysts.^{8,19} Furthermore, the electrocatalytic activity of the synthesized Co-MOF was analysed towards the oxygen evolution reaction using a standard three-electrode electrochemical set-up. All the linear sweep voltammograms were obtained in a 1 M KOH electrolyte at the rotation of 1600 rpm at the sweep rate of 5 mV s^{-1} (Fig. 2.9a).

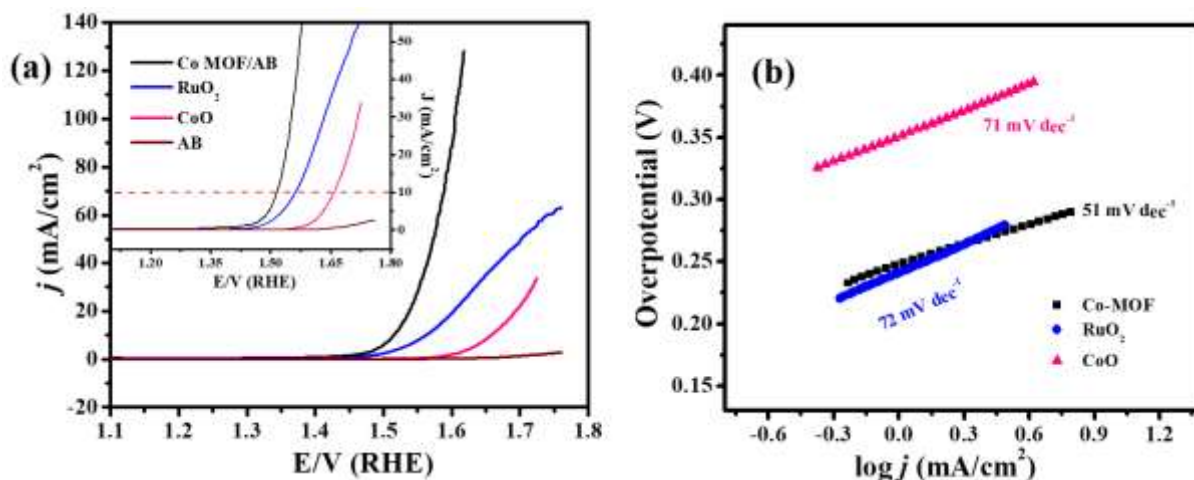


Figure 2.9 (a) LSVs for the OER by Co-MOF/AB, commercial RuO₂, CoO (after TGA), and AB in a 1 M KOH electrolyte at the sweep rate of 5 mV s⁻¹ and (b) the corresponding Tafel plot.

To eliminate the negative influence of the electrolyte and material resistance as well as to determine the intrinsic electrocatalytic performances of the sample, all the observed potentials were iR compensated using the solution resistance obtained from the Nyquist impedance measurement (Fig. 2.10).

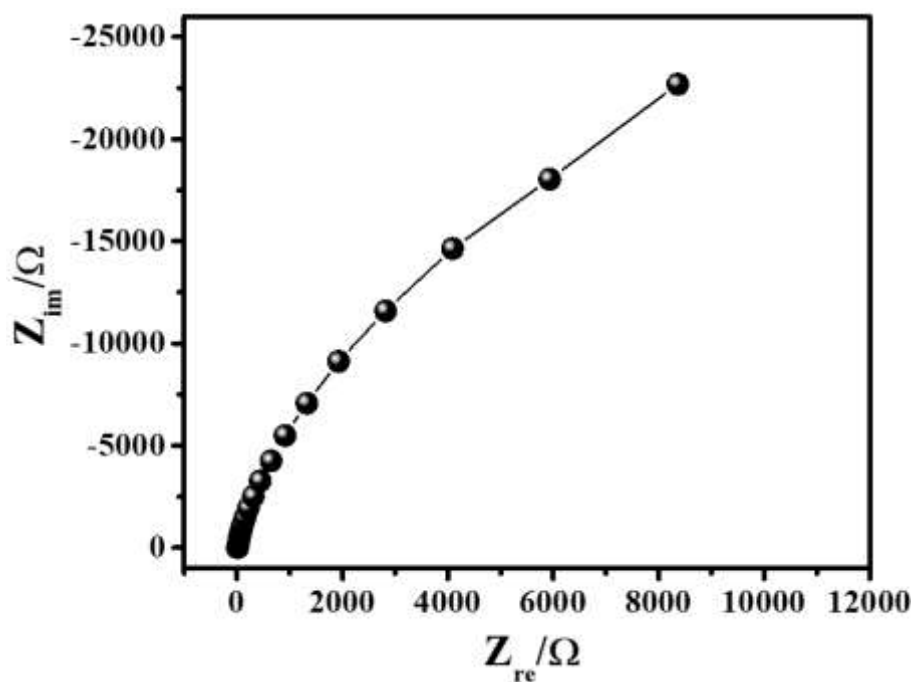


Figure 2.10 Nyquist impedance spectrum of Co-MOF.

The LSVs obtained before and after iR compensation are presented in Fig. 2.11. Notably, the Co-MOF shows the lower onset potential of 1.25 V vs. RHE as compared to the commercial RuO₂ nanoparticles (1.45 V vs. RHE), demonstrating better electrocatalytic performances. Moreover, for comparison, the as-obtained CoO (after TGA of Co-MOF) was modified on the GCRDE, and the LSV and Tafel data are shown in Fig. 2.9a and Fig. 2.9b.

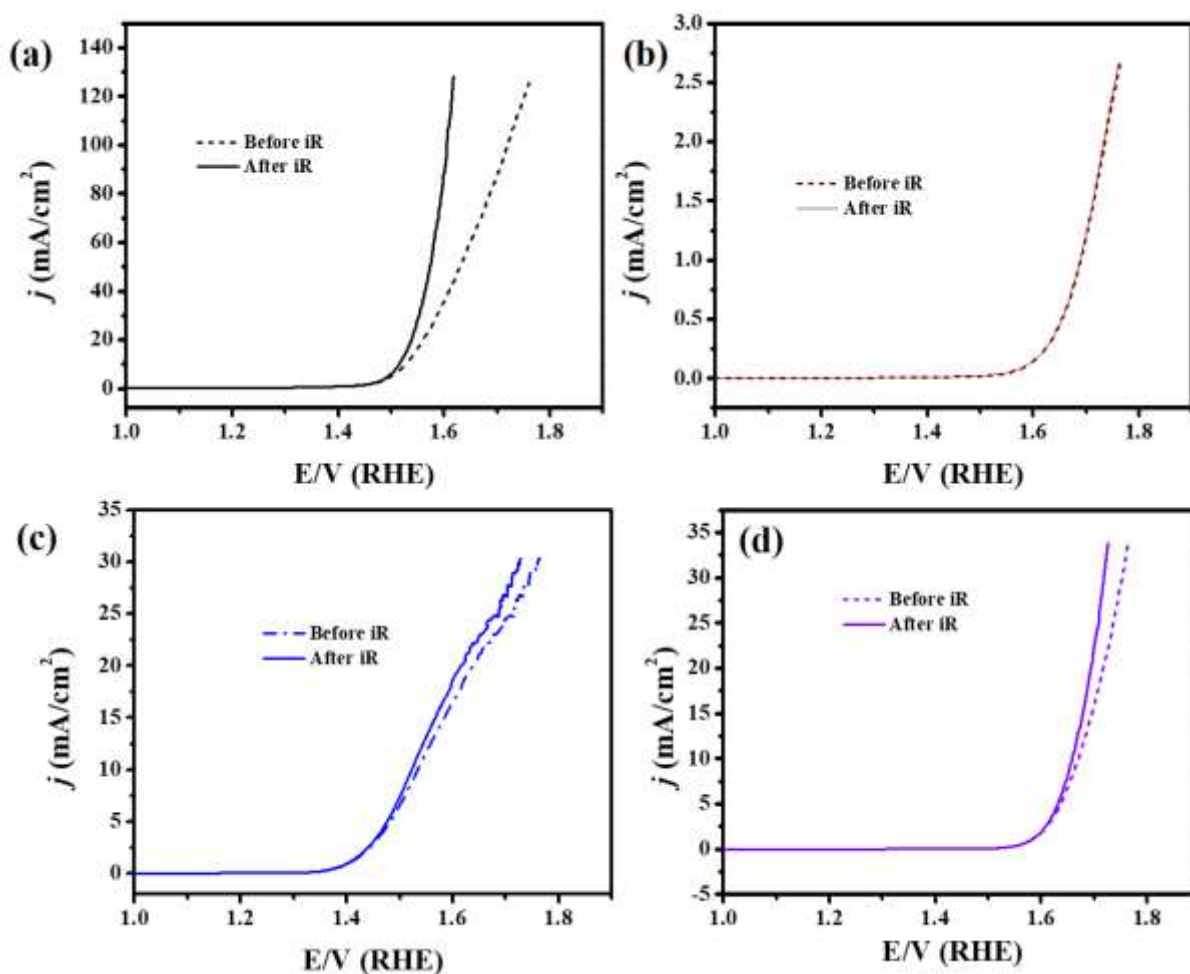


Figure 2.11 Linear sweep voltammograms for (a) Co-MOF (b) AB, (c) commercial RuO₂ and (d) CoO after TGA for OER before and after the iR-compensation in 1 M KOH electrolyte at a sweep rate of 5 mV/s.

To accurately evaluate the catalytic performance, the overpotential needed to generate the 10 mA cm⁻² current density was determined via the standard method. It has been observed that the Co-MOF needs only 280 mV overpotential to deliver the benchmark current density of 10

mA cm⁻², which is far less than that needed in the cases of RuO₂ (330 mV) and CoO (430 mV). The better electrocatalytic performance of the Co-MOF is very prominent than that of the recently reported materials summarized in Table 2.1. From the polarization curves, the Tafel plot has been derived, and the calculated Tafel slope is 51 mV dec⁻¹ that is lower than that of the RuO₂ sample (72 mV dec⁻¹), demonstrating superior reaction kinetics of the Co-MOF-based electrocatalysts (Fig. 2.9b). In addition, the Co-MOF delivers the exchange current density of 7×10^{-5} A cm⁻², which is larger than that of most of the Co-based OER electrocatalysts reported earlier.^{20,21} Further understanding of this magnificent catalytic performance towards the OER, the double layer capacitance (C_{dl}), electrochemical active surface area (ECSA) and roughness factor (R_f) of the Co-MOF and RuO₂ nanoparticles (the calculation details are provided in the Experimental section) were estimated. The C_{dl} was calculated from the CV obtained in the non-faradaic region of the potential window and is presented in Fig. 2.12a and b.

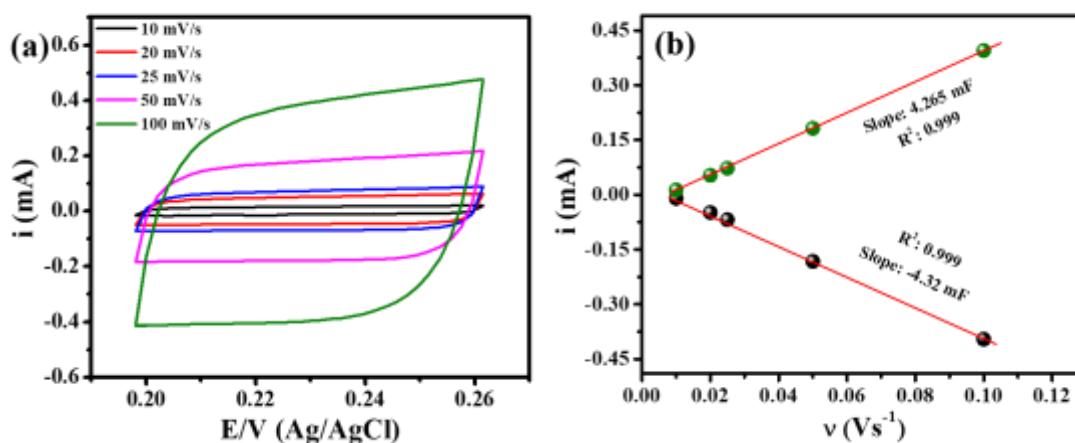


Figure 2.12 (a) Cyclic voltammograms at different sweep rates in 1 M KOH electrolyte, (b) plot of current density at 0.23 V vs. Ag/AgCl to the sweep rate to determine the double layer capacitance of Co-MOF.

The double layer capacitance also determined by various materials shown in Fig. 2.13 and found that the Co-MOF shows the average C_{dl} of more than ~ 14 times that of the commercial RuO₂ with the same catalyst loading.

Table 2.1 Comparison of activity of the Co-MOF with the reported metal organic frameworks for oxygen evolution reaction.

Catalysts	Electrolyte (Conc)	Overpotential (mV)	Tafel Slope (mV/dec)	Reference
NiCo-UMOFNs	1 M KOH	250@10 mA cm ⁻²	142	Nat. Energy, 2016, 1, 16181.
[Co(C ₁₂ H ₆ O ₄)(H ₂ O) ₄]	0.1 M KOH	520@10 mA cm ⁻²	42	J. Am. Chem. Soc. 2014, 136, 13925
Fe ₃ -Co ₂	0.1 M KOH	GC:283@10 mA·cm ⁻² Cu Foam:237@10 mA cm ⁻²	43 79	J. Am. Chem. Soc. 2017, 139, 1778
Co-WOC-1	0.1 M KOH	390@1 mA cm ⁻²	128	Angew. Chem. Int. Ed. 2016, 55, 2425.
Cu-MOF	0.5 M H ₂ SO ₄	310@2 mA cm ⁻²	65	Adv. Funct. Mater. 2013, 23, 5363.
Co-TpBpy	pH = 7	400@1 mA cm ⁻²	59	Chem. Mater. 2016, 28, 4375.
CoO _x -ZIF	1 M KOH	318@10 mA cm ⁻²	70.3	Adv. Funct. Mater. 2017, 1702546.
NiFe LDH/NF	1 M KOH	240@10 mA cm ⁻²	----	Science 2014, 345, 1593
MAF-X27-OH	1 M KOH	387@10 mA cm ⁻²	----	J. Am. Chem. Soc. 2016, 138, 8336-8339
Co-ZIF-9	pH = 13.4	510@10 mA cm ⁻²	----	Nanoscale 2014, 6, 9930-9934.
FeTPyP-Co	0.1 M NaOH	330@10 mA cm ⁻²	----	J. Am. Chem. Soc. 2016, 138, 3623-3626
CoTPyP	0.1 M NaOH	400@10 mA cm ⁻²	----	J. Am. Chem. Soc. 2016, 138, 3623-3626
FeTPyP	0.1 M NaOH	400@10 mA cm ⁻²	----	J. Am. Chem. Soc. 2016, 138, 3623-3626
NU-1000	pH = 11	566@10 mA cm ⁻²	----	ACS Appl. Mater. Interfaces 2015, 7, 28223-28230.
Co-MOF	1 M KOH	280@10 mA cm⁻²	51	This work
Commercial RuO₂	1 M KOH	330@10 mA cm⁻²	72	
Co₃O₄ (post TGA)	1 M KOH	430@10 mA cm⁻²	71	

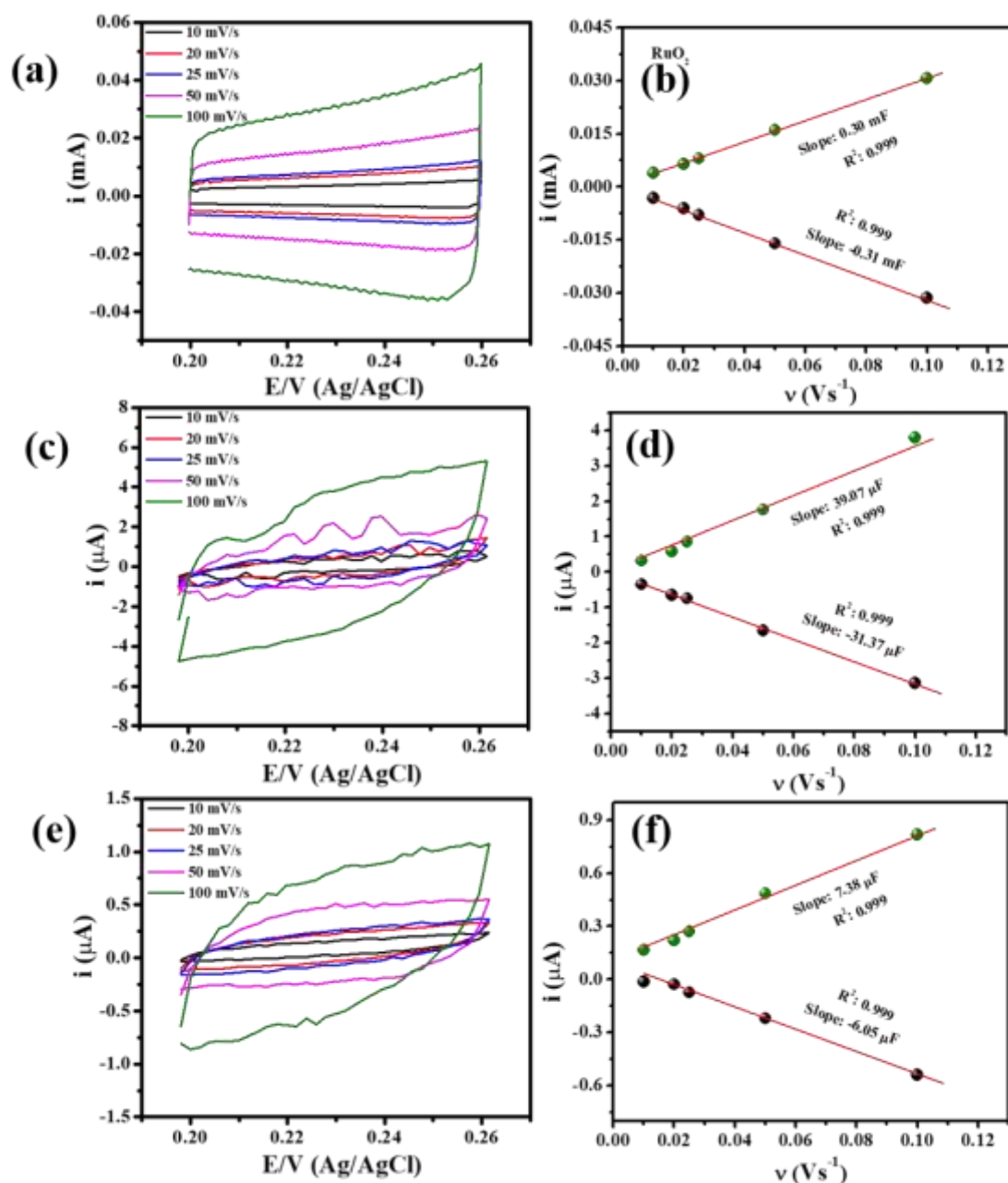


Figure 2.13 Cyclic voltammogram at different sweep rates and plot of current density at 0.23 V vs. Ag/AgCl to the sweep rate to determine the double layer capacitance by commercial RuO₂ (a, b), Co₃O₄ (c, d) and AB (e, f) modified GCE in 1 M KOH electrolyte.

Moreover, the Co-MOF has a higher value of ECSA (105.5 cm²) and R_f (566) than the commercial RuO₂ with similar electrocatalyst loading presented in Table 2.2. The number of active sites (in moles) present in the samples was calculated by dividing the molecular masses with the mass of the electrocatalyst loaded onto the electrode surface. Herein, we observed the

Table 2.2 Comparison of various parameters of Co-MOF, commercial RuO₂, and CoO under similar electrochemical condition with similar loading of electrocatalyst.

Catalyst	$\eta@10$ mA/cm ²	Mass activity @ $\eta=350$ mV (A/g)	ECSA (cm ²)	Roughness factor (R _f)	TOF (s ⁻¹)@ $\eta=350$ mV
Co-MOF/AB	280 mV	360.06	105.5	566	93.21
RuO ₂	330 mV	55.44	7.62	40.13	3.64
CoO	430 mV	4.12	0.875	4.6	0.154

presence of a higher number of active sites (6.950×10^{-9} moles) in Co-MOF as compared to that of state-of-the-art RuO₂ nanoparticles (0.490×10^{-9} moles) and CoO (0.057×10^{-9} moles). The existence of more active sites aids in availing more active reaction centres for catalysing the OER efficiently.

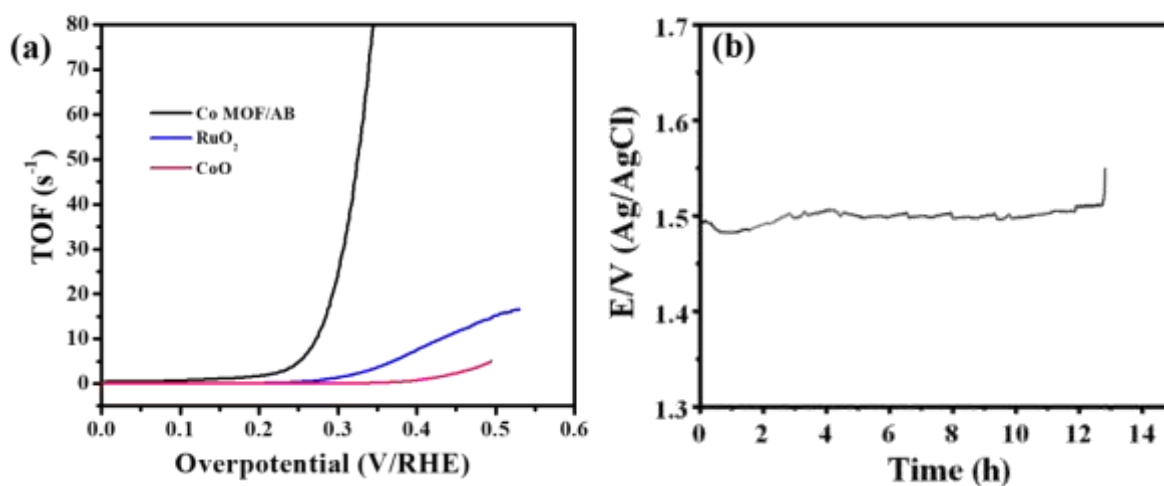


Figure 2.14 (a) plot of turn over frequency against overpotential (b) stability test for OER at a current density of 10 mA cm⁻².

The intrinsic catalytic activity of the Co-MOF towards OER has been evaluated from the turn over frequency by speculating that all the metal ions are catalytically active centres. At 350 mV overpotential, Co-MOF, RuO₂ and CoO show the TOF value of 93.21 s⁻¹, 3.64 s⁻¹ and

0.154 s⁻¹, respectively (Fig. 2.14a). Herein, we observed that the TOF value for the Co-MOF was nearly 19 times that of the commercial RuO₂ and many more times higher than that of the recently reported MOF and nanoparticle-based electrocatalysts.^{22–26} The outstanding OER performance of the Co-MOF may have resulted from its higher accessible surface area and existence of a large number of catalytic active centres. In addition, the rod-like morphology causes easy access of the electrolyte and better ion transport to the active centres, leading to better catalytic performance. The operational durability is an important factor for considering a catalyst for practical application in the energy conversion devices. Therefore, the durability of the Co-MOF was accessed using the chronopotentiometry technique at the applied current density of 10 mA cm⁻² under similar experimental conditions (Fig. 2.14b). The Co-MOF shows a very small (15 mV) increase in overpotential even after more than 13 hours of electrolysis. This is presumed to be due to the catalytic weight loss during the electrolysis process, demonstrating its excellent stability towards the OER. Furthermore, the change in the

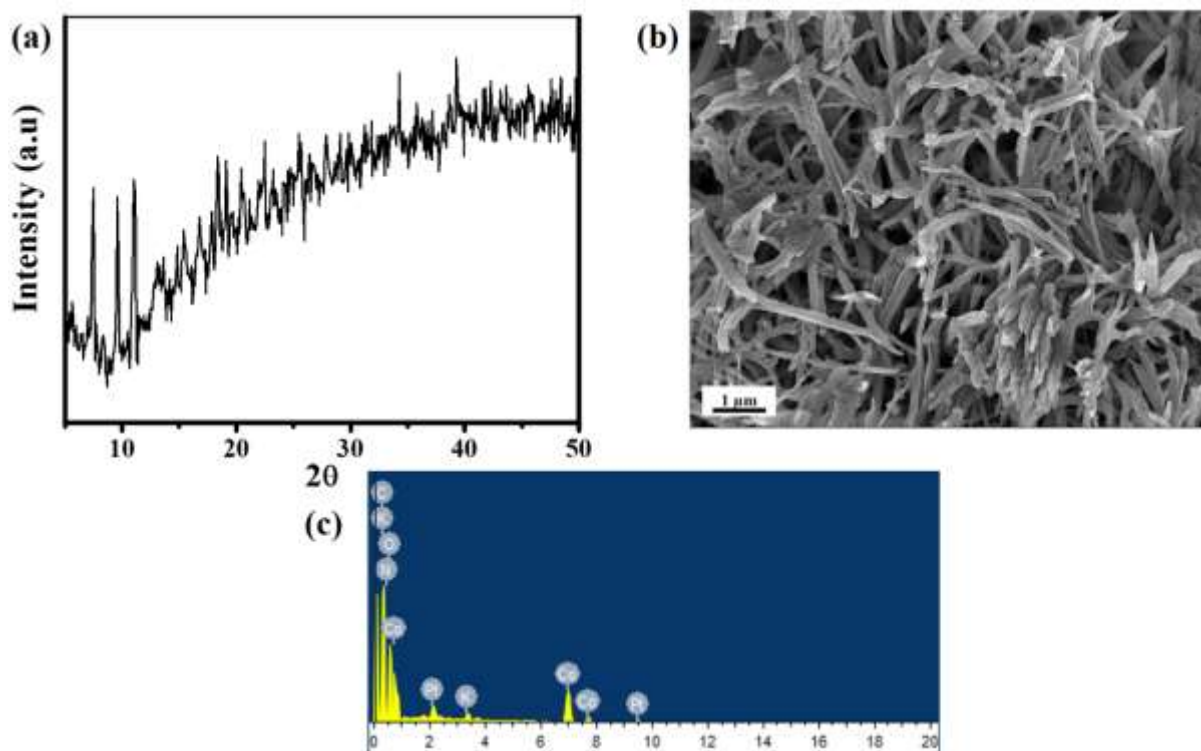


Figure 2.15 (a) XRD pattern (b) FESEM, (c) EDS of Co-MOF after the OER stability measurement.

morphology and crystallinity of the Co-MOF was determined by the FESEM and powder X-ray diffraction data obtained after the durability test (Fig. 2.15a, b, c). Likewise, ORR, herein, an unaltered diffraction pattern of the Co-MOF was revealed via the XRD analysis after the OER. However, a slight distortion in the morphology was observed in the FESEM images, demonstrating the excellent stability of the Co-MOF during the OER in an alkaline medium.

2.9 Conclusions

In summary, this study demonstrates a single-step solvothermal synthesis of rod-structured Co MOF that serves as a bi-functional electrocatalyst for the ORR and OER in an alkaline medium. The Co-MOFs catalyse the ORR with lower onset potential via a four-electron reduction path. It shows robust durability and tolerance to the addition of methanol; this demonstrates its application as an efficient material in future direct methanol fuel cells and metal–air batteries. Additionally, the Co-MOF has been used as an anode electrode material, and its OER activity has been successfully studied. It catalyses the OER process with low onset potential, lower Tafel slope and better catalytic durability than the commercial RuO₂. Moreover, it needs only 280 mV of overpotential to achieve the 10 mA cm⁻² current density. Furthermore, the post catalysis samples were analysed by the FESEM and powder XRD pattern, showing its structural robustness. The excellent electrocatalytic activity of this Co-MOF can be attributed to its 3D porous structure, rapid ion transport along with the existence of higher accessible surface area and a greater number of active sites. The results provide an in-depth understanding of the MOF-based electrocatalysts and their potential to be applied as energy materials in the fuel cell, water-splitting devices and other renewable energy systems.

References

- 1 B. Dunn, H. Kamath and J. M. Tarascon, *Science* (80-.), 2011, **334**, 928–935.
- 2 S. Zhao, Y. Wang, J. Dong, C. T. He, H. Yin, P. An, K. Zhao, X. Zhang, C. Gao, L. Zhang, J. Lv, J. Wang, J. Zhang, A. M. Khattak, N. A. Khan, Z. Wei, J. Zhang, S. Liu, H. Zhao and Z. Tang, *Nat. Energy*, 2016, **1**, 1–10.
- 3 A. A. Gewirth, J. A. Varnell and A. M. Diascro, *Chem. Rev.*, 2018, **118**, 2313–2339.
- 4 S. L. Morales and A. M. Fernández, *Int. J. Electrochem. Sci.*, 2013, **8**, 12692–12706.
- 5 W. Chen, Y. Zhang, G. Chen, R. Huang, Y. Zhou, Y. Wu, Y. Hu and K. Ostrikov, *J. Mater. Chem. A*, 2019, **7**, 3090–3100.
- 6 C. Guan, X. Liu, W. Ren, X. Li, C. Cheng and J. Wang, *Adv. Energy Mater.*, 2017, **7**, 1–8.
- 7 Y. V. Kaneti, J. Tang, R. R. Salunkhe, X. Jiang, A. Yu, K. C. W. Wu and Y. Yamauchi, *Adv. Mater.*, , DOI:10.1002/adma.201604898.
- 8 C. Xuan, B. Hou, W. Xia, Z. Peng, T. Shen, H. L. Xin, G. Zhang and D. Wang, *J. Mater. Chem. A*, 2018, **6**, 10731–10739.
- 9 J. Mao, L. Yang, P. Yu, X. Wei and L. Mao, *Electrochem. commun.*, 2012, **19**, 29–31.
- 10 M. Jiang, L. Li, D. Zhu, H. Zhang and X. Zhao, *J. Mater. Chem. A*, 2014, **2**, 5323–5329.
- 11 H. Wang, F. Yin, B. Chen and G. Li, *J. Mater. Chem. A*, 2015, **3**, 16168–16176.
- 12 E. M. Miner, L. Wang and M. Dincă, *Chem. Sci.*, 2018, **9**, 6286–6291.
- 13 E. M. Miner, S. Gul, N. D. Ricke, E. Pastor, J. Yano, V. K. Yachandra, T. Van Voorhis and M. Dincă, *ACS Catal.*, 2017, **7**, 7726–7731.
- 14 E. M. Miner, T. Fukushima, D. Sheberla, L. Sun, Y. Surendranath and M. Dinca, *Nat. Commun.*, 2016, **7**, 1–7.
- 15 L. Zhao, B. Dong, S. Li, L. Zhou, L. Lai, Z. Wang, S. Zhao, M. Han, K. Gao, M. Lu,

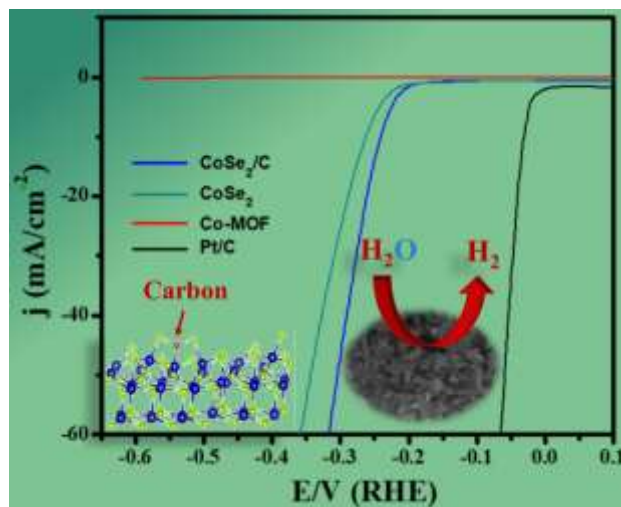
- X. Xie, B. Chen, Z. Liu, X. Wang, H. Zhang, H. Li, J. Liu, H. Zhang, X. Huang and W. Huang, *ACS Nano*, 2017, **11**, 5800–5807.
- 16 S. Gonen and L. Elbaz, *Curr. Opin. Electrochem.*, 2018, **9**, 179–188.
- 17 R. K. Tiwari and J. N. Behera, *CrystEngComm*, 2018, **20**, 6602–6612.
- 18 J. Masa, C. Batchelor-McAuley, W. Schuhmann and R. G. Compton, *Nano Res.*, 2014, **7**, 71–78.
- 19 C. Xuan, B. Hou, W. Xia, Z. Peng, T. Shen, H. L. Xin, G. Zhang and D. Wang, *J. Mater. Chem. A*, 2018, **6**, 10731–10739.
- 20 I. H. Kwak, H. S. Im, D. M. Jang, Y. W. Kim, K. Park, Y. R. Lim, E. H. Cha and J. Park, *ACS Appl. Mater. Interfaces*, 2016, **8**, 5327–5334.
- 21 Y. Zhang, Q. Xiao, X. Guo, X. Zhang, Y. Xue, L. Jing, X. Zhai, Y. M. Yan and K. Sun, *J. Power Sources*, 2015, **278**, 464–472.
- 22 L. Gan, J. Fang, M. Wang, L. Hu, K. Zhang, Y. Lai and J. Li, *J. Power Sources*, 2018, **391**, 59–66.
- 23 H. Xu, Z. X. Shi, Y. X. Tong and G. R. Li, *Adv. Mater.*, 2018, **30**, 1–8.
- 24 Z. Xue, Y. Li, Y. Zhang, W. Geng, B. Jia, J. Tang, S. Bao, H. P. Wang, Y. Fan, Z. wen Wei, Z. Zhang, Z. Ke, G. Li and C. Y. Su, *Adv. Energy Mater.*, 2018, **8**, 1–7.
- 25 B. Chen, Z. Jiang, L. Zhou, B. Deng, Z. J. Jiang, J. Huang and M. Liu, *J. Power Sources*, 2018, **389**, 178–187.
- 26 W. Kong, X. Luan, H. Du, L. Xia and F. Qu, *Chem. Commun.*, 2019, **55**, 2469–2472.

CHAPTER-3

DFT supported cobalt metal-organic framework (Co-MOF) derived CoSe₂/C hybrid nanostructures for electrochemical hydrogen evolution reaction

- 3.1** Abstract
- 3.2** Introduction
- 3.3** Motivation of the work
- 3.4** Experimental section
 - 3.4.1** Synthesis of Co-MOF
 - 3.4.2** Synthesis of Co-MOF derived CoSe₂/C and bare CoSe₂
- 3.5** Characterization
- 3.6** Electrochemical measurements
- 3.7** Calculations of ECSA and R_f
- 3.8** Results and discussions
- 3.9** Conclusions
- 3.10** References

3.1 Abstract



This chapter focuses on generation of molecular hydrogen by electrochemical water splitting by using Co-MOF $[Co_4(BTC)_3(BIm)_6]$ as starting precursor, graphitic carbon encapsulated $CoSe_2$ nanostructures has been prepared through a single step selenization method. The carbon network in the $CoSe_2/C$ hybrid nanostructure form channels facilitating the accessibility of the electrolyte ions and maximize the utilization of catalytic active centres. Specifically, it needs only 240 mV of overpotential to reach the benchmarked current density (10 mA/cm^2) with a lower Tafel slope. Further the experimental findings have been supported by the theoretical analysis of the structure and electronic properties of $CoSe_2$ and $CoSe_2/C$ hybrid by density functional theory (DFT) simulations. The interaction between $CoSe_2$ and C is due to charge transfer from Co 3d orbital and Se 4p orbital of $CoSe_2$ to the 2p orbital of Carbon. Also, populated electronic states near Fermi level for C doped $CoSe_2$ may infer towards increased conductivity of the material. Computed overpotential for HER activities shows the qualitative order of $CoSe_2/C < CoSe_2$, matching nicely with the experimental data. The synergic effect of increased conductivity, improved surface area and superior electro-catalytic activity due to C doping is responsible for superior HER catalytic performance.

3.2 Introduction

Molecular hydrogen (H_2) considered as the clean and green fuel and is a suitable one to substitute the traditional fossil fuels. Although various methodologies have been developed for the generation of H_2 , but the electrochemical splitting of water presumed to be an efficient one in terms of ease of operation and cost effectiveness.^{1,2} However, the electrocatalyst played a determinant role to judge the efficiency of the process and among various electrocatalysts the platinum-based nanostructures acknowledged to be most efficient. But their high cost and limited reserve restricts their scale up and commercialization. Therefore, the interest on development of low-cost non-novel metal-based catalyst with better durability and minimal overpotential/Tafel slope have been intensified. As can be found from the literature, the pyrite type transition metal dichalcogenides have lower Gibb's free energy change for the adsorption and desorption of hydrogen.^{2,3} And also their diversity in electronic structure and chemical composition tunability make them promising electrocatalysts for HER. Therefore, more focus has been given for the synthesis and electrocatalytic performance exploration of metal sulphides and selenides.⁴⁻⁸

In particular many synthesis protocols have been put forward for the preparation of cobalt and nickel di-selenides.⁹⁻¹¹ In a particular work, Kong et al., have prepared a series of transition metal (ME, M= Fe, Co, Ni; E=S, Se) dichalcogenides on glassy carbon substrate and demonstrated their electrocatalytic performances.¹² Among them the $CoSe_2$ nanoparticles showed better electrocatalytic performances towards HER. However, these $CoSe_2$ nanostructures observed to be aggregated which reduced the exposure of the catalytic active centres impeding the electrocatalytic activity. In order to achieve maximum catalytic performances, these TMDs were composited with various conductive carbons and grown over different conductive substrates which not only needs additional synthesis steps but also adds more cost to the catalyst.^{9,13} Lu et al., have derived $CoSe_2$ nanoparticles encapsulated in a N-

doped carbon polyhedra from a zeolitic imidazolate framework-67. The nanostructure catalyses the HER requiring 234 mV overpotential for 10 mA/cm² current density with a Tafel slope of 62 mV/dec.¹⁴ Although a few works are done in electrocatalyst synthesis but the development of new methodologies remains strictly indispensable to sketch out the preparation of cobalt di-selenides with better electrocatalytic HER efficacy.

Metal organic frameworks (MOFs) are crystalline multi- dimensional structures made from the coordination of the organic ligands to the metal ions.^{15,16} However, these MOFs were observed to be unstable when employed as electrode material for electrocatalysis study in acidic as well as alkaline electrolytic environments. Therefore, current research focuses on the designing of methodologies to derive metal nanostructures from these MOFs and make composites with carbon to achieve better electrocatalytic behaviour.¹⁷⁻¹⁹ In this report, we designed a novel approach for the synthesis of CoSe₂ encapsulated in a graphitic carbon network from cobalt metal organic framework [Co₄(BTC)₃(BIm)₆] by selenization through a solvothermal method. Here the single reaction step simultaneously makes the possible selenization of the metal centres as well as graphitization of the carbon framework present in the MOF forming the hybrid structure (CoSe₂/C). The carbon network in the CoSe₂/C hybrid nanostructure form channels facilitating the accessibility of the electrolyte ions. This makes the hybrid to show higher electrochemical accessible surface area, lower charge transfer resistance and improved catalytic durability thereby increasing the electrocatalytic hydrogen evolution reaction. Particularly, the CoSe₂/C hybrid needs only 240 mV overpotential to reach the state-of-the-art current density of 10 mA/cm² which is lower to that in case of the CoSe₂, Co-MOF. These experimental findings are also supported by the theoretical calculations using DFT simulations. The total density of states (TDOS), partial density of states (PDOS), Bader charge transfer analysis and charge density plot have been presented which clearly showed the

modification in electronic properties and orbital interactions due to graphitized carbon doping in CoSe₂.

3.3 Motivation of the work

A large proportion of MOFs have wide application in gas storage, magnetism, sensor due to availability of hierarchy surface morphology, tunable chemical structures, ultra-high specific surface area and presence of more active centres. It has been observed that a large proportion of the MOFs are insulator and they are facing stability issues in different electrolyte medium. To get rid of these issues, MOF derived materials are getting more attention for electrochemical energy conversion and storage purposes. This can be attained by annealing MOFs at different temperature or hydrothermal process. Therefore, in a one-step facile hydrothermal approach, we synthesized a MOF-derived CoSe₂/C hybrid nanomaterial from a HER inactive pristine Co-MOF in acidic media.

3.4 Experimental Section

Synthesis of Co-Metal Organic Framework (Co-MOF)

The Co-MOF [Co₄(BTC)₃(BIm)₆] [DMF] was synthesized by following the synthetic procedure of our previous study.²⁰ Typically, 0.25 mmol of cobalt acetate tetrahydrate was dissolved in 1 ml of dimethylformamide (DMF) followed by addition of 0.25 mmol of benzene tricarboxylic acid and 0.25 mmol of benzimidazole (Co: BTC: BIm = 1:1:1) under constant stirring. After 60 minutes, the whole solution was transferred to a Teflon lined stainless steel autoclave (7 ml) and heated at 120 °C for 48 hours. After cooled down to room temperature, the rod-shaped crystals (Co–BTC–BIm MOF) were collected by filtration, powdered thoroughly and stored. Here the as synthesized Co–BTC–BIm MOF powder was named as Co-MOF.

Synthesis of cobalt selenide/carbon hybrid (CoSe₂/C) and bare CoSe₂

For the synthesis of CoSe₂/C, the as prepared Co-MOF was taken as the starting precursor. At first, 50 mg of Co-MOF was added to 10 ml of DMF and kept stirring to form a homogeneous mixture. Thereafter 39 mg of selenium powder was added to the mixture and kept stirring for another one hour. The whole mixture was poured into a Teflon lined stainless steel autoclave and placed in a hot air oven at 200 °C for 12 hours. After cooled down, the residues were collected, washed with deionised water and absolute ethanol and stored for further characterization and electrochemical study. For comparison, CoSe₂ was prepared by using Co (NO₃)₂ · 6H₂O as the starting precursor in place of Co-MOF keeping all other reaction conditions unaltered.

3.5 Characterization

The phase purity and crystallinity of the as prepared Co-MOF was analysed by single crystal X-ray diffractometer (Bruker AXS-KAPPA Apex II diffractometer with Mo K α radiation) at room temperature. Further the powder X-ray diffraction pattern was obtained using the Bruker D8 Advance diffractometer equipped with a Cu-K α radiation source ($\lambda = 1.5418 \text{ \AA}$). The surface morphology of the Co-MOF was verified by a field emission scanning electron microscope (FESEM, Merlin Compact with a GEMINI-I electron column, Zeiss Pvt. Ltd, Germany) and transmission electron microscope (HRTEM, JEOL 2100F, operated at 200 kV). Furthermore, the thermal stability of the sample was verified by thermogravimetric analysis (by TA Instruments-Waters Lab) at the ramp rate of 10 °C min⁻¹ under a constant flow of nitrogen gas. The elemental composition and oxidation state of the metal centre was analysed by X-ray photoelectron spectroscopy (XPS, JEOL JPS-9010 MC, USA).

3.6 Electrochemical Measurement

All the electrochemical studies were carried out by a three-electrode electrochemical set up using Biologic Electrochemical workstation (SP-200). Here the sample modified glassy carbon

rotating disk electrode (GCRDE; geometrical surface area is 0.07 cm^{-2}), bare platinum wire and aqueous Ag/AgCl were taken as working, counter and reference electrodes and the measurements were performed in 0.5 M aqueous H_2SO_4 solution. Prior to the electrode preparation, the glassy carbon rotating disk electrode (GCRDE; geometrical surface area is 0.07 cm^{-2}) was polished with alumina slurry (1.0, 0.3, 0.05 μm sequentially) and washed properly to a mirror polished surface. At the meantime, the electrocatalyst ink was prepared by dispersing 1mg of CoSe_2 sample in 100 μl ethanol-Nafion mixture (95:5 % v/v). An optimized volume of the ink was drop casted onto the polished GCRDE (with a mass loading of 0.3 mg/cm^2) and dried properly in a vacuum desiccator before each of the electrochemical measurement. The electrocatalytic activity of the CoSe_2 nanostructure was demonstrated by using the cyclic voltammetry (CV), linear sweep voltammetry (LSV) and electrochemical impedance spectroscopic (EIS) techniques. The EIS (Nyquist Impedance) was carried out in a frequency range of 1 MHz to 0.1 Hz with an AC amplitude of 5 mV. Here all the potential values were recorded with respect to the aqueous Ag/AgCl and presented here in reversible hydrogen electrode (RHE) as per the following Nernst equation,

$$E_{\text{RHE}} = E_{\text{Ag}/\text{AgCl}} + 0.059 \text{ pH} + E_{\text{Ag}/\text{AgCl}}^0 \dots\dots\dots (3.1)$$

Here, pH of the electrolyte is 0.3 and $E_{\text{Ag}/\text{AgCl}}^0$ is the standard potential for the Ag/AgCl reference electrode (0.21 V).

Computational Details

For electronic and orbital interaction analysis density functional theory-based VIENNA ab initio simulation package (VASP) with projector-augmented wave (PAW) functional was employed.^{21–23} We have employed generalized-gradient approximation (GGA) for exchange-correlation functional.²³ For geometry optimizations and single point electronic energy calculations, the convergence criteria of 0.01 eV/Å and 10^{-5} eV was implemented for force and energy respectively. For a plane-wave basis, kinetic energy cut-off was set at 500 eV. The

Brillouin zones were sampled using K points mesh with Monkhorst-Pack scheme grid of 5x5x1 for optimization and 7x7x1 for accurate Density of States (DOS) calculations respectively.²⁴

3.7 Calculation of ECSA and R_f

The electrochemical accessible surface area was calculated from the double layer capacitance measured from the cyclic voltammograms as per the following equation:

$$ECSA = \frac{C_{dl}}{C_s} \dots\dots\dots (3.2)$$

For this measurement, the CVs were obtained in a non-faradaic region (-0.08 to -0.18 V vs. Ag/AgCl) of the potential window in a 0.5 M H₂SO₄ electrolyte at different sweep rates (25, 50, 100, 150 and 200 mV s⁻¹). The C_s is the specific capacitance of an atomically smooth surface of the material and is taken as 0.04 mF cm⁻².

3.8 Result and Discussions

At first the Co-MOF was synthesized by using cobalt acetate tetrahydrate (as metal source), 1,3,5 Benzene tricarboxylic acid (BTC) and Benzimidazole via a hydrothermal method. The asymmetric unit contains 53 non-hydrogen atoms, two crystallographically distinct Co²⁺ ions (Co1 is square pyramidal, and Co2 is tetrahedral), three BIm and one and a half molecules of BTC anions. Four different BTC anions unit offering four bidentate carboxylate groups around the metal–metal axis to form a one-dimensional interconnected paddle-wheel-like arrangement. The alternate right and left-handed helical structure found in the crystal lattice further connected via the paddle-wheel secondary unit; this led to the formation of a layered structure, producing overall a three-dimensional (3D) network structure, where the axial position was occupied by BIm (as discussed in our previous report).²⁰ The Co-MOF crystals were powdered mechanically using a mortar pestle and synthesized the hastite CoSe₂ belonging to orthorhombic system nanostructures by mixing with the selenium powder in dimethyl formamide via solvothermal method. The diffraction pattern clearly shows the formation of

orthorhombic CoSe₂ (JCPDS NO: 00-053-0449) nanostructures with distinguished planes of (200), (210), (211), (220), (221), (311) and (230) at 2θ of 23.8°, 30.1°, 34.2°, 38.1°, 43.8°, 46.3°, 51.6° and 56.3° (Fig. 3.1a). Fig. 3.1b displays the Raman spectrum of CoSe₂/C, that constitutes four peaks at 173 cm⁻¹, 467 cm⁻¹, 510 cm⁻¹, 670 cm⁻¹. Specifically, the peak at 173 cm⁻¹ and at 670 cm⁻¹ are attributed to the Ag (Se-Se stretching) and A_{1g} modes of orthorhombic CoSe₂/C. Additionally, the presence of two prominent peaks at 1350 cm⁻¹ and 1585 cm⁻¹ assigned to the D and G-band of graphitic carbon. This might be developed from the linkers and ligands used in the Co-MOF synthesis. Therefore, we presumed that during the course of selenization of Co-MOF, not only the CoSe₂ was formed but also the graphitization of the carbon moieties taken place forming CoSe₂/C hybrid structure.

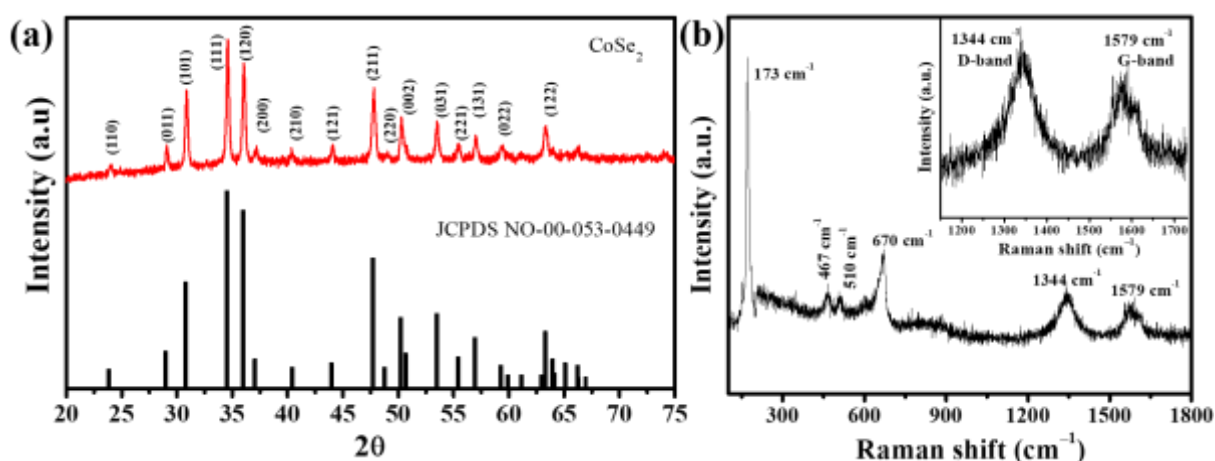


Figure 3.1 (a) Powder X-ray diffraction and (b) Raman spectrum of CoSe₂/C hybrid nanostructure.

Further the X-ray photoelectron spectroscopy confirms the elemental composition of the as synthesized CoSe₂/C hybrid structure. The high-resolution spectrum of Co 2p deconvoluted into two distinguished peaks at binding energies of 778 eV and 793.3 eV assigned to the Co 2p_{3/2}, Co 2p_{1/2} (Fig. 3.2a).²⁵⁻²⁷ Likewise, the 3d peak of selenium at 54.6 eV corresponds to the Co-Se bond (Fig. 3.2b). On further analysis, the peak at 54.6 eV, 55.8 eV and 59.3 eV are found and assigned to the Se 3d_{5/2}, Se 3d_{3/2} and Se-C linkage respectively.^{25,26,28}

The high-resolution C 1s peak can be deconvoluted into two different peaks at 284.4 eV and 286.3 eV assigned to the graphitic sp^2 carbon (C=C) and C-OH respectively.^{29,30} The XPS analysis confirms the presence of Co and Se in +2 and +4 oxidation states respectively and the existence of graphitic carbon in the CoSe₂/C hybrid structure again supporting the Raman analysis. Also, the area under the curve reveals the presence of Co and Se in nearly 1:2 ratio justifying the stoichiometric composition of CoSe₂.

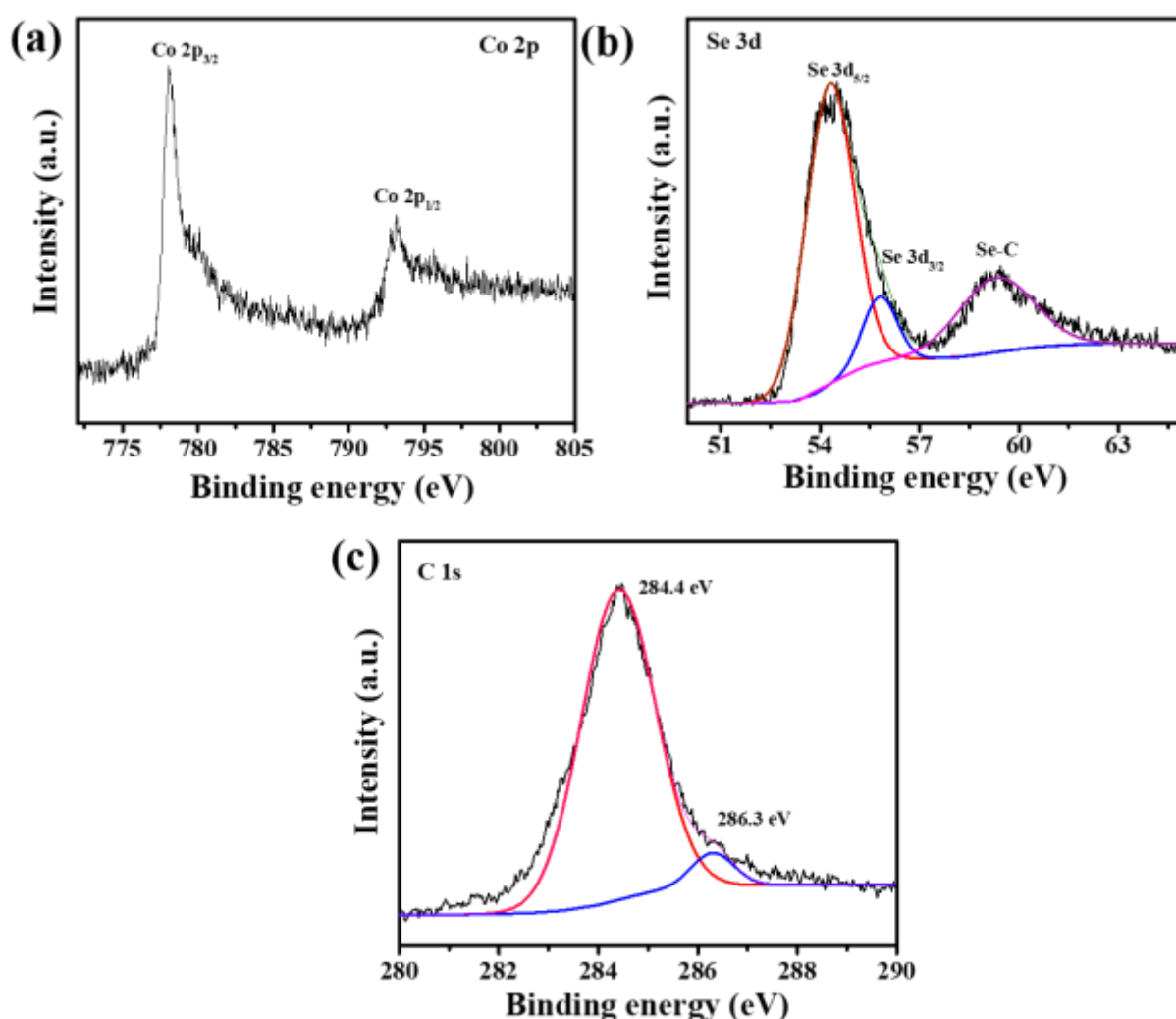


Figure 3.2 High resolution X-ray photoelectron spectrum of (a) Co 2p, (b) Se 3d and (c) C 1s of CoSe₂/C hybrid nanostructure.

The thermal stability of the sample was analysed by performing the thermogravimetric analysis at the ramp rate 10 °C/min. under constant flow of nitrogen gas (Fig. 3.3a). The CoSe₂ found to be stable up to 475 °C followed by a weight loss up to 590 °C (observed 44.92%, calculated 51.17%) which might be due to the removal of selenium in form of SeO₂. On further heating, the removal of residual selenium was observed and the CoSe₂ found to convert to the CoO after 900 °C. The phase transformation of post TGA has been analysed by the PXRD pattern (Fig. 3.3b) that completely matches with the cubic lattice of CoO (PDF#01-070-2856).

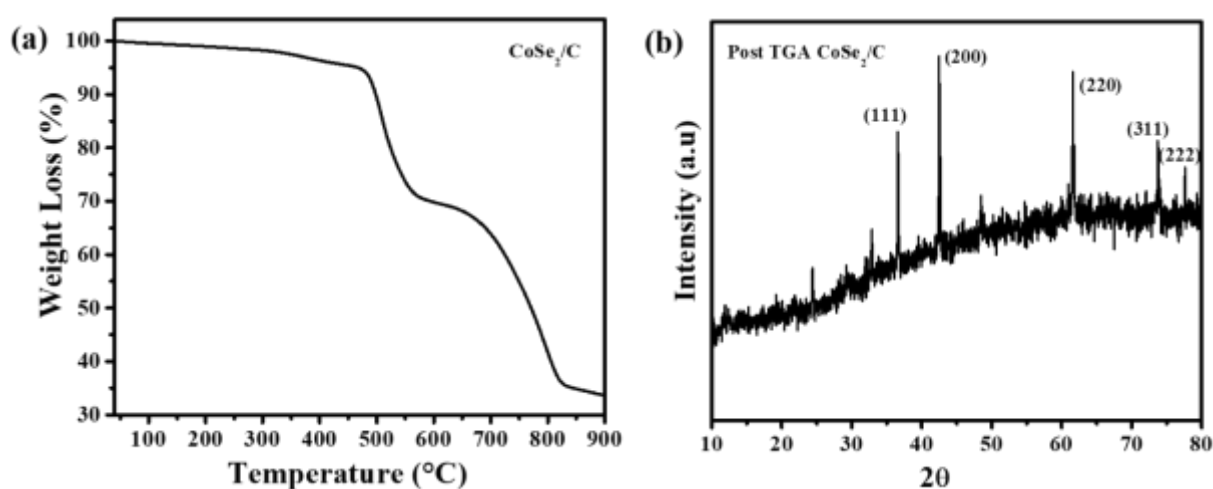


Figure 3.3 (a) TGA of CoSe₂/C hybrid (b) Powder X-ray diffraction pattern of post TGA CoSe₂/C hybrid sample.

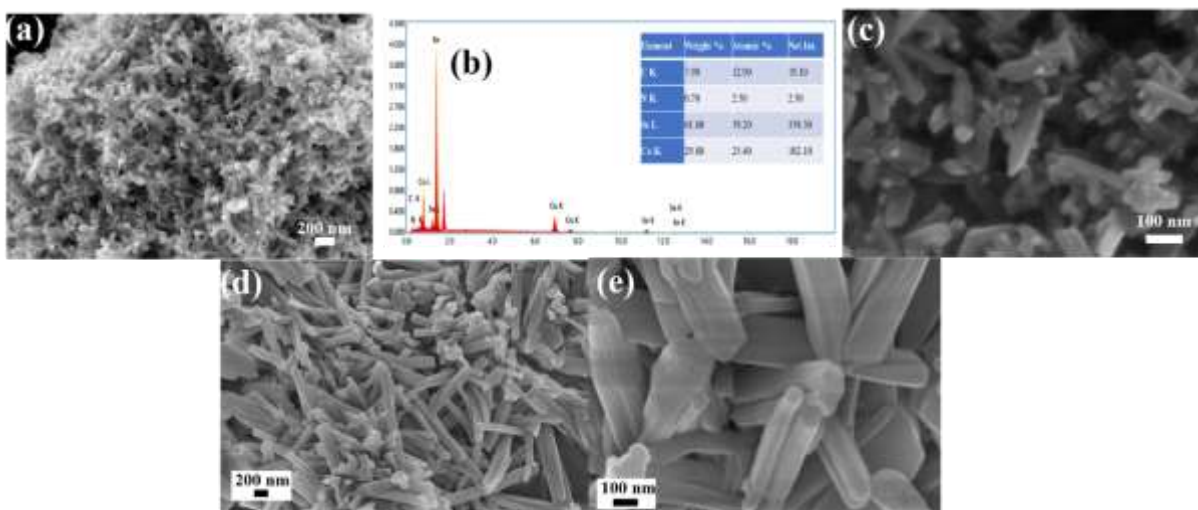


Figure 3.4 (a, c) FESEM images (b) EDS Spectrum of CoSe₂/C hybrid nanostructure (d, e) FESEM images of pristine Co-MOF.

Further, the FESEM suggests the retention of rod-shaped morphology like that of the pristine Co-MOF (Fig. 3.4a, c). However, after the selenization process, the dimension of the rods observed to be reduced ($\sim 100 \times 50$ nm length \times width). The presence of Co, Se and C in CoSe_2/C has been conformed from the EDS spectrum (Fig. 3.4b). the scanning electron microscopic images of the rod-shaped morphology was presented in Fig. 3.4d, e shows smooth surface of 1-2 μm length. Similar observation has been found from the transmission electron microscopic analysis (Fig. 3.5). The well distinguished fringes (Fig. 3.5a) at 0.26 nm and 0.37 nm are assigned to the (111) and (110) plane of CoSe_2 which in turn coincide with the SAED (Fig. 3.5b) and PXRD pattern.

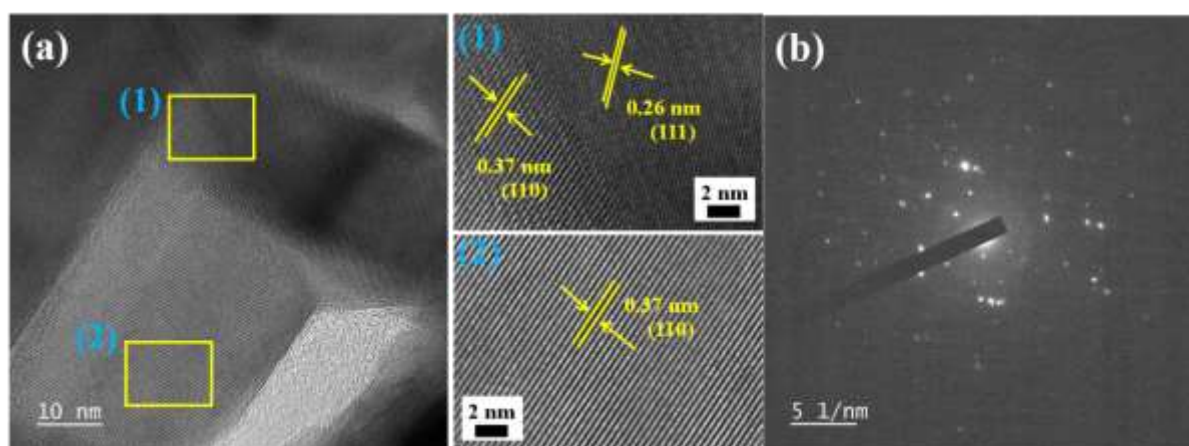


Figure 3.5 (a) TEM images and (b) corresponding SAED pattern for CoSe_2/C hybrid nanostructure.

In order to explore the electrocatalytic HER performance, the linear sweep voltammograms of CoSe_2/C was recorded in 0.5 M aqueous H_2SO_4 solution and presented in Fig. 3.6a. For comparison, the LSVs of pristine Co-MOF, CoSe_2 and commercial Pt/C (10 wt%) were recorded as well. Here, all the LSVs were iR compensated and the intrinsic catalytic properties of the electrocatalysts are discussed. Among the Co-MOF, CoSe_2 and CoSe_2/C hybrid structures, the CoSe_2/C showed better electrocatalytic activity showing only 240 mV overpotential at 10 mA/cm^2 of current density. On the other hand, the Co-MOF showed very poor electrocatalytic activity and CoSe_2 need 265 mV overpotential to reach the marked

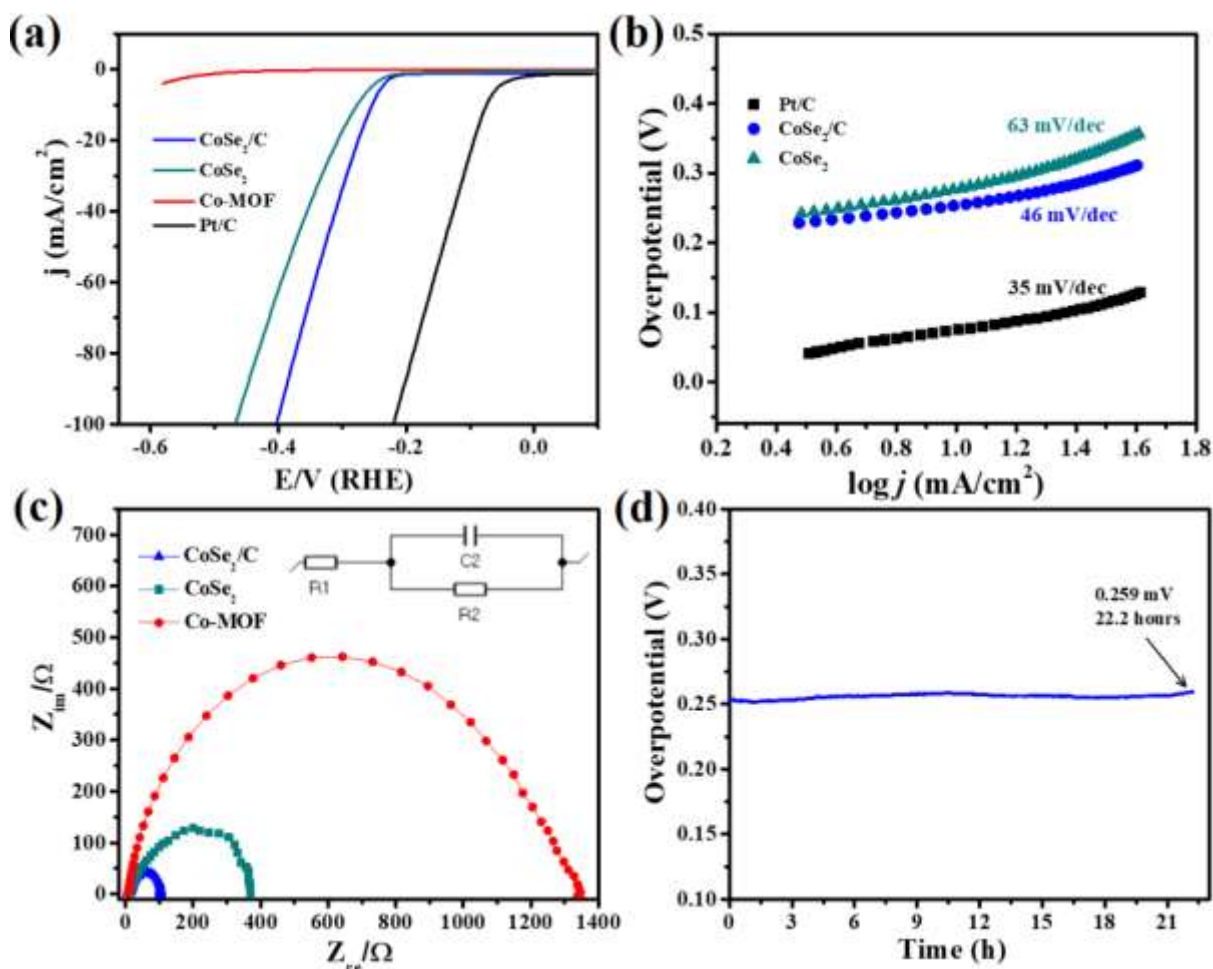


Figure 3.6 (a) Linear sweep voltammograms by CoSe₂/C, CoSe₂, Co-MOF and Pt/C showing HER in 0.5 M H₂SO₄, (b) corresponding Tafel slopes, (c) Nyquist impedance spectrum for CoSe₂/C, Co-MOF and CoSe₂ nanostructures and (d) stability of CoSe₂/C catalyst for HER at 10 mA/cm² current density.

current density. Additionally, the CoSe₂/C shows lower onset potential of 120 mV overpotential which is lowest among the samples studied here and also reported electrocatalysts (Table 3.1). Further, the Tafel slope of the sample was calculated from the Tafel plot (plot of log of current density against overpotential) derived from the LSVs. As shown in Fig. 3.6b, the Tafel slope of CoSe₂/C is 54 mV/dec which is smaller than the CoSe₂ (76 mV/dec.) and higher to that of the commercial Pt/C (31 mV/dec). This observation clearly suggests that the as prepared hybrid structure showed a faster reaction kinetics for HER and followed the Volmer-Heyrovsky process.^{14,31} Further the electrochemical impedance spectrum

Table 3.1 The electrocatalytic activity of CoSe₂/C hybrid with other reported nanostructures.

Catalysts	Electrolyte (Conc.)	Overpotential(mV) @10 mA/cm ⁻²	Tafel slope (mV/dec)	Reference
CoSe ₂ /C	0.5 M H ₂ SO ₄	-196	45.73	International journal of hydrogen energy, 2019, 44, 22787-22795
CoSe ₂ -CNT	0.5 M H ₂ SO ₄	-174	37.8	Small, 2017, 13, 1700068
CoSe ₂ /CF	1 M KOH	-95	52.0	Nano Research 2016, 9, 2234-2243
Carbon Supported Cobalt Diselenide	0.1 M KOH	-270	118.5	Journal of the Electrochemical Society, 2020 167 026507
CoSe ₂ /SDGC	0.5 M H ₂ SO ₄	-203	58.0	International journal of hydrogen energy, 2019, 44, 1344-13431
CoSe ₂ /NC-170	0.5 M H ₂ SO ₄	-159.	83.0	International journal of hydrogen energy 43 (2018) 17021 e17029
CoSe ₂ /C	0.5 M H ₂ SO ₄	-224.0	34.0	j. mater.sci,54.22 (2019): 14123-133
Fe-CoSe ₂ @NC	0.5 M H ₂ SO ₄	-143	40.0	ACS Sustainable Chem. Eng. 2018, 6, 8672-8678
CoSe₂/C	0.5 M H₂SO₄	-253.0	46.0	Present work

of the samples was recorded as Nyquist impedance (plot of imaginary impedance against real impedance) and presented in Fig. 3.6c. As can be seen to the corresponding Randle's equation, the EIS data can be fitted with three components as solution resistance (R_s), charge transfer resistance (R_{ct}) and double layer capacitance. Although all the samples show nearly similar R_s value but the CoSe_2/C hybrid possess lower value of R_{ct} compared to other samples. The long-term stability of the CoSe_2/C electrocatalyst for HER has been evaluated by using chronopotentiometry technique at 10 mA/cm^2 current density (Fig. 3.6d).

After 22 hours of electrolysis, a little change in overpotential of 8 mV has been realised demonstrating excellent durability. During the electrolysis process, the H_2 get generated from the working electrode surface in form of bubbles and shed there.

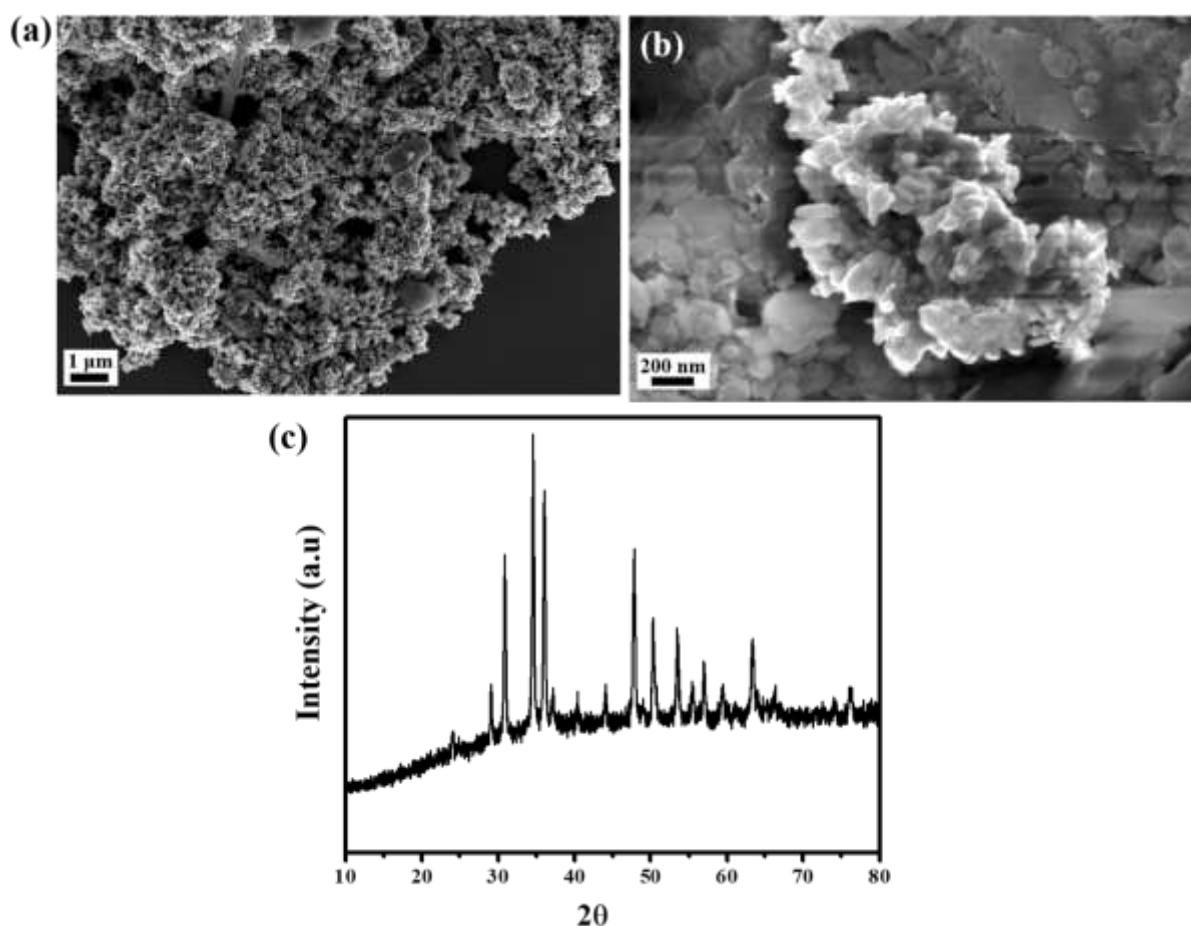


Figure 3.7 (a, b) FESEM and (c) PXRD of CoSe_2/C after HER stability test.

This makes the working electrode partially passivation to contact to the electrolyte thereby increasing the overpotential. The stability of the electrocatalyst has also been observed by analysing the diffraction pattern and microscopic images of the post stability HER sample. As can be seen in Fig. 3.7, there is no change in the diffraction pattern has been revealed and also the surface morphology remains intact demonstrating the robustness of the CoSe₂/C hybrid nanostructure towards HER.

The catalytic behaviour also attested by accessing the electrochemical active surface area of the electroactive materials. Since, the double layered capacitance is directly related to the ECSA (as per the equation 3.2), so at first the CVs were recorded at various sweep rates in a non-Faradaic potential region (Fig.3.8 a-c). Thereafter, by linear fitting the plot of cathodic and anodic current vs. sweep rate at a particular potential (-0.13 V vs. Ag/AgCl) gives the value of C_{dl} (Fig. 3.8 d-f).

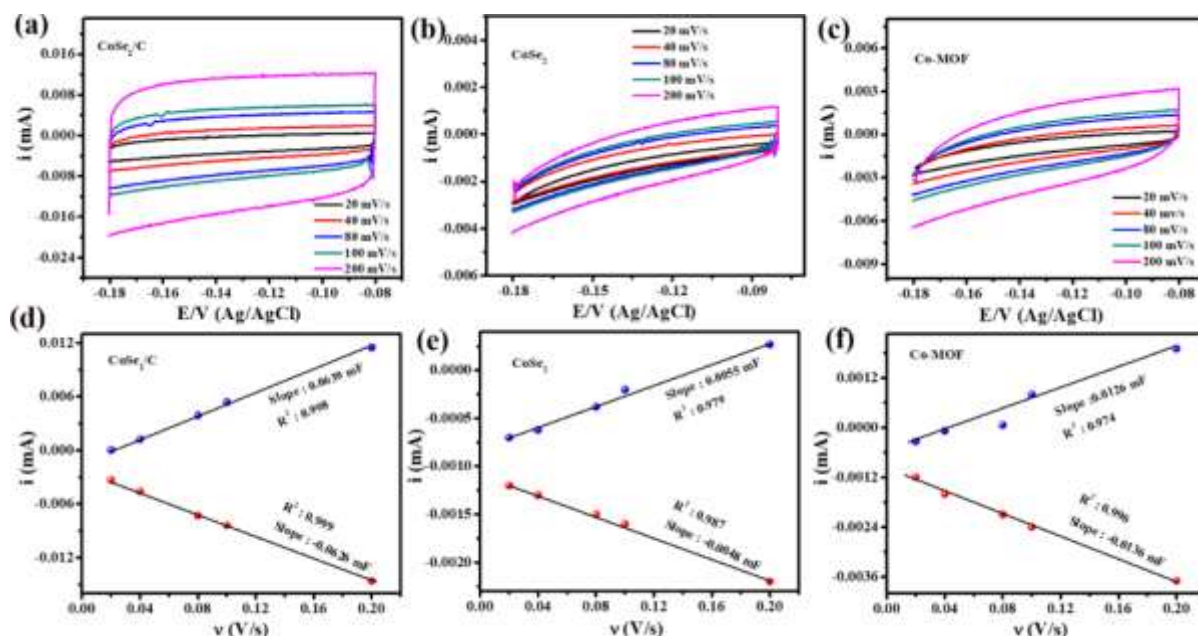


Figure 3.8 (a-c) Cyclic voltammograms showing the charging currents measured in a non-Faradaic region at a scan rate of 20, 40, 80,100, 200 mV/s respectively and (d-f) the plot of cathodic and anodic charging currents measured at -0.13 V (vs. Ag/AgCl) against scan rates for CoSe₂/C, CoSe₂ and Co-MOF respectively.

As predicted the CoSe₂/C showed higher ECSA value (5.325 cm²) compared to that of CoSe₂ (1.5 cm²) and Co-MOF (1.4 cm²) demonstrating the availability of more accessible surface to the electrolyte ions which in turn facilitate the electrocatalytic process and reduce the charge transfer resistance. With these observations, we can speculate that the introduction of graphitic carbon network on the CoSe₂ nanostructure not only reduce the charge transfer resistance but also avails more accessible surface to the electrolyte ions thereby facilitating the electrocatalytic HER performances. Not only the availability of more catalytic active centres in CoSe₂ but also the electron transport channel made by the conductive graphitic carbon in the CoSe₂/C hybrid synergistically improved the electrocatalytic HER activity.

Computational calculations and discussions

Structural Properties

Transition metal dichalcogenide, CoSe₂ exhibits orthorhombic crystal structure with space group of Pmnn. The unit cell has two Co atoms attached to six Se atoms having average Co-Se bond length as 2.4 Å. The optimized bulk CoSe₂ structure is as shown in Fig. 3.9a.

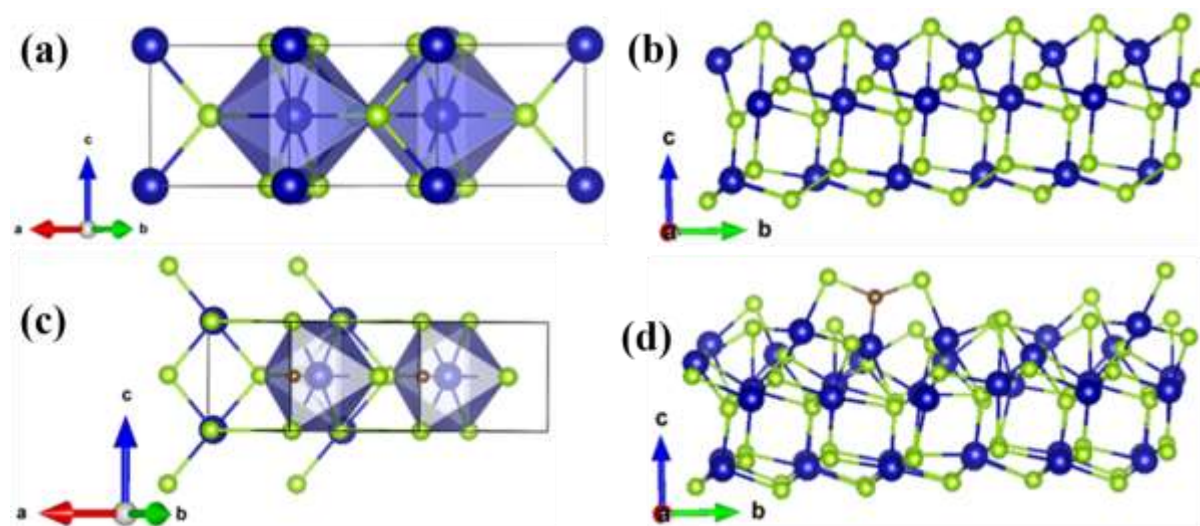


Figure 3.9 DFT optimized structure of (a) bulk CoSe₂ (b) CoSe₂ (101) layer (c) bulk CoSe₂ after C doping (d) CoSe₂ (101) layer after C doping; blue, green and brown represent Cobalt, Selenium and Carbon respectively.

Our optimized lattice parameters are $a = 4.88 \text{ \AA}$, $b = 5.82 \text{ \AA}$, $c = 3.66 \text{ \AA}$ and $\alpha = \beta = \gamma = 90^\circ$ matches well with experimentally observed values of $a = 4.84 \text{ \AA}$, $b = 5.72 \text{ \AA}$, $c = 3.60 \text{ \AA}$ and $\alpha = \beta = \gamma = 90^\circ$.³⁸ For HER study we have taken CoSe_2 layer along (101) plane corresponding to maximum intensity peak in X-ray diffraction pattern. Optimized CoSe_2 (101) layer is shown in Fig. 3.9b. To study the influence of C doping, we have doped one C atom for both bulk and (101) plane of CoSe_2 . The DFT optimized structures of C doped CoSe_2 are displayed in Fig. 3.9c and Fig. 3.9d. After doping of carbon into bulk CoSe_2 there is a variation of Co-Se bond length from initial value of 2.4 \AA to 2.7 \AA , resulting a net elongation of crystal structure which provides greater accessible surface area. This is in well accordance with the experimental observations. The corresponding total DOS plot is given in supplementary Fig. 3.10.

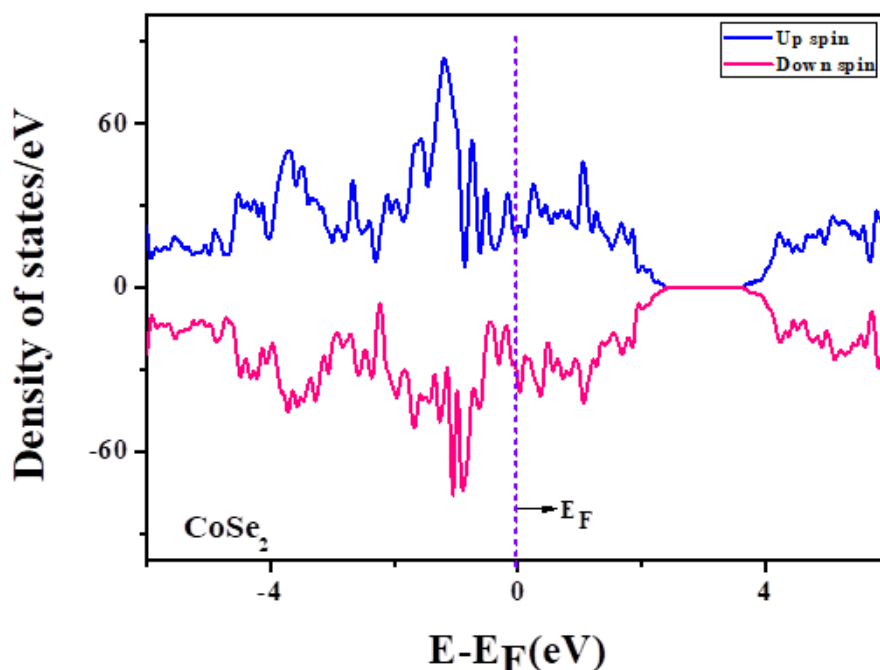


Figure 3.10 TDOS plot for CoSe_2 (101) layer.

Electronic Structure and orbital interactions

To get better understanding of electronic properties and orbital interactions for CoSe_2 and C doped material CoSe_2/C , the electronic Density of States (DOS) is presented. The total density of states (TDOS) plots for Bulk CoSe_2 (Upper panel) and doping CoSe_2/C (Lower panel) are

shown in Fig. 3.11. As depicted in Fig. 3.11 (Upper panel), the absence of energy bandgap and presence of finite states at fermi level on either side reveals the metallic nature of CoSe_2 .³²

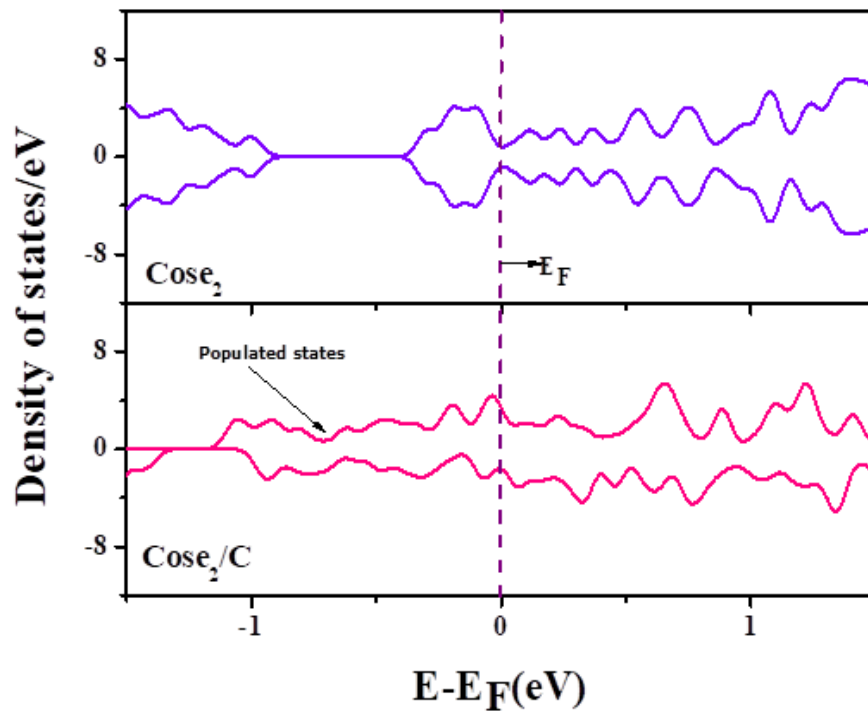


Figure 3.11 TDOS plot for Bulk CoSe_2 (Upper) and CoSe_2/C (Lower).

Also, the symmetry between up-spin and down-spin channels in the electronic states points towards a non-magnetic character. The total DOS for doped material CoSe_2/C in Fig. 3.11 shows appearance of new states close to Fermi level which may points towards increased conductivity of material after C doping.

Furthermore, the orbital interactions and direction of charge transfer has been analysed by plotting the partial density of states (PDOS) for 3d orbital of Co, 4p orbital of Se, and 2p orbital of C before and after doping as shown in Fig. 3.12. From Fig. 3.12a and 3.12b, it is observed that for the Co 3d and Se 4p orbitals for doped material CoSe_2/C , there is a reduction of states near Fermi level compared to that of pristine CoSe_2 which may be due to charge loss by CoSe_2 to C atom. Again, 2p orbital of C exhibits populated new states close to Fermi level for doped material CoSe_2/C compared to that of isolated C atom as displayed in Fig. 3.12c. These three

PDOS plots, indicates the overall charge loss experienced by CoSe_2 due to charge transferred to carbon adsorbed in the structure.

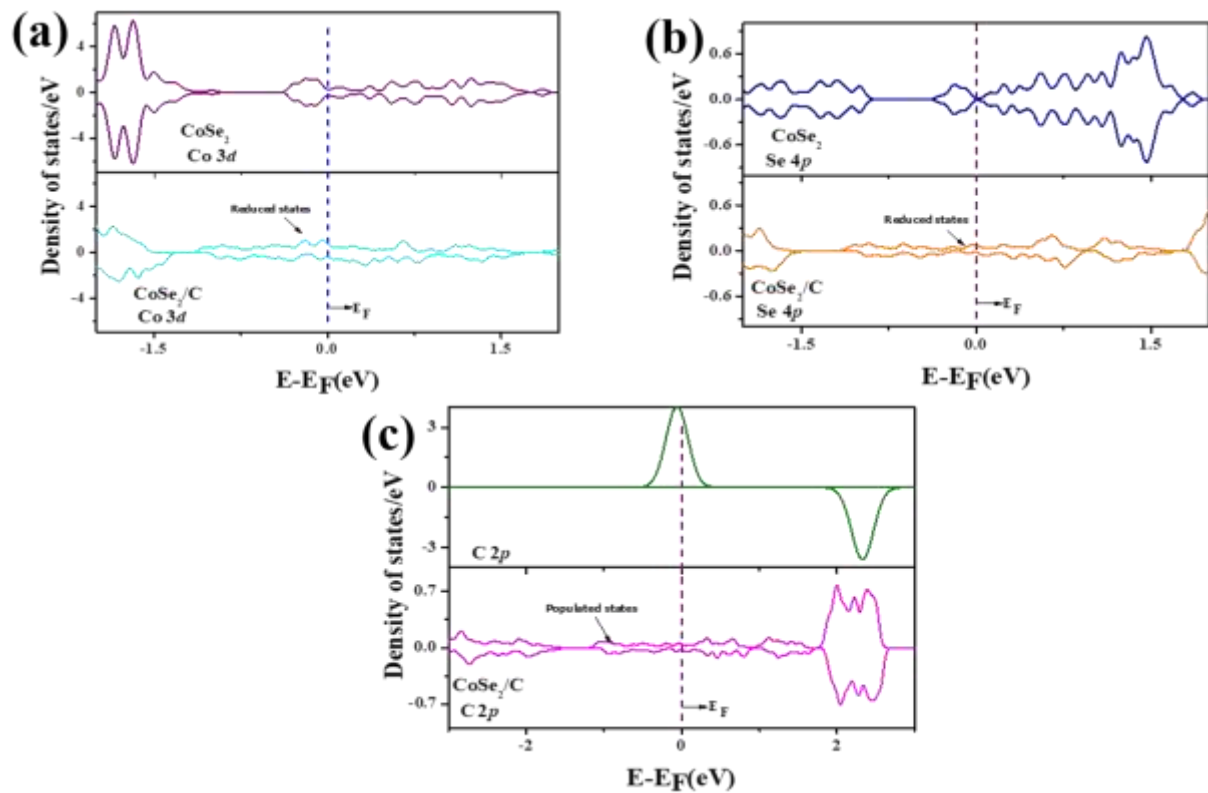


Figure 3.12 PDOS plot before and after C adsorption on CoSe_2 for (a) Co 3d orbital (b) Se 4p orbital and (c) C 2p orbital; dotted line shows Fermi level at zero eV.

To analyse charge transfer quantitatively, we have done Bader charge analysis for both CoSe_2 and doped material CoSe_2/C .³³

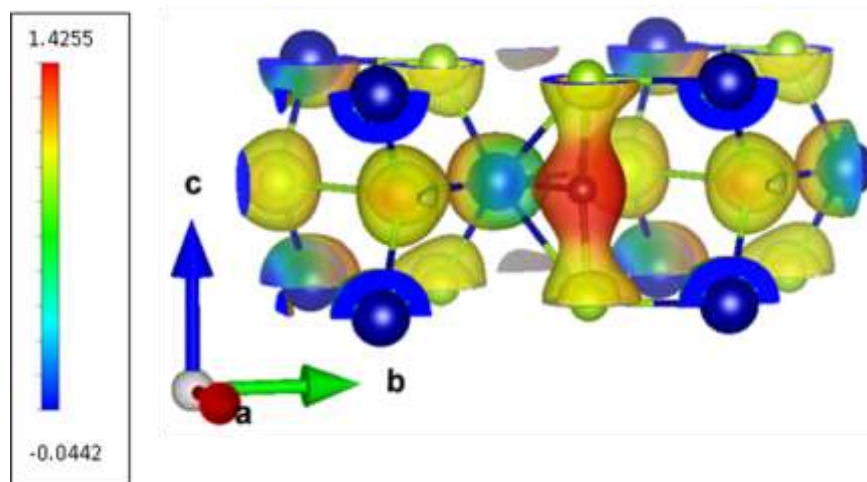
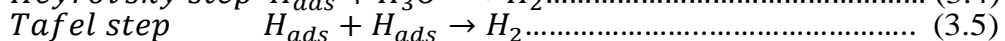
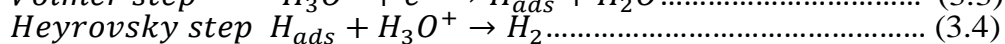
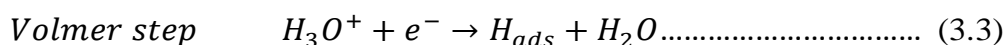


Figure 3.13 Charge density difference plot between CoSe_2/C and CoSe_2 for an iso value of $0.117e$; the charge gain region is shown in red and the charge loss region is shown in yellow.

The charge gain by C 2p orbital after doping is 3.17e while the adjacent atoms Se 4p orbital has maximum loss and Co 3d orbital shows negligible loss. It is in the similar line as that of qualitative PDOS analysis. To visualize the spatial distribution of charge density in 3D, the charge density difference between CoSe₂/C and CoSe₂ for an isovalue of 0.117e has been plotted as seen in Fig. 3.13. The red region is the charge gaining Carbon whereas the yellow region indicates the charge loss by CoSe₂.

Computation of overpotential for HER

The metallic character of CoSe₂ with the excess of electronic states near fermi level reveals its suitability as HER electrocatalyst. Also, these electronic states are populated on doping with the graphitised carbon. This may be the one of the reasons for improvement for HER activity. We have theoretically computed the overpotential for HER activity for both pristine CoSe₂ and the doped material CoSe₂/C. The HER involves electrochemical conversion of H⁺ to H₂ summing discharge step (eq. 3.3), electrochemical desorption step (eq. 3.4), and recombination step (eq. 3.5) as described below³⁴



The Gibb's free energy during hydrogen evolution is expressed as

$$\Delta G^H = E_{ads}^H + \Delta ZPE - T\Delta S \dots\dots\dots (3.6)$$

Here, E^H_{ads} indicate the hydrogen adsorption energy. The zero-point energy correction term (ΔZPE) can be calculated from vibrational frequency and the entropic terms (TΔS) are obtained from standard tables. The overpotential (η) for hydrogen evolution reaction is given by

$$\eta^{HER} = \Delta G^H / e \dots\dots\dots (3.7)$$

While, to identify the best stable possible site for hydrogen adsorption in CoSe₂ and doping CoSe₂/C, we have tried H adsorption on different sites and those with subsequent minimal ΔG^H are considered. The optimum adsorption configuration is depicted in Fig. 3.14.

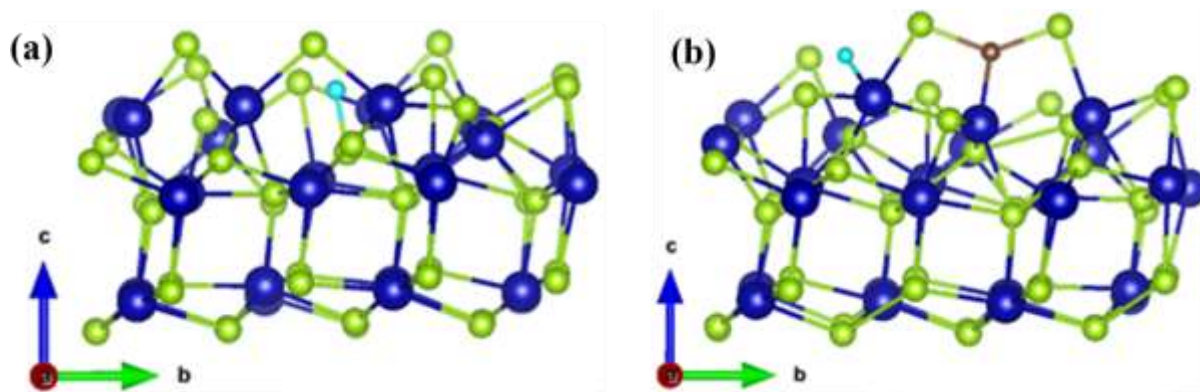


Figure 3.14 DFT optimized structure after H adsorption for (101) layer of (a) CoSe_2 (b) CoSe_2/C ; blue, green, brown and cyan represent Cobalt, Selenium, Carbon and Hydrogen.

Finally, we have predicted theoretical values for HER overpotential for hydrogen adsorption for both CoSe_2 and doped material CoSe_2/C (Fig. 3.15). The computed HER overpotential are 314 and 286 mV for CoSe_2 and for doped material CoSe_2/C respectively. We can see that the estimated overpotential for HER activity follows the qualitative trend of $\text{CoSe}_2 > \text{CoSe}_2/\text{C}$, justifying the superior HER activity for CoSe_2/C as measured in the experiment.

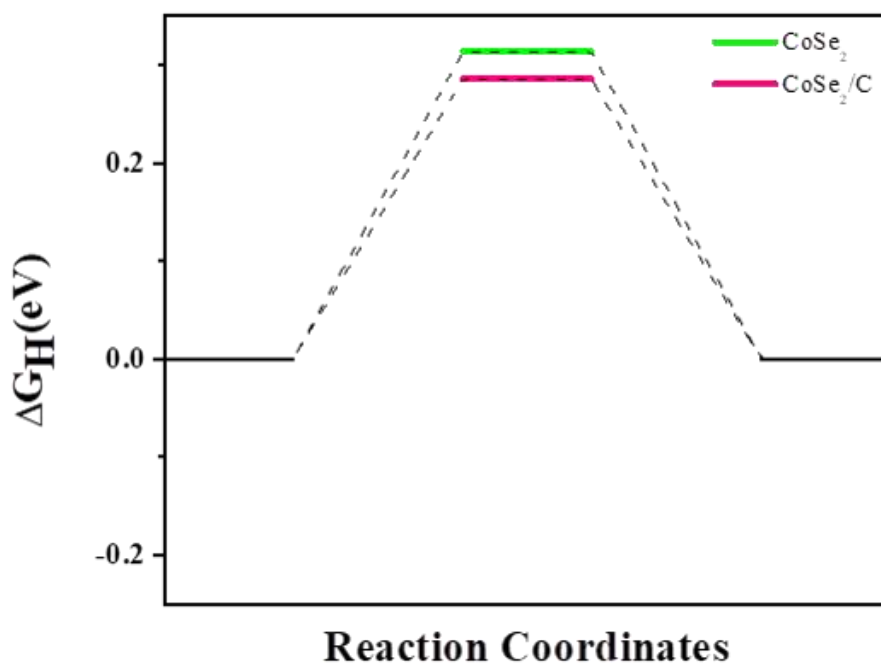


Figure 3.15 Reaction coordinates for HER of (101) layer of CoSe_2 and CoSe_2/C .

A comparison of overpotential for HER activity between computational and experimental data is presented in Table 3.2. Here the outstanding catalytic activity and excellent durability of the CoSe₂/C can be assigned to the (a) uniform one dimensional rod like surface morphology, (b) the encapsulation of CoSe₂ nanorods into the graphitic carbon network creates channels for electrolyte ion movement thereby increases the electrocatalytic accessible surface area, (c) the synergy among the CoSe₂ nanorods and graphitic carbon increases the overall conductivity of the electrode material thereby reducing the charge transfer resistance. Therefore, we prospect that this synthesis process can be scaled up and the CoSe₂/C hybrid nanostructure can be employed as cathode electrocatalyst for HER in future electrolyser.

Table 3.2 Comparison of overpotential between experimental and computational study.

System	Experimental η @10 mA/cm ² (mV)	Theoretical η @10 mA/cm ² (mV)
CoSe ₂	276	314
CoSe ₂ /C	253	286

3.9 Conclusion

In this work, we have successfully synthesized CoSe₂ nanorods encapsulated in graphitic carbon network using Co-MOF [Co₄(BTC)₃(BIm)₆] as the starting precursor. After the physicochemical characterizations, the CoSe₂/C hybrid nanostructure were used as the active electrode material and the electrocatalytic activity towards HER has been demonstrated. The as formed carbon network creates channels for the ease passage of electrolyte ions and increases the overall conductivity thereby increasing the electrocatalytic activity. As a result, the CoSe₂/C hybrid needs only 240 mV of overpotential to deliver the benchmarked current density (10 mA/cm²) and proceeds through a Volmer-Heyrovsky reaction path with a Tafel slope of 54 mV/dec. Moreover, the hybrid showed robust catalytic durability with only increase of 8 mV overpotential to deliver the benchmarked current density after 22 hours of electrolysis.

Further, using DFT simulations, the structural, electronic properties and computed the overpotential for HER activity for CoSe₂, and for doped material CoSe₂/C has been analysed. The improved HER activity for CoSe₂/C is due to the increased conductivity and electrocatalytic surface area due to interactions of C on CoSe₂ facilitated by charge transfer from CoSe₂ to carbon. The computed overpotential for HER activity matches nicely with the experimental data.

3.10 References

- 1 X. Zou and Y. Zhang, *Chem. Soc. Rev.*, 2015, **44**, 5148–5180.
- 2 S. Anantharaj, S. R. Ede, K. Sakthikumar, K. Karthick, S. Mishra and S. Kundu, *ACS Catal.*, 2016, **6**, 8069–8097.
- 3 J. Wang, W. Cui, Q. Liu, Z. Xing, A. M. Asiri and X. Sun, *Adv. Mater.*, 2016, **28**, 215–230.
- 4 I. H. Kwak, H. S. Im, D. M. Jang, Y. W. Kim, K. Park, Y. R. Lim, E. H. Cha and J. Park, *ACS Appl. Mater. Interfaces*, 2016, **8**, 5327–5334.
- 5 T. Tian, L. Huang, L. Ai and J. Jiang, *J. Mater. Chem. A*, 2017, **5**, 20985–20992.
- 6 M. A. Lukowski, A. S. Daniel, C. R. English, F. Meng, A. Forticaux, R. J. Hamers and S. Jin, *Energy Environ. Sci.*, 2014, **7**, 2608–2613.
- 7 M. S. Faber, R. Dziedzic, M. A. Lukowski, N. S. Kaiser, Q. Ding and S. Jin, *J. Am. Chem. Soc.*, 2014, **136**, 10053–10061.
- 8 D. Merki and X. Hu, *Energy Environ. Sci.*, 2011, **4**, 3878–3888.
- 9 X. Wang, F. Li, W. Li, W. Gao, Y. Tang and R. Li, *J. Mater. Chem. A*, 2017, **5**, 17982–17989.

- 10 M. R. Gao, X. Cao, Q. Gao, Y. F. Xu, Y. R. Zheng, J. Jiang and S. H. Yu, *ACS Nano*, 2014, **8**, 3970–3978.
- 11 S. Li, S. Peng, L. Huang, X. Cui, A. M. Al-Enizi and G. Zheng, *ACS Appl. Mater. Interfaces*, 2016, **8**, 20534–20539.
- 12 D. Kong, J. J. Cha, H. Wang, H. R. Lee and Y. Cui, *Energy Environ. Sci.*, 2013, **6**, 3553–3558.
- 13 J. Deng, P. Ren, D. Deng, L. Yu, F. Yang and X. Bao, *Energy Environ. Sci.*, 2014, **7**, 1919–1923.
- 14 H. Lu, Y. Zhang, Y. Huang, C. Zhang and T. Liu, *ACS Appl. Mater. Interfaces*, 2019, **11**, 3372–3381.
- 15 H. Bin Wu and X. W. Lou, *Sci. Adv.*, 2017, **3**, 1–17.
- 16 H. Wang, Q. L. Zhu, R. Zou and Q. Xu, *Chem*, 2017, **2**, 52–80.
- 17 W. Wang, X. Xu, W. Zhou and Z. Shao, *Adv. Sci.*, 2017, **4**, 1600371.
- 18 S. Liu, Z. Wang, S. Zhou, F. Yu, M. Yu, C. Y. Chiang, W. Zhou, J. Zhao and J. Qiu, *Adv. Mater.*, 2017, **29**, 1–10.
- 19 M. K. Sahoo, A. K. Samantara and J. N. Behera, *Inorg. Chem.*, 2020, **59**, 12252–12262.
- 20 R. K. Tiwari and J. N. Behera, *CrystEngComm*, 2018, **20**, 6602–6612.
- 21 P. E. Blochl, *Phys. Rev. B: Condens. Matter Mater. Phys.*, 1994, **50**, 17953–17979.
- 22 J. P. Perdew, J. A. Chevary, S. H. Vosko, K. A. Jackson, M. R. Pederson, D. J. Singh and C. Fiolhais, *Phys. Rev. B: Condens. Matter Mater. Phys.*, 1993, **48**, 4978.
- 23 J. M. Shi, F. M. Peeters, G. Q. Hai and J. T. Devreese, *Phys. Rev. B*, 1991, **44**, 5692–5702.

- 24 J. D. Monkhorst and H. J. Pack, *Phys. Rev. B: Solid State*, 1976, **13**, 5188–8192.
- 25 J. Yang, G. H. Cheng, J. H. Zeng, S. H. Yu, X. M. Liu and Y. T. Qian, *Chem. Mater.*, 2001, **13**, 848–853.
- 26 J. Yang, H. Gao, S. Men, Z. Shi, Z. Lin, X. Kang and S. Chen, *Adv. Sci.*, 2018, **5**, 1-13
- 27 J. Yang, H. Gao, D. Ma, J. Zou, Z. Lin, X. Kang and S. Chen, *Electrochim. Acta*, 2018, **264**, 341–349.
- 28 X. Zhao, H. Yang, P. Jing, W. Shi, G. Yang and P. Cheng, *Small*, 2017, **13**, 1603279.
- 29 A. K. Samantara, S. Chandra Sahu, A. Ghosh and B. K. Jena, *J. Mater. Chem. A*, 2015, **3**, 16961–16970.
- 30 A. K. Samantara and S. Ratha, *Metal oxides/chalcogenides and composites : emerging materials for electrochemical water splitting*, springer, ISBN-9783030248604, 2019.
- 31 S. S. Sekhon, P. Kaur, Y. H. Kim and S. S. Sekhon, *npj 2D Mater. Appl.*, 2021, **5**, 21.
- 32 B. Chakraborty, P. Ray, N. Garg and S. Banerjee, *Int. J. Hydrogen Energy*, 2021, **46**, 4154–4167.
- 33 J. C. McGlynn, T. Dankwort, L. Kienle, N. A. G. Bandeira, J. P. Fraser, E. K. Gibson, I. Cascallana-Matías, K. Kamarás, M. D. Symes, H. N. Miras and A. Y. Ganin, *Nat. Commun.*, 2019, **10**, 4916.
- 34 D. Lu, X. Ren, L. Ren, W. Xue, S. Liu, Y. Liu, Q. Chen, X. Qi and J. Zhong, *ACS Appl. Energy Mater.*, 2020, **3**, 3212–3219.

CHAPTER-4

Electrochemically activated prussian blue analogue (PBA) derived amorphous CoB nanostructures: Efficient electrocatalyst for oxygen evolution reaction

4.1 Abstract

4.2 Introduction

4.3 Motivation of the work

4.4 Experimental section

4.4.1 Synthesis of Co- PBA

4.4.2 Synthesis of CoB@300, CoB@450, CoB@550 and CoB@650

4.5 Characterization

4.6 Electrochemical measurements

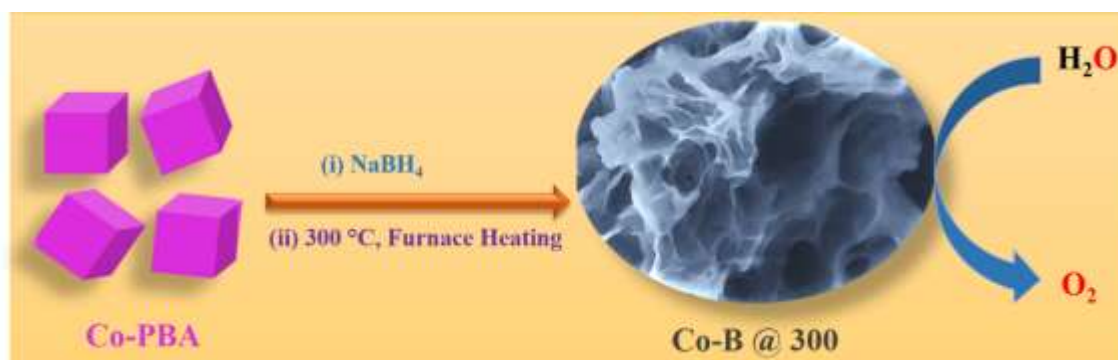
4.7 Calculations of ECSA and R_f

4.8 Results and discussions

4.9 Conclusions

4.10 References

4.1 Abstract



This chapter describes that the oxygen evolution reaction being a kinetically sluggish half-cell reaction plays an important role in tuning the efficiency of various electrochemical energy conversion systems. However, this process can be facilitated by manipulating the composition and morphology of the electrocatalyst. Here, by tuning the annealing temperature, a series of cobalt boride (CoB@300, CoB@450, CoB@550 and CoB@650) is synthesized from a metal-organic framework Prussian blue analogue (PBA) following boronization. In alkaline electrolyte, the in-situ surface transformation of the boride working electrode to the corresponding metaborite and cobalt oxyhydroxide took place and thereafter acted as the active catalytic sites for OER. Interestingly, the amorphous form of the cobalt boride (i.e., CoB@300) presents many folds catalytic activity compared to those of the crystalline CoB and commercial RuO₂ requiring only 290 mV overpotential to reach the benchmarked 10 mA/cm² current density and the trend follows the order as CoB@300 > CoB@450 > CoB@550 > CoB@650 > PBA. The dominant catalytic activity of the amorphous cobalt boride nanostructure is attributed particularly to its amorphous nature and synergy between the in-situ formed catalytic active centres (metaborites and cobalt oxyhydroxide).

4.2 Introduction

The oxygen evolution reaction (OER) plays an important role in many of the electrochemical energy conversion systems. Particularly, as an anodic half-cell reaction, (i) it monitors the efficiency of the hydrogen evolution reaction (cathodic half-cell reaction) of a water electrolyser, (ii) it is an indispensable process for metal-air batteries and (iii) fuel cells.^{1,2} But the poor performance of these systems is witnessed by the higher OER overpotential which is due to its sluggish reaction kinetics and complex reaction mechanism.³ But there is a possibility to minimize the overpotential by tuning the composition, crystal structure and morphology of the electrocatalyst. As an efficient electrocatalyst, the Ir/Ru based nanostructures and bulk materials are the front side candidates, but their high cost, poor catalytic durability and non-sustainability in harsh alkaline condition demands to explore new catalyst materials.^{4,5} In this regard, the nickel and cobalt based nanostructures like selenides, sulphides, phosphides and borides have been extensively explored as the active electrocatalyst for OER.^{3,6-8} However, the designing of earth abundant electrocatalysts for the OER still is an ongoing challenge to streamline the smooth running of electrolyser. As per the recent literatures, the transition metal borides show better catalytic activity over the chalcogenides and oxides towards electrochemical splitting of water.^{9,10} However, the method of synthesis and crystal structure plays an important role in tuning the catalytic performance. Generally, the borides can be synthesized either by annealing the precursors (oxides/hydroxides) with boron contained molecules (generally boric acid) at higher temperature or by reducing the precursor with a suitable boron containing reducing agent (i.e., NaBH_4).¹¹ As compared to high temperature annealing, the chemical reduction method is a facile procedure where the structure and composition of the resulted borides can be tuned.^{7,12,13} In most of the synthetic strategies, the borides were synthesized either through chemical reduction using the metal salts ($\text{CoCl}_2 \cdot 6\text{H}_2\text{O}$,

NiCl₂.6H₂O, etc.) as starting material or solid state boronization. In a particular work, Wang's group have prepared nickel foam supported Ni, Co-bimetallic boride by reducing the CoCl₂ and NiCl₂ with aqueous NaBH₄ solution.¹⁰ Li et al. have prepared Ni₃B by solid state boronization coupled with *in situ* electrochemical etching.⁹ Some reports follow the chemical reduction of metal chlorides coupled with high temperature annealing under vacuum.¹⁴ Although, there have been many reports on the synthesis of transition metal borides, new strategies are needed to develop the synthesis of highly catalytic efficient borides in a cost effective and facile process. Recent focus has been given to derive different nanostructured materials using metal-organic frameworks (MOFs) as starting material.^{3,15,16} Particularly, the Prussian blue analogue (PBA, a sort of metal-organic framework family) are used as the starting precursor to derive various metal nanostructures like hydroxides, phosphides and chalcogenides and also for the synthesis of mono and bimetallic borides.^{7,17,18} However, the effect of chemical reduction and annealing temperature on the crystal structure, morphology and electrocatalytic activity is rarely reported and required to explore to complete the proposed reaction strategy. In this work, we present a novel strategy for improvising the electrocatalytic activity of cobalt borides (CoB) by tuning the annealing temperature, which is accomplished by the formation of CoB via chemical reduction of Co-Prussian blue analogue (Co-PBA) integrated with high temperature annealing. Four different samples at different annealing temperature namely CoB@300, CoB@450, CoB@550 and CoB@650 have been synthesized and their catalytic properties towards OER have been studied. The annealing temperature as well as the electrochemical activation of the resulted boride plays the important role in tuning the electrocatalytic efficiency of the CoB. Here, the primary CoB acts as the pre-electrocatalyst and surface activated CoB as the real electrocatalyst for OER. The activation process transforms the surface of CoB electrode to a layer consisting of metaborate and cobalt oxyhydroxide as the catalytically active phase. The electrochemically activated amorphous

CoB@300 shows better OER electrocatalysis in terms of lower overpotential (required to deliver the benchmarked current density) and catalytic durability with increase of only 15 mV overpotential after 15 hours of electrolysis.

4.3 Motivation of the work

The unique chemical composition of Prussian blue material makes it a promising candidate for electrochemical application. Also, due to presence of special kind of bonding, PBA are considered as a new class of metal-organic framework materials. Hence, due to availability of unique morphology and reactivity, Prussian blue analogue (PBA) materials as well as their derivatives are extensively investigated as precursors or template to develop new functional nanomaterials. So, we were able to synthesise Co-B varying the temperature from 300 to 650 °C using Co-PBA as sacrificial template via a chemical redox approach followed by annealing process. The unique cubical morphology of Co-PBA fused to spherical nanoparticles and fused nanoparticles on increasing the temperature. Furthermore, we explore its electrocatalytic properties towards oxygen evolution reaction in alkaline conditions.

4.4 Experimental Section

4.4.1 Synthesis of Co-Prussian blue analogue (Co-PBA)

The cobalt Prussian blue analogue $\text{Co}_3[\text{Co}(\text{CN})_6]_2 \cdot x\text{H}_2\text{O}$ (Co-PBA), has been prepared by a co-precipitation method. At first, solution-A was prepared by adding 0.175g of Cobalt (II) nitrate hexahydrate and 0.265g of trisodium citrate to 10 ml water in a 100 ml round bottom flask. On the other hand, solution-B was prepared by dissolving 0.133g of potassium hexacyano cobaltate (III) in 10 ml water taken in a beaker. Thereafter, the solution-B was added to the stirred solution-A in a dropwise manner. The resulting Co-PBA precipitate was allowed to stand in the mother liquor for 24 hours, collected by filtration, washed and stored for further characterization and electrocatalysis study.

4.4.2 Synthesis of CoB

After synthesis of Co-PBA, the cobalt boride (CoB) was prepared by using a chemical reduction method followed by annealing in an inert atmosphere. 60 mg of the as-prepared Co-PBA was added to 20 ml water in a 100 ml beaker and stirred for 15 minutes. To this solution, 10 ml of freshly prepared 0.5M NaBH₄ (0.214g in 10 ml) solution was added in a dropwise manner. The black coloured precipitates thus formed were washed by absolute ethanol and deionised water repeatedly by centrifugation and dried overnight at 60 °C. Thereafter, the collected black powder was annealed at 300, 450, 550 and 650 °C for 4 hours under argon atmosphere. Based on the annealing temperature (300, 450, 550 and 650 °C), the samples are named as CoB@300, CoB@450, CoB@550 and CoB@650 respectively. After cooling down, the samples were washed with ethanol and water and stored for further characterization and electrocatalysis study.

4.5 Characterization

The phase and purity of all the samples were analysed by powder X-ray diffraction (Bruker D8 Advance diffractometer equipped with a Cu-K α radiation source ($\lambda = 1.5418 \text{ \AA}$)). The surface morphology was determined by FESEM (Merlin Compact with a GEMINI-I electron column, Zeiss Pvt. Ltd, Germany) and high-resolution transmission electron microscopy HRTEM, JEOL 2100F, operated at 200 kV. For the HRTEM analysis, a very dilute suspension of the synthesized sample in a mixture of ethanol and water was prepared by sonication and casted onto a 200-mesh carbon coated copper grid. The grid was properly dried under table lamp and used for the morphology analysis. The elemental composition of the sample was performed by X-ray photoelectron spectroscopy (PHI Versa Probe III).

4.6 Electrochemical measurement

All the electrochemical measurements were performed in a two compartment three electrode electrochemical cell using Biologic electrochemical workstation (SP-200). Here, the glassy carbon rotating disk electrode (GCRDE), bare platinum wire and alkaline mercury-mercury

oxide electrode (Hg/HgO) were used as working electrode, counter electrode and reference electrode respectively. Prior to each measurement, the GCRDE was well polished with an alumina slurry (1, 0.3, 0.05 μ of alumina in deionised water), washed in a bath sonication and dried in a vacuum desiccator. Thereafter, the GCRDE was casted by the catalyst ink (prepared by dispersing the sample in absolute ethanol and Nafion) maintaining the loading of 0.25 mg/cm². The electrocatalytic performance of the sample towards OER was analysed by recording the linear sweep voltammograms (LSV) and cyclic voltammograms (CV) in 1.0 M aqueous KOH electrolyte. In this work, all the measurements were performed with alkaline Hg/HgO reference electrode and presented in reversible hydrogen electrode (RHE) as per the following Nernst equation,

$$E_{RHE} = E_{Hg/HgO} + 0.059 \text{ pH} + E_{Hg/HgO}^0 \dots \dots \dots (4.1)$$

Here, pH of 1.0 M KOH electrolyte was measured to be 14. The $E_{Hg/HgO}^0$ is the standard reference electrode and its value is 0.098 V.

4.7 Calculation of ECSA and R_f

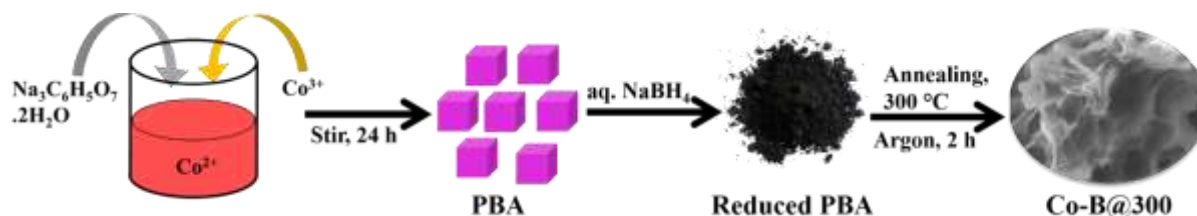
Further, the profound electrocatalytic activity is also supported by analysing certain parameters like electrochemical accessible surface area (ECSA), roughness factor (R_f) and turnover frequency (TOF) etc. For ECSA, at first the CVs at different sweep rates have been recorded in a non-Faradaic region of the potential window and the ECSA was determined from the double layer capacitance (C_{dl}) as per the following equation,

$$ECSA = \frac{C_{dl}}{C_s} \dots \dots \dots (4.2)$$

Here, C_s is the specific capacitance (40 μ F/cm²) of an atomically smooth metal oxide surface in alkaline electrolyte. From the ECSA, the roughness factor (R_f) was calculated by dividing the geometrical surface area of the working electrode.

4.8 Result and discussion

The CoB nanostructure derived from the Co-PBA has been performed via a simple two steps method as presented in scheme 4.1.



Scheme 4.1 Synthesis of PBA and PBA derived CoBs.

Here, the Co-Prussian blue analogue (PBA) was prepared by a coprecipitation method and used as the starting precursor and template for the synthesis of CoB. The crystallinity of Co-PBA, confirmed by X-ray powder diffraction analysis (Fig. 4.1a), shows a typical powder diffraction pattern of a PBA, which can be indexed as face centred cubic phase with space group $Fm\bar{3}m$ (PDF#01-077-1161).

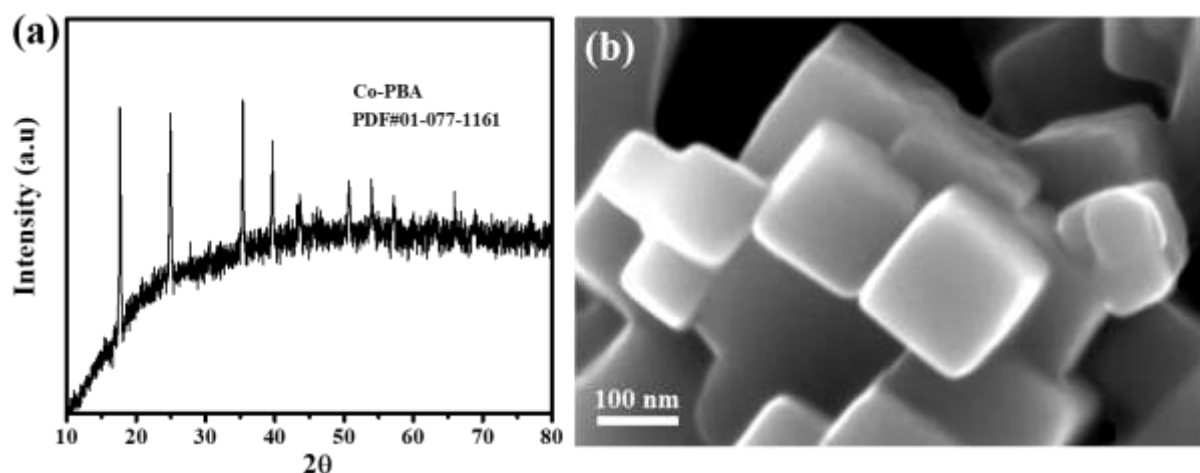


Figure 4.1 (a) X-ray diffraction pattern and (b) FESEM for the Co-PBA.

The CoB was then prepared by a two-step method where the first step involves the treatment of PBA with NaBH_4 followed by annealing at variable temperatures in an inert atmosphere (300, 450, 550 and 650 °C) in the second step. The crystallinity of the as-prepared borides has been analysed by powder X-ray diffraction as presented in Fig. 4.2a. However, the diffraction

peaks are observed to be vanished after annealing the reduced Co-PBA at 300 °C (Fig. 4.2b and c). This clearly demonstrates the amorphous nature of the CoB@300 and might be due to the lattice distortion caused by the insertion of boron and annealing.^{19–21}

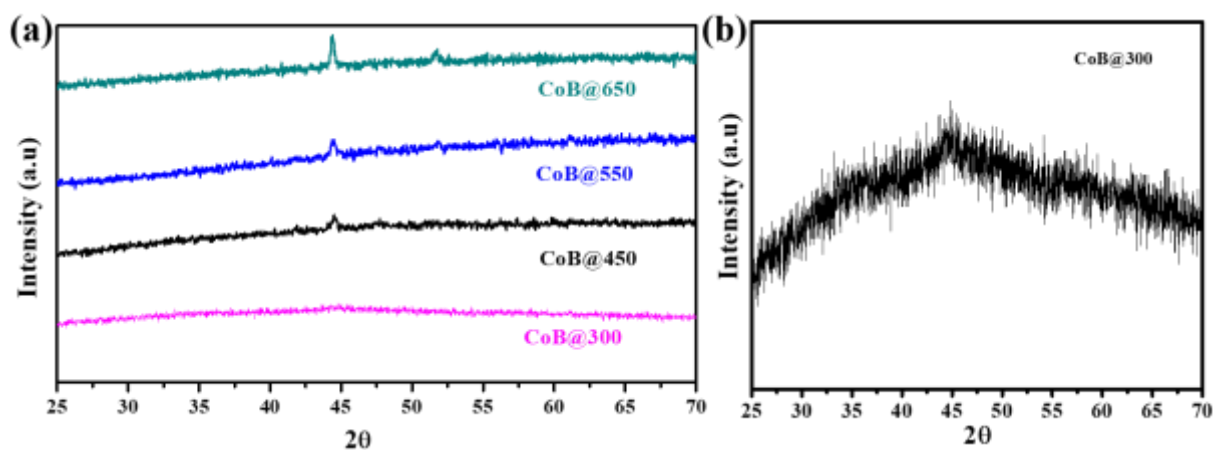


Figure 4.2 (a) Powder X-ray diffraction pattern of CoB@300, CoB@450, CoB@550 and CoB@650 and (b) the PXR pattern for CoB@300 showing a broad peak at 2θ of 45° .

However, on increasing the annealing temperature from 450 °C to 650 °C, the crystalline behaviour resumed with a significant diffraction peak at $2\theta = 45^\circ$ (assigned to the 021 plane of CoB) suggesting the formation of amorphous CoB at 300 °C and crystalline CoB at 450, 550 and 650.^{22,23} As per the literature survey, the borides of Ni and Co show an unusual metal-metalloid nanostructure with tiny metal nano crystallites rooted in a matrix of amorphous phase of borides (i.e., metal borides, borates and oxides).^{10,24} In such crystalline structure, the B-containing species act as a stabilizer and protect the nanocrystalline metallic core from growth and oxidation. Before the reduction with NaBH_4 , the Co-PBA has distinct cube like morphology (Fig. 4.1b). However, the amorphous CoB@300 has a thin sheet like surface structure, while the crystalline forms possess small nanoparticles and fused structures (Fig. 4.3). At elevated temperature, the agglomeration of Co-B occurs leading to significant change in morphology, also responsible for decrease in electrocatalytic behaviour.¹⁰ This layered structure improves the accessibility as well as adsorption of electrolyte ion thereby enhancing

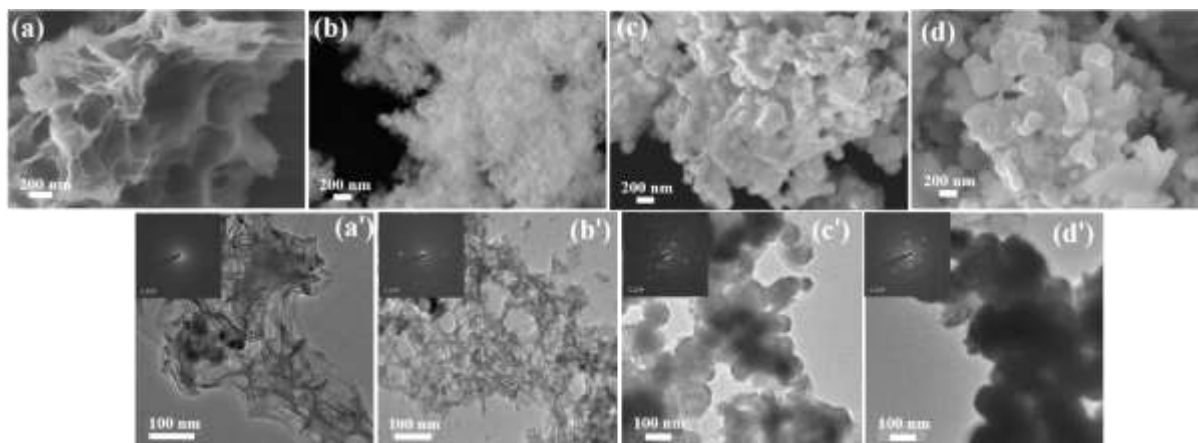


Figure 4.3 (a–d) FESEM and (a’–d’) TEM for CoB@300, CoB@450, CoB@550 and CoB@650. The inset in (a’–d’) shows the corresponding SAED patterns.

the electrocatalytic performance. The high-resolution surface morphology and crystalline structure of all the samples were further verified from the HRTEM and SAED pattern as shown in Fig. 4.3 a' to d'. Though at higher annealing temperature, crystalline behaviour of the CoB was resumed but no distinct well-defined lattice spacing was found from the HRTEM analysis. It clearly reveals the formation of both the amorphous and crystalline CoB. The existence of fused concentric rings in CoB@300 and rings with dot pattern in CoB@450, CoB@550 and CoB@650 revealed the amorphous nature and crystalline nature supporting the PXRD pattern (insets of Fig. 4.3 a' to d'). The EDS and elemental mapping suggest the presence of Co, B, C, N and O in all the samples studied here (Fig. 4.4).

Further, the elemental valence state and surface chemical composition of the CoB@300 has been analysed by X-ray photoelectron spectroscopy (Fig. 4.5). The high resolution XPS spectrum of Co 2p shows four peaks at binding energies 780.8, 786.3, 796.1 and 802.8 eV (Fig. 4.5a). The peaks at 780.8 and 796.1eV are ascribed to the Co 2p^{3/2} and Co 2p^{1/2} of Co (II) respectively, while 786.3 and 802.7 eV are the satellites peaks. The B 1s spectra of CoB@300 shows two distinct peaks at 184.1 and 191.6 eV (Fig. 4.5b). The former one is assigned to the interaction of B with Co, in CoB again conforming the formation of CoB after following the

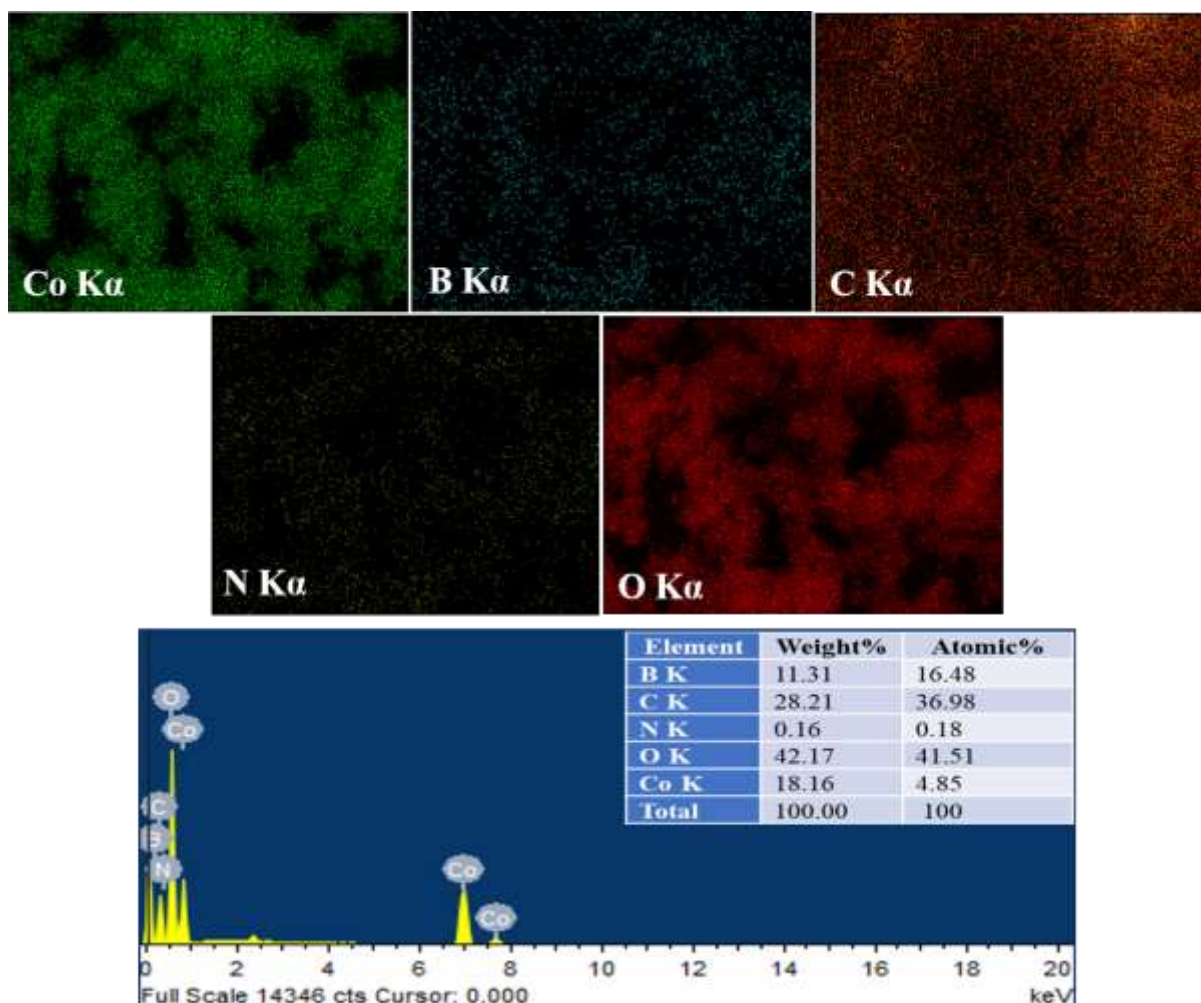


Figure 4.4 Elemental mapping for CoB@300. The EDS showing the presence of different elements in CoB

boronization process. Since the borides are highly prone to oxidise on exposure to air, the second peak (191.6 eV) found is associated to the different oxide species of boron as observed in the reports published elsewhere. The high-resolution C 1s spectrum can be deconvoluted into two different peaks corresponding to the C=C/C-C (284.6 eV) and C=N (288.3 eV) species (Fig. 4.5c). Further, the N 1s spectrum shows the presence of nitrogen (399.1 eV) species which might be due to the PBA template used for the synthesis of CoB (Fig. 4.5d). After synthesis and characterization, the catalytic activity of all the samples towards the oxygen evolution reaction has been demonstrated. It has been observed that calcination temperature has a profound effect on electrocatalytic activity of the borides. Therefore, all the

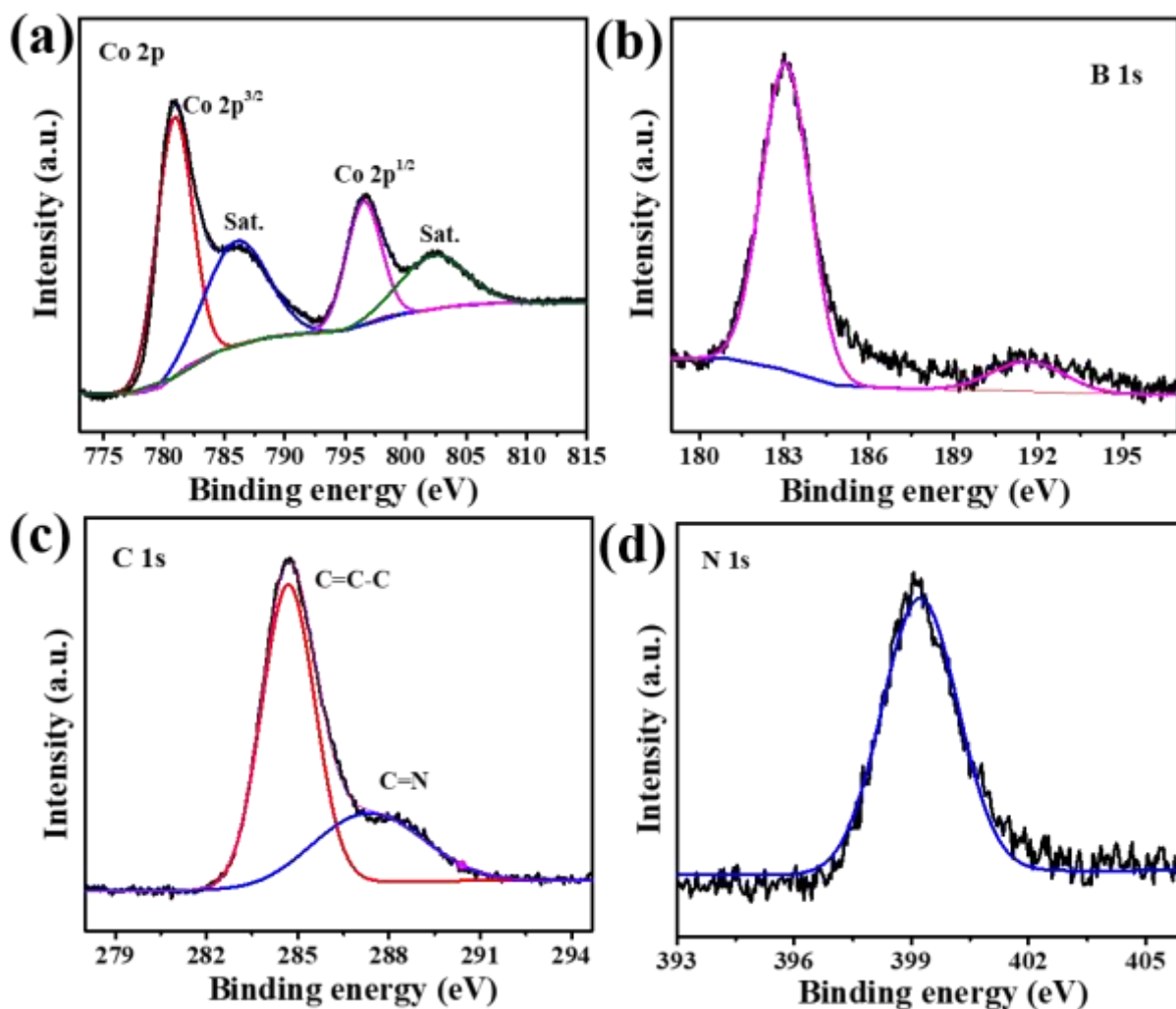


Figure 4.5 High-resolution X-ray photoelectron spectrum of (a) Co 2p, (b) B 1s, (c) C 1s and (d) N 1s of CoB@300.

samples i.e., CoB@300, CoB@450, CoB@550 and CoB@650 were casted on glassy carbon working electrode and their electrocatalytic activity was recorded in 1 M KOH electrolyte. Fig. 4.6a shows the polarization curves of CoB annealed at different temperatures, RuO₂ and the PBA modified electrode at 5 mV/s sweep rate with an electrode rotation of 1600 rpm. As can be seen, the CoB@300 shows better catalytic activity and the trend follows the order as CoB@300 > CoB@450 > CoB@550 > CoB@650 > PBA. The CoB@300 catalyses the OER

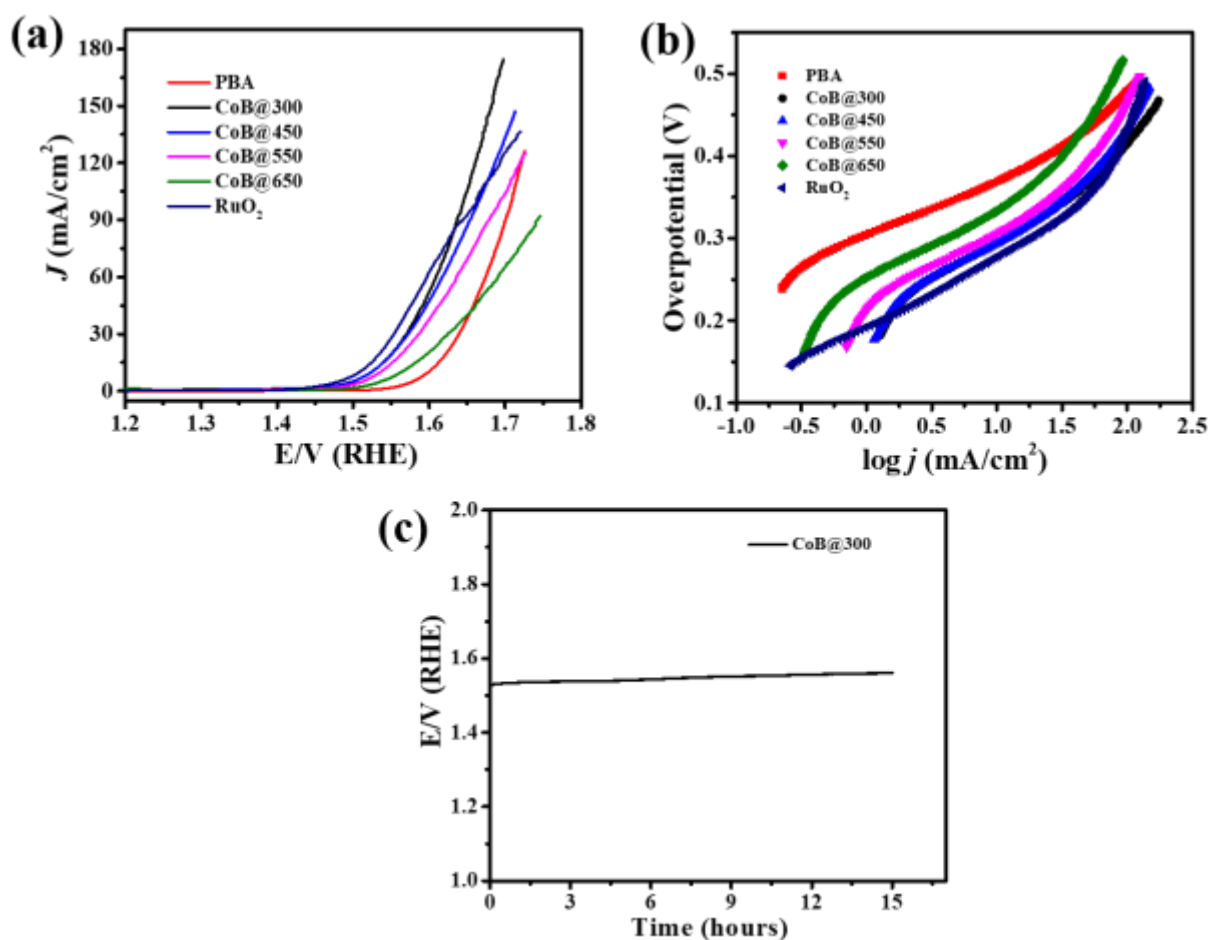


Figure 4.6 (a) Linear sweep voltammogram, (b) Tafel plot (c) Chronopotentiometric curve collected at an applied current density of 10 mA cm^{-2} .

with an onset potential of 1.47 V (vs. RHE) and requires only 290 mV overpotential to reach the benchmarked current density (10 mA/cm^2). However, a relatively higher overpotential required in case of CoB@450 (295 mV), CoB@550 (300 mV), and CoB@650 (355 mV), demonstrating their relatively poor catalytic behaviour. Moreover, the CoB@300 exhibits a Tafel slope of 62 mV/dec. which is lower as compared to commercial RuO₂ (75 mV/dec.), CoB@450 (76 mV/dec), CoB@550 (78 mV/dec) and CoB@650 (82 mV/dec) (Fig. 4.6b). The catalytic activity of CoB@300 presumably comparable to those of noble metal based electrocatalysts and higher than that of most of the non-noble metal based electrocatalysts as tabulated in the Table 4.1.

Table 4.1 Table showing the comparison of the electrocatalytic activity of CoB.

Catalysts	Electrolyte (Conc.)	Overpotential (mV) @10 mA/cm ⁻²	Tafel Slope (mV/dec)
Ni-Co-B	1 M KOH	300	113
Ni _x B-300	1 M KOH	380	89
Ni-B @ Ni(OH) ₂ @ Ni foam	1 M KOH	300@ 100mA/cm ⁻²	49.0
Ni-Fe-B/rGO	1 M KOH	265	58
Ni _x B/f-MWCNT	1 M KOH	286	46.3
Co-B/C	1 M KOH	320	75.00
Co-B/NF	1 M KOH	315	56.00
Co-3Mo-B	1 M NaOH	320	155.0
Fe ₂ B	1 M KOH	296	52.4
Fe _x B	1 M KOH	260	57.9
Ni-B _i @NB	1 M KOH	302	52.0
Ni-B-O @ Ni ₃ B	1 M KOH	264	127.0
NiB	1 M KOH	240	58
Ni ₃ B	1 M KOH	300	43
CNBO-NSs	1 M KOH	300	60
Co-Ni-B @NF	alkaline	313	120
CoFe-B	1 M KOH	261	61
CoB@300	1 M KOH	290	62

To gather more information regarding the real catalytic active sites, powder XRD pattern of the sample after first CV cycle (recorded at a scan rate of 5 mV/s) has been collected and analysed shown in Fig. 4.7a. An irreversible redox behaviour has been noticed from the cyclic voltammogram which is assigned to the transformation of surface metal Co centres from (II) to (III) oxidation state. And also, the metalloid boron species get oxidised to the corresponding

metaborites which is supported by the PXRD pattern (Fig. 4.7b, PDF#01-076-0745). Therefore, we presumed that during the anodic scan in alkaline electrolyte, the surface of the sample casted GCE get oxidised forming a core-shell like structure with the boride (CoB) as the core and the corresponding oxyhydroxide (CoOOH) as shell.¹⁰

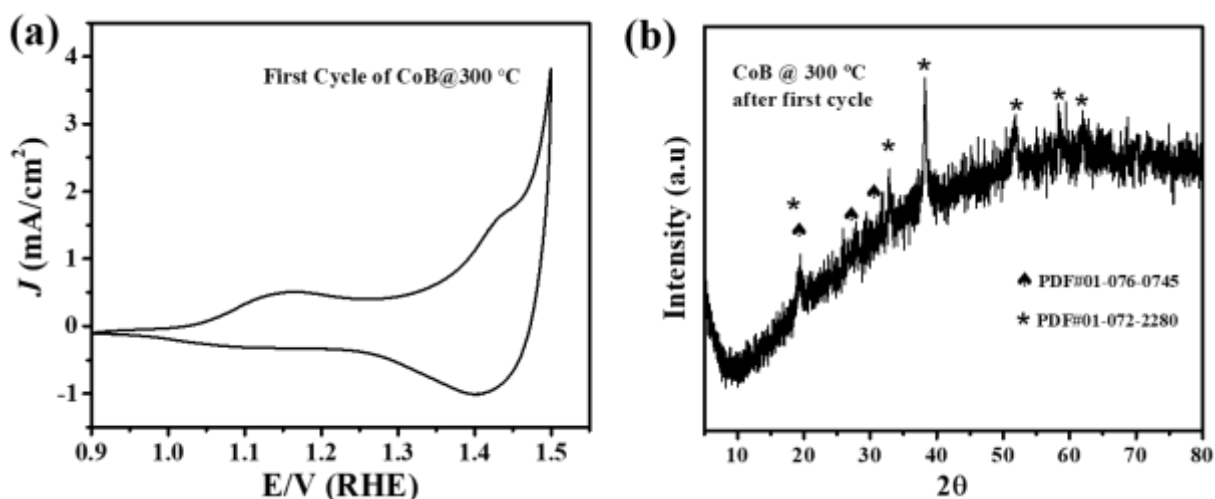


Figure 4.7 (a) cyclic voltammogram, (b) X-ray diffraction spectrum after the first CV cycle.

Here, the oxide shell acts as catalytic active sites and conductive boride core for the electron transport. Similar type of observations has also been previously reported in case of Ni and Co based borides, sulphides, selenides, nitrides and etc.²⁵ As per the theoretical studies, the CoOOH is the thermodynamically stable phase in most of the Co based electrocatalysts in alkaline electrolytic conditions.^{26,27} and the oxygen evolution reaction over the CoOOH is thermodynamically limited by the formation of OOH/OH as the reaction intermediates. However, in CoB@300 a significant enhancement in the catalytic activity is due to the presence of metaborite and amorphous nature of the CoB@300. The amorphous form of CoB@300 has locally disordered structures with more coordinatively unsaturated sites and surface defects thereby showing better electrocatalytic activity compared to its crystalline counterparts CoB@450, CoB@550 and CoB@650.^{7,28} Further, the profound electrocatalytic activity is also supported by analysing certain parameters like electrochemical accessible surface area

(ECSA), roughness factor (R_f) and turnover frequency (TOF) etc. For ECSA, at first the CVs at different sweep rate has been recorded in a non-Faradaic region of the potential window and the ECSA was determined from the double layer capacitance (C_{dl}) as per the following equation 4.2 (Fig. 4.8).

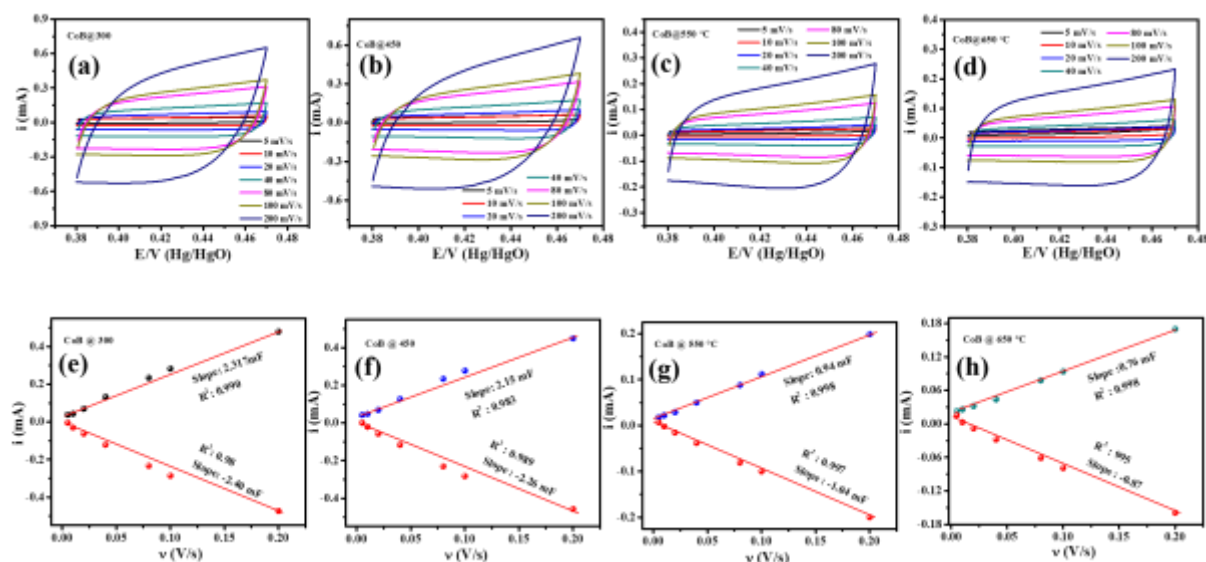


Figure 4.8 (a-d) Cyclic voltammograms and (e-h) plot of current at different sweep rate for CoB@300, CoB@450, CoB@550 and CoB@650.

Here, C_s is the specific capacitance ($40 \mu\text{F}/\text{cm}^2$) of an atomically smooth metal oxide surface in alkaline electrolyte. The CoB@300 shows higher ECSA (63.75 cm^2) compared to the CoB@450 (55.10 cm^2), CoB@550 (24.75 cm^2) and CoB@650 (20.37 cm^2) thereby showing maximum coverage of the electrolyte ions leading to improved electrocatalysis. Not only the ECSA but also the CoB@300 shows higher roughness factor (R_f) demonstrating the availability of more catalytic sites than the other samples. All the parameters studied are shown in Table 4.2. Also, the CoB@300 showed higher value of turnover frequency compared to the other catalysts studied here at 400 mV overpotential (Fig. 4.9). Thereafter, the catalytic durability of CoB@300 has been verified by performing the chronopotentiometry at an applied current density of $10 \text{ mA}/\text{cm}^2$. As can be seen, there is an increase of 15 mV overpotential found after 15 hours of electrolysis demonstrating robust durability shown in Fig. 4.6c. In order

Table 4.2 Table showing the OER activity of different catalysts.

Sample	$\eta@10$ mA/cm ² (mV)	$\eta@50$ mA/cm ² (mV)	Tafel slope (mV/dec.)	ECSA (cm ²)	Roughness factor (R _f)	TOF (s ⁻¹) @ $\eta=400$ mV
Co@300	290	360	62	63.75	910.7	11.25
Co@450	295	375	76	55.10	787.1	9.78
Co@550	300	392	78	24.75	353.5	7.70
Co@650	355	441	82	20.37	291.0	4.39

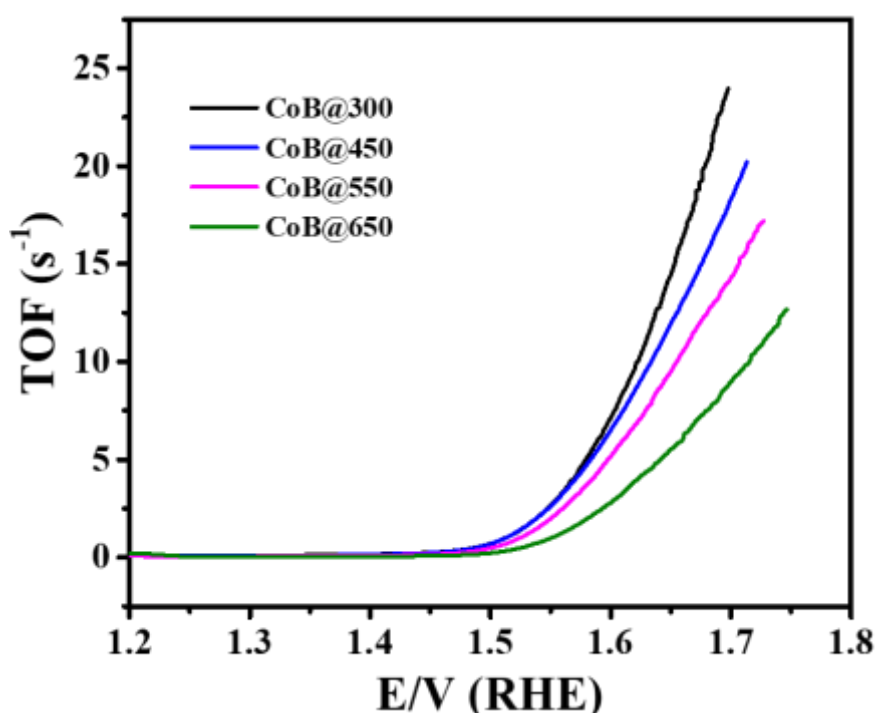


Figure 4.9 Plot showing the turnover frequency for CoB@300, CoB@450, CoB@550 and CoB@650.

to access the structural and morphological changes during the course of electrolysis, the FESEM, PXRD and X-ray photoelectron spectrum of the post OER stability sample has been performed (Fig. 4.10). Compared to the diffraction spectrum after first CV cycle, the post OER sample showed similar pattern demonstrating the intactness of the electrocatalyst during the catalysis study. However, after OER stability, the layered CoB@300 observed to be broken into small layered structure which can be seen in the FESEM analysis (Fig. 4.10b). Further, the

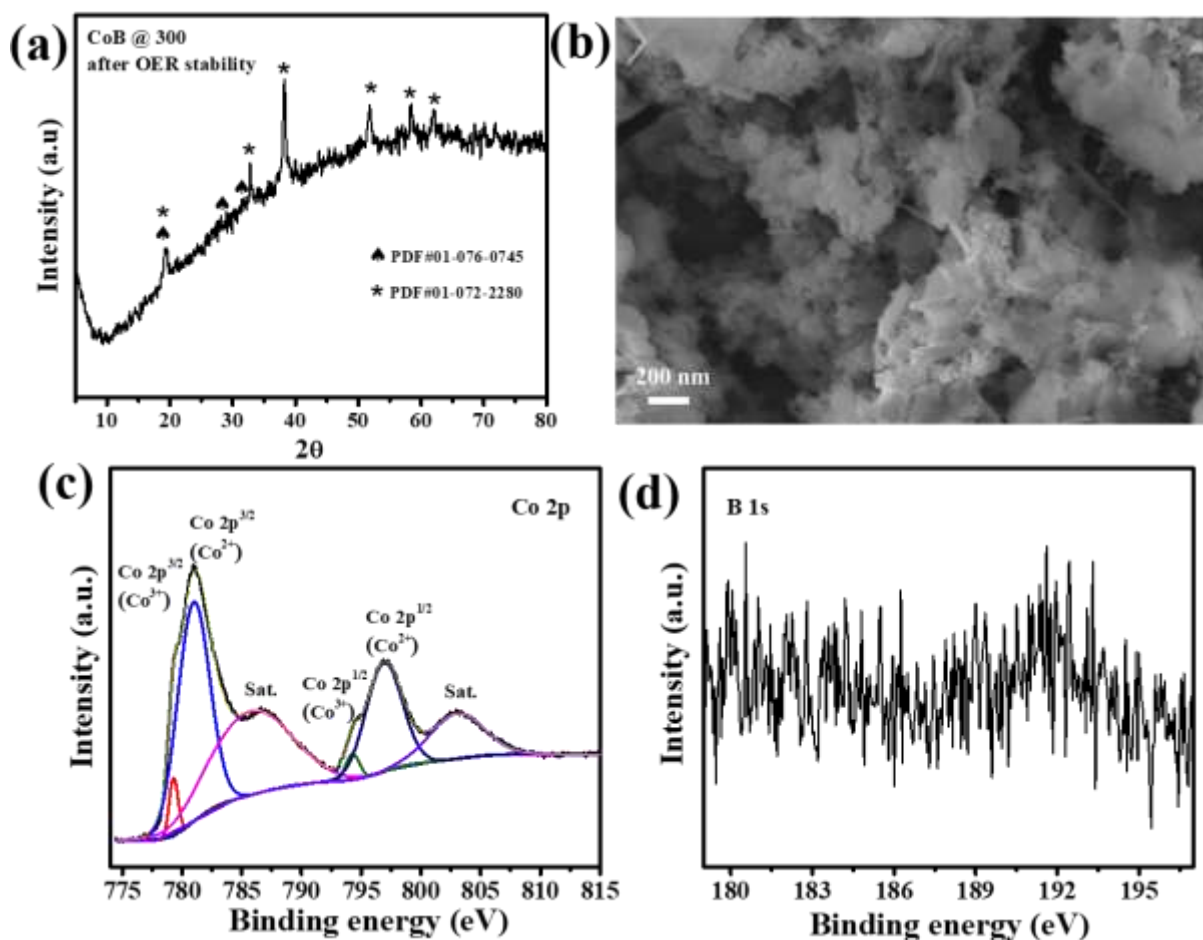


Figure 4.10 (a) X-ray diffraction pattern, (b) FESEM, high-resolution X-ray photoelectron spectrum for (c) Co 2p and (d) B 1s of CoB@300 after 15 hours of electrolysis.

change in valence state and surface chemical composition has been verified from the X-ray photoelectron spectrum. The high-resolution spectrum of Co 2p deconvoluted into six peaks i.e., two doublets and two shake up satellites. Compared to the XPS spectrum of CoB@300, the post stability sample shows two additional peaks at 779.0 and 794 eV assigned to the $2p_{3/2}$ and $2p_{1/2}$ of Co^{3+} respectively (Fig. 4.10c). It clearly suggests the transformation of the Co^{2+} to Co^{3+} during the course of OER due to which the surface of the CoB got partially oxidised to the corresponding oxyhydroxides (CoOOH). In the B 1s spectrum (Fig. 4.10d), the peak at 184.1 eV (assigned to the Co-B interaction) vanished with intensifying the peak at 191.6 eV (assigned to the oxides of boron). It clearly suggests the surface oxidation of the CoB during

the course of OER. Particularly, during the first CV cycle, the surface of CoB@300 got activated by transforming into the corresponding oxyhydroxide and catalysed the OER and remained intact even after the long-term stability test. Therefore, we presume that the designed synthesis protocol can be scaled up and can be used as suitable pre-electrocatalyst for the quantitative evolution of oxygen.

4.9 Conclusions

Here, we have synthesized a series of CoB by reducing the precursor Co-PBA with NaBH₄ followed by annealing in inert atmosphere at various temperatures. Interestingly, at 300 °C, thin sheets of amorphous CoB were formed and on changing the annealing temperature from 450 to 650 °C crystalline CoB were obtained. Diverse characterization of the samples and experimental measurements have demonstrated that the improved electrocatalytic activity of the CoB@300 over other borides (CoB@450, CoB@550 and CoB@650) studied here is ascribed to the synergistic effect of its thin layered like morphology and amorphous nature. This avails more exposed electrocatalytically active sites thereby facilitating the electrocatalysis. Prior to the electrocatalysis study, the catalyst was electro-activated by performing CV during which the surface of the boride gets transformed to the corresponding oxyhydroxides and then catalyses the OER. Interestingly, the crystallinity of the activated electrocatalyst as well as the surface morphology remained intact even after the continuous electrolysis for 15 hours with a minimal increase in overpotential. This work provides a unique method for the synthesis of amorphous cobalt boride as the pre-electrocatalyst towards the electro-oxidation of water.

4.10 References

- 1 Y. Gorlin and T. F. Jaramillo, *J. Am. Chem. Soc.*, 2010, **132**, 13612–13614.
- 2 F. Cheng and J. Chen, *Chem. Soc. Rev.*, 2012, **41**, 2172–2192.
- 3 R. K. Tripathy, A. K. Samantara and J. N. Behera, *Sustain. Energy Fuels*, 2021, **5**, 1184–1193.

- 4 Y. H. Deng, C. Ye, B. X. Tao, G. Chen, Q. Zhang, H. Q. Luo and N. B. Li, *J. Power Sources*, 2018, **397**, 44–51.
- 5 R. K. Tripathy, A. K. Samantara and J. N. Behera, *Dalt. Trans.*, 2019, **48**, 10557–10564.
- 6 L. L. Feng, G. Yu, Y. Wu, G. D. Li, H. Li, Y. Sun, T. Asefa, W. Chen and X. Zou, *J. Am. Chem. Soc.*, 2015, **137**, 14023–14026.
- 7 T. He, J. M. V. Nsanzimana, R. Qi, J. Y. Zhang, M. Miao, Y. Yan, K. Qi, H. Liu and B. Y. Xia, *J. Mater. Chem. A*, 2018, **6**, 23289–23294.
- 8 Y. Y. Ma, C. X. Wu, X. J. Feng, H. Q. Tan, L. K. Yan, Y. Liu, Z. H. Kang, E. B. Wang and Y. G. Li, *Energy Environ. Sci.*, 2017, **10**, 788–798.
- 9 J. Li, H. Chen, Y. Liu, R. Gao and X. Zou, *J. Mater. Chem. A*, 2019, **7**, 5288–5294.
- 10 N. Xu, G. Cao, Z. Chen, Q. Kang, H. Dai and P. Wang, *J. Mater. Chem. A*, 2017, **5**, 12379–12384.
- 11 H. Li, P. Wen, Q. Li, C. Dun, J. Xing, C. Lu, S. Adhikari, L. Jiang, D. L. Carroll and S. M. Geyer, *Adv. Energy Mater.*, 2017, **7**, 1–12.
- 12 J. Masa, P. Weide, D. Peeters, I. Sinev, W. Xia, Z. Sun, C. Somsen, M. Muhler and W. Schuhmann, *Adv. Energy Mater.*, 2016, **6**, 1–10.
- 13 W. J. Jiang, S. Niu, T. Tang, Q. H. Zhang, X. Z. Liu, Y. Zhang, Y. Y. Chen, J. H. Li, L. Gu, L. J. Wan and J. S. Hu, *Angew. Chemie - Int. Ed.*, 2017, **56**, 6572–6577.
- 14 J. Masa, I. Sinev, H. Mistry, E. Ventosa, M. de la Mata, J. Arbiol, M. Muhler, B. Roldan Cuenya and W. Schuhmann, *Adv. Energy Mater.*, 2017, **7**, 1–8.
- 15 H. Shin, H. Xiao and W. A. Goddard, *J. Am. Chem. Soc.*, 2018, **140**, 6745–6748.
- 16 H. Zhang, X. Li, A. Hähnel, V. Naumann, C. Lin, S. Azimi, S. L. Schweizer, A. W. Maijenburg and R. B. Wehrspohn, *Adv. Funct. Mater.*, 2018, **28**, 1706847.
- 17 L. Han, X.-Y. Yu and X. W. D. Lou, *Adv. Mater.*, 2016, **28**, 4601–4605.

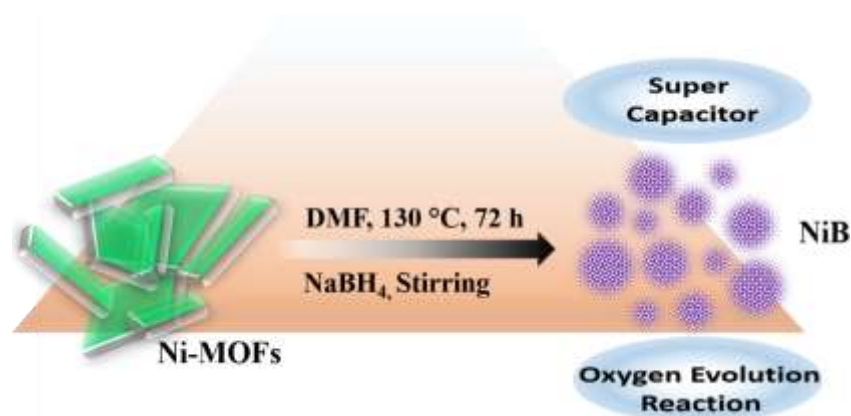
- 18 X. Y. Yu, Y. Feng, B. Guan, X. W. D. Lou and U. Paik, *Energy Environ. Sci.*, 2016, **9**, 1246–1250.
- 19 B. Jiang, H. Song, Y. Kang, S. Wang, Q. Wang, X. Zhou, K. Kani, Y. Guo, J. Ye, H. Li, Y. Sakka, J. Henzie and Y. Yusuke, *Chem. Sci.*, 2020, **11**, 791–796.
- 20 U. B. Demirci and P. Miele, *Phys. Chem. Chem. Phys.*, 2010, **12**, 14651–14665.
- 21 J. Lee, K. Y. Kong, C. R. Jung, E. Cho, S. P. Yoon, J. Han, T. G. Lee and S. W. Nam, *Catal. Today*, 2007, **120**, 305–310.
- 22 S. Gupta, N. Patel, A. Miotello and D. C. Kothari, *J. Power Sources*, 2015, **279**, 620–625.
- 23 S. Gupta, N. Patel, R. Fernandes, R. Kadrekar, A. Dashora, A. K. Yadav, D. Bhattacharyya, S. N. Jha, A. Miotello and D. C. Kothari, *Appl. Catal. B Environ.*, 2016, **192**, 126–133.
- 24 J. Geng, D. A. Jefferson and B. F. G. Johnson, *Chem. Commun.*, 2007, 969–971.
- 25 Y. X. Yang, B. L. Li, Q. Zhang, W. H. Guo, X. H. Wang, L. J. Li, H. Q. Luo and N. B. Li, *Energy Technol.*, 2021, **9**, 2000178.
- 26 M. García-Mota, M. Bajdich, V. Viswanathan, A. Vojvodic, A. T. Bell and J. K. Nørskov, *J. Phys. Chem. C*, 2012, **116**, 21077–21082.
- 27 M. Bajdich, M. García-Mota, A. Vojvodic, J. K. Nørskov and A. T. Bell, *J. Am. Chem. Soc.*, 2013, **135**, 13521–13530.
- 28 J. Nai, H. Yin, T. You, L. Zheng, J. Zhang, P. Wang, Z. Jin, Y. Tian, J. Liu, Z. Tang and L. Guo, *Adv. Energy Mater.*, 2015, **5**, 1401880.

CHAPTER-5

Amorphous nickel boride: A metal-organic framework-derived electroactive material for energy conversion and storage.

- 5.1** Abstract
- 5.2** Introduction
- 5.3** Motivation of the work
- 5.4** Experimental section
 - 5.4.1** Synthesis of Ni-MOF
 - 5.4.2** Synthesis of Nickel Boride
 - 5.4.3** Synthesis of GO, RGO
- 5.5** Characterization
- 5.6** Electrochemical measurements
- 5.7** Calculations of ECSA and R_f
- 5.8** Results and discussions
- 5.9** Conclusions
- 5.10** References

5.1 Abstract



This chapter introduces an effective chemical redox method meant for the tuning of crystalline and electronic structure of a metal organic framework (Ni-MOF) to improve its electrocatalytic as well as charge storage performance. The single step redox approach transformed the crystalline Ni-MOF to amorphous nickel boride (NiB) showing an increased exposed catalytic active centres and accessible surface area thereby improving electrochemical performances. Interestingly, the NiB efficiently catalyses the OER delivering the benchmarked current density (10 mA/cm^2) at only 240 mV along with excellent electrocatalytic durability. On the other hand, it shows higher value of specific capacitance (2580 F/g), remarkable energy (72.55 Wh/kg) and power (33.43 kW/kg) densities with outstanding cycle life (85.45%) retention of initial capacitance after 5000 cycles. In order to validate the practical application, an asymmetric supercapacitor (ASC) is devised in a Swagelok type electrode with rGO and NiB as cathode and anode electrode material respectively. The rGO//NiB ASC device shows a specific capacitance of 83.33 F/g (at 0.5 A/g) with an energy density of 26.04 Wh/kg at a specific power of 2.08 kW/kg with excellent durability (96% specific capacitance retention after 5000 GCD cycles).

5.2 Introduction

The composition and morphology of electroactive material have a significant role in the improvement of its electrochemical performances. In particular, more accessible surface area and higher number of electroactive centres in a material increase its electrocatalytic as well as charge storage efficacies. Although a number of transition metal based inorganic nanomaterials have been developed, but till now the noble metals (Pt, Ru, Rh, and Ir) and their oxides (RuO₂, IrO₂ etc.) are the real players.¹⁻⁴ However, their scarce reserve and high cost restrict their scalability and widespread technological applications demanding the exploration of non-noble metal based electroactive material. Therefore, intensive research activities have been devoted in preparation of electroactive materials from various earth abundant non-precious elements. In this regard, focus has been given on the synthesis of various transition metal-based electrode materials like metal oxides, chalcogenides, phosphides and their composites and their electrocatalytic and charge storage performances were demonstrated.⁵⁻¹⁰ In addition, the transition metal borides (or metal-boron alloys) were also assumed as a group of promising electrocatalysts for oxygen and hydrogen evolution reactions.^{11,12} The metal borides like Ni_xB, Co_xB, etc. form ultrafine particle size that showed a reduced path length for the diffusion of ions thereby increasing the utilization of active sites.^{13,14} In this regard, a series of mono metallic and bimetallic borides and their nanostructures with various morphologies have been explored. However, the performances could not meet the requirements demanding designing of new materials. As an efficient storage technology, supercapacitors (SCs) have gained immense attention due to their ultrahigh specific power and excellent cycle life compared to batteries. The electrode materials of SCs are basically categorized into electrochemical double layer capacitive (EDLCs) and pseudocapacitive (or battery type) materials depending upon their charge storage mechanism.¹⁵ Among them, the battery materials possess energy densities higher than that of EDLCs but much lesser than the lithium-ion batteries thereby limiting the

practical application. Therefore, many trials have been executed to improve the energy densities of the capacitors without compromising the power density and cycle life. One of the efficient processes is to assemble these two types of materials in a single device called asymmetric/hybrid supercapacitor (ASC/HSC).¹⁶ The hybrid capacitor thus resulted from the integration of EDLCs (capacitive material) with pseudocapacitive (battery type material) materials shows higher energy densities without compromising the specific power and cycle life of the device. Generally, carbon-based materials like graphene, reduced graphene oxide, activated carbon etc. are used as capacitive materials, while the pseudocapacitive type electrode materials still have a lot of room for improvement.^{17,18} It is worth noting that the rational design of a pseudocapacitive type electrode material remains a vital factor to achieve high energy density of the hybrid capacitor. Metal organic frameworks (MOFs), are the class of crystalline inorganic materials having metal centres and multitopic organic ligands, best known for their magnetism and gas storage activities. Recent investigations of MOFs have been stimulated by a growing interest in multifunctional materials and a revival in the chemistry of electrocatalysis and charge storage devices.¹⁹⁻²³ Moreover, compared to the inorganic nanostructures; tunable porosity, diverse topology structure and presence of abundant metal centres make MOFs a promising material for both electrocatalysis and energy storage applications.^{19,22,24-26} However, the poor conductivity, having inadequate number of active centres, slow mass transfer and instability in the experimental electrolytic condition hinders their direct electrochemical application. Therefore, using various approaches, (i) converting the MOFs to their corresponding metal oxides/hydroxides and chalcogenides, (ii) integrating the MOFs with other metal oxides/chalcogenides and (iii) converting to the carbon-based composites; these MOFs were used as active electrode materials and their electrocatalytic as well as energy storage performances were studied. It has been found that in most of the cases, either the MOFs are annealed at higher temperature (~300-1000 °C) or composited with other nanostructures to

improve the electrocatalytic and charge storage activities. However, the requirement of such high temperature, maintenance of inert atmosphere and employment of other metal nanostructure adds more cost to the material. Though these derived nanostructures have good electrochemical properties compared to those synthesised directly, but they were found to be active either for energy conversion or storage. However, the designing of a single material having both the energy conversion and storage ability will be appropriate not only to reduce the cost of the device but also minimizes the time required for materials preparation. To achieve these goals, in this present work we have presented a novel and convenient method for the synthesis of nickel boride (NiB) from a metal-organic framework (Ni-MOF; [Ni (HBTC) (4,4'-bipy) ·3DMF]) through an efficient chemical redox approach. The NiB thus formed is amorphous in nature and avails abundant number of defects promoting higher electrochemical performances. It possesses excellent electrocatalytic (towards oxygen evolution reaction) and pseudocapacitive performances proving their suitability as an efficient electrode material for both the electrochemical energy conversion (OER) and storage (Supercapacitor) application. The NiB requires a low overpotential of 240 mV to drive the OER current density of 10 mA/cm² in aqueous 1.0 M KOH electrolyte. The catalytic performance of NiB is not only superior to that of commercial NiO and benchmarked RuO₂ but also outperformed many of the reported transition metal based electrocatalysts. The NiB shows excellent pseudocapacitive behaviour showing a specific capacitance of 2580 F/g in a three-electrode electrochemical cell containing 5.0 M KOH electrolyte. This inspired us to design an asymmetric supercapacitor device in a Swagelok cell configuration with NiB and reduced graphene oxide (rGO) as the anode and cathode (rGO//NiB) respectively. The rGO//NiB showed a capacitance of 83.33 F/g with higher specific energy (26.24 Wh/kg) at a power density of 2.08 kW/kg with better reversibility and cyclic durability (96% retention of initial capacitance after 5000 cycles). The characterization of NiB and post OER stability of NiB reveals that the higher electrochemically

accessible surface area, existence of more catalytically active centres, improved redox properties and synergy among the in-situ formed surface oxyhydroxides shell and core NiB contribute to such significant electrocatalytic OER activity and charge storage performances. We assumed that this synthetic methodology is a suitable one and will be adopted for scalable preparation of NiB for future energy storage and conversion systems.

5.3 Motivation of the work

Nowadays, metal organic frameworks (the new class of inorganic crystalline materials) are the best sources not only in magnetism and gas storage but also in electrocatalysis and charge storage devices. Tunable porosity, diverse topology structure and abundant metal centres are the specific features that make MOFs a suitable alternative for electrocatalysis and charge storage against inorganic nanostructures and noble metal based electrocatalyst. However, the poor conductivity, having inadequate number of active centres, slow mass transfer and instability in the experimental electrolytic condition hinders their direct electrochemical application. Therefore, instead of direct MOFs, MOFs derived materials are more focused to encounter these issues by several approaches such as converting the MOFs to their corresponding metal oxides/hydroxides and chalcogenides, integrating the MOFs with other metal oxides/chalcogenides or converting to the carbon-based composites. These MOFs were used as active electrode material and their electrocatalytic as well as energy storage performances were studied. However, the designing of a single material having both the energy conversion and storage ability will be appropriate not only to reduce the cost of the device but also minimizes the time required for materials preparation. In this study, we report metal organic frameworks derived less explored nickel boride for energy conversion and storage.

5.4 Experimental Section

5.4.1 Synthesis of Nickel MOF (Ni-MOF)

Ni-MOFs ([Ni (HBTC) (4, 4'-bipy) ·3DMF]) was synthesized following a reported procedure.²⁷ In detail, a mixture of H₃BTC (0.5 mmol), Ni (NO₃)₂·6H₂O (0.5 mmol) and 4, 4'-bipy (0.5 mmol) in 10 ml of DMF solution was prepared by using magnetic stirrer. The whole solution was transferred into a 23 ml Teflon lined stainless steel autoclave, sealed properly and placed in a hot air oven at 130 °C for 72 hours. After cooling down, the as prepared crystals were washed with ethanol several times and stored for further characterization. The crystals thus obtained are named as Ni-MOF.

5.4.2 Synthesis of Nickel Boride (Ni-B)

In a typical synthetic procedure, 50 mg of the as synthesized Ni- MOF crystals were dispersed in a mixture of ethanol (10 ml) and water (20 ml) (1:2 proportion) and stirred for 30 minutes with a magnetic stirrer. To this, 5 ml of 0.4 M sodium borohydride (NaBH₄) was then added in a dropwise manner under constant stirring. After one hour, the black precipitate thus formed was collected by a suction filtration, washed with ethanol three times prior to drying in the hot air oven at 80 °C. The purified black coloured powder thus formed is the nickel boride and named as NiB.

5.4.3 Synthesis of Graphene Oxide (GO)

Graphene oxide (GO) was synthesized by following the modified Hummer's method.^{28,29} In detail, 1g of graphite powder was added to a beaker containing 25 ml of concentrated H₂SO₄ and stirred to mix properly in an ice bath. Under the continuous stirring condition, 3.5g of KMnO₄ was added slowly and left to stir for next 2 hours in a water bath. The mixture was then diluted by adding deionized water followed by addition of sufficient amount of H₂O₂ (30%) to it till the effervescence of the gasses ceased. The brown coloured suspension thus formed was filtered and repeatedly washed with 0.1 M HCl and deionized water. The washed graphene oxide was dried by rotary evaporator and stored in a desiccator for future use.

5.4.4 Synthesis of reduced graphene oxide (rGO)

Reduced graphene oxide (rGO) was synthesized by following a single step hydrothermal reduction method. Briefly, a GO suspension (1mg/ml) in deionized water was prepared by ultrasonication for 30 minutes. Then the suspension was transferred to a Teflon lined stain less steel autoclave (volume: 50 ml) and placed in a hot air oven at 200 °C for 24 hours. After cooled down to the room temperature; the precipitates were collected, repeatedly washed with the deionized water, dried in oven and stored in a desiccator for future use.

5.5 Characterization

The phase and crystallinity of the sample is analysed by X-ray diffraction patterns. Prior to the analysis, a suitable single crystal was carefully selected under a polarizing microscope and mounted at the tip of a thin glass fiber using cyanoacrylate (super glue) adhesive. Then the single crystal structure determination by X-ray diffraction was performed on a Bruker AXS-KAPPA Apex II diffractometer equipped with a normal focus, 2.4 kW sealed-tube X-ray source (Mo-K α radiation, $\lambda = 0.71073 \text{ \AA}$) operating at 50 kV and 30 mA. Further the powder X-ray diffraction (PXRD) pattern has been recorded with the Bruker D8 Advance diffractometer, equipped with Cu-K α radiation ($\lambda = 1.5418 \text{ \AA}$). The thermal stability of the sample was verified by thermogravimetric analysis (by TA Instruments-Waters Lab) at the ramp rate of 10 °C min⁻¹ under a constant flow of nitrogen gas. The surface morphology and elemental distribution has been analysed by the field emission scanning electron microscope (FESEM, Merlin Compact with a GEMINI-I electron column, Zeiss Pvt. Ltd, Germany). Using X-ray photoelectron spectroscopy, the elemental composition of the synthesized sample and post OER sample has been studied (PHI Versa Probe III). The specific surface area of NiB was determined by Brunauer-Emmett-Teller (BET) nitrogen adsorption/desorption methods at 77 K using Quanta chrome Instruments version 5.21.

5.6 Electrochemical Measurement

At first, the electrocatalyst ink has been prepared by dispersing 1 mg of sample (either NiB, Ni-MOF, RuO₂ or NiO) in a mixture of absolute ethanol (95 μl) and 5% nafion (5 μl) through bath sonication. In the meantime, the glassy carbon rotating disk electrode (GCRDE; geometrical surface area is 0.19 cm²) was polished with alumina slurry (1.0, 0.3, 0.05 μm sequentially) and washed properly to a mirror polished surface using deionized water in a bath sonicator. Thereafter the ink was drop casted onto the GCRDE surface in a vacuum desiccator with a mass loading of 0.2 mg/cm². For OER studies, the cyclic voltammogram (CV) and linear sweep voltammogram (LSV) were recorded using Biologic electrochemical Workstation (SP-200) in a three-electrode electrochemical cell comprising the sample modified GCRDE, platinum wire and alkaline Hg/HgO as working, counter and reference electrodes respectively in an aqueous 1.0 M KOH electrolyte. The electrochemical impedance spectroscopy (Nyquist Impedance) was carried out in a frequency range of 1 MHz to 0.1 Hz with an AC amplitude of 5 mV. The stability of the NiB towards OER has been analysed by using the Chrono potentiometric technique at an applied current density of 10 mA/cm². All the measurements were carried out with respect to the Hg/HgO reference electrode and converted to the reversible hydrogen electrode (RHE) scale as per the following Nernst equation

$$E_{RHE} = E_{Hg/HgO} + 0.059pH + E^{\circ}_{Hg/HgO} \dots\dots\dots (5.1)$$

The energy storage performance of NiB and Ni-MOF were evaluated by measuring the CV and galvanostatic charge-discharge profiles in 5 M KOH electrolyte. Here, similar electrode preparation procedure and experimental conditions were followed as in case of OER measurement.

5.7 Calculation of ECSA and R_f

The electrochemical active surface area has been calculated by measuring the double layer capacitance (*C_{dl}*) of NiB, RuO₂, Ni-MOF and NiO. For this, CVs are collected in a non-Faradaic region (0.1-0.16 V vs. Hg/HgO) at different scan rates (5, 10, 25, 50, 100 mV/s). The

average slope calculated from the plot of scan rate against cathodic and anodic peak current at 0.13 V (vs. Hg/HgO) gives the value of C_{dl} and then the ECSA has been calculated as per the following equation,

$$ECSA = \frac{C_{dl}}{C_s} \dots\dots\dots (5.2)$$

Roughness factor was calculated from ECSA by dividing geometrical surface area of the working electrode.

5.8 Result and discussions

Nickel boride (NiB) has been prepared following a two-step synthesis method. At first, the Ni-MOF ([Ni(HBTC)(4, 4'-bipy)·3DMF]) was prepared from Ni(NO₃)₂·6H₂O using H₃BTC

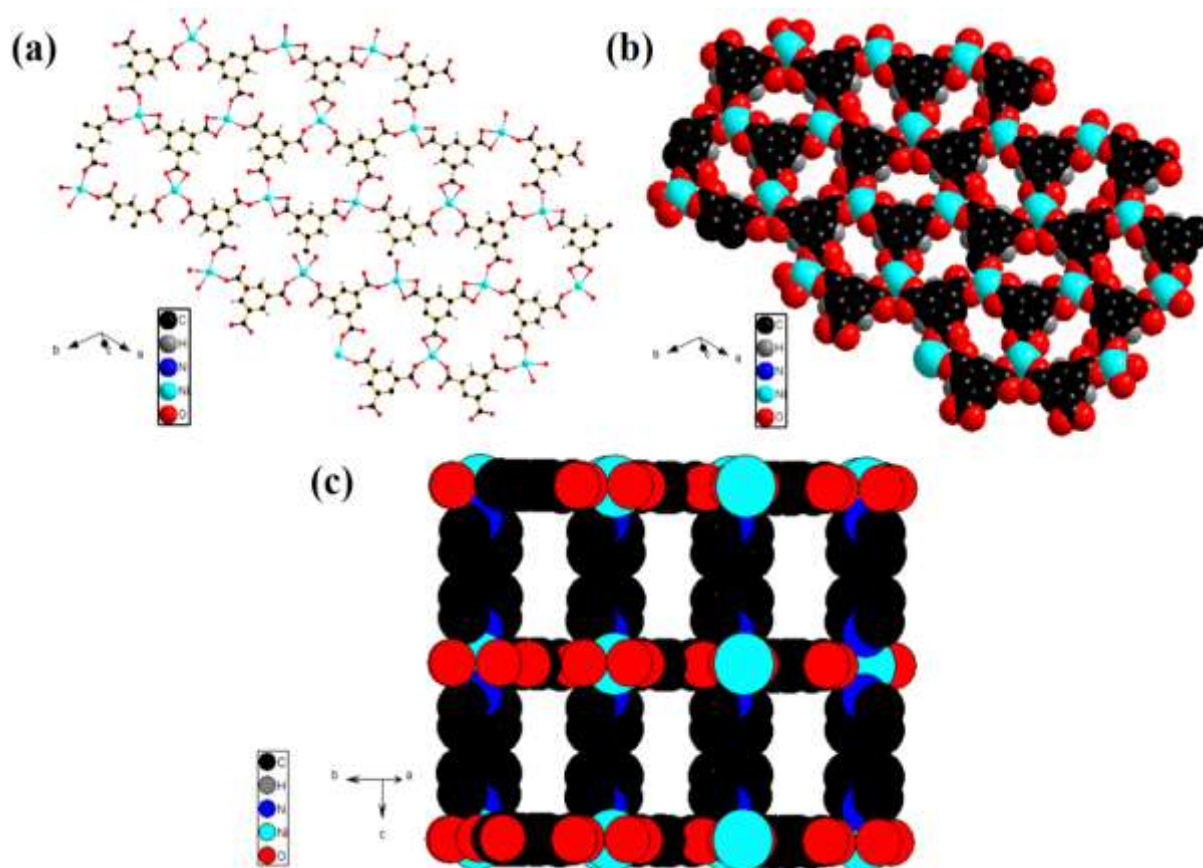


Figure 5.1(a) 3D view of [Ni(HBTC)(4, 4'-bipy)·3DMF] showing the (b) honeycomb channels along *c*-axis and (c) rectangular channels parallel to the layers extending through out *ab*-plane.

and 4, 4'-bipy in DMF solution via a simple solvothermal method. We check with the structure carefully, it has been observed that the honeycomb grid layers constructed by Ni²⁺ ions and BTC groups are linked by 4, 4'-bipy pillars to form a 3D highly porous framework (Fig. 5.1a). The most interesting feature of this MOF is that it contains two distinct channels, one in the opening of the Ni (HBTC) layers aligned to generate honeycomb channels running along the *c*-axis (Fig. 5.1b) and the other through the 4, 4'-bipy pillars giving a rectangular channel parallel to the layers extending throughout the *ab*-plane (Fig. 5.1c). When Ni-MOF was subjected to boronization, amorphous NiB formed. Here, NaBH₄ was used as the boron source and the boronization process was carried out by adding aqueous NaBH₄ in a dropwise manner. During the course of the reaction, the Ni²⁺ centres of Ni-MOF get transformed to the corresponding Ni-B as per the following formula,³⁰



Hereafter, the Ni-B is mentioned as NiB. It is a single step chemical redox approach that tunes the electronic and crystal structure of Ni-MOF. It greatly improves the redox behaviour of Ni-MOF thereby increasing the electrochemical performances.

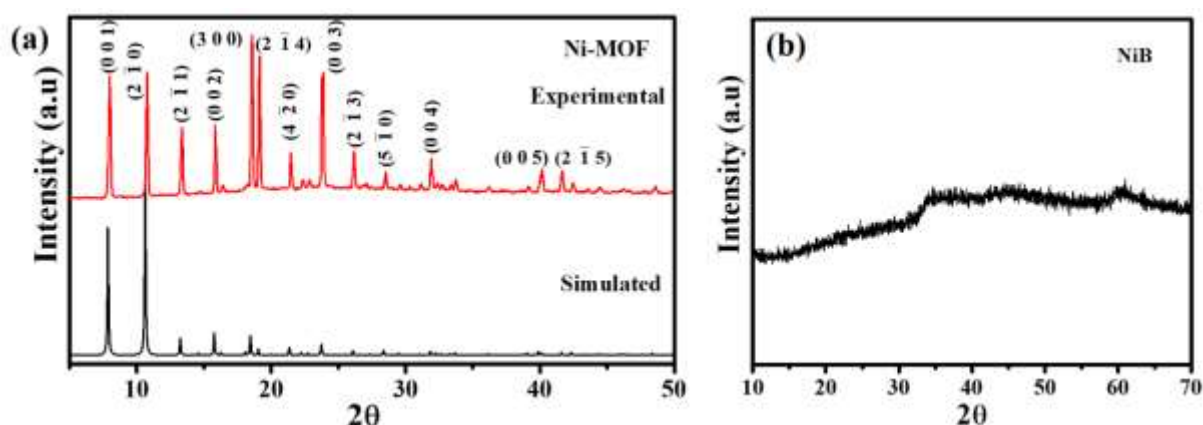


Figure 5.2 (a) simulated and experimental X-ray diffraction pattern of Ni-MOF, (b) powder X-ray diffraction pattern of NiB.

The sharp diffraction patterns clearly signify the higher crystallinity of the synthesized Ni-MOF (fig. 5.2a). The phase purity of the synthesized Ni-MOF was verified from the matching of experimental diffraction pattern with the simulated one as shown in the Fig. 5.2a. However, on boronization, a drastically transformation of the crystalline Ni-MOF to amorphous NiB has been observed showing a broad diffraction peak at $2\theta = 45^\circ$. This can be clearly understood from the PXRD pattern of NiB as shown in Fig 5.2b.

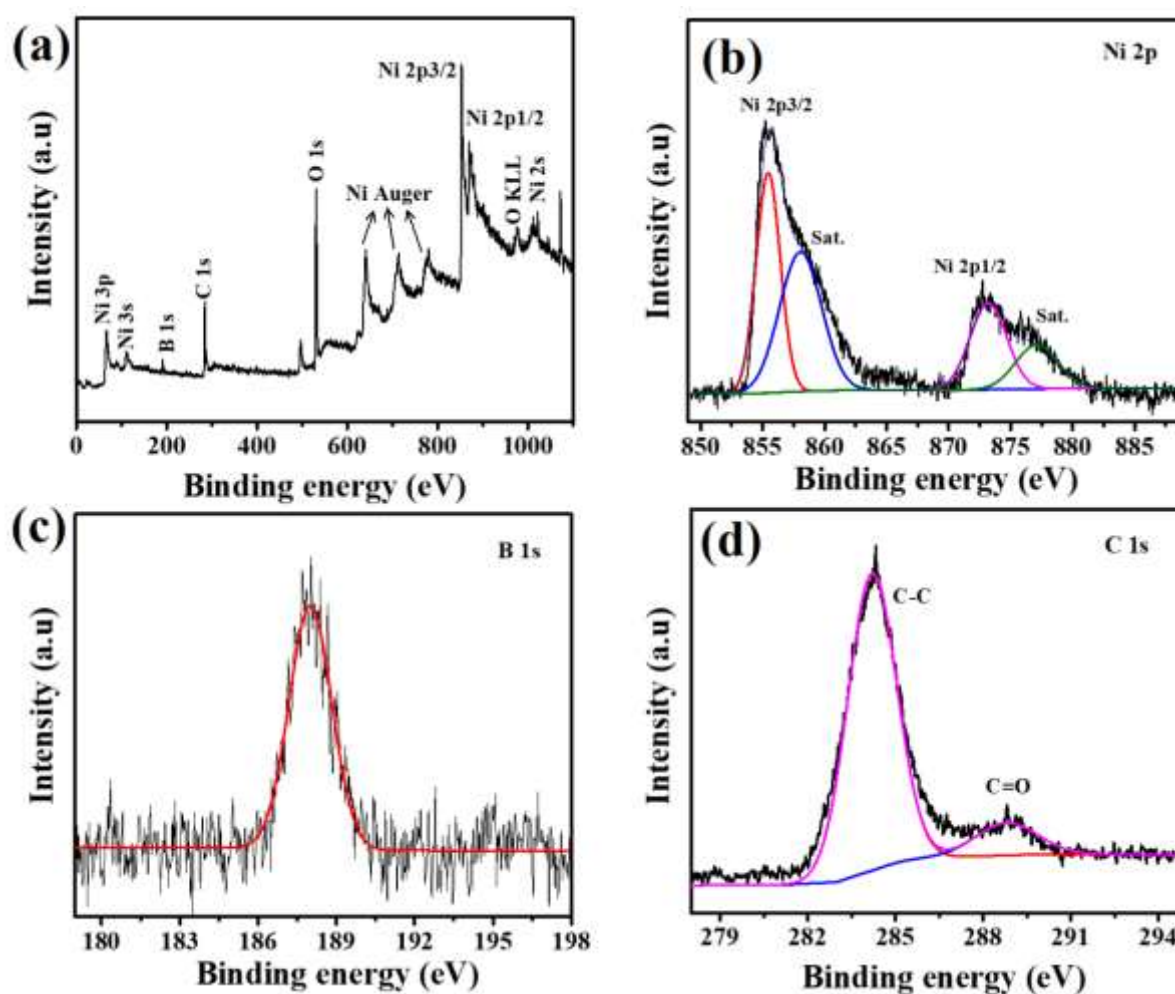


Figure 5.3 High-resolution X-ray photoelectron survey spectrum of (a) NiB (b) Ni 2p (c) B 1s and (d) C 1s of NiB.

Further the stoichiometry and oxidation state of the constituents of NiB has been conformed from the X-ray photoelectron spectroscopic analysis. The XPS survey spectrum clearly shows the presence of Ni, B, C and O elements (Fig.5.3a). The high-resolution XPS spectrum of Ni can be deconvoluted into two peaks at 855.52 and 873.160 eV assigned to the

Ni $2p_{3/2}$ and Ni $2p_{1/2}$ of metallic nickel (Ni^0) respectively (Fig.5.3b).³¹ However, the peaks located at slightly higher binding energy (859.2 and 878.1 eV) are assigned to the corresponding satellite peaks, whereas the existence of elemental boron (B^0) has been clearly observed from the peak at 187.9 eV in the high-resolution B 1s spectrum (Fig. 5.3c). Further, the high-resolution spectrum of C1s signifies the presence of C-C/C=C (284.45 eV) and C=O (288.5 eV) in NiB which might be due to the remaining ligands of the Ni-MOF after the reduction (Fig. 5.3d). The above analysis suggests the presence of elemental Ni and B in the form of amorphous Ni-B alloy further supporting the PXRD pattern.

The thermogravimetric analysis (TGA) of NiB was carried out under nitrogen flow between the temperature range 30-800 °C with a heating rate of 10 °C per minute. It shows one step weight loss (only 25% weight loss up to 550 °C) and thereafter the curve remains stable (Fig. 5.4a). We have collected the NiB sample after TGA (after 800 °C) and performed PXRD to analyse the end product. The black coloured powder thus collected was found to be highly crystalline with distinguishable diffraction peaks assigned to the (111), (200), (220) and (311) planes of NiO (JCPDS#47-1049) (Fig. 5.4b).

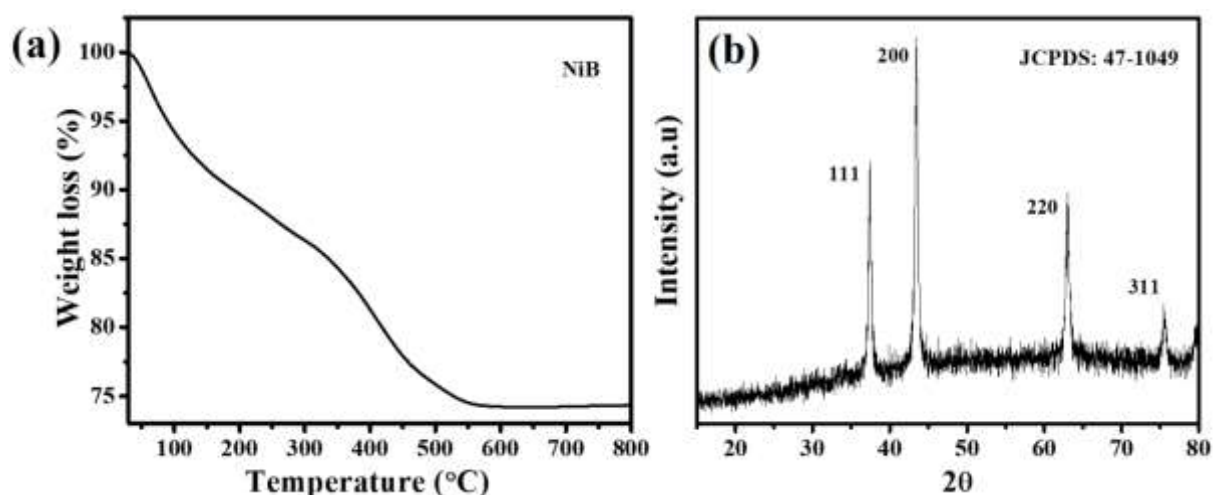


Figure 5.4 (a) Thermogravimetric analysis and (b) powder X-ray diffraction pattern of post TGA NiB after 800 °C.

The surface morphology of the Ni-MOF and NiB has been studied by using FESEM and transmission electron microscopic (TEM) images. As shown in Fig. 5.5a, the Ni-MOF possess inhomogeneous large block like morphology, whereas on boronization, these Ni- MOF get transformed to tiny spherical particles of NiB with an average diameter of ~22 nm (Fig. 5.5 b, c). The diffuse Debye rings were found in the selected area electron diffraction pattern signifying existence of short-range order instead of long range further confirming the amorphous nature of the synthesized NiB nanostructures (Fig. 5.5d).

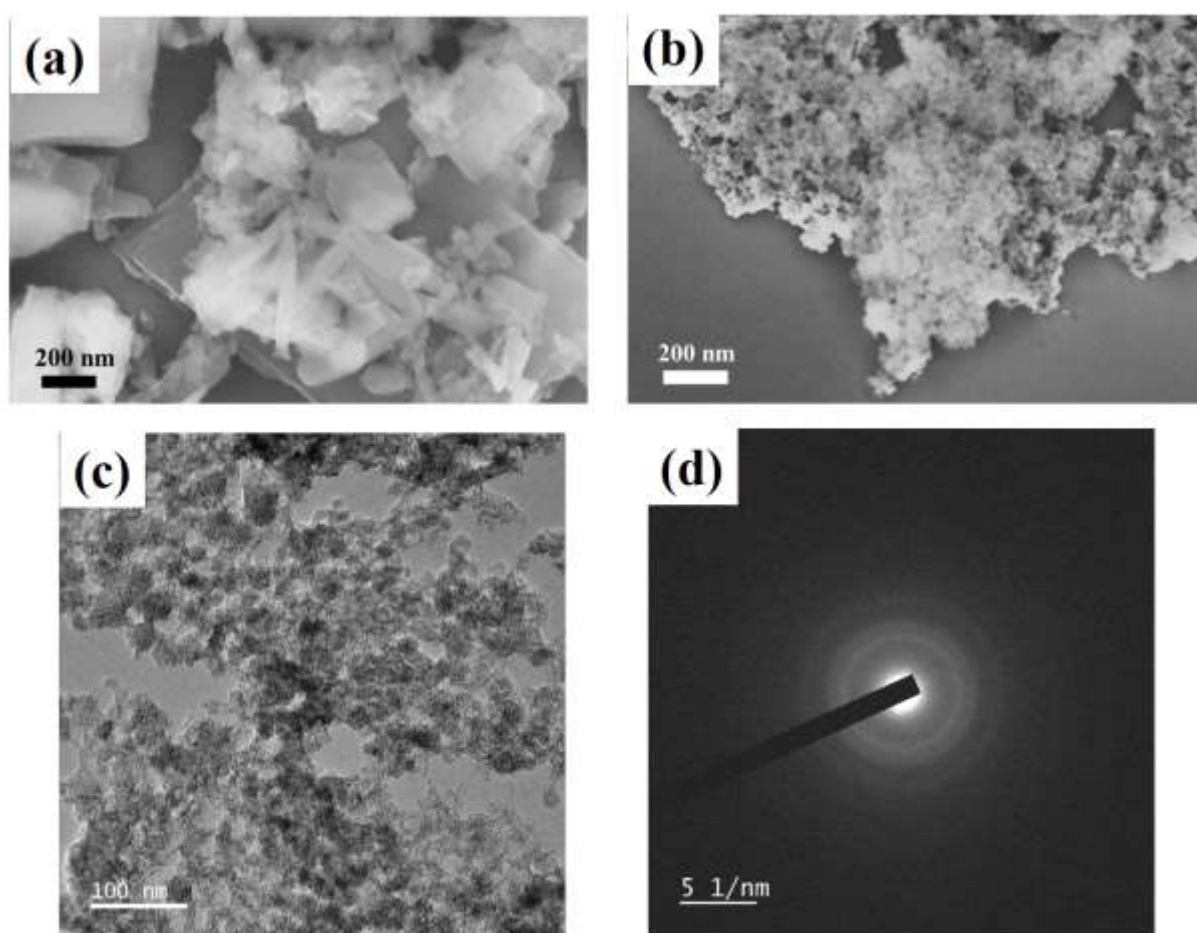


Figure 5.5 (a) FESEM image of Ni-MOF, (b) FESEM, (c) TEM and (d) SAED pattern of NiB.

From both the TEM analysis and PXRD pattern, we concluded that the NiB derived from the Ni-MOF is amorphous in nature. The specific surface area (SSA) of NiB has been evaluated

by using the N₂ adsorption/desorption method and NiB shows surface area (SSA) of 159.25 m²/g (Fig. 5.6) that is higher in comparison to many of the MOF derived metal oxides and sulphides. However, the reduction in SSA in comparison to the parent Ni-MOF might be due to the collapse of the well-defined 3D highly porous framework to the amorphous spherical NiB nanostructures during the redox reaction with NaBH₄.

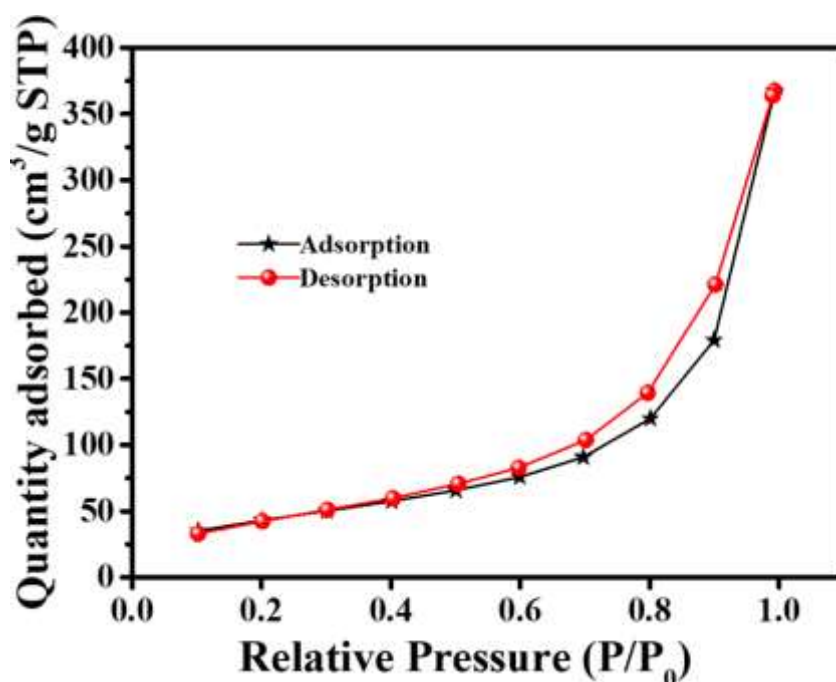


Figure 5.6 Adsorption and desorption isotherms for nitrogen (at 77 K) of NiB.

Electrochemical energy conversion studies towards OER:

It has been observed that the NiB shows better electrocatalytic OER activity over the whole potential range showing higher current densities (Fig. 5.7a). Further the activity of NiB was compared with the parent Ni-MOF (from which it has been derived), commercial NiO and RuO₂ under similar experimental conditions. The overpotential (η) required for NiB to drive the benchmarked current density of 10 mA/cm² was found to be very low (240 mV) compared to that of RuO₂ (290 mV), Ni-MOF (310 mV) and NiO (350 mV). At lower overpotential, NiB shows a lower Tafel slope (58 mV/dec.) in comparison to that of the commercial RuO₂ (72 mV/dec) again supporting the similar surface chemistry in OER (Fig. 5.7b). Fig. 5.7c shows

the comparison of OER activities of the samples studied here with the reported one. During the LSV scanning, we observed an oxidation peak at around 1.35 V (vs. RHE) in case of NiB, NiO and Ni-MOF which is assigned to the oxidation of Ni^{2+} to Ni^{3+} in alkaline condition under anodic potential.

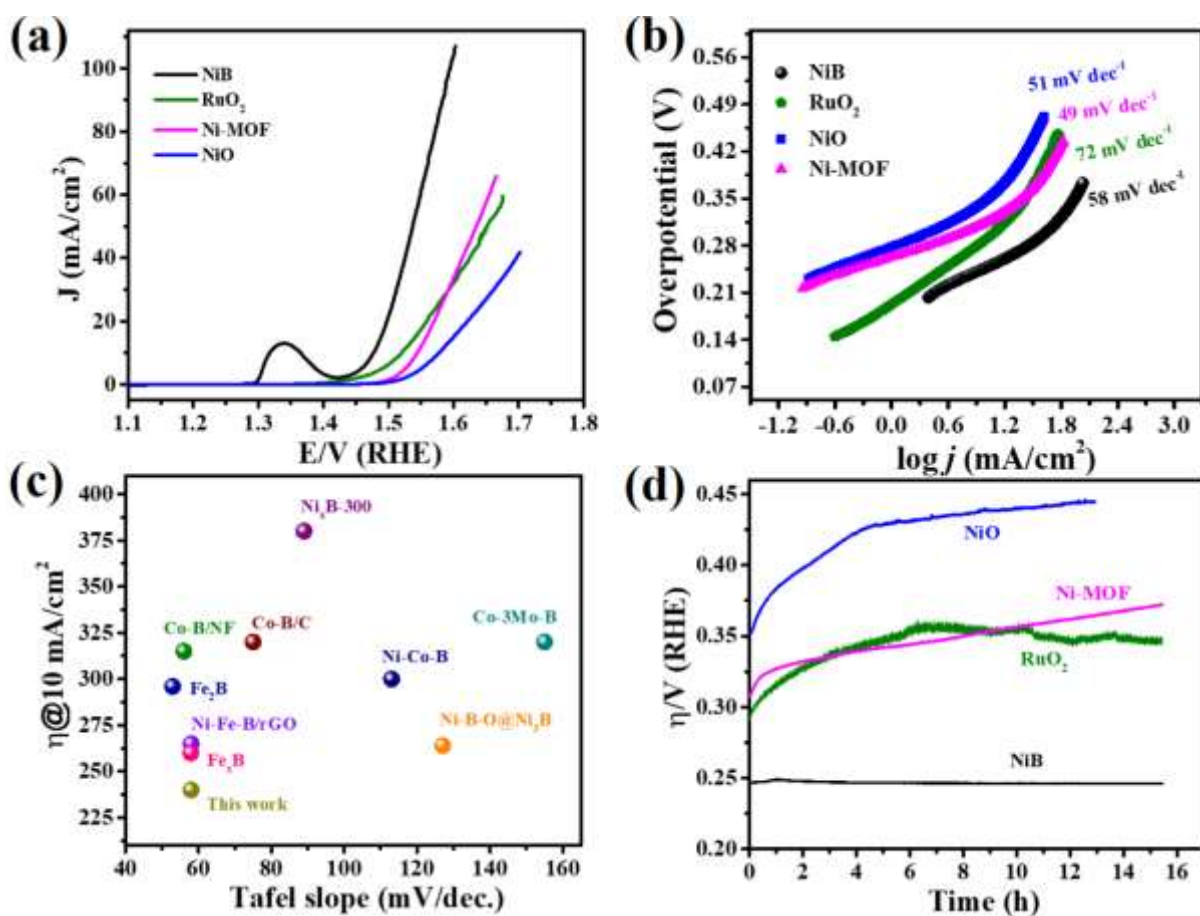


Figure 5.7 OER activity of NiB. (a) linear sweep voltammograms of NiB, RuO_2 , Ni-MOF and NiO electrocatalysts in 1.0 M KOH solution on GCRDE at a scan rate of 5 mV s^{-1} and rotation of 1600 rpm, (b) corresponding Tafel plots, (c) comparison on the overpotential at 10 mA cm^{-2} and Tafel slopes of recently reported boride based OER catalysts, (d) chrono potentiometric curve of NiB, Ni-MOF, NiO and RuO_2 dripped glassy carbon electrode at constant current density of 10 mA cm^{-2} .

To better understand the superior performance, the CV measurement of all these three samples were conducted at lower sweep rate of 5 mV/s. All the CVs showed an anodic peak and a corresponding cathodic peak assigned to the oxidation of Ni^{+2} to Ni^{+3} and reduction of Ni^{+3} to Ni^{+2} (Fig 5.8).

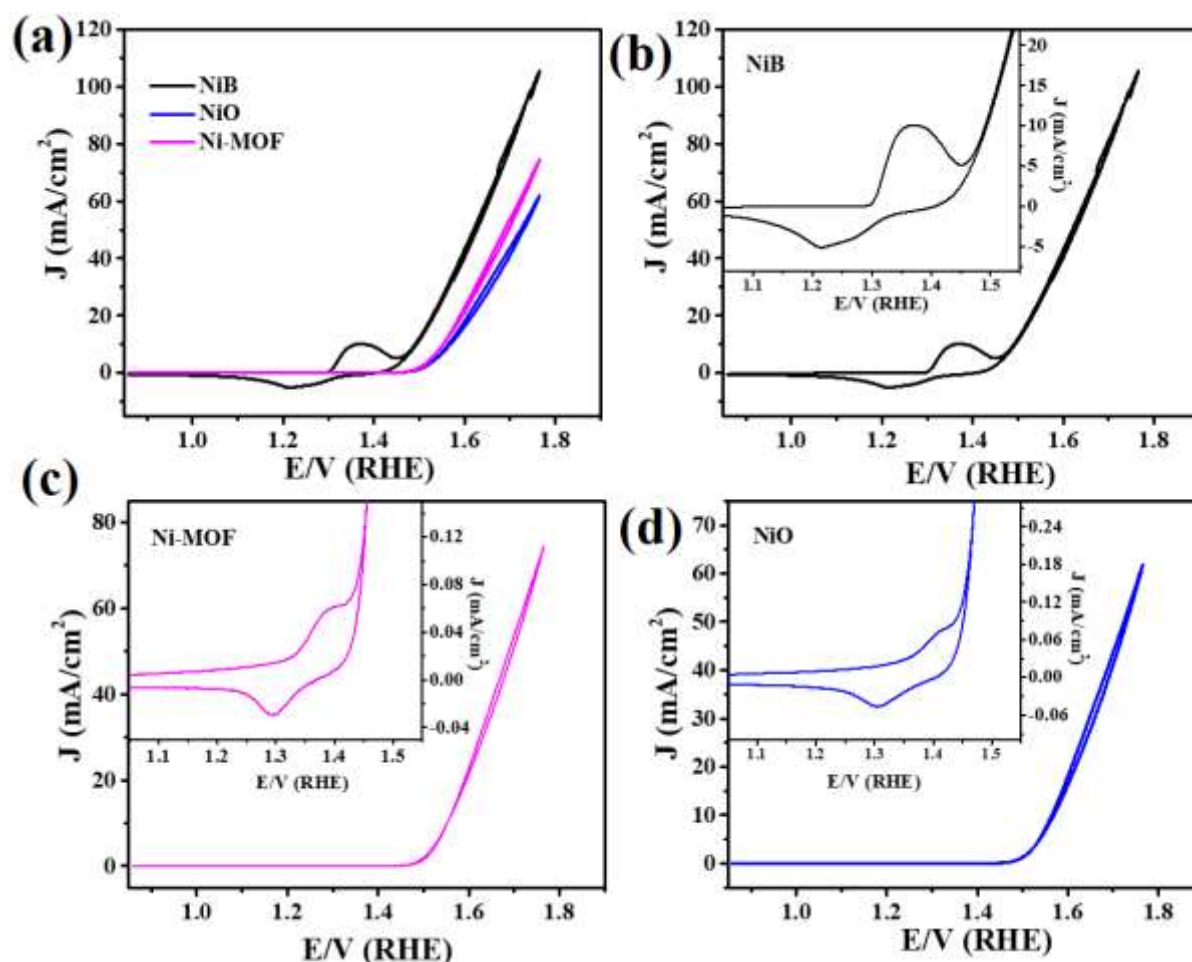


Figure 5.8 Cyclic voltammograms of NiB, NiO and Ni-MOF at 5 mV/s scan rate in 1.0 M KOH electrolyte.

Not only in this study but this is a general phenomenon observed by others also in most of the Ni based electrocatalysts during the electrochemical studies under alkaline condition.^{20,32–34} The peak current density as well as the area under the complete CV curve of NiB is found to be more compared to Ni-MOF, commercial NiO and RuO_2 suggesting the availability of more surface area to execute the electrocatalysis. All LSV polarization curves presented here were

iR compensated with the solution resistance (R_s) as measured by the Nyquist impedance spectrum (Fig. 5.9).

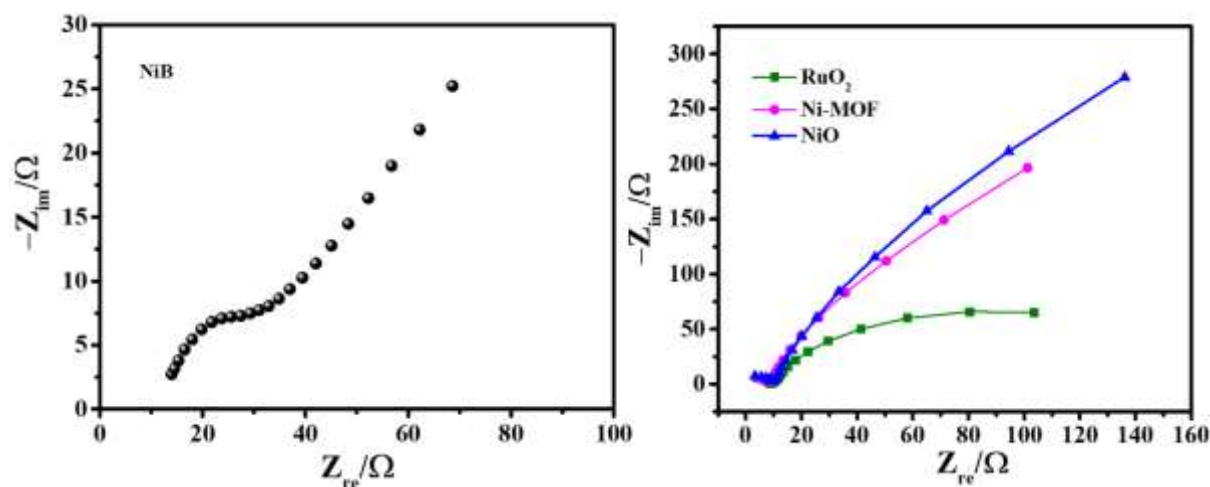


Figure 5.9 Nyquist impedance spectrum of (a) NiB and (b) RuO₂, Ni-MOF and NiO in 1 M KOH electrolyte.

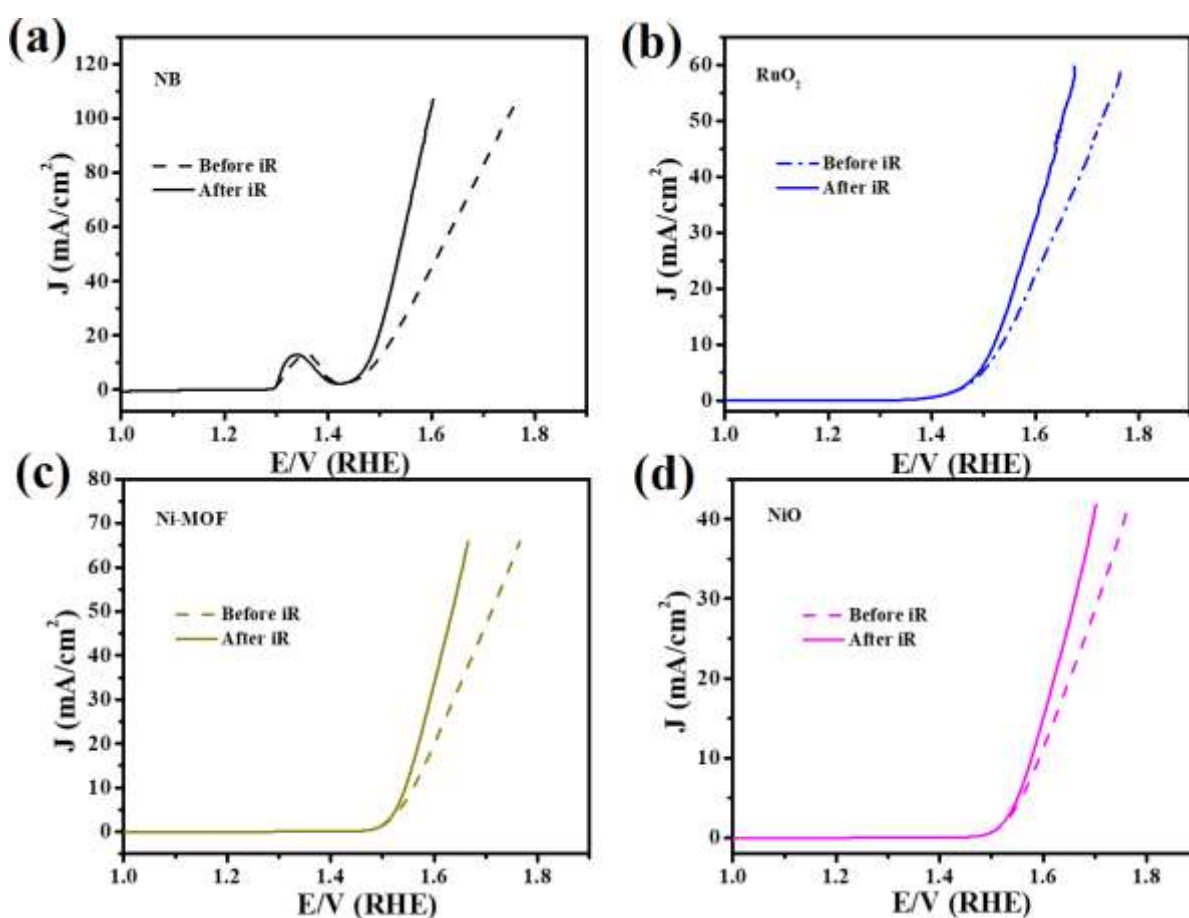


Figure 5.10 OER polarization curve obtained with the NiB, RuO₂, Ni-MOF and NiO modified electrodes in 1.0 M KOH electrolyte at scan rate of 5 mV/s with and without iR-compensation.

The uncompensated LSV curves are presented in Fig. 5.10. Further, the dominant OER performance of NiB has been analysed by measuring a number of parameters i.e., electrochemical accessible surface area (ECSA), roughness factor (R_f), mass activity (MA) and turnover frequency (TOF). At first, CVs at various scan rate are recorded in a non-Faradaic region (0.1- 0.16 V vs. Hg/HgO) and ECSA has been calculated from their surface specific double layer capacitances (C_{dl}) as per the equation 5.2 (Fig. 5.11, 5.12).

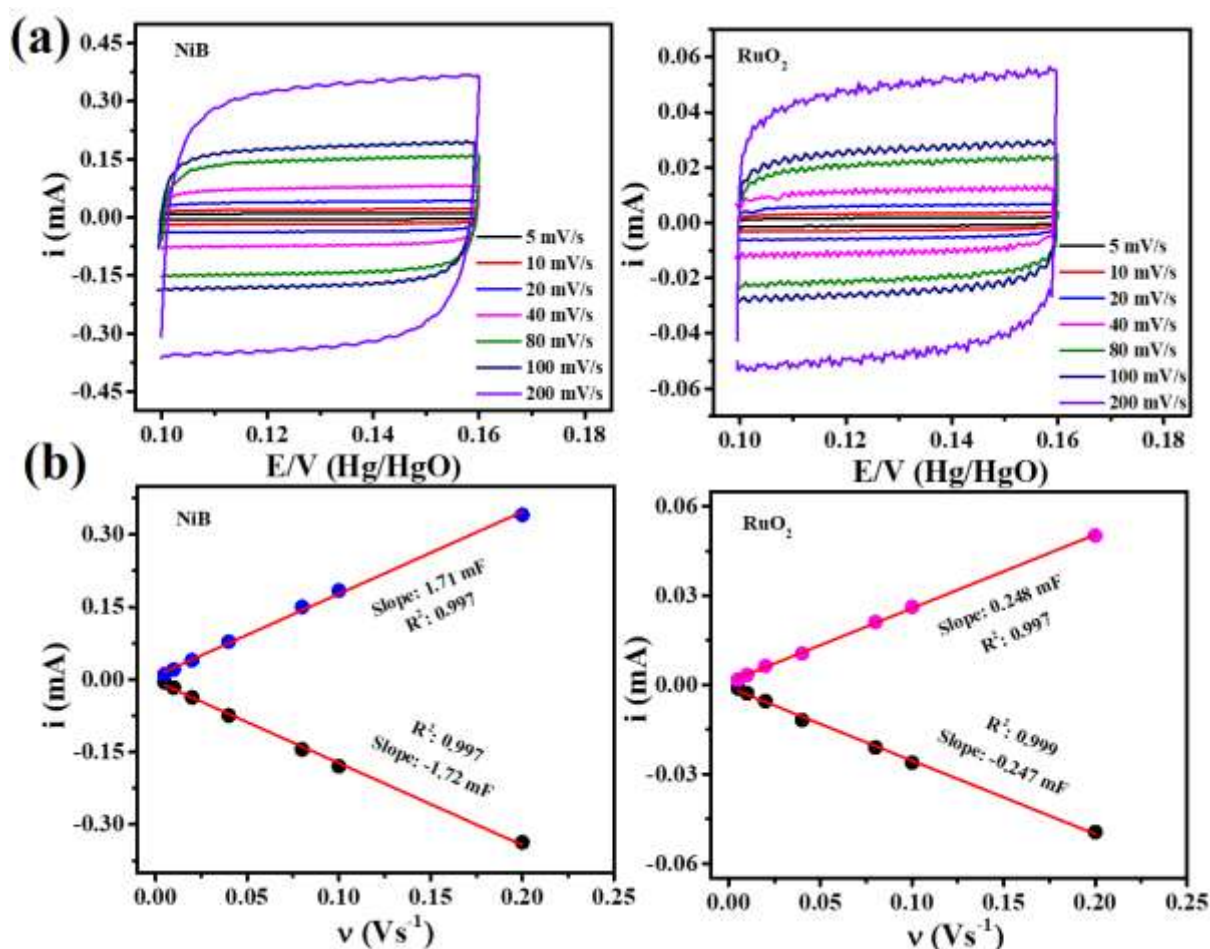


Figure 5.11 (a) CV for NiB and RuO₂ showing the charging currents measured in a non-Faradaic region at a scan rate of 5, 10, 20, 40, 80, 100, 200 mV/s respectively and (b) the plot of cathodic and anodic charging currents measured at 0.13 V (vs. Hg/HgO) against scan rates.

The NiB shows higher ECSA (42.875 cm²) compared to Ni-MOF (0.21 cm²), commercial NiO (0.927 cm²) and RuO₂ (6.187 cm²). It can be seen that the ECSA of NiB is much larger

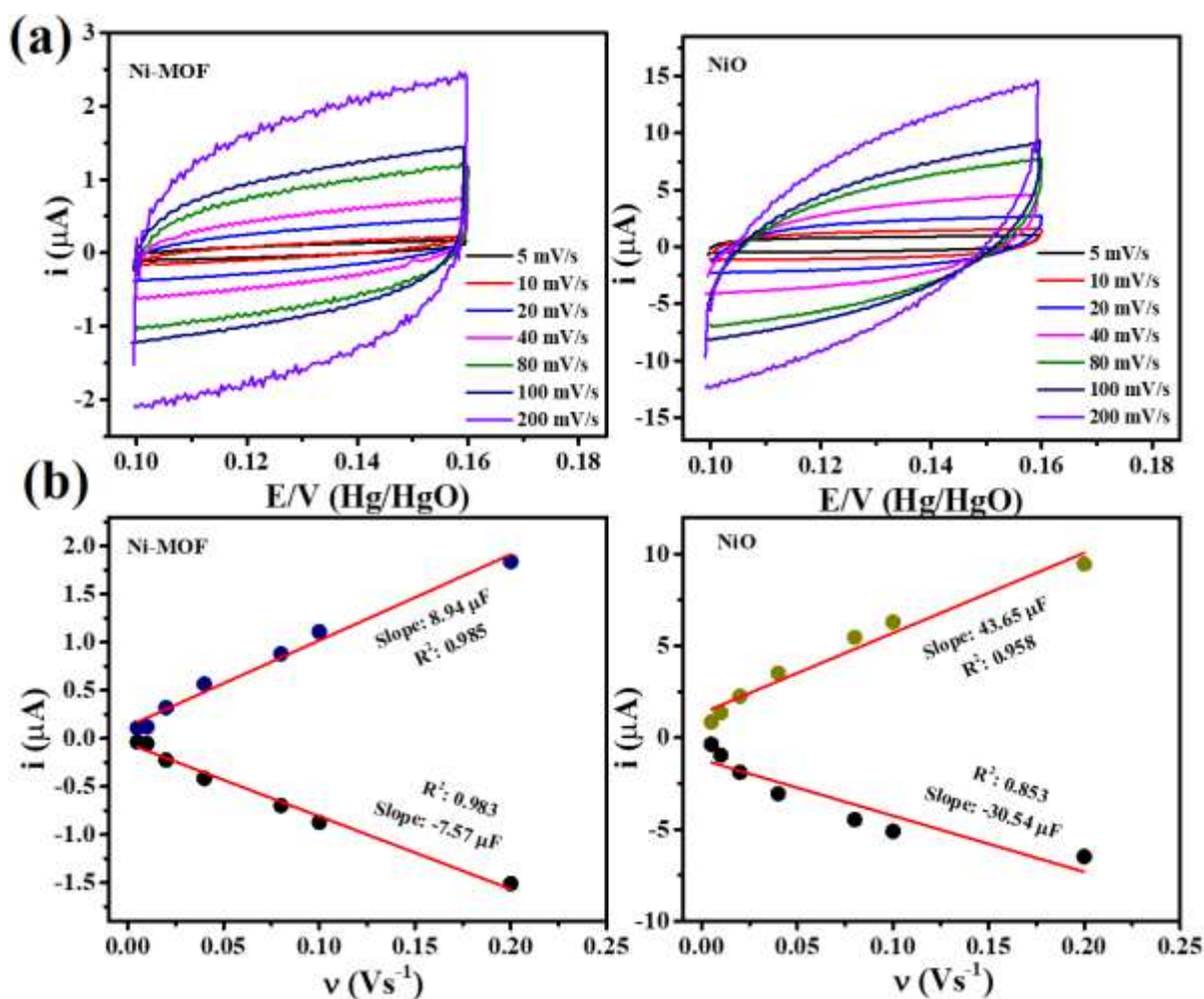


Figure 5.12 (a) CV for Ni-MOF and NiO showing the charging currents measured in a non-Faradaic region at a scan rate of 5, 10, 20, 40, 80, 100, 200 mV/s respectively and (b) the plot of cathodic and anodic charging currents measured at 0.13 V (vs. Hg/HgO) against scan rates.

compared to that of the parent Ni-MOF from which it has been derived demonstrating an improved electrochemical performance in aqueous electrolytic conditions passing the transcendence of this amorphous nature. Apart from a rigorous requirement of higher catalytic activity, the operational durability is an important key parameter for screening of an electrocatalyst towards its practical application. Therefore, the long-term stability test of NiB electrocatalyst was examined using chronopotentiometry technique (Fig. 5.7d) at 10 mA/cm² current density. Interestingly, it shows robust durability with a negligible increase (~5 mV) in overpotential after 15 hours of electrolysis. However, the Ni-MOF, NiO (after 13 hour) and

RuO₂ showed an increase of 62, 94 and 55 mV of overpotential after 15 hours of electrolysis. Here the strong interaction among the metal-metalloids centres of Ni-B might be responsible for such electrocatalytic stability in alkaline condition. As per the recent studies, the surfaces of metal chalcogenides, phosphides and nitrides based electrocatalysts are found to be partially oxidized to their corresponding metal oxides/oxyhydroxides during the process of OER in alkaline medium. Therefore, we have performed the morphology and compositional characterizations of the post OER stability NiB to analyse whether the similar phenomenon is happening in the present case or not.

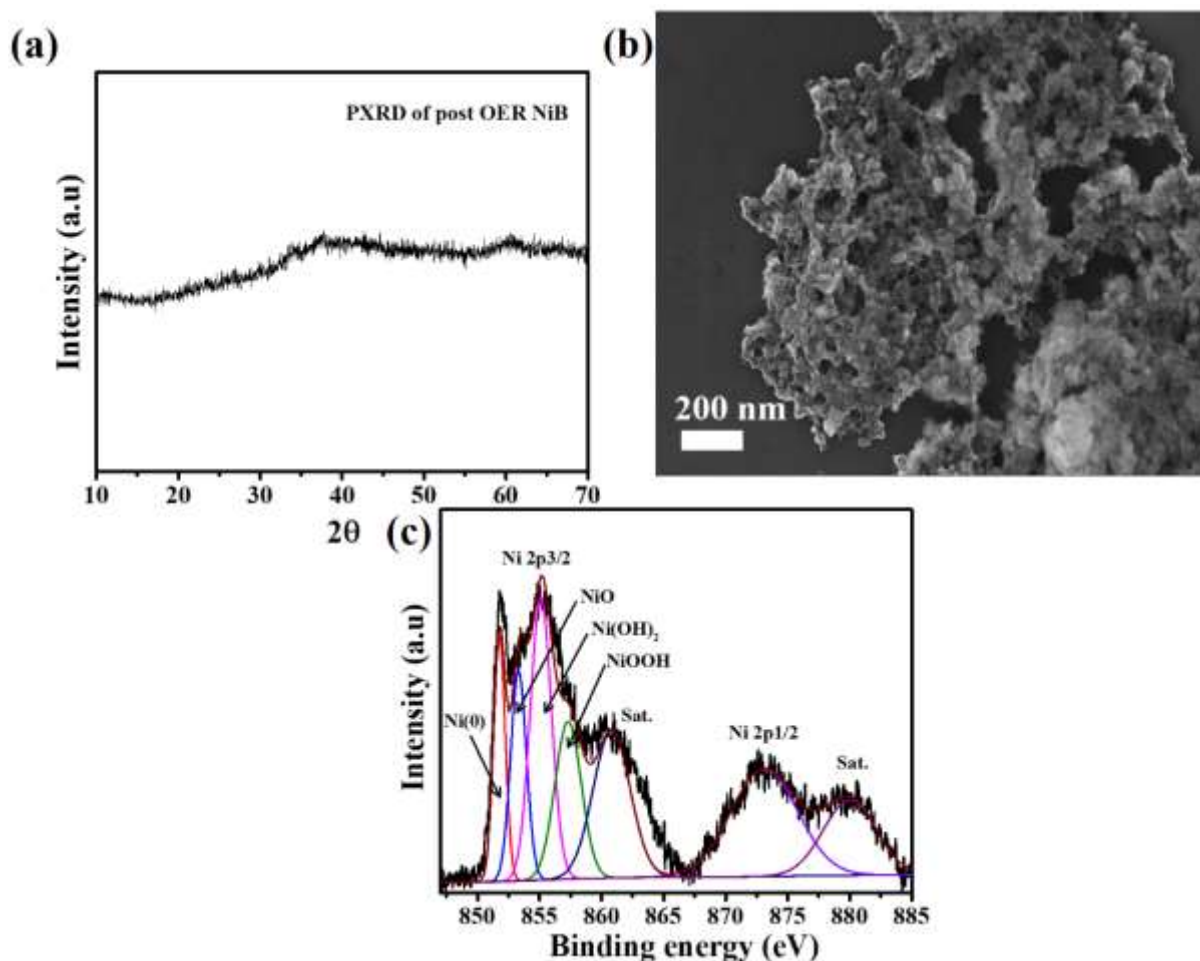


Figure 5.13 (a) powder X-ray diffraction and (b) FESEM of post OER stability (c) XPS of NiB.

At first, the powder X-ray diffraction of the post OER NiB has been analysed that shows almost amorphous as observed in the pristine NiB sample (Fig.5.13a). Also, NiB shows an unaltered surface morphology with a little aggregation which has been found in the FESEM images (Fig.5.13b). Further to elucidate the exact surface composition, the X-ray photoelectron spectroscopy of the post OER NiB sample has been analysed (Fig. 5.13c). It shows a reduced intensity of Ni 2p of Ni-B compared to that of pure NiB as discussed in the above section along with the existence of some oxidized species of Ni. On the basis of these findings, we propose that some of the Ni sites of NiB modified electrode get partially oxidized to the corresponding oxyhydroxides during the process of OER in such harsh alkaline condition.^{20,32} Therefore an in-situ formation of a core shell (NiB/NiOOH) like structure is assumed with NiB as the core and NiOOH shell and the observed dominated OER activity is ascribed to this NiB/NiOOH structure instead of the NiB alone. This might be the reason for better performance of this material over reported monometallic and bimetallic borides shown in table 5.1.

Table 5.1 Electrocatalytic OER activity of different electrocatalyst.

Catalysts	Electrolyte (Conc.)	Overpotential (mV) @ 10 mA/cm ⁻²	Tafel Slope (mV/dec)	References
Ni-Co-B	1 M KOH	300	113	Electrochim. Acta, 2019, 296 , 644–652.
Ni _x B-300	1 M KOH	380	89	Adv. Energy Mater., 2017, 7 , 1700381.
Ni _x B/f-MWCNT	1 M KOH	286	46.3	J. Mater. Chem. A, 2019, 7 , 764–774.
Ni-B-O @ Ni ₃ B	1 M KOH	264	127.0	Chem Electro Chem, 2019, 6 , 764–770.
NiB	1 M KOH	240	58	Present work

Electrochemical energy storage (Supercapacitor):

As per the above discussion, the NiB modified electrode shows more exposed surface area (i.e., higher ECSA) as well as anodic oxidation current density, which inspired us to analyse its energy storage performances. Thereafter, the potential application of NiB towards energy storage were assessed in a three-electrode set up using similar electrode arrangement (sample modified glassy carbon, Hg/HgO and platinum wire as working, reference and counter electrode respectively) in aqueous 5.0 M KOH electrolyte. In order to avoid the OER activity, the CVs were recorded in a narrow potential window of 0.45 V vs. Hg/HgO (in a range from 0-0.45 V vs. Hg/HgO) at different scan rates (1, 5, 10, 25, 50, 100 mV/s). As shown in Fig.

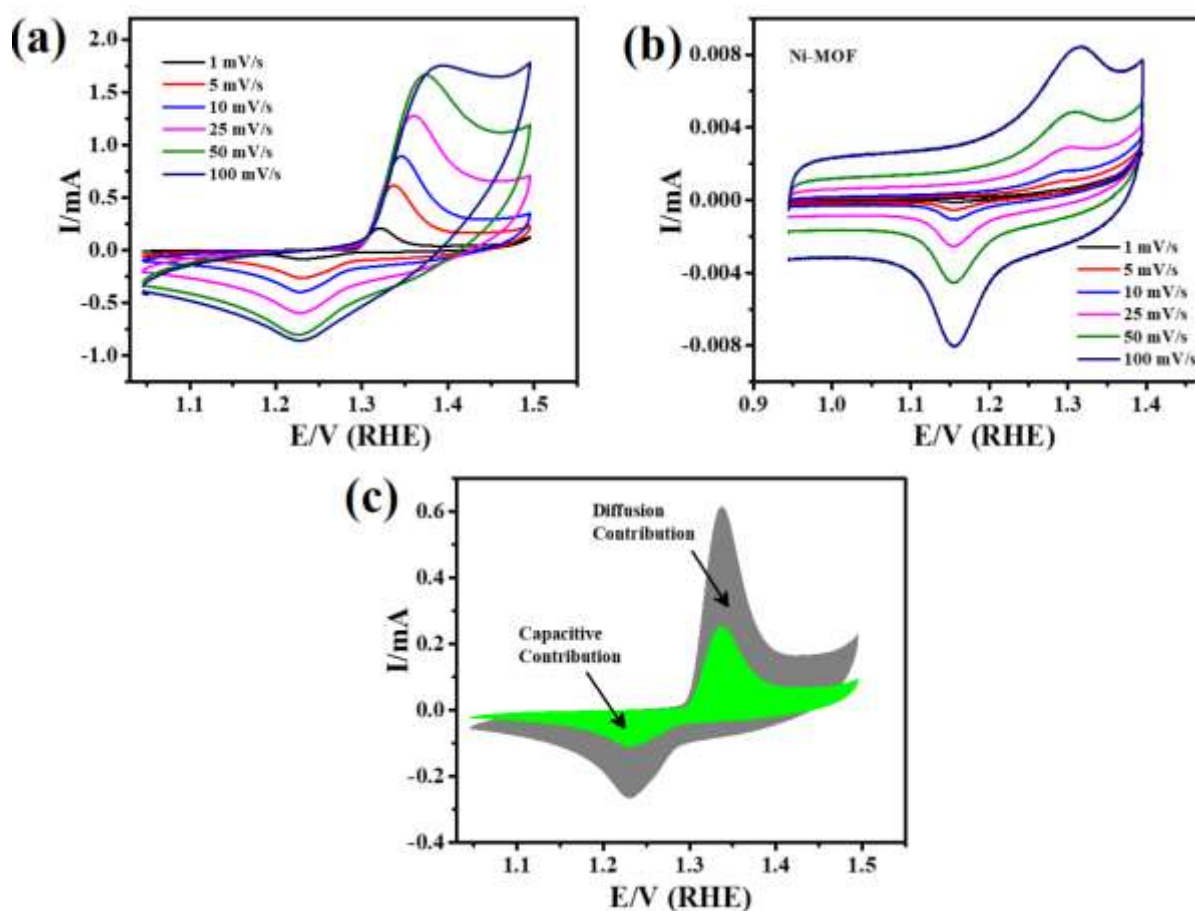


Figure 5.14 (a) CV curves of NiB modified electrode at different scan rates, (b) Cyclic voltammogram of Ni-MOF modified electrode at different sweep rate in 5.0 M KOH electrolyte (c) the CV curve at 5 mV/s scan rate showing the capacitive and diffusion contribution towards the net charge storage by NiB.

5.14a, the current densities of redox peaks increase proportionally with increase in the scan rates suggesting a relatively lower resistance and faster redox reactions at the electrode/electrolyte interfaces. Similar behaviour has also been noticed in CV of Ni-MOF modified electrode (Fig. 5.14b). However, compared to the parent Ni-MOF (7.0 F/g), the as derived NiB shows many folds higher value of specific capacitance (2580 F/g) with higher specific energy (72.55 Wh/kg) and power (33.43 kW/kg). Since the net stored charge is the sum of (i) surface capacitive and (ii) diffusion-controlled contributions, we have tried to qualitatively divide the percentage of contributions in both the Ni-MOF and NiB. Out of these two processes, the former process involves the adsorption/desorption of charged ions at the electrode/electrolyte interfaces (forming double layer) whereas the diffusion of ions among the electrode material and electrolyte drives the charge storage in latter case.^{21,35} At 5 mV/s scan rate, the NiB modified electrode stores charge through 41% of capacitive and 59% of diffusion-controlled processes (Fig. 5.14c). At first, the CVs of NiB modified electrode from 0.2 to 1.0 mV/s scan rate has been recorded (as Fig. 5.15a) and found well preservation of the CV shape with increasing of scan rate.

Thereafter, the degree of capacitive effect has been calculated from the relation among the observed current (*i*) and scan rate (*v*) from the CV curves as per the following equation,

$$i = av^b \dots\dots\dots (5.4)$$

Here both the “a” and “b” are the constants and the value of “b” varies from 0.5 to 1.0 that

calculated from the slope of the plot of $\log i$ vs. $\log v$ (Fig. 5.15b) Moreover, the galvanostatic charge-discharge profiles clearly coincide with the charge storage performances of NiB as observed from the CV profiles.

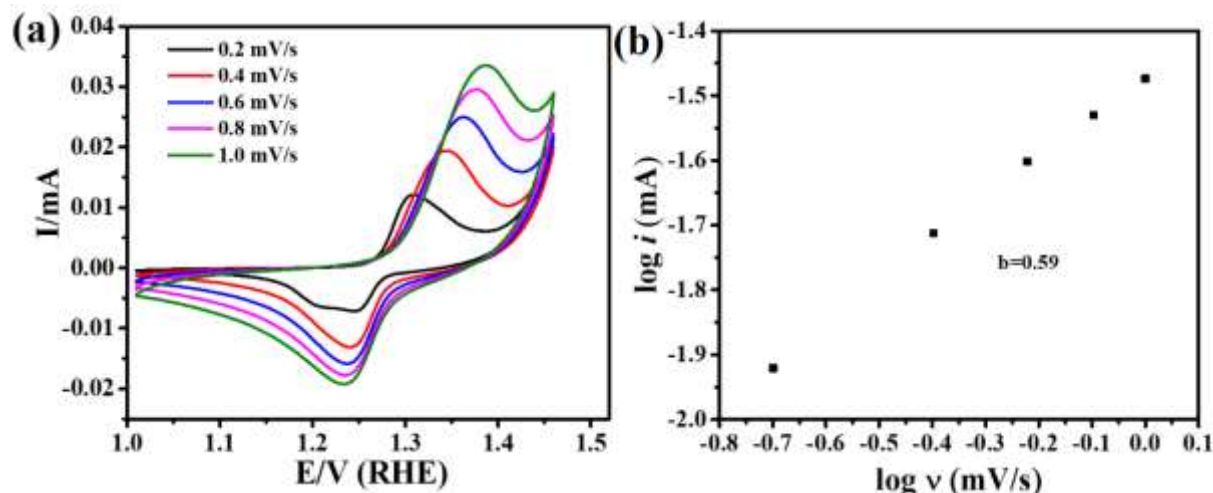


Figure 5.15 (a) CV curves at various scan rates of NiB and (b) plot of logarithm of anodic peak current and logarithm of scan rate.

As presented in Fig. 5.16a, a symmetrical behaviour of the GCD profiles at different applied current densities has been observed demonstrating better electrochemical reversibility of NiB.

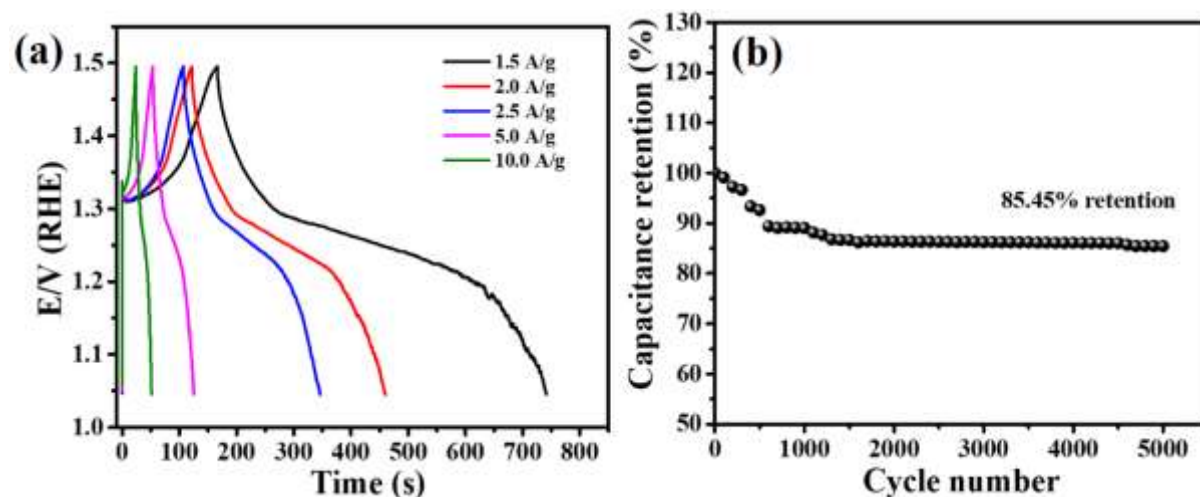


Figure 5.16 (a) GCD profiles at different applied current densities and (b) cycle life of NiB modified electrode.

These observations clearly justify the benefits of boronization of the synthesized MOF which not only tuned the crystal structure but also changed the redox behaviour of the sample thereby improving the electrochemical properties compared in table 5.2. Further, the NiB showed an excellent value of retention of initial capacitance (85.45%) after 5000 repeated cycles (Fig. 5.16b).

Table 5.2 Comparison of electrochemical charge storage performances of NiB with reported materials.

Electrode material	Specific Capacitance (F/g)	Power Density (W/kg)	Energy density (Wh/kg)	References
Ni-Co-B	2226.96	788.91	66.40	J. Power Sources, 2017, 341 , 75–82.
Co-Ni/Boride/Sulfide	1281	857.7	50.0	Adv. Mater., 2019, 31 , 1905744.
Ni _{0.33} Co _{0.67})Se ₂	827.9	800.0	291.0	Electrochim. Acta, 2018, 281 , 109–116.
Ni/Co-MOF-5 derived Ni-Co-S	1377.5	1066.42	36.9	Dalton Trans., 2018, 47 , 5639–5645.
NiB	2580.0	33.43 kW/kg	72.55	Present work

Asymmetric Supercapacitor (ASC) device fabrication and performance evaluation

Although, the NiB shows better electrochemical energy storage performances compared to the recently reported metal borides and other transition metal nanostructures but the narrow potential window (0.45 V) restricts its practical usability of interest.

Therefore, an asymmetric supercapacitor (rGO//NiB) has been devised by using the as synthesized rGO as the negative and NiB as positive electrode material. Prior to the device assembly, the potential window optimization and mass calculation were carried out. At first, the three-electrode measurement was performed taking the sample (rGO, NiB) modified GCE, Hg/HgO and bare platinum wire as the working, reference and auxiliary electrode in 5 M KOH aqueous electrolyte. In both the cases, the cyclic voltammograms were recorded at a sweep rate

of 25 mV/s varying the potential window. As illustrated in the Fig. 5.17 a, b, the shape of the CV plots for the rGO are of nearly rectangular in shape up to the potential of 1.05 V, and at higher potential a slight inclination was observed. Moreover, the potential ranges from 0 to -1.05 V without any redox peaks demonstrating the EDLCs behaviour. Similarly, in case of the NiB modified electrode, due to the oxidation of aqueous electrolyte, a rapid rise in oxidation current in the CV profile was observed on moving beyond 0.45 V. However, in the potential range of 0 to 0.45 V, the CVs show a slight EDLC and major redox contribution, demonstrating a dominating pseudo capacitive behaviour.

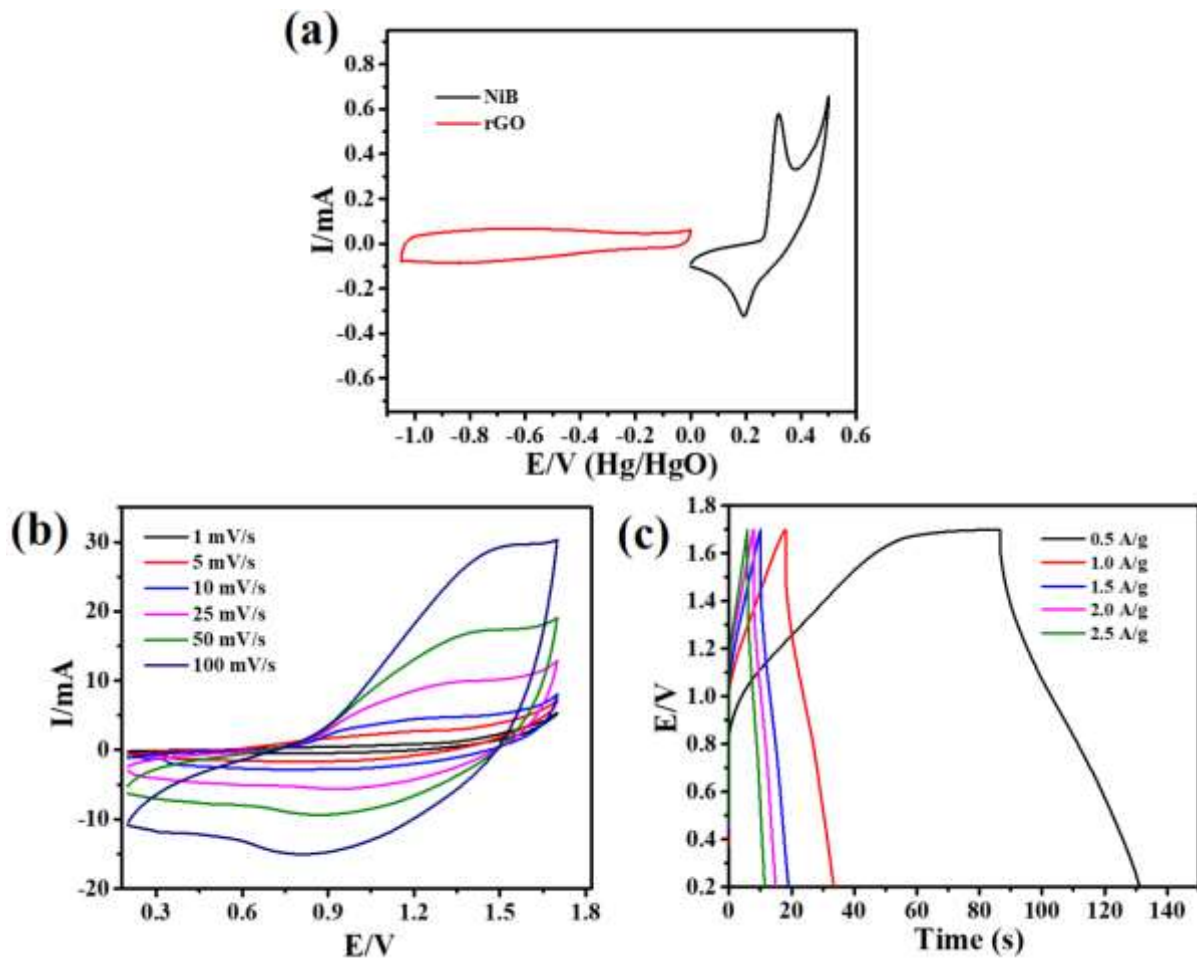


Figure 5.17 (a) CV curves showing the optimized potential window for rGO and NiB, (b) CV, (c) GCD of rGO//NiB ASC device.

From these observations, it was found that the lower potential for the negative electrode material and the upper potential limit for the positive electrode materials are -1.05 and 0.45 V respectively and the optimized potential window for the rGO//NiB ASC is 1.5 V (Fig.5.18a).

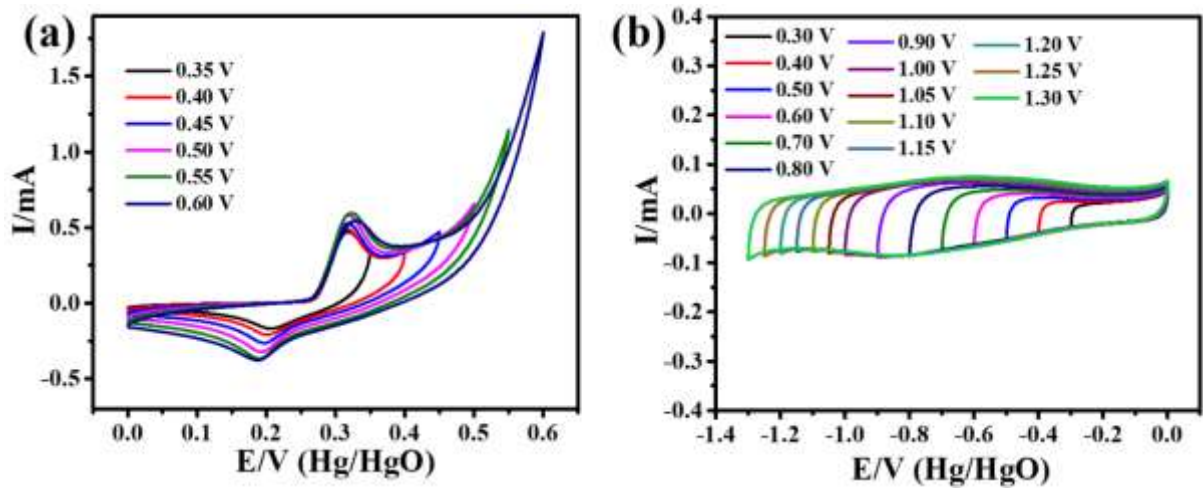


Figure 5.18 Cyclic voltammograms showing the potential window optimization for the (a) NiB and (b) rGO in 5 M KOH electrolyte at a scan rate of 25 mV/s.

Thereafter, the mass ratio of rGO to NiB was calculated by balancing the charge as per the following equation,³⁶

$$\frac{m^+}{m^-} = \frac{C_s^- \Delta v^-}{C_s^+ \Delta V^+} \dots\dots\dots (5.5)$$

Here, m , C_s and ΔV are the mass, specific capacitance and the optimized potential window for the positive (NiB) and negative(rGO) electrodes. Therefore, the calculated mass ratio for the NiB and rGO is 1:1.5. After getting the preliminary data, a prototype ASC in the Swagelok type cell (inset of Fig. 5.19a) configuration have been assembled. In details, 5 M KOH soaked PVDF membrane as separator is impregnated in between the rGO (cathode) and NiB (anode) casted stainless-steel electrodes and the cell was assembled properly (tightening the cell by hand) prior to each measurement. The CVs and GCD profiles were recorded at various scan rates and applied current densities and presented in Fig. 5.18b and c. The CVs show nearly rectangular in shape with very slight redox peaks suggesting behaviour different from both of

the rGO and NiB modified electrodes. It is due to the reason that, the asymmetric SCs integrates the performances of both the positive and negative electrodes and gave a mutual complementary shape to the CV profiles. A specific capacitance of 83.33 F/g (at 0.5 A/g) was calculated from the GCD profiles with an energy density of 26.04 Wh/kg at a specific power of 2.08 kW/kg. In order to verify the operational durability of the as fabricated ASC device, the cyclic stability was performed by using the GCD technique at an applied current density of 2 A/g and presented in Fig. 5.19a.

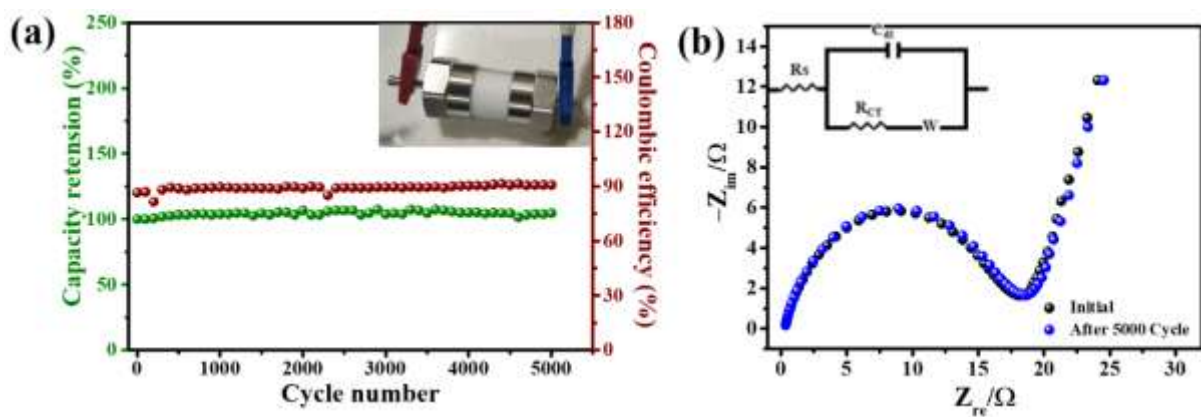


Figure 5.19 (a) Plot showing capacitance retention and coulombic efficiency of the ASC. (b) Nyquist impedance spectrum of the rGO//NiB ASC before and after 5000 GCD cycles. The inset in (a) is the Swagelok electrode of rGO//NiB ASC device.

It has been observed that there is a negligible change in the capacitance retention value with 96% after 5000 continuous GCD cycles, demonstrating excellent long term cyclic stability. Besides, it shows coulombic efficiency of 90% depicting better reversible properties of the electrode material. In addition to it, the Nyquist impedance spectrum was recorded at the initial stage and after 5000 cycles and is presented in Fig. 5.19b. It has been found that, after 5000 repeated cycles, the ASC cell exhibits almost similar charge transfer resistance of 18 Ω at the higher frequency region, demonstrating the maintained charge transfer property of the device. Further, the powder X-ray diffraction (Fig. 5.20a) and FESEM image (Fig.5.20b) of NiB after stability measurement has been collected and presented in Fig. 5.20 a, b. The diffraction pattern

indicates the existence of NiB in amorphous form with an unaltered surface morphology (with a little aggregation as observed in case of post OER stability NiB).

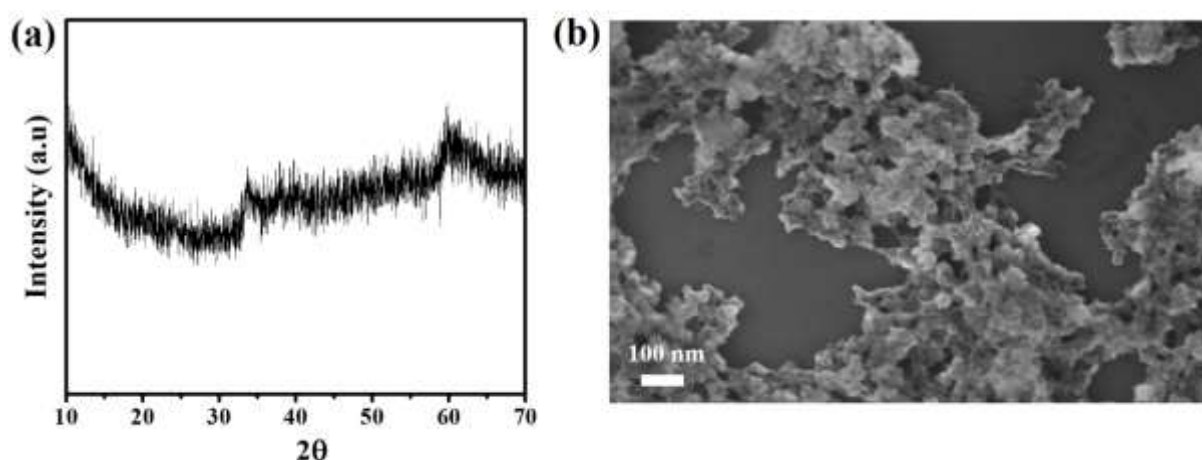


Figure 5.20 (a) powder X-ray diffraction and (b) FESEM of post supercapacitor stability NiB.

The less expensive, facile synthetic approach, excellent electrocatalytic activity and charge storage performances present the suitability of the NiB to be employed in future energy conversion and storage systems.

5.9 Conclusions

In summary, a single step redox approach is presented here for the synthesis of amorphous NiB from a crystalline Ni-MOF. It develops more electrochemical catalytic active centres as well as accessible surface area thereby improving the electrocatalytic and charge storage performances of the MOF. The NiB found to catalyse the OER efficiently compared to not only the commercial benchmarked catalyst RuO_2 , parent Ni-MOF and commercial NiO but also outperforms many of the reported boride based electrocatalysts. It needs only 240 mV overpotential to generate 10 mA/cm^2 current density with robust stability (showing a negligible change in overpotential after 15 hour of electrolysis). Though the structural and crystallinity robustness has been noticed from the FESEM and PXRD analysis of post OER stability NiB sample, but the transformation of NiB surface to the corresponding oxyhydroxides has been revealed from the XPS analysis. Therefore, we presumed that the formation of a core shell

(NiB/NiOOH) like structure with NiB as the core and NiOOH shell acts as the real active electrocatalytic centre for OER. Moreover; the NiB modified electrode exhibits very high specific capacitance of 2580 F/g with better cyclic stability (85.45% capacitance retention after 5000 repeated cycles). Therefore, an asymmetric supercapacitor is devised in a Swagelok type electrode with rGO and NiB as cathode and anode electrode material respectively. The rGO//NiB ASC device smoothly operates in a wider potential window (1.5 V) delivering a specific capacitance of 83.33 F/g (at 0.5 A/g) with an energy density of 26.04 Wh/kg at a specific power of 2.08 kW/kg with excellent durability (96% specific capacitance retention after 5000 GCD cycles). With these interesting observations, we highly anticipated that this synthetic approach would provide valuable insights in the redox behaviour regulation of MOFs towards designing of efficient electrode materials for future energy conversion and storage systems.

5.10 References

- 1 T. Reier, Z. Pawolek, S. Cherevko, M. Bruns, T. Jones, D. Teschner, S. Selve, A. Bergmann, H. N. Nong, R. Schlögl, K. J. J. Mayrhofer and P. Strasser, *J. Am. Chem. Soc.*, 2015, **137**, 13031–13040.
- 2 Y. Lee, J. Suntivich, K. J. May, E. E. Perry and Y. Shao-Horn, *J. Phys. Chem. Lett.*, 2012, **3**, 399–404.
- 3 X. Li, Y. Fang, X. Lin, M. Tian, X. An, Y. Fu, R. Li, J. Jin and J. Ma, *J. Mater. Chem. A*, 2015, **3**, 17392–17402.
- 4 C. Yuan, H. Bin Wu, Y. Xie and X. W. Lou, *Angew. Chemie - Int. Ed.*, 2014, **53**, 1488–1504.
- 5 M. Gong, D. Y. Wang, C. C. Chen, B. J. Hwang and H. Dai, *Nano Res.*, 2016, **9**, 28–46.
- 6 F. Lyu, Q. Wang, S. M. Choi and Y. Yin, *Small*, 2019, **15**, 1–17.

- 7 S. Siracusano, N. Van Dijk, E. Payne-Johnson, V. Baglio and A. S. Aricò, *Appl. Catal. B Environ.*, 2015, **164**, 488–495.
- 8 S. Anantharaj, S. R. Ede, K. Sakthikumar, K. Karthick, S. Mishra and S. Kundu, *ACS Catal.*, 2016, **6**, 8069–8097.
- 9 W. Xia, A. Mahmood, R. Zou and Q. Xu, *Energy Environ. Sci.*, 2015, **8**, 1837–1866.
- 10 V. Augustyn, P. Simon and B. Dunn, *Energy Environ. Sci.*, 2014, **7**, 1597–1614.
- 11 S. Wang, P. He, Z. Xie, L. Jia, M. He, X. Zhang, F. Dong, H. Liu, Y. Zhang and C. Li, *Electrochim. Acta*, 2019, **296**, 644–652.
- 12 R. Chen, L. Liu, J. Zhou, L. Hou and F. Gao, *J. Power Sources*, 2017, **341**, 75–82.
- 13 S. Li, C. Shu, Y. Chen and L. Wang, *Ionics (Kiel)*, 2018, **24**, 201–209.
- 14 S. Li, L. Wang, J. Chu, H. Zhu, Y. Chen and Y. Liu, *Int. J. Hydrogen Energy*, 2016, **41**, 8583–8588.
- 15 G. Wang, L. Zhang and J. Zhang, *Chem. Soc. Rev.*, 2012, **41**, 797–828.
- 16 J. Yan, Q. Wang, T. Wei and Z. Fan, *Adv. Energy Mater.*, 2014, **4**, 1300816.
- 17 H. Ji, X. Zhao, Z. Qiao, J. Jung, Y. Zhu, Y. Lu, L. L. Zhang, A. H. MacDonald and R. S. Ruoff, *Nat. Commun.*, 2014, **5**, 3317.
- 18 Q. Wang, J. Yan and Z. Fan, *Energy Environ. Sci.*, 2016, **9**, 729–762.
- 19 X. Luo, Q. Zhou, S. Du, J. Li, L. Zhang, K. Lin, H. Li, B. Chen, T. Wu, D. Chen, M. Chang and Y. Liu, *ACS Appl. Mater. Interfaces*, 2018, **10**, 42335–42347.
- 20 K. Srinivas, Y. Chen, B. Wang, B. Yu, X. Wang, Y. Hu, Y. Lu, W. Li, W. Zhang and D. Yang, *ACS Appl. Mater. Interfaces*, 2020, **12**, 31552–31563.
- 21 Q. Wang, Y. Luo, R. Hou, S. Zaman, K. Qi, H. Liu, H. S. Park and B. Y. Xia, *Adv. Mater.*, 2019, **31**, 1–8.
- 22 R. K. Tripathy, A. K. Samantara and J. N. Behera, *Dalt. Trans.*, 2019, **48**, 10557–10564.

- 23 C. Chen, M. K. Wu, K. Tao, J. J. Zhou, Y. L. Li, X. Han and L. Han, *Dalt. Trans.*, 2018, **47**, 5639–5645.
- 24 T. Wang, R. Jin, X. Wu, J. Zheng, X. Li and K. Ostrikov, *J. Mater. Chem. A*, 2018, **6**, 9228–9235.
- 25 X. Li, S. You, J. Du, Y. Dai, H. Chen, Z. Cai, N. Ren and J. Zou, *J. Mater. Chem. A*, 2019, **7**, 25853–25864.
- 26 J. Cheng, S. Chen, D. Chen, L. Dong, J. Wang, T. Zhang, T. Jiao, B. Liu, H. Wang, J. J. Kai, D. Zhang, G. Zheng, L. Zhi, F. Kang and W. Zhang, *J. Mater. Chem. A*, 2018, **6**, 20254–20266.
- 27 C. Gao, S. Liu, L. Xie, Y. Ren, J. Cao and C. Sun, *CrystEngComm*, 2007, **9**, 545–547.
- 28 W. S. Hummers and R. E. Offeman, *J. Am. Chem. Soc.*, 1958, **80**, 1339.
- 29 J. K. Das, A. K. Samantara, S. R. K. A., C. S. Rout and J. N. Behera, *Dalt. Trans.*, 2019, **48**, 15955–15961.
- 30 J. Masa, I. Sinev, H. Mistry, E. Ventosa, M. de la Mata, J. Arbiol, M. Muhler, B. Roldan Cuenya and W. Schuhmann, *Adv. Energy Mater.*, 2017, **7**, 1–8.
- 31 M. Zeng, H. Wang, C. Zhao, J. Wei, K. Qi, W. Wang and X. Bai, *ChemCatChem*, 2016, **8**, 708–712.
- 32 X. Chen, Z. Yu, L. Wei, Z. Zhou, S. Zhai, J. Chen, Y. Wang, Q. Huang, H. E. Karahan, X. Liao and Y. Chen, *J. Mater. Chem. A*, 2019, **7**, 764–774.
- 33 M. W. Louie and A. T. Bell, *J. Am. Chem. Soc.*, 2013, **135**, 12329–12337.
- 34 R. Chen, H. Y. Wang, J. Miao, H. Yang and B. Liu, *Nano Energy*, 2015, **11**, 333–340.
- 35 D. Chao, P. Liang, Z. Chen, L. Bai, H. Shen, X. Liu, X. Xia, Y. Zhao, S. V. Savilov, J. Lin and Z. X. Shen, *ACS Nano*, 2016, **10**, 10211–10219.
- 36 M. S. Javed, N. Shaheen, S. Hussain, J. Li, S. S. A. Shah, Y. Abbas, M. A. Ahmad, R. Raza and W. Mai, *J. Mater. Chem. A*, 2019, **7**, 946–957.

Summary

